Probing galaxy evolution below the noise threshold with radio observations

Author:

Eliab D. Malefahlo

Supervisor:

Prof Mario Santos

Prof Matt Jarvis

A thesis submitted in fulfilment of the requirements

for the degree of

Doctor of Philosophy

in the

Centre for Radio Cosmology

Department of Physics and Astronomy

University of the Western Cape

Declaration of Authorship

I, Eliab D. Malefahlo, declare that this thesis titled, 'Probing galaxy evolution below the noise threshold with radio observations' and the work presented in it is my own work, that it has not been submitted for any degree or examination in any other university, and that all the sources I have used or quoted have been indicated and acknowledged by complete references.

The work in this thesis has been done under the supervision of Mario Santos (University of the Western Cape/SARAO) and Matt Jarvis (University of Oxford/University of the Western Cape). In collaboration with Sarah White (Rhodes University) and Jonathan Zwart.

Part of this thesis has been published in peer-reviewed journal:

- Chapter 2 and Chapter 3: Eliab Malefahlo, Mario G. Santos, Matt J. Jarvis, Sarah V. White, and Jonathan T. L. Zwart. The optically selected 1.4-GHz quasar luminosity function below 1 mJy. *MNRAS*, 492(4):5297–5312, March 2020a. doi: 10.1093/mnras/staa112.
- Chapter 4 (Submitted): Eliab D. Malefahlo, Matt J. Jarvis, Mario G. Santos, Sarah V. White, Nathan J. Adams, and Rebecca A. A. Bowler. A deep radio view of the evolution of the cosmic star-formation rate density from a stellar-mass selected sample in VLA-COSMOS. *arXiv e-prints*, art. arXiv:2012.09797, December 2020b.

April 2021

UNIVERSITY OF THE WESTERN CAPE

Abstract

Faculty of Physical Science
Department of Physics and Astronomy

Doctor of Philosophy

Probing galaxy evolution below the noise threshold with radio observations

by Eliab D. Malefahlo

The faint radio population consisting of star forming galaxies (SFG) and radio-quiet active galactic nuclei (AGN) is important in the study of galaxy evolution. However, the bulk of the faint population is below the detection threshold of the current radio surveys. I study this population through a Bayesian-stacking technique that I have adapted to probe the radio luminosity function (RLF) below the typical 5σ detection threshold. The technique works by fitting RLF models to radio flux densities extracted at the position of galaxies selected from an auxiliary catalogue. I test the technique by adding Gaussian noise (σ) to simulated data and the RLF models are in agreement with the simulated data for up to three orders of magnitude (3 dex) below the detection threshold (5σ).

The source of radio emission from radio quiet quasars (subset of AGN) is widely debated. I apply the technique to 1.4-GHz flux densities from the Faint Images of the Radio Sky at Twenty-cm survey (FIRST) at the positions of the optical quasars from the Sloan Digital Sky Survey (SDSS). The RLF models are constrained to 2 dex below the FIRST detection threshold. I found that the radio luminosity where radio-quiet quasars emerge coincides with the luminosity where SFGs are expected to start to dominate the RLF. This Implies that the radio emission of radio-quiet quasars and radio-quiet AGN, in general, could have a significant contribution from star formation in the host galaxies.

Unaffected by dust, radio observations provide a largely unbiased view of star formation in galaxies and can potentially measure the unbiased cosmic star formation rate density (SFRD). I apply the Bayesian-stacking technique using RLF models

with AGN and SFG components to radio flux densities from the VLA-COSMOS 3-GHz survey at the position of stellar mass-limited galaxies from UltraVista. The cosmic SFRD is inferred from the RLF models of SFGs at different redshifts using a radio to star formation rate conversion. I measure a SFRD, that is constrained to lower radio luminosities, up to $z \sim 3.5$ and find that the SFRD increases from $z \sim 0.3$ to $z \sim 1.5$. Above $z \sim 1.5$ the SFRD declines towards higher redshifts.

Acknowledgements

Firstly I would like to thank the Lion King of Judah the, living God for the life He has granted me. I wish to express my sincere appreciation and gratitude to my supervisors Mario and Matt for their guidance, encouragement, patience and willingness to help. Completing this work during a pandemic had extra complications and your continuous support made it possible. I would like to thank Jonathan for his help with the code and proofreading my earlier work. A big thank you to Sarah for her help with the SF project. I would also like to thank Nathan and Rebecca for providing the data for the SFRD project.

A special thanks to the head of our group Roy, you were always ready and willing to help us with problems that hindered our research. A massive thanks to the people that maked things happen in the department Michelle, Nonmbuyiselo, Mfundo, Lisa, Egraim and Angela. A massive thanks to the CRC and Astro group at large, for creating a conducive environment for research. I would also like to thank my office mates for their support over the years; Marc, Tk, Sbonelo, Siyanda, Sultan, Sheean, Sbu, Modisha, Una, Nicole, Xola, Narusha, Junaid, with special thanks to my brother Siya, my neighbour Brandon and my homeboy Emanuel. There was never a dull moment in the office, which I sincerely missed during the lockdown. Big thanks to postdocs who supported me during this journey; Margarita, Imogen, Matt, Martha, Jingying and Jose.

A big thanks to Garret, Ashling and the Newton Fund for providing the opportunity for me to do my research in Oxford.

I would like to thank my spiritual family for their support, firstly, the two I have relied on over the years, Priests Masekwameng and Photo. My brothers; Tebatso (Mr TK), Nhlamolo, Lotanang, Mateala, Mohau (my Chair), Ndo, Phomolo and Sbu. My sisters; Tebogo (sesi T), Texco and Gift. Huge thanks to my relatives for always supporting me and cheering me on especially sesi Maki and sesi Keko. I would like to thank my siblings (T-man, Pabi, BB, Tshire) for always cheering me on. I definitely would not have made it this far without the love and continued support from my parents. Special thanks to my mothers; Mamogolo, Mrs Adams, Mme Saya, Mme Mamsimang, Mme Phosa.

Lastly, I would like to acknowledge the National research foundation (NRF), South African Radio observatory (SARAO) and CRC for their financial assistance during

my studies. I thankfully acknowledge the computer resources from the Centre of high performance computing (CHPC).

Contents

Declaration of Authorship ii

Abstract ii

Acknowledgements v

Contents vii

1 Introduction 1
- 1.1 Galaxy formation and evolution . . . 1
- 1.2 Galactic processes . . . 3
  - 1.2.1 Star formation . . . 3
    - 1.2.1.1 Molecular clouds . . . 4
    - 1.2.1.2 Gravitational collapse . . . 4
    - 1.2.1.3 Protostar . . . 4
    - 1.2.1.4 Star formation rate . . . 6
    - 1.2.1.5 Far-Infrared Radio correlation . . . 8
    - 1.2.1.6 Star formation main sequence . . . 9
  - 1.2.2 Active nuclei . . . 10
    - 1.2.2.1 Unification model of AGN . . . 11
    - 1.2.2.2 Radio loudness . . . 13
  - 1.2.3 Feedback . . . 15
- 1.3 Radio sky . . . 17
  - 1.3.1 Brief History . . . 17
  - 1.3.2 Radio emission . . . 19
    - 1.3.2.1 Free-free emission . . . 19
    - 1.3.2.2 Synchrotron radiation . . . 22
  - 1.3.3 Radio sources . . . 24
    - 1.3.3.1 Bright radio sky . . . 24
    - 1.3.3.2 Sub-mJy and μJy radio populations . . . 25
- 1.4 Optical and near-infrared emission . . . 27
- 1.5 Science below the detection threshold . . . 28

1.5.1 P(D) analysis . . . 29
1.5.2 Stacking . . . 31
1.6 Thesis outline . . . 33

2 Beyond stacking **35**
2.1 Introduction . . . 35
2.2 Bayesian framework for measuring the RLF . . . 37
2.2.1 Likelihood function . . . 38
2.2.2 Radio luminosity function models . . . 39
2.2.3 Priors . . . 43
2.3 Tests on simulated data . . . 43
2.3.1 Shallow sample . . . 44
2.3.2 Deep sample . . . 49
2.4 Summary . . . 50

3 1.4-GHz quasar luminosity functions **53**
3.1 Introduction . . . 53
3.2 Data . . . 54
3.2.1 The optical quasar sample . . . 55
3.2.2 Radio data . . . 56
3.2.3 Cross-matching catalogues . . . 57
3.3 Results . . . 63
3.3.1 Quasars at $0.2 < z < 0.45$ . . . 63
3.3.2 Higher-redshift bins . . . 68
3.4 Discussion . . . 69
3.4.1 Radio-loud quasars . . . 69
3.4.2 Radio-quiet quasars . . . 71
3.5 Conclusions . . . 73
3.6 Appendix . . . 74
3.6.1 Triangle plots . . . 74

4 Cosmic star-formation rate density **81**
4.1 Introduction . . . 81
4.2 Data . . . 82
4.2.1 Near-infrared data . . . 82
4.2.1.1 Photometric redshifts and stellar masses . . . 82
4.2.1.2 Sample . . . 84
4.2.1.3 Completeness . . . 84
4.2.2 Radio data . . . 85
4.2.3 Flux-density extraction . . . 85
4.3 Results . . . 91
4.3.1 The binned RLF . . . 91
4.3.2 The free RLF models . . . 92
4.3.3 The fixed RLF model . . . 93
4.4 Cosmic history of star formation . . . 95

4.4.1 Comparison to the literature 99
4.4.1.1 Comparison with the radio-selected cosmic SFRD . 99
4.4.1.2 Comparison to other studies 100
4.4.2 Contribution from different stellar mass populations 102
4.5 Conclusions 105
4.6 Appendix 107

5 Conclusions **118**
5.1 Summary of results 119
5.2 Future work 121

Bibliography **123**

Chapter 1

Introduction

1.1 Galaxy formation and evolution

According to the Λ Cold Dark Matter model (ΛCDM, the most accepted cosmological model), the primordial density of the universe was nearly uniform, with minor fluctuations (Peebles, 1982; Bardeen et al., 1986; Sugiyama, 1995). The density fluctuations led to the accretion of dark matter, through gravitational interactions, forming dense clumps called dark matter halos (White and Rees, 1978). The dark matter halos continued interacting gravitationally, accreting dark matter and hierarchically merging with other halos to form larger halos. Primordial gas (composed of $\sim$ 75% hydrogen and $\sim$ 25% helium) is also accreted into the halos and if the mass is large enough, the gas collapses, fragments, cools and eventually forms (proto)galaxies and stars (Larson, 1974; Silk, 1977; Rees and Ostriker, 1977). As a result, the galaxy properties are linked to the properties and interactions of the parent halo (Press and Schechter, 1974). The galaxies continued to form stars (see Chapter 1.2.1), interact and hierarchically merge with other galaxies (see Dayal and Ferrara, 2018, for a recent review of cosmic evolution and galaxy formation).

Today, galaxies are observed with a variety of different properties, such as colours, shapes and sizes, composition, masses, stellar populations, and luminosities. Some of these features have been observed since 1845 when William Parsons recorded a spiral structure in what was then known as a nebula within the Milky Way. Hubble (1925) showed that some of these nebulae were galaxies in their own right that came with a large variety of morphologies. This led to the first classification scheme, known as Hubble's Tuning Fork, which contained spiral and elliptical galaxies and

their sub-classes (Hubble et al., 1936). The current galaxy classification schemes are more complex with more galaxy types and sub-classes. How galaxies evolved from the first galaxies to the different galaxy types observed today is one of key goals of cosmology.

Large samples of galaxies are required to study the formation and galaxy evolution. Over the years, various surveys at different wavelengths have been conducted. The observations have been used to formulate and test theoretical models. The simplest and most straightforward experiments to perform with sources from these surveys is to count sources with certain flux densities per sky area, source counts. Source counts are a useful tool for probing galaxy evolution, as their shape are linked to the evolution of the sources and geometry of the universe (e.g. Ryle, 1955; Ryle and Scheuer, 1955). Using additional information about the distance of the sources, such as redshift, a more powerful tool called a luminosity function (LF) can be generated. A LF for a certain class of galaxies is the distribution of the luminosities (i.e. the relative number of galaxies with luminosities between L and ΔL) in the comoving volume in which the galaxies are observed. The LF is a powerful tool to probe galaxy evolution and formation, as it combines the luminosity of a galaxy with relative abundance.

One of the methods used to understand galaxy evolution is through a comparison of cosmological simulations governed by theoretical models with observable statistical properties such as source counts and LF from observations. Simulations have been used successfully to model and reproduce the dark matter distribution and large scale structure in the universe (e.g Davis et al., 1985; Springel et al., 2005), by considering gravitational interactions. However, these simulations are unable to fully model the formation and evolution of galaxies because some physical processes are not well understood. These processes are largely centred around dissipative gas dynamics. Semi-analytical simulations use approximations to describe the physical processes that are not understood (e.g. White and Frenk, 1991). The simulations were able to reproduce some of the observable properties. However, the bright and faint end of the galaxy LFs overestimated the observed LF in the local local universe (e.g. White and Frenk, 1991). Reconciling the galaxy LF from simulations to those from observations led to the introduction of a 'feedback' mechanism that prevents gas from cooling and forming stars in the simulations (e.g Benson et al., 2003; Granato et al., 2004; Croton et al., 2006). The increase in computational power has led to more complex approximation of the physical processes down to $\sim$

kiloparsec scales or lower. Current simulations, such as the Evolution and Assembly of Galaxies and their Environments (EAGLE Schaye et al., 2015) and SIMBA (Davé et al., 2019) are able to reproduce the rich diversity of observed colors, morphologies and star formation activity as well as know relations such as the black hole-galaxy properties (Thomas et al., 2019) and the Tully-Fisher relation (Glowacki et al., 2020).

1.2 Galactic processes

The diversity in galaxy properties observed today is a result of gas dynamical dissipative processes and gravitational interactions within the galaxy and with other systems such as galaxies (which can lead to mergers) or intergalactic dust. The gravitational interactions are well understood, however the physics that governs some of these internal galactic processes is not fully understood. These processes include: internal structures of gas, the radiative cooling of gas to form stars, production of heavy elements, effects of magnetic fields, generation of galactic outflows, Active galactic nuclei (AGN, Chapter 1.2.2) accretion and the effects of feedback.

Stars are one of the fundamental components of a galaxy. Furthermore, they trace the visible matter of the universe. Therefore, determining the buildup of stellar mass over cosmic time (also know as the cosmic history of star formation) can give some insight on the processes by which galaxies form and evolve. Determining the cosmic history of star formation relies on measuring the cosmic star formation rate density (SFRD, see Madau and Dickinson, 2014, for a review) over cosmic time.

1.2.1 Star formation

Star formation is a fundamental process that converts gas into stars. Most of the process that are not fully understood are linked to star formation. This process of star formation has been extensively studied in the literature . Below is a brief summary of the main ideas behind the process of star formation (for a recent detailed review, see Girichidis et al. 2020, and references therein).

1.2.1.1 Molecular clouds

Star formation in galaxies takes place in the interstellar medium (ISM). The ISM contains mainly two components, hot diffuse gas and cooler, denser molecular clouds. The molecular clouds are made up of molecular hydrogen (H_2), helium (He), dust grains of different shapes and sizes (Stecher and Donn, 1965; Mathis et al., 1977; Weingartner and Draine, 2001), carbon monoxide (CO) and other molecules (the first stars, referred to as Population III stars were born from primordial gas which only contained hydrogen and helium Yoshida et al. 2006). The molecular clouds were always thought to be uniform, however, over the years high-resolution observations of the molecules, gas and dust have proven them to have complex internal structures (André et al., 2010; Heyer and Dame, 2015; Kalberla and Kerp, 2016). These structures may be due to magneto-hydro-dynamical turbulence (Brandenburg and Lazarian, 2013).

1.2.1.2 Gravitational collapse

The molecular cloud remains in viral equilibrium, gravity being balanced by turblence pressure (Mac Low and Klessen, 2004). However, the filaments formed in reaction to the turbulence start to accrete surrounding material and individually grow in mass. The filaments, no longer in viral equilibrium owing to the increased mass, start to collapse into clumps. The individual clumps continue to accrete and collapse, while the central density increases. The increase in density increases the number of collisions between particles and the radiation generated from these interactions. The conservation of angular momentum causes the collapsing material to rotate, which leads to the formation of a circumstellar disk. The high density in the central regions leads to the central region becoming opaque and the heat generated in the collapse is trapped, which leads to an increase in temperature (Tohline, 1982).

1.2.1.3 Protostar

The clump continues to contract and when the central region reaches 20 000 K, the clump becomes a protostar. The protostar continues to collapse until the central regions reach the required temperature needed to ignite nuclear fusion. The fusion generates outward (radiation) pressure that balances the gravitation force (and hydrostatic equilibrium is reached again), which marks the birth of a new

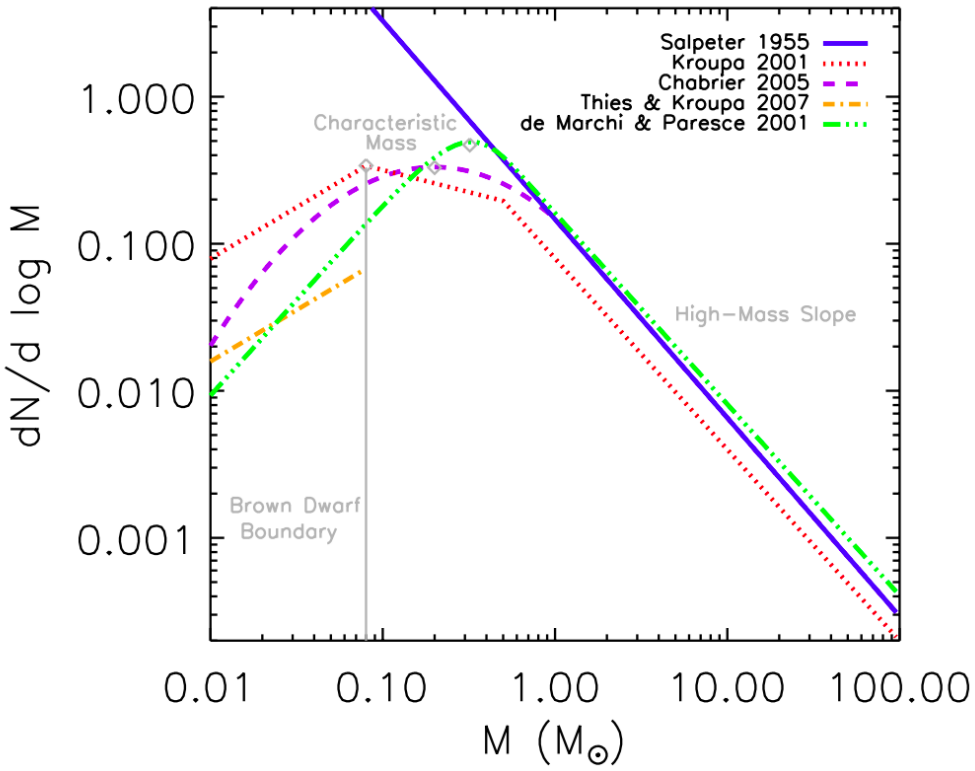

FIGURE 1.1: The initial mass functions (IMFs) from various stellar systems in our galaxy. The x-axis is the stellar mass and the y-axis is the number of stars in a logarithmic stellar mass range. Credit Offner et al. (2014)

star. protostars with insufficient mass do not reach the pressures and temperatures required to ignite fusion are called brown dwarfs (Laughlin and Bodenheimer, 1993; Burrows et al., 2001). Conversely, protostars with higher masses require higher pressure (and temperatures) to balance the self-gravitational force which leads to higher fusion rates and a more luminous protostar.

The other clumps (from the same cloud) have a chance of also collapsing and forming stars, resulting in the formation of a stellar group or association (Kruijssen, 2012). The newly formed stars have a range of masses, which depends on the mass of the individual clump and other factors such as accretion and interactions with other clumps/protostars during the collapse (Bonnell and Bate, 2006). Despite the importance of massive stars, (their high luminosity and role in feedback Chapter 1.2.3), it is not fully understood how they are formed. Simulations suggest that massive stars form in response to, i) the clumps/protostars accrating material from the parent molecular cloud or other clumps/protostars (Bonnell et al., 1997) or ii) clumps/protostars merging (Bonnell and Bate, 2002).

The mass distribution of the stars is such that there are few massive mass stars and the number of stars increase with decreasing mass. The relative number of stars of a certain mass produced during star formation is called the initial mass function (IMF) and it is often assumed to be universal for all star formation processes Salpeter (1955). The IMF is well described by a power law as shown in Figure 1.1 and well constrained at high masses, as massive stars are easier to observe owing to their high luminosities [1] (Salpeter, 1955). A number of studies that have investigated IMF in star associations and groups within our galaxy (Thies and Kroupa, 2007; Bastian et al., 2010) and in nearby galaxies (Massey and Olsen, 2003; Sabbi et al., 2008) show that the power law from Salpeter (1955) overestimates the number of low-mass sources. The actual shape of the low-mass end is still debated. Some authors suggest that the IMF is a double power law (with a different slope for the low mass-end, Kroupa, 2001) and others suggest it follows a modified Schechter function (a log-normal power law with a smooth transition between the high and low mass slopes Chabrier, 2003, 2005).

1.2.1.4 Star formation rate

The star formation rate (SFR, the total mass of stars formed per year) of a galaxy is measured in solar masses per year ($M_{\odot}$ yr^{-1}). The SFR of a galaxy depends on the amount of molecular gas available, as well the efficiency at which the molecular gas is converted into stars. The efficiency of SF depends on factors such as magnetic fields, heating or removal of material by shock waves or winds from AGN or supernova feedback (Chapter 1.2.3).

The SFR is measured through the light produced by the luminous young massive stars. The measurement relies on the conversion of light to mass as well as the IMF to get the total mass of stars formed given the most massive (e.g Kennicutt, 1998). Measuring the SFR in galaxies can be done with light from a variety of wavelengths including optical, ultraviolet (UV), far infrared (FIR) and radio (see Kennicutt, 1998; Kennicutt and Evans, 2012). The most sensitive tracer of luminous young massive stars ($> 8\ M_{\odot}$) within star-forming regions of galaxies comes from rest-frame UV observations. The depth that can be reached with current telescopes

[1] Although the bulk of the newly formed stars are low-mass, their contribution to their the total luminosity is negligible compared to the much more luminous high mass stars with high fusion rates. For this reason massive stars have short life spans because they burn thought their fuel faster.

means that very low star-formation rates can potentially be reached to very high redshifts (McLure et al., 2013; Bouwens et al., 2015; Adams et al., 2020; Bowler et al., 2020). Measurements from optical wavelengths are usually derived from hydrogen recombination lines in HII regions ionized by the UV emission from the most massive stars ($> 10\ M_{\odot}$). However, the rest-frame UV and optical are both readily absorbed by dust in the molecular clouds from which the stars were formed and along the line of sight to distant galaxies. This results in the SFR measurements made at these wavelengths having lower limits. The dust that absorbs this UV radiation is heated and re-radiates the energy at FIR wavelengths with a spectrum close to a blackbody (the thermal bump, see Fig. 1.5). The combination of UV, through to the FIR emission, can provide measurements of the total SFR in galaxies, both unobscured and obscured by dust (Burgarella et al., 2005; da Cunha et al., 2008; Berta et al., 2013; Smith and Hayward, 2018).

Unfortunately, FIR observations are generally limited in their spatial resolution. For example, the *Herschel* Space Observatory has a resolution of 18 arcsec at 250 μm (Pilbratt et al., 2010), leading to imaging surveys that are generally limited by source confusion. ALMA can detect this dust emission at much higher angular resolution, but these surveys are limited in area (e.g. Dunlop et al., 2017; Dudzevičiūtė et al., 2020a; Franco et al., 2020; Gruppioni et al., 2020; Yamaguchi et al., 2020), or rely on pointed observations of pre-selected samples (e.g. Boogaard et al., 2019; Zavala et al., 2019; Simpson et al., 2020). Thus, it is unsurprising that over the past few years, alternative tracers of star-formation rates of galaxies have been considered at other wavelengths (e.g. Ouchi et al., 2010; Drake et al., 2013; Schober et al., 2015; Aird et al., 2017). Possibly the most promising one comes from deep radio continuum observations at GHz frequencies. The radio SFR estimate relies on the FIR SFR through the far-infrared–radio correlation (FIRC) a tight correlation between the radio luminosity and the FIR luminosity of galaxies. The drawback of using radio luminosities to infer SFR is that there is no distinction between synchrotron-associated star-formation and that associated with the AGN. Multi-wavelength data are then required to disentangle the SF and AGN emission.

The different SFR estimates probe star formation at different timescales. The optical traces more massive stars with lifespans of 10 Myr, while UV and FIR trace SFR averaged over 100 Myr and radio over 10 Myr. This can lead to different estimations during an event that quenches or enhances star formation (e.g merger, starburst or Feedback, Hayward et al., 2014).

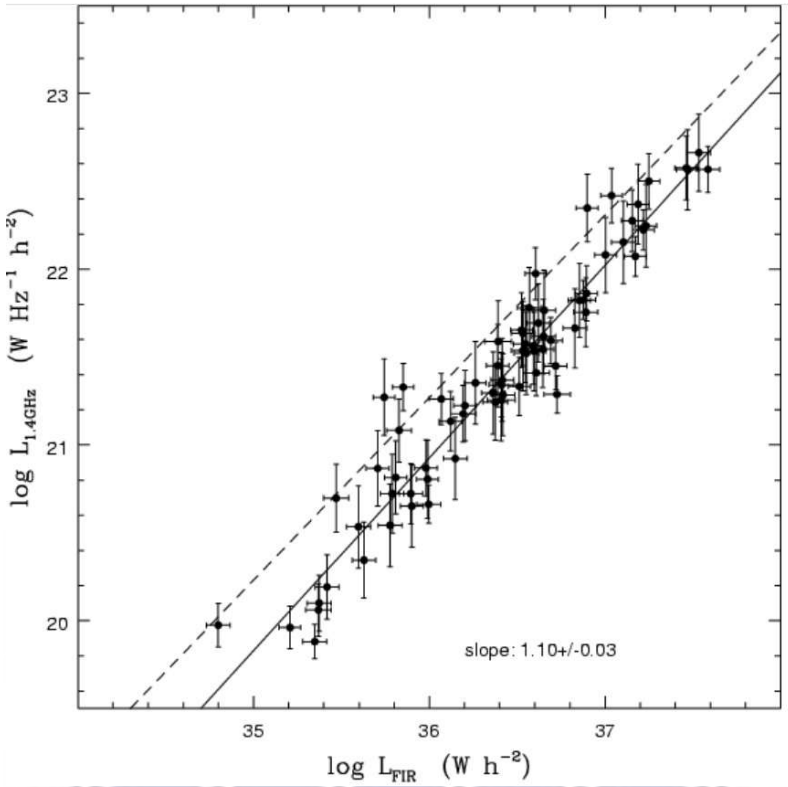

FIGURE 1.2: The far infrared radio correlation. The x-axis is the far infrared luminosity and the y-axis is the 1.4 GHz radio luminosity both in logarithmic scale. Credit Pierini et al. (2003)

1.2.1.5 Far-Infrared Radio correlation

The FIRC is a tight correlation between the radio luminosity and the total infrared (IR) luminosity of galaxies (e.g. van der Kruit, 1971; de Jong et al., 1985; Condon et al., 1991; Jarvis et al., 2010; Delhaize et al., 2017). The correlation spans over three orders of magnitude, as shown in Figure 1.2. Its existence has been attributed to young massive stars. After their short life-span, of a few million years, the massive stars reach a catastrophic end in a supernova explosion [2], which accelerates electrons that then emit synchrotron radiation observed in the radio. During their short lifetimes these same massive stars emit optical and UV radiation that is then absorbed and re-radiated into the IR by surrounding dust, thus resulting in a correlation between the radio synchrotron emission and the dust continuum emission. The correlation also holds for the total infrared luminosity (e.g. Delhaize et al., 2017), as re-radiated emission spans over the full IR spectrum (8 - 1000 μm).

[2]The explosion is responsible for releasing metals created in the core of the stars to the ISM

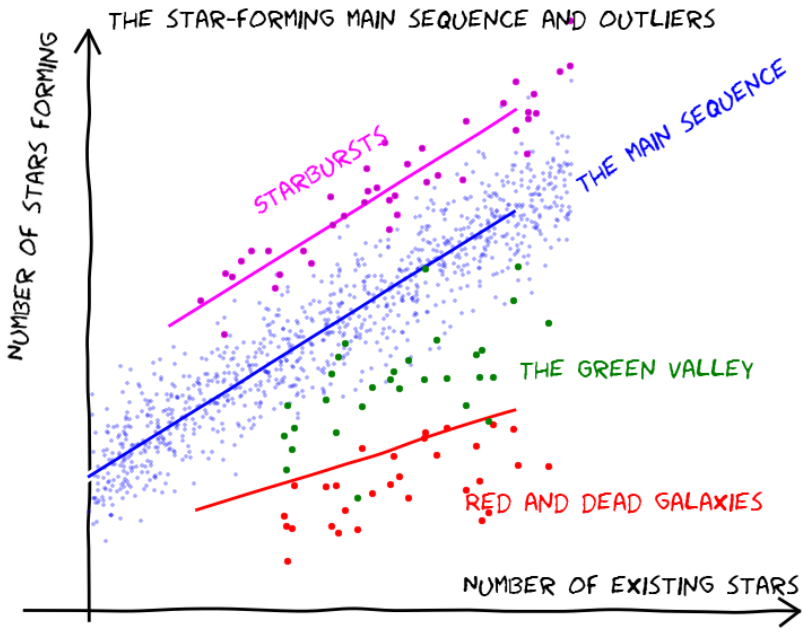

FIGURE 1.3: The star formation main sequence. The blue dots represent star forming galaxies in the sequence, the purple represents galaxies with high SFR, starburst. The green and red represents quenching and quenched galaxies. From http://candels-collaboration.blogspot.com/2013/02/star-formation-in-mountains.html

In recent years, it has become apparent that the form of the FIRC may also depend on other properties of the galaxy (e.g. Molnár et al., 2018; Read et al., 2018; Delvecchio et al., 2020). These dependencies could be due to excess radio emission due to AGN activity, or to the FIR emission not fully accounting for the total star-formation rate in some galaxies. Indeed, using a total star-formation rate from full spectral energy distribution modelling or combining UV and FIR emission may alleviate some of these concerns, or possibly complicate them further for certain types of galaxies (e.g. Gürkan et al., 2018b).

1.2.1.6 Star formation main sequence

Noeske et al. (2007) noticed an interesting correlation between the number of stars forming (i.e. SFR) and the number of existing stars (i.e. stellar mass) in a galaxy. The correlation was named the main sequence of SF galaxies shown in Figure 1.3. The main sequence has a scatter of ~ 0.3 dex along with a few outliers (e.g. Noeske et al., 2007; Daddi et al., 2007; Whitaker et al., 2014; Johnston et al., 2015). The

outliers include starburst galaxies, with large-scale SFRs > 100 $M_{\odot}yr^{-1}$ triggered by mergers (e.g. Sanders and Mirabel, 1996), are above the sequence. Other outliers are a galaxy class with low/quenched levels of star formation, known as quiescent, passive or red and dead galaxies; these are below the main sequence. The last outliers are the green valley galaxies. These are galaxies that are in the process of being quenched and in transition between main sequence and quiescent galaxies (e.g. Wyder et al., 2007; Martin et al., 2007; Brownson et al., 2020),

1.2.2 Active nuclei

AGN are the energetic central region of a galaxy. Throughout this thesis, AGN refers to both the core of a galaxy and to a galaxy that contains an active core. They are far more luminous than 'normal' galaxies that are mainly powered by stars (nuclear fusion). This radiation spans a wide range of the electromagnetic spectrum, from radio to even γ-rays (e.g. Kubo et al., 1998). The radiation excites material in the galaxy leading to unique narrow line or broad line emission. AGN also show variability of their compact (optical and radio) flux on the time scales of weeks to years Matthews and Sandage (1963); Dietrich et al. (2012). AGN also display powerful radio jets. A galaxy is classified as an AGN if it contains one or more of the above characteristics.

There are several types of AGN, which are classified by their properties including their optical emission lines, variability and radio observations. The main types are Seyferts, radio galaxies, quasars and blazars.

Seyferts

Seyferts were discovered in 1943 owing to the strange, broad emission lines in their spectrum (Seyfert, 1943). They were found to have broad lines corresponding to rapid rotation. They are the most common AGN in the local universe where the host galaxies are resolved, and are typically hosted by spiral galaxies (Adams, 1977). Seyferts have relatively weak radio emission compared their optical emission (radio-quiet). They are divided into two types, Type I containing both broad emission lines and narrow emission lines (Khachikian and Weedman, 1971). Type II have strong IR while having weak UV and X-ray emission.

Radio galaxies

Radio galaxies are resolved AGN often associated with giant ellipticals, and are observed with very powerful radio jets or lobes. They are classified into two types, narrow line radio galaxy and broad line radio galaxies (analogous to Seyferts).

Quasars

Quasi-stellar radio sources (quasars) are a subset of the AGN population, discovered (Schmidt, 1963) in the radio as bright point sources with star-like counterparts in the optical band. Their star-like appearance makes them indistinguishable from stars if looking solely at their morphology, but they have a broad emission spectrum different from any star (Schmidt, 1963). They were found to be galaxies at high redshifts (assuming their redshifts are cosmological). Radio-loud quasars are the same as radio galaxies and radio-quiet quasars are the same as Seyferts. Quasars are the most luminous members of the AGN family and span a large redshift range to $z \sim 7.5$ (e.g. Momjian et al., 2014; Bañados et al., 2018). Analogous to Seyferts Quasars are also divided into two Type I and Type II.

Blazars

Blazars like Quasars, are star-like AGN that outshine their host galaxies. The key distinguishing feature of blazars is that they are believed to have a radio jet oriented towards us. Their have variable optical luminosities and strong radio emission. They are divided into two types, BL Lac and optically violently variable quasars (OVV). BL Lac where initially thought to be variable stars but later found to be AGN. They have very weak (or sometimes no) emission or absorption lines. OVV have both narrow and broad emission lines.

1.2.2.1 Unification model of AGN

The unification theory of AGN suggests that AGN are all the same type of objects and the various types are a result of the observer's viewing angle,instead of differences in underlying physical properties (Antonucci, 1993; Urry and Padovani, 1995). This typical AGN contains a super massive black hole (SMBH), surrounded by a

thin accretion disk, a hot corona, a thick dusty torus in the plane of the accretion flow and collimated jets along the poles of the torus (Antonucci, 1993). Fig. 1.4 shows the typical AGN and how the various types can be explained.

The source of radiation in AGN is linked to accretion of material into the SMBH (Rees, 1984). The radiation is mainly continuum emission (which is a combination of blackbody, Bremsstrahlung and synchrotron, see Chapter 1.3.2) released from the collision and heating of infalling material rotating in the accretion disk. The thermal radiation emitted is realised in the optical, UV (the blue bump, see Fig. 1.5), X-ray and re-radiated to the IR (IR bump) spectrum (Barvainis, 1987; Abramowicz and Fragile, 2013). The continuum emission excites the surrounding materials. The material near the SMBH radiate Doppler-broadened optical emission lines (broad line region) due to the rapid rotation and the material far from the SMBH have narrow emission (narrow line region). AGN with broad line emission are those with a viewing angle such that is not obscured by the torus and those without are obsured by the torus. All the AGN with broad line emission have variability associated with minor changes in the accretion flow.

There are believed to be two modes of accretion, cold-mode and hot-mode accretion (Best et al., 2005; Hardcastle, 2007). Cold-mode also known as quasar-mode is when cold material is accreted into the SMBH which results in high excitation lines traditionally associated with AGN. While the hot-mode or radio-mode accretion occurs when hot material is accreted, which leads to low-excitation lines. The lack optical lines suggests the lack of a dusty torus.

The radiation emitted exerts pressure on the surrounding material (radiation pressure), which can lead to outflows if the pressure exceeds the gravitational pull of the SBMH. If the outflow is ordered (collimated) it is referred to as jets, otherwise, it is referred to as winds. Outflows in AGN might be associated with magnetodynamic instabilities (turbulence), due to magnetic fields being squeezed by the rotation in the accretion disk, causes the infalling material to lose angular momentum (Balbus and Hawley, 1991). This will cause the infalling material to spirals inwards, increasing velocity, the number of collisions and temperature. The radiation pressure as a result of the increased collisions leads to outflows in the form of winds or even jets (Blandford and Payne, 1982). The main production of powerful jets occurs through turbulence caused by spin or the SMBH or infalling material in the innermost part of the accretion disk (Blandford and Znajek, 1977).

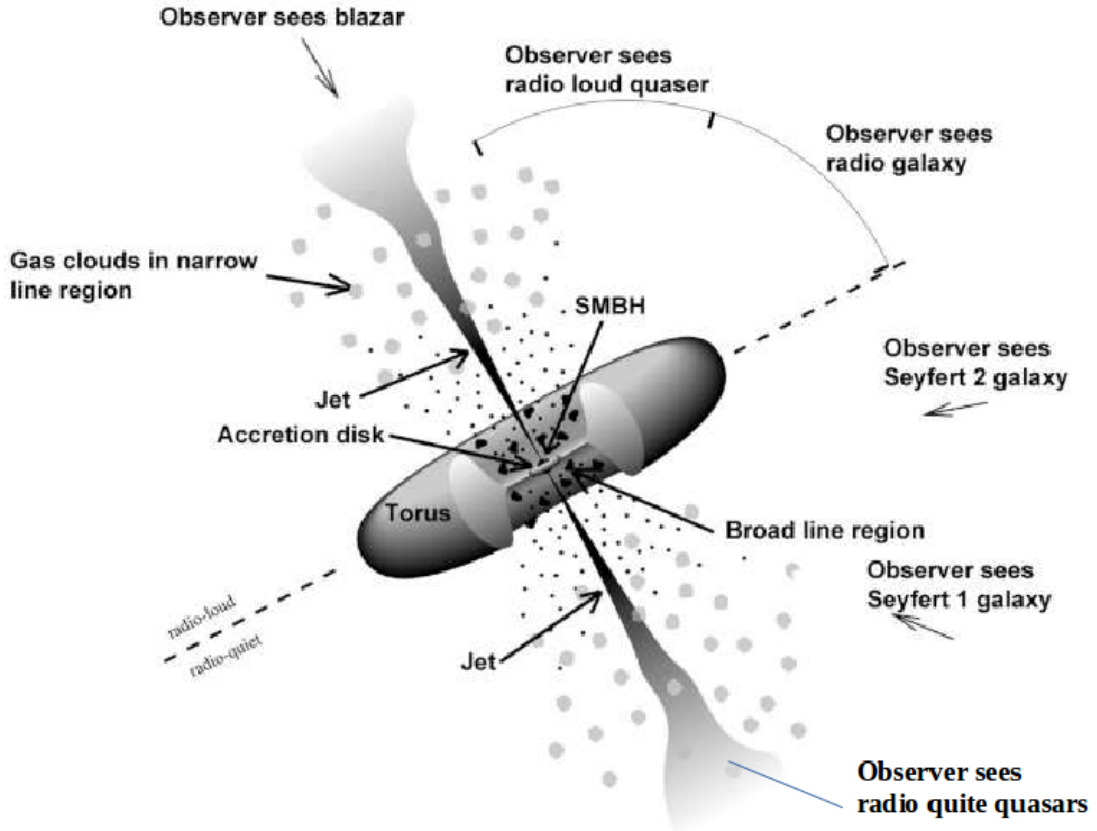

FIGURE 1.4: The unified AGN model. The model explains the types of AGN different observation angles.Credit Padovani et al. 1997

1.2.2.2 Radio loudness

Radio observations show that only $\sim 10\%$ of the AGN observed in the optical wavelengths have powerful jets and these are termed radio-loud AGN. Radio-loudness was initially defined by just the radio luminosity of the source (e.g. $\log_{10}[L_{8\mathrm{GHz}}\mathrm{WHz}^{-1} > 25$ Hooper et al. 1996). However, an improved definition of radio-loudness is given by the ratio between optical and radio luminosities, $R = L(4400\text{Å})/\mathrm{L(6cm)}$ where $R < 10$ represents radio-quiet AGN. Fig. 1.5 shows the spectral energy distribution of a radio-loud and radio-quiet AGN.

Radio-loud AGN

Radio-loud AGN are those that show powerful jets or lobes. Radio-loud quasars, blazars and radio galaxies fall in this category. These are all extremely luminous AGNs with typical luminosities $24 \lesssim \log_{10}[L_{1.4\mathrm{GHz}}\ \mathrm{WHz}^{-1}] \lesssim 28$. Radio-loud AGN dominate the radio sky above flux densities of 1 mJy at 1.4 GHz (e.g Mitchell and

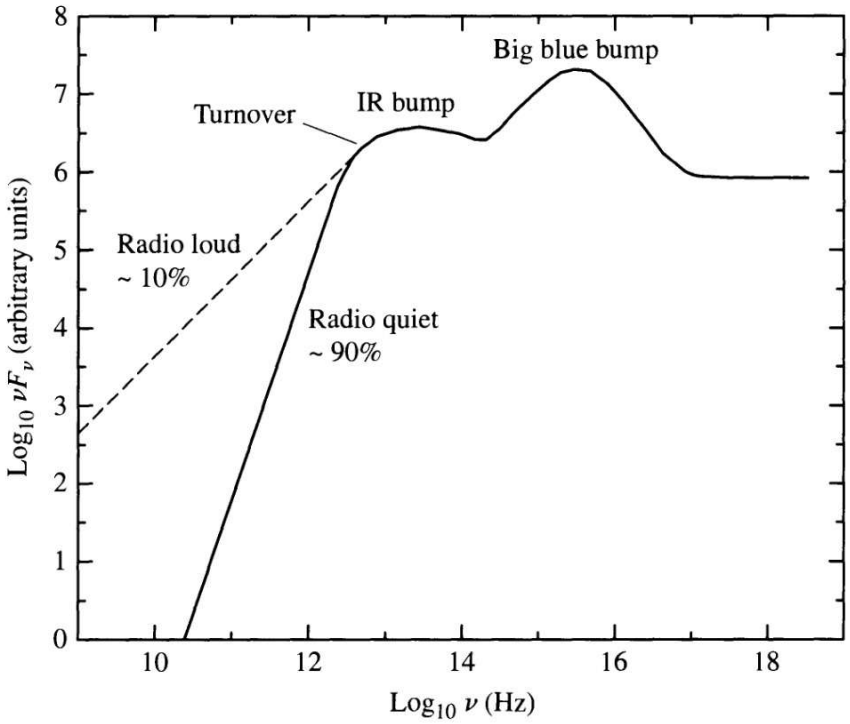

FIGURE 1.5: A rough sketch of the radio to X-ray spectral energy distribution (SED) of a radio-quiet (solid line) and radio-loud (dashed line) AGN. The x-axis is frequency and y-axis are the intensity both in logarithmic scale. Credit: Carroll and Ostlie (2007)

Condon (1985); Condon et al. (2012)). They are associated synchrotron emission with a steep spectrum ($\alpha < -0.5$, where the spectral index α is defined as $\alpha \equiv \log[S/S_0]/\log[\nu/\nu_0]$).

A further classification of radio-loud AGN (particularly radio galaxies) is based on the properties of the jets, Faranoff-Riley (FR) type I and type II (Fanaroff and Riley, 1974) or a composite (Gopal-Krishna and Wiita, 2000; Harwood et al., 2020). FR I are associated with twin radio jets with most of their luminosity concentrated near the centre (centre-brightened). FR II have radio jets with lobes that contains bright hotspots at the ends (edge-brightened). FRII were found to typically be more luminous than FR I (Fanaroff and Riley, 1974). However, recent studies with fainter sources argue against a difference in luminosity (e.g. Mingo et al., 2019).

Radio-quiet AGN

Radio-quiet AGN make up sources which have fainter radio luminosities and make up ~ 90 % of the the AGN population. At 1.4 GHz, radio-quiet AGN have lumionsities $\log_{10}[L_{1.4\mathrm{GHz}}\ \mathrm{WHz}^{-1}] \lesssim 24$. The main source of radio emission in radio-quiet sources has been debated for decades. One suggestion is that the radio emission from radio-quiet AGN is a result of synchrotron radiation associated with star formation in the host galaxy, rather than being the result of AGN processes (e.g. Terlevich et al. 1987, 1992; Padovani et al. 2011; Kimball et al. 2011; Bonzini et al. 2013; Condon et al. 2013; Kellermann et al. 2016; Gürkan et al. 2018a; Stacey et al. 2018). The major challenge in this case being able to disentangle snychrotron emission from star formation and AGN related process. However, some authors suggest the radio emission in radio-quiet AGN is still dominated by AGN-related processes such as low-power jets (e.g. Falcke and Biermann, 1995; Wilson and Colbert, 1995; Hartley et al., 2019), accretion disk winds (e.g. Jiang et al., 2010; Zakamska and Greene, 2014; Roy et al., 2018), coronal disk emissions (Laor and Behar, 2008; Laor et al., 2019) or a combination of these process (see Panessa et al. 2019 for a review). Factors such as different accretion rates (Fernandes et al., 2011), SMBH spin (Blandford and Znajek, 1977; Schulze et al., 2017), SMBH mass (Dunlop et al., 2003; McLure and Jarvis, 2004), host-galaxy morphology (Bessiere et al., 2012), galactic environments (Fan et al., 2001), or a combination of these, being also responsible for a lack of powerful jets.

1.2.3 Feedback

Studies on local galaxies have shown an interesting correlation between the mass of an SMBH and the total stellar mass of the bulge (Fig. 1.6 left; Tremaine et al. 2002) and an even tighter correlation between the SMBH mass and the stellar bulges' velocity dispersion (Fig. 1.6 right; Gebhardt et al. 2000; Ferrarese and Merritt 2000). Furthermore, the SFR density (SFR per comoving volume) and SMBH accretion rate density share a similar evolution, they both peak at $z \sim 2$ and decline towards lower redshifts (Boyle and Terlevich, 1998; Madau and Dickinson, 2014; Burgarella et al., 2016). These correlations suggest that there is a connection between the formation and evolution of SMBH and the host galaxy (Gebhardt et al., 2000).

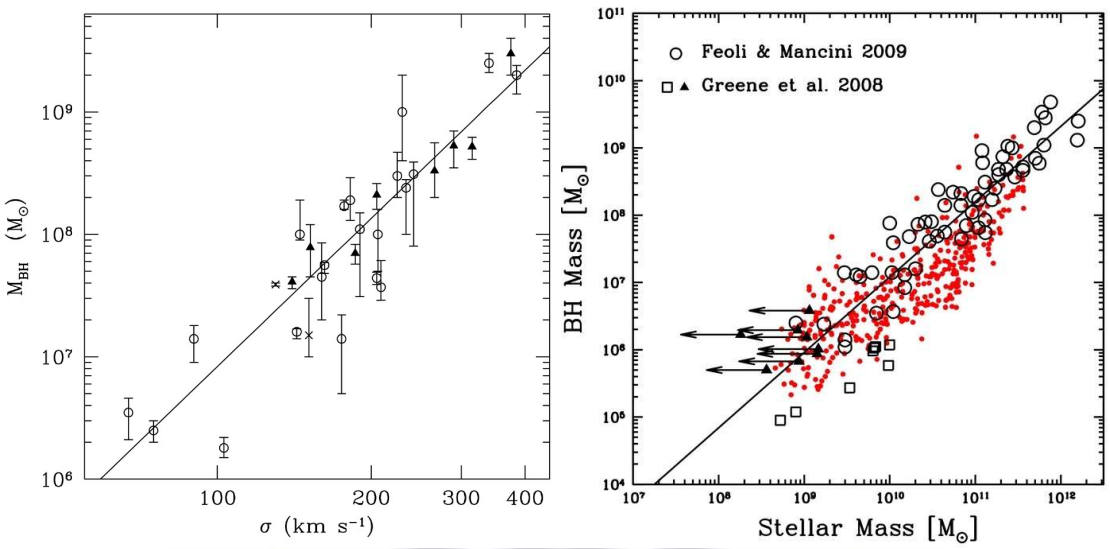

FIGURE 1.6: (left) The supermassive black hole mass (M_{BH}) and dispersion velocity (σ) correlation, Credit: Kormendy and Richstone (1995). (right) The correlation between total stellar mass in the bulge and the mass of the supermassive black hole (BH mass). The red dots are from a simulation by Jahnke and Macciò (2011); the open circles and triangles are observed data from Feoli and Mancini (2009) and Greene et al. (2008) respectively.

Feedback is a process that regulates the growth of a galaxy; positive feedback leads to growth and negative feedback suppresses growth. It can be thought of as the language the SMBH, stars, gas and host galaxy as a whole use to communicate and self-regulate. There are various types of feedback processes, the main ones being supernova feedback and AGN feedback. Supernova feedback occurs during a catastrophic explosion sends shock waves and energy to the ISM (Silk, 2013; Springel et al., 2005). The supernova can lead to both positive feedback, where the shock waves trigger a collapse of a molecular cloud in the ISM, or negative feedback, where the explosion heats up (radiative) the ISM or expels (mechanical) gas, both leading to suppressing star formation (quenching. Best, 2007). However, supernova feedback is unable to account for the quenching observed in massive galaxies as the expelled gas eventually rejoins the galaxy and heated gas eventually cools (Oppenheimer et al., 2010; Pontzen et al., 2017).

AGN also have radiative and mechanical feedback modes that are typically more powerful than their supernova counterparts. During mechanical feedback the gas is expelled from the galaxy by winds and jets, which leads to quenching. The expelled gas could affect the accretion rate, as the gas could have fuelled the AGN (Morganti et al., 2013)). Silk (2013) suggests that jets can initiate SF by stimulating

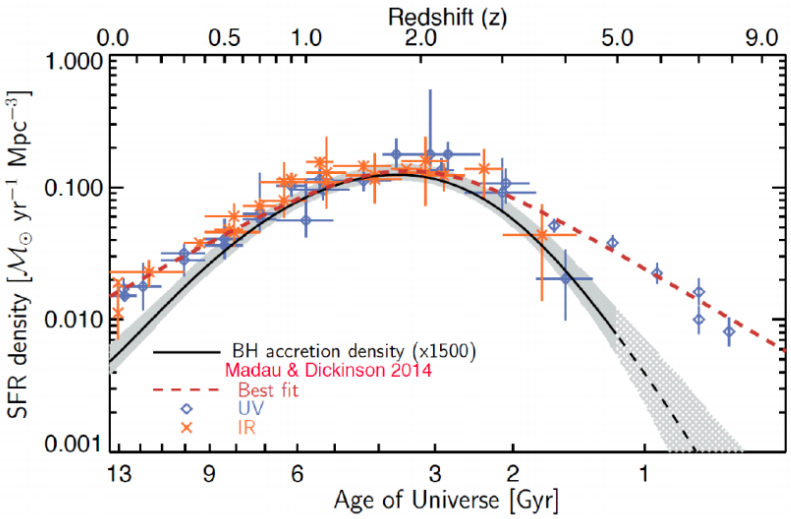

FIGURE 1.7: The comparison between the history of SMBH accretion density and the history SFR density is represented by the black line and red dashed line respectively. The black hole accretion density is scaled by 1500 to make it easier to compare the evolutionary trends. The blue circles and orange cross represent the infrared and dust-correct ultraviolet measurements for the SFR density (Madau and Dickinson, 2014). Credit: Burgarella et al. (2016)

the collapse of a molecular cloud (positive feedback). Further observational evidence of positive feedback in high-redshift quasars is shown by Kalfountzou et al. (2014).

1.3 Radio sky

1.3.1 Brief History

Radio astronomy started in the 1930s when an engineer, Karl Jansky, was tasked to investigate an issue of static interference in telephone calls. Jansky built a rotating antenna operating at 20.5 MHz. After several months of observations he found two main sources of static, thunderstorms, both nearby and at a distance, and an unknown source in the Sagittarius constellation (Jansky, 1933). Because of the great depression the company did not fund any further investigation into the extraterrestrial source of static noise.

Inspired by the results Jansky achieved, in 1939 Grote Reber built the first 9.5 m parabolic radio telescope and after several attempts at different frequencies (3300 MHz, 900 MHz and 160 MHz), managed to observe the (previously unknown source) galactic centre, the sun and the brightest radio galaxies (Reber, 1944). Jan Oort verified

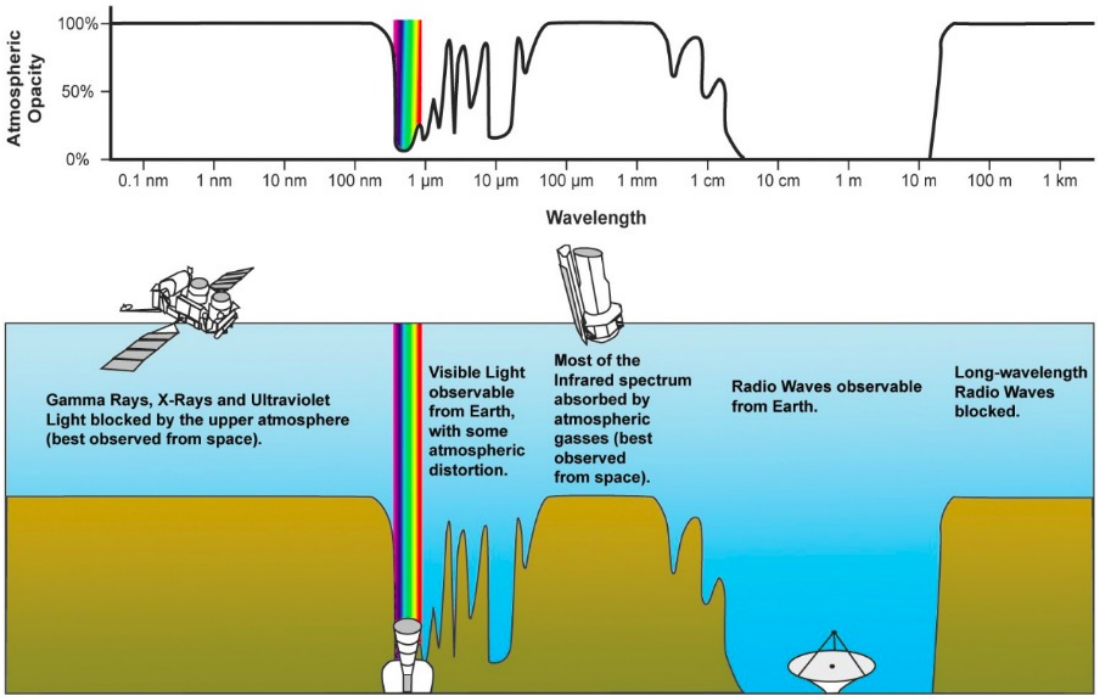

FIGURE 1.8: The atmospheric opacity at different wavelengths from Earth. Brown represents wavelengths that are absorbed by the atmosphere. Optical (represented by the rainbow colours) and radio (represented by the radio telescope) wavelengths are observable from earth. Credit: NASA http://gsp.humboldt.edu/OLM/Courses/GSP$_2$16_*Online*/*lesson*2 − 1/*atmosphere.html*

the results, attributing the emission to broad spectrum emission. This broadband spectrum increases with frequency, which is opposite to thermal emission (from a blackbody) that decreases with frequency. The mystery of this radiation was solved when the theory of synchrotron radiation was discovered (Ginzburg and Syrovatskii, 1965; Elder et al., 1947). Oord and Hendrik van de Huls theorised the existence of the 21 cm line which was subsequently observed (Ewen and Purcell, 1951) and used to map the shape of the Milky Way.

As radio astronomy evolved, most of the radio sky was mapped by individual sources; radio galaxies were observed and catalogued. Other major radio astronomy findings include the discovery of the cosmic microwave background (CMB McKellar, 1941; Penzias and Wilson, 1965) the discovery of the quasar (Sandage, 1965) and the pulsar (Hewish et al., 1968).

Radio observations have the advantage of a much wider spectrum window from earth, as seen in Fig. 1.8, and of not being affected by dust. One of the drawbacks of radio observations was the limited resolution (the smallest separation angle between

two objects). The resolution of a telescope is proportional to the wavelength λ and inversely proportional diameter D,

$$\theta \approx \lambda / D. \tag{1.1}$$

As a consequence, the largest single-dish radio telescope, the Five-hundred-meter Aperture Spherical Radio Telescope (FAST, NAN et al., 2011) with a diameter of 500 m (observing at 10 cm) has the resolving power of a 14 mm optical telescope (observing at 5.5×10^{-7}m). Because of these issues, radio interferometry was developed. This technique combines the observations of two or more radio telescopes to increase the total surface area and diameter. The effective diameter is the longest distance between two telescopes. The longest radio interferometry (space very long baseline interferometery) is able to achieve eight micro-arcseconds resolutions; however, the technique sacrifices diffuse emission or large scale structures as a result of a gap between the telescopes.

1.3.2 Radio emission

There are various mechanisms that lead to radio emission, including atomic and molecular transitions such as radio recombination lines, and the 21 cm signal associated with the spin flip of the neutral hydrogen and rotation emission from a CO molecule or thermal black body radiation. The main radio emission from extraterrestrial sources is from some form of Bremsstrahlung radiation (Condon et al., 2002), which is radiation produced by a charged particle accelerated/decelerated by an electromagnetic force, namely free-free emission and synchrotron.

1.3.2.1 Free-free emission

Free-free emission is the emission radiated by a free particle moving at velocity (v_1) accelerated to v_2 by the Coulomb force from another particle (Oster, 1961; Scheuer, 1960; Karzas and Latter, 1961). The energy of the photon ($h\nu$) is the difference between the (kinetic) energy particle before and after the interaction. High-energy X-ray photons are released when the particles interact strongly, while radio photons are released from weak interactions. The photons released from the electron-electron (Haug, 1989) and electron-positron (Haug, 1987) particle interaction are negligible for the weak interaction case. They contribute at X-ray frequencies when the speed

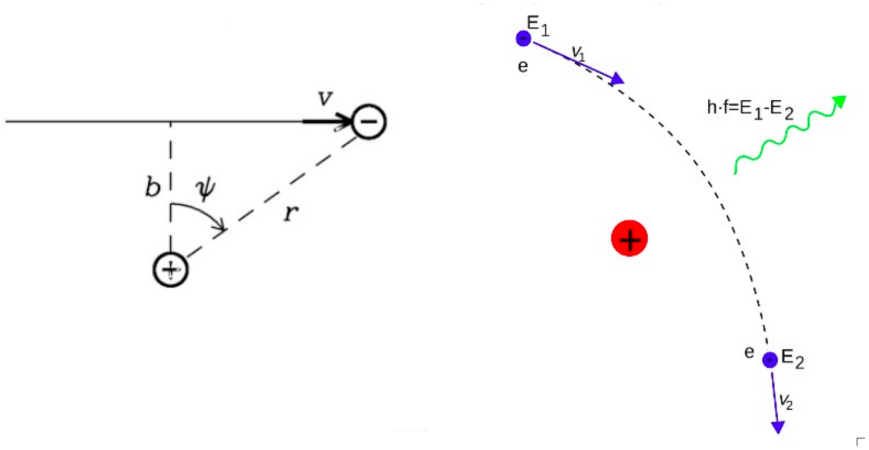

FIGURE 1.9: Free-free radiation emitted when a moving electron interacts with a proton at an angle of ψ and distance of r. The right panel shows the electron before and after the interaction. Credit: https://www.slideshare.net/KhaledEdris/radio-astronomy-emission-mechanisms

of the electrons is relativistic (Maxon and Corman, 1967). At radio frequencies the most significant interactions are between an electron and proton (or ions), illustrated in Fig. 1.9. The pulse energy (total power radiated over time) per frequency (ν) from a free electron with mass (m_e) moving at a velocity (v_1), at an angle ψ and distance r with a minimum distance b from the proton (Z=1) is approximated by,

$$W_\nu \approx \frac{\pi^2}{2}\left(\frac{Z^2e^6}{m_e^2c^3}\right)\frac{1}{(bv_1)^2}e^{-2\pi\nu b/v}. \tag{1.2}$$

Fig. 1.10 shows the spectrum of the pulse energy of a single electron. The spectrum is flat at a frequency below $\nu \approx v_1/(2\pi b)$ and decreases exponentially above that frequency. Both the electron and proton release photons from the interaction but because the proton is $\sim$ 2000 times more massive, the power radiated by the proton is negligible. Astronomically, free-free is commonly associated with ionized HII regions. The energy radiated by the electrons is a function of the electron velocities (v_1), which depends on the electron temperature, the distance and angle between the two particles (which depends on the number density of both electrons (n_e) and ions [n_i]). Assuming that the ionized gas is in local thermal equilibrium (LTE) the velocities of the ions depends on the electron temperature, such that the probability of an electron having v_1 between v and $v + dv$ follows a Maxwellian distribution:

$$f(v) \propto v^2 \exp\left[-\frac{mv^2}{2kT}\right]. \tag{1.3}$$

At low frequencies the electron will emit radiation with energy that is comparable

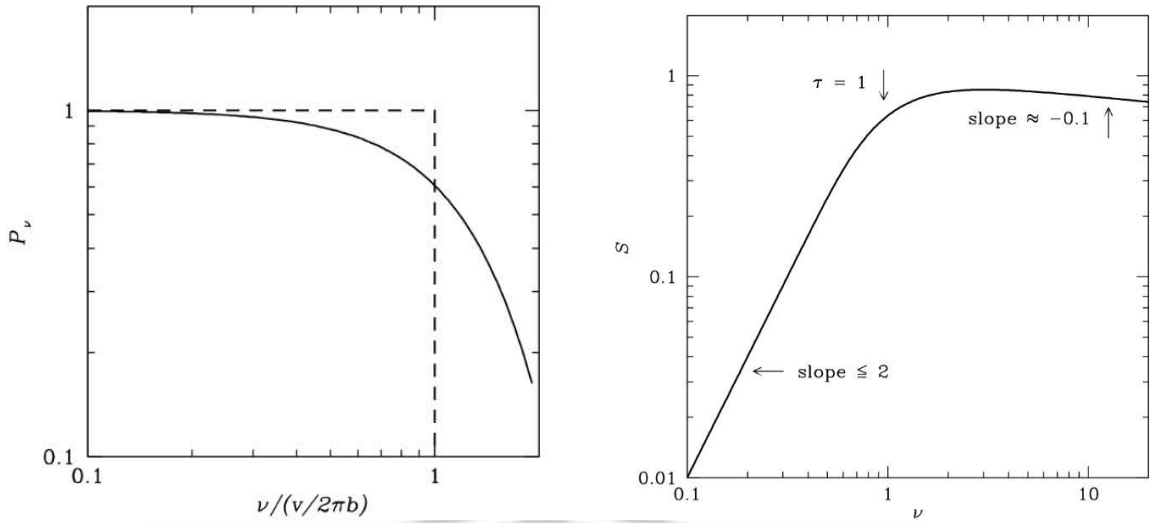

FIGURE 1.10: The left panel is the power spectrum of the pulse energy as a function of frequency. The solid line is the pulse energy from a single electron and the dashed line is an approximation. The right panel shows the spectrum of the intensity of light from a typical HII region. Credit: NRAO https://www.cv.nrao.edu/ sransom/web/Ch4.html

to the electron kinetic energy. Assuming that the environment is in LTE then the electron will equally absorb and emit photons like a blackbody. This will result in the entire source becoming more optically thick at energies approaching the electron kinetic energy. When the absorbed emission is free-free emission from a different electron-proton pair, this process is called free-free self-absorption. The total spectrum is divided by two regions, low frequencies where the gas is optically thick ($\tau \gg 1$),

$$S \propto \nu^2, \tag{1.4}$$

and at high frequencies where the gas is opaque ($\tau \ll 1$),

$$S \propto \nu^{-0.1}. \tag{1.5}$$

The overall spectrum from free-free emission is shown in Fig. 1.10. It behaves like a blackbody at low frequencies, where it is opaque. The environment gets more transparent towards higher frequencies until the peak of the spectrum at a frequency where the optical depth depth ($\tau \sim 1$). At higher frequencies the spectrum flattens or drops, depending on the opacity of the environment.

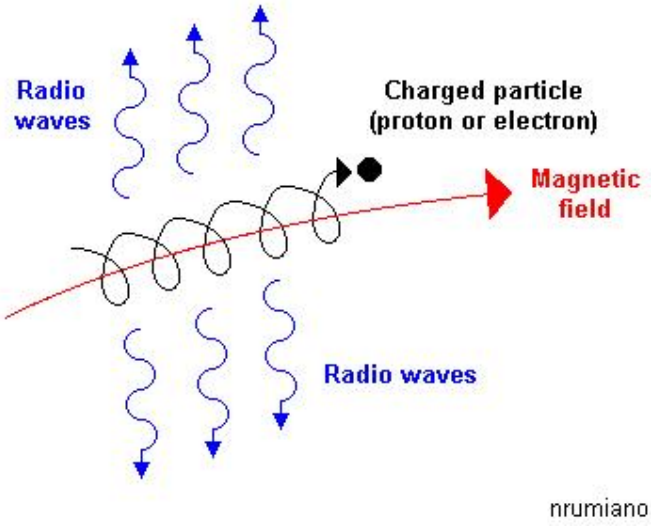

FIGURE 1.11: The production of synchrotron radiation from relativistic electrons spiraling due to a magnetic field. Credit: www.ucc.ie/en/raagn/restop/radioem

1.3.2.2 Synchrotron radiation

Synchrotron emission is the radiation produced when cosmic rays, charged particles moving at ultra-relativistic velocities, are accelerated circularly due to a magnetic field Elder et al. (1947); Ginzburg and Syrovatskii (1965). The radiation is released tangential to the rotation of the particles, as illustrated in Fig. 1.11. The frequency (ω_B) of the rotation depends on the strength of the magnetic field (B),

$$\omega_B = \frac{eB}{(\gamma m_e)c}, \tag{1.6}$$

where e is the charge of the electron, c is the speed of light, γ is the Lorentz factor and γm_e the relativistic mass of the electron. The power radiated by an electron is given by (Rybicki and Lightman, 1979),

$$P = \frac{2e^2}{3c^3}\gamma^4 \frac{v^2 e^2 B^2}{(\gamma m_e)^2 c^2} \sin^2\theta, \tag{1.7}$$

where v is the velocity of the cosmic-ray electron and θ is the angle between the velocity and magnetic field. The spectrum of the radiation from a single cosmic-ray electron is shown in Fig. 1.12. Most of the power is radiated at the $\nu_{\max}$,

$$\nu_{\max} = \frac{3\gamma^3 qB}{2\gamma m_e c.} \tag{1.8}$$

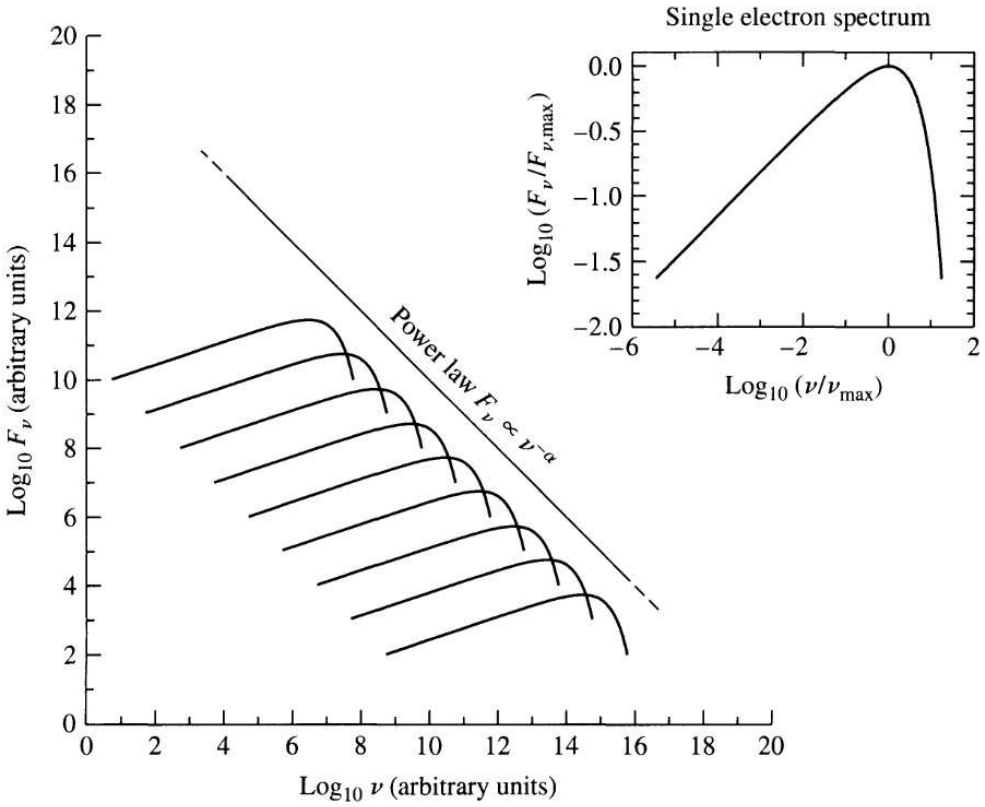

FIGURE 1.12: The top right is the spectrum of synchrotron radiation from a single cosmic-ray electron emitting mostly at ν_{max}. The total observed spectrum from multiple cosmic-ray electrons (left panel) is given by a power law which is approximately the superposition of each individual synchrotron spectrum at ν_c. Credit: Carroll and Ostlie (2007)

When considering the collective power of cosmic-ray electrons, the velocity distribution follows a power law and not a Maxwellian distribution as in the free-free case. This is because the cosmic-ray electrons are accelerated by external forces. For this reason, synchrotron radiation is referred to as non-thermal. The energy distribution of the cosmic-ray electrons follows a power law $n(E)dE \propto E^{-\delta}dE$. The total spectrum from the cosmic-ray electrons is approximated by adding just the peak contribution ($\nu_{\rm max}$), from each spectrum which, also gives a power law,

$$P(\nu) \propto B^{(\delta+1)/2}\nu^{-(\delta-1)/2}, \tag{1.9}$$

where $\alpha = (\delta - 1)/2$ is the spectral index. In the optically thin case such as, synchrotron emission from jets and lobes in radio-loud AGN, the spectral index is typically steep ($\alpha < -0.5$). In the optically thick case such as, synchrotron emission near the central regions of a AGN or from supernova surrounded by molecular

clouds, the spectral index is flat ($\alpha > -0.5$). Similar to free-free case, at low frequencies a particle in LTE will equally emit and absorb photons of certain energies (from a Maxwellian distribution). In this case where synchrotron emission is being absorbed, this is referred to as synchrotron-self-absorption. This again implies that the below a certain frequency the cosmic-ray electrons become opaque which leads to a blackbody tail at the low frequencies of the total synchrotron emission (Ghisellini et al., 1988)

$$I(\nu) \propto B^{-1/2}\nu^{5/2}. \tag{1.10}$$

It should be noted that the slope is slightly different from the free-free case; this is because the brightness temperature of a relativistic particle is different from the non-relativistic one. The total synchrotron emission from cosmic-ray electrons is shown in Fig. 1.12.

Fig. 1.13 shows the spectrum from a local starburst galaxy (short-lived phase of a galaxy undergoing a large burst of star formation) in the radio and FIR frequencies. It also includes the total spectrum from free-free emission (dashed line) from HII regions in a starburst galaxy (the high-frequency end of the blackbody is excluded) which dominates the total emission in the frequency range $30 \lesssim \nu \lesssim 110$ GHz. At low frequencies the starburst is dominated by synchrotron emission.

1.3.3 Radio sources

The radio sky is dominated by synchrotron emission from star forming galaxies and AGN (see Padovani, 2016, for a review on the faint and bright radio sky).

1.3.3.1 Bright radio sky

Since the early days, radio astronomy has been mostly limited to powerful sources dominated by non-thermal synchrotron radiation from jets/lobes. Theses sources that dominate the bright radio sky are predominately radio galaxies (including FRI and FRII) and radio loud quasars (Laing et al., 1983). In the 1960s it turned out that these powerful sources are rare, only a small fraction of the optically selected quasars; the rest did not have radio detections (Sandage, 1965). In the 1980s the source count was found to flatten around 1 mJy (at 1.4 GHz), which could not be explained by any sensible evolution of (radio-loud) AGN (Condon and Mitchell,

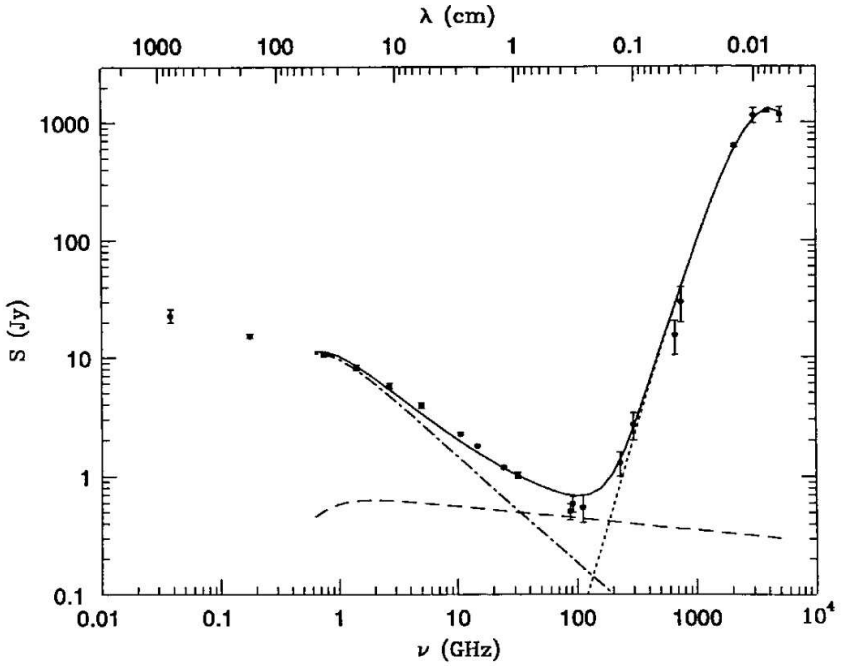

FIGURE 1.13: The total radio to far-infrared emission spectrum (solid line) from the local starburst galaxy M82. The dashed-dotted line is the Synchrotron emission from electrons accelerated by supernova in star-forming regions. The dashed line represents the free-free eimission from the ionised HII regions. The dotted lines are thermal emission re-radiated by dust. Credit:Condon et al. (2002)

1984; Fomalont et al., 1984; Windhorst et al., 1984). This indicated the emergence of a different population of galaxies with different evolution.

1.3.3.2 Sub-mJy and μJy radio populations

This faint population (sub-mJy) was thought to be starburst and normal SFG as these dominate the local source counts at low flux densities (Windhorst et al., 1985; Condon, 1984). A lot of effort has been invested in understanding the nature of this sub-mJy population, which was below the detection threshold of all large sky radio surveys. Narrow, deep surveys such as the Very Large Array (VLA)'s Hubble Deep Field (HDF, Richards et al., 1999), covering 40 arcmin down to a detection threshold of 40 μJy, broke down the relative fraction of the sub-mJy of 60% to be normal disk galaxies associated with star formation, 20% associated with AGN and 20% with no counterpart. The sub-mJy population was then confirmed to contain both SFGs and low-luminosity radio-loud AGN. However, Jarvis and Rawlings (2004) suggested the radio quiet-AGN also contribute to the sub-mJy population.

Various subsequent deep narrow surveys were carried out with different sensitivities to confirm these findings (e.g. Prandoni et al., 2001; Simpson et al., 2006; Huynh et al., 2008). However, the relative abundance or mix of AGN vs SFG varied and was debated (e.g. Ibar et al., 2009). There were two issues: i) the lack of larger deep surveys with less cosmic variance and ii) the lack of multiwavelengh data or VLB observations required to disentangle between SF and AGN contributions. Furthermore, even with complementary data some of the sources are faint in the optical/near-infrared (NIR) wavelengths, which requires long observation times. Padovani et al. (2011, 2014) found that the relative contribution from the sub-mJy sources changes with flux density, above ~ 0.5 mJy the contribution from SFG and radio-quiet increases towards lower flux densities but radio-loud still dominate the counts. Below 0.1 mJy (the μJy population) SFG dominate the source counts and radio-quiet AGN dominate the AGN population.

The μJy population is crucial for galaxy evolution, as they represents the 'normal' galaxies which make-up the bulk of the galaxies observed at the optical and NIR wavelengths. These are the galaxies in that have the interplay between AGN and star formation which leads to a link between SMBH and galaxy properties (see Chapter 1.2.3). Furthermore, radio observations are not affected by dust, giving an unbiased view of star formation and AGN activity that might otherwise be missed at other wavelengths. They contain important information about the AGN as well as the history of star formation. The drawback is that the bulk of the μ-Jy population at higher redshifts (z$\sim$ 2) is below the detection threshold of most radio surveys.

In the last decade a few radio telescopes were upgraded, such as JVLA (Perley et al., 2011) and Giant Metrewave Radio Telescope (GRMT) as well as the development of SKA pathfinders such as the Low-Frequency Radio Array (LOFAR; van Haarlem et al. 2013, Australian SKA Pathfinder (ASKAP, Norris et al. 2011) and MeerKAT (Jonas and MeerKAT Team, 2016). Their improved sensitivity and survey speed allow for the detection of the μJy population over larger fields. These improvements have allowed for the first measurement of radio SFRD out to $z \sim 5$, which shows that the UV estimates have underestimated the SFRD due to dust obscuration Novak et al. 2017. However, it should be noted that above $z \sim 1$ the predicted contribution from normal galaxies is an extrapolation since a detection threshold of ~ 0.25 μ-Jy is required to account for most of the star formation from these faint galaxies. (Mauch et al., 2020). Mauch et al. (2020) demonstrated that observations

from MeerKAT's DEEP2 field are deep enough to constrain the majority of the history of star formation of the Universe using a P(D) analysis (see Chapter 1.5.1).

The next generation of radio telescopes such as the SKA will revolutionize radio astronomy as it will reach unprecedented sensitivities and resolutions. There are three major surveys planned: i) a large <1000-5000 deg^2 down to an rms of 1 μ-Jy, ii) a deep survey over 10-30 deg^2 down to 200 nJy and iii) an ultra-deep survey that will cover $\sim$ 1 deg^2 down to 50 nJy (Prandoni and Seymour, 2015). These observations will allow for the study of the μ-Jy population up to high redshifts ($z \sim 7$) which will account for most of the cosmic star formation history (Jarvis et al., 2015; Orienti et al., 2015). This will also resolve the questions regarding the nature of radio quiet AGN emission (the relative contribution from star formation and AGN related emission) as well as the quasar radio-loudness dichotomy (McAlpine et al., 2015).

1.4 Optical and near-infrared emission

Probing galaxy formation and evolution in the μJy regime poses a few challenges. The first is disentangling synchrotron emission from the star formation and AGN (i.e. classification). Secondly, radio continuum emission does not have redshift information, which is essential for this kind of study. Multi-wavelength data (sub-mm or FIR, optical/NIR, X-ray and UV) is required to classify the galaxies accurately and get the redshift from optical/NIR spectroscopy. A large fraction of galaxies with spectroscopic redshifts come from high resolution spectrographs on 8-10 m class telescopes (e.g VIMOS VLT deep survey Le Fèvre et al. 2005, VANDELS ESO public spectroscopic survey McLure et al. 2018) or from large spectroscopic follow-up surveys such as the Sloan digital sky survey (SDSS York et al., 2000) Baryon Oscillation Spectroscopic Survey (Eisenstein et al., 2011). However, obtaining redshifts for faint galaxies still remains a challenge as they require long observational times. In such case, photometric redshifts are used instead. In simple terms, the (photometric) redshift of the galaxy is obtained by fitting its SED to various galaxy templates. NIR observations and spectroscopy become increasingly important at higher redshifts where optical lines are redshifted to the NIR. However, it should be noted that photometric redshifts are a statistical measure for the population, rather than an accurate measure for individual sources.

Both optical and NIR emission in a galaxy primarily trace the approximate blackbody emission radiated by stars. The optical wavelength is dominated by young blue (O and B) stars with intermediate to high masses. The NIR traces redder, older stars and does not suffer from attenuation as much as optical. Since NIR observations are not heavily affected by dust and are not biased to massive stars, the NIR (particularly K-band) to good approximation provides a sample selected on stellar mass (e.g. Daddi et al., 2007). Optical emission from an AGN is thermal free-free radiation from ions in the accretion disc (blue bump). The NIR AGN emission is also from the blue bump but there is also a contribution from the IR bump from re-radiated UV. Optical and NIR spectral emission lines also provide information about HII regions.

The last decade has seen a wave of deep NIR surveys such as the United Kingdom Infrared Deep Sky Survey Ultra-Deep Survey (UKIDSS UDS, Lawrence et al., 2007), UltraVISTA (McCracken et al., 2012) and The VISTA Deep Extragalactic Observations (VIDEO, Jarvis et al. 2013) survey thanks to the advance in large IR-sensitive arrays.

1.5 Science below the detection threshold

Although the current generation of radio telescopes are able to detect some of the μJy population in relatively narrow surveys, there is still a relatively large fraction of sources in the optical/NIR below the detection threshold of these radio surveys[3]. There are several techniques that have been developed to probe measurements below the detection threshold.

Survey catalogues usually have a detection threshold (flux density limit), typically 5 times the total rms noise (5σ). This detection threshold is enforced to ensure the reliability of the catalogue. At the 5σ level one avoids flux density uncertainties associated with effects such as confusion[4], two or more faint sources overlapping due to a relatively large synthesised beam, and artifacts, which are also related to the synthesised beam. Because of these effects most of astronomy is done above the detection threshold.

[3] In fact, it will take the full SKA for continuum surveys to be comparable to optical/NIR.

[4] This refers to instrumental confusion and not natural confusion. Natural confusion occurs when two or more sources overlap/blend owing to their angular sizes and source density. At 1.4 GHz natural confusion becomes a problem far below 0.01 μ Jy (Windhorst, 2003)

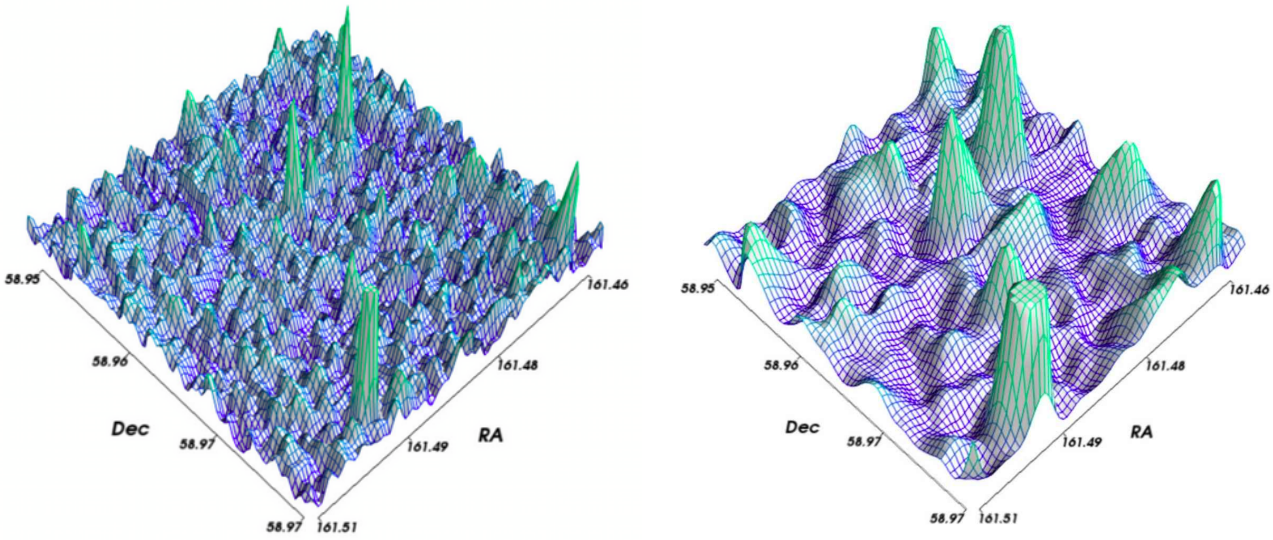

FIGURE 1.14: The three-dimensional plot of the 3GHz Karl Jansky Very Large Array (VLA) observations of the Lockman Hole North. (left) High-resolution observations in the CnB configuration with noise $\sigma = 1.15$ μJy beam^{-1} and a synthesis beam size $\theta = 2.75$ arcsec. (right) Observations in the C configuration with a synthesis beam size $\theta = 8$ arcsec and noise $\sigma = 1$ μJy beam^{-1} . The tall structures with green ends represent detected sources and the blue ones represent sources/fluctuations below the detection threshold. Credit: Vernstrom et al. (2016)

However, although the individual source information is not reliable below the detection threshold, there is a lot of information buried in the noise. For example, Fig. 1.14 (right) shows that there are fluctuations that correspond to real sources (be it confused, discussed below) in the high-resolution plot. However, doing science with this information requires a proper statistical analysis and full understanding of the noise properties. The two techniques that are used to study (but not limited to) continuum radio surveys include the probability of deflection (P(D)) and stacking (see Zwart et al., 2015a, for an overview).

1.5.1 P(D) analysis

P(D) is a statistical analysis of fluctuations in the sky to probe the number of faint sources, too faint to be individually detected, contributing to these fluctuations (Scheuer 1957). Hewish (1961) was among the first to apply the technique to estimate the 4C source counts. The technique was moved from an analogue to a digital regime by Condon (1974), who derived the analytical form of the P(D) assuming that the source counts obey a power law. In this regime the P(D) can be defined as

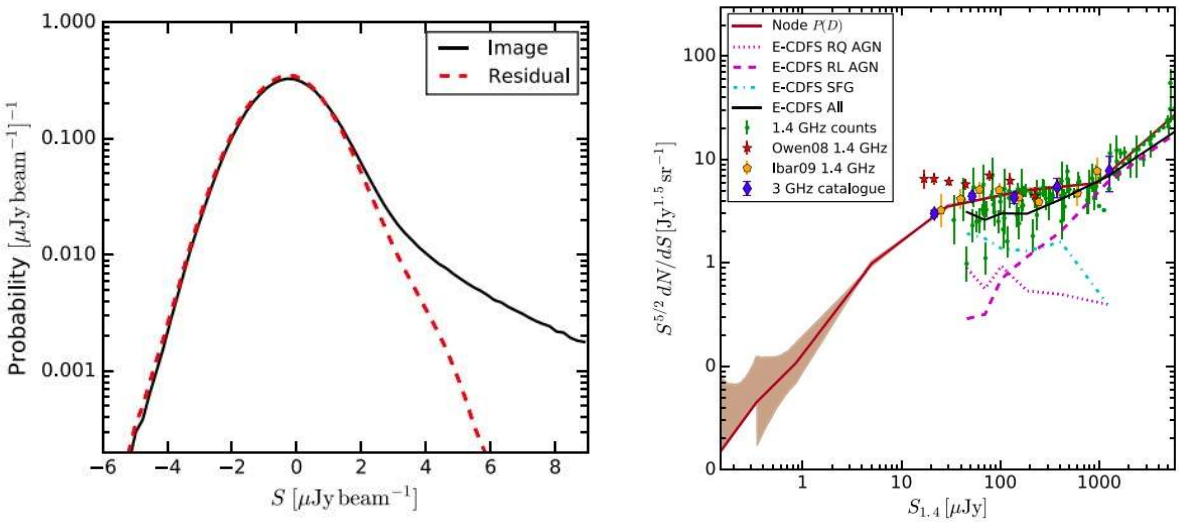

FIGURE 1.15: (left) The pixel flux density distribution of the combined C and CB map of the VLA Lockaman Hole observations. The black line represents the flux density of all the sources and the red, dashed line represents the sources below 5σ. (right) The Euclidean normalised source count. The Blue circles show the detected sources from the map. The red line is the P(D) counts and the brown is the 68% region. Credit: Vernstrom et al. (2016)

a statistical analysis of the pixel flux density distribution to infer the number faint sources contributing to the fluctuations in flux density.

The technique has been applied to data at various frequencies including X-ray (e.g. Barcons and Fabian, 1990; Toffolatti and Barcons, 1992), infrared (e.g, Väisänen et al., 2001) and sub-mm (e.g. Toffolatti et al., 1998). More sophisticated models where adopted to describe the source counts such as a double power law (broken power law) (Friedmann and Bouchet, 2004) or a multi-node model, by Patanchon et al. (2009) who also adopted the technique into a Bayesian likelihood analysis. Vernstrom et al. (2014) improved the analysis by correcting for pixel-to-pixel correlation of the fluxes as well as demonstrating the performance of the P(D) in the presence of sources with extended emission. Franzen et al. (2016) applied the P(D) to a Murchison Widefield Array (MWA) image with artifacts due to sidelobe confusion (as a result of sources being far from the primary beam).

Fig. 1.15 is an application of the technique to confused 3 GHz VLA observations of the Lockman Hole (Fig. 1.14). The P(D) reconstructs the source counts at least 3 dex below the detection threshold (Vernstrom et al., 2016).

1.5.2 Stacking

The P(D) is a powerful technique, however, it is only applicable to confusion-limited maps. Hence, the most popular means of studying sub-mJy and μJy sources in the past two decades have involved some form of 'stacking' (Ivezić et al., 2002; White et al., 2007; Hodge et al., 2008; Mitchell-Wynne et al., 2014; Roseboom and Best, 2014; Zwart et al., 2015a).

Stacking is commonly associated with co-adding two or more observations of the same field to increase the signal-to-noise ratio of faint sources. In this context stacking is the co-adding of a certain population of faint sources to increase the signal-to-noise ratio to achieve a statistical detection. The information regarding this population being stacked is acquired from another survey at a different wavelength, in the same field, where it is detected. The technique relies on the noise (σ) in the map following a known distribution, Gaussian in most cases. As such, when N maps, each with random noise σ, are stacked; the noise of the stacked map is reduced to $\sim \sigma/\sqrt{N}$. Therefore, the technique requires good astrometry from both surveys, as well as large coverage to ensure good statistics.

Staking was first applied by Caillault and Helfand (1985) to get the mean X-ray flux of undetected stars in the Pleiades cluster, using optical data as the prior data. The technique has been applied to data at various frequencies, including X-ray Brandt and Chandra Deep Field North Team (2001); Bartelmann and White (2003), optical Zibetti and Ferguson (2004); Zibetti et al. (2005); Gawiser et al. (2007), IR Dole et al. (2006); Hogg et al. (1997), sub-mm (Webb et al., 2004; Wang et al., 2006) and radio (White et al., 2007; Dunne et al., 2009; Zwart et al., 2014). At radio frequencies stacking has been applied to extend the FIR-radio correlation to the faint radio sources using infrared galaxies without radio defections (Boyle et al., 2007; Beswick et al., 2008). Stil et al. (2014) used stacked polarized intensities to investigate the polarization of faint radio sources. One can infer the average SFRs from undetected 1.4-GHz radio flux densities of NIR selected-sources selected by stellar mass (e.g. Dunne et al. 2009; Karim et al. 2011, Zwart et al. 2014) to study properties of radio-quiet AGN (Hodge et al., 2008) and radio-quiet quasars (White et al., 2007; Perger et al., 2019).

Stacking has been used in two ways in the literature: 1) extracting cut-outs (of a certain pixel size) centred at the position of the auxiliary data and co-adding the cutouts. For example, Fig. 1.16 shows the stacked Faint Image of the Radio Sky at

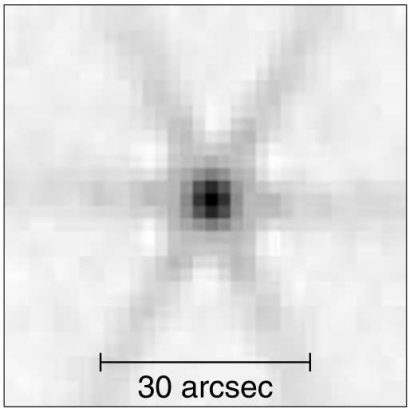

FIGURE 1.16: The stacked FIRST radio image of 41 295 SDSS DR3 radio-quiet quasars with a signal-to-noise ratio of ($\sim 75:1$) and a peak flux density of 80 μJy. The six extended structures are a result of the sidelobes as the undetected maps are not CLEANed. Credit: White et al. (2007)

Twenty-cm (FIRST, Becker et al., 1995) image of radio-quiet quasars in the Sky Digital Sloan Survey (SDSS, York et al., 2000) with a high signal-to-noise peak median flux density of 80 μJy $\sim$ 50% of the FIRST noise σ = 150 μJy. 2) The second approach involves extracting the flux density at the position of each source which results in a flux density distribution similar to that of the P(D) (see Fig. 1.15). Garn and Alexander (2009) showed that for a point sources with Gaussian noise, the flux densities from the stacked images are similar to the median of the individual flux densities.

One of the questions asked in stacking experiments is about the right average to use, mean or median. The mean is straightforward to compute and can be easily interpreted. The problem is that it is sensitive to outliers, i.e. a bright source will considerably shift the mean to the positive side. The median value is a more robust statistic, as it is less sensitive to outliers; however, it also has a number of biases, including the shape of the population and the map noise (Bourne et al., 2012). The challenge with the median is interpreting it. That being the case, most authors choose to use the median stack (White et al., 2007; Hodge et al., 2008; Perger et al., 2019)

There are various biases that can affect the results of a stacking experiment (see Zwart et al., 2015a; Stil, 2015, for an in depth discussion). These biases can arise from the sky or the image calibration or during the application of the technique. The sky bias is a result of confusion, especially when the deeper prior survey has a much higher resolution than the survey map being stacked. This might lead to

a situation where two or more sources are found in one pixel. There are several techniques to deal with confused sources in stacking experiments (Kurczynski and Gawiser, 2010; Wright et al., 2016); however, these techniques have mainly been developed for the sub-mm and FIR backgrounds. The FIRST catalogue was known to have a bias that underestimated the flux density of detected sources Becker et al. (1995) however an additional multiplicative bias that affects undetected sources was discovered by White et al. (2007). This bias is also thought to be associated with the image calibration. The bias associated with the stacking experiment has to do with mismatching of the sources owing to: 1) astrometry accuracy of the two surveys; or 2) misalignment due to the nature of emission in each frequency (i.e optical emission originating in the galaxy and radio emission originating from jet/lobes). Understanding and interpreting the results from stacking experiments requires an in-depth knowledge of the noise properties and the data. Simulations are therefore essential in addressing the biases.

1.6 Thesis outline

The aim of this thesis is to investigate the nature of faint radio population which consists of SFG and radio-quiet AGN. The questions I attempted to answer are: what is the main source of radio emission of theses radio-quiet AGN? and 2) What is the evolution of the cosmic SFRD measured through unbiased radio observations? I attempt to address both problems through radio luminosity functions, which have rich information about the abundance of sources with certain radio luminosity. In both cases I probe the RLF below the detection threshold because the bulk of radio quiet AGN and SFG are below the detection threshold of most current radio surveys.

In Chapter 2 I derive the stacking technique used to obtain the RLFs below the detection threshold. In Chapter 3 I apply the technique to FIRST data using optically selected quasars from the SDSS to obtain the quasar RLF. In Chapter 4 I apply the technique to VLA data using near-infrared selected data from UltraVista to obtain galaxy RLF. I then use the SFG component of the RLF and the radio-infrared correlation to obtain an estimation of the SFRD. Chapter 5 is the conclusion.

Throughout the thesis I use the following ΛCDM cosmology, with $H_0 = 70$ km^{-1} Mpc^{-1}, $\Omega_\Lambda = 0.7$ and $\Omega_M = 0.3$. All quoted optical and NIR magnitudes are in the

AB system (Oke and Gunn, 1983). I assume a spectral index with $\alpha = -0.7$, when converting flux density to luminosity and one reference frequency to another.

Chapter 2

Beyond stacking

2.1 Introduction

Average stacking techniques have added a great deal to the understanding of faint source populations below the detection threshold. However, they generally return a single statistic, and all the information about the distribution of these sources below the detection threshold is lost.

Mitchell-Wynne et al. (2014) developed a technique that went beyond stacking by probing the source counts of galaxies below the detection threshold. This technique combines a stacking approach, in using positional information of pre-selected sources from another survey to extract noisy flux densities, with a pure background noise analysis, where the characteristics of the noise are studied. Armed with statistical behaviour of the noise, the underlining source count is constrained by fitting a source count model using maximum-likelihood. The technique was used to probe the source counts of FIRST ($\sigma = 150\,\mu$Jy) galaxies extracted at VLA-COSMOS 1.4-GHz ($\sigma = 12\,\mu$Jy) positions down to $110\,\mu$Jy, which are in good agreement with the VLA-COSMOS 1.4-GHz counts shown in Fig. 2.1.

Zwart et al. (2015b) then extended the technique of Mitchell-Wynne et al. (2014) to a fully Bayesian framework (BAYESTACK[1] Zwart et al. 2015b), which allows for model selection. They applied the technique to the Square Kilometre Array Design Study (SKADS) simulation (Wilman et al., 2008, 2010) and VLA data extracted at VISTA Infra-red Deep Extragalactic Observations (VIDEO) survey (Jarvis et al.,

[1] https://github.com/jtlz2/bayestack

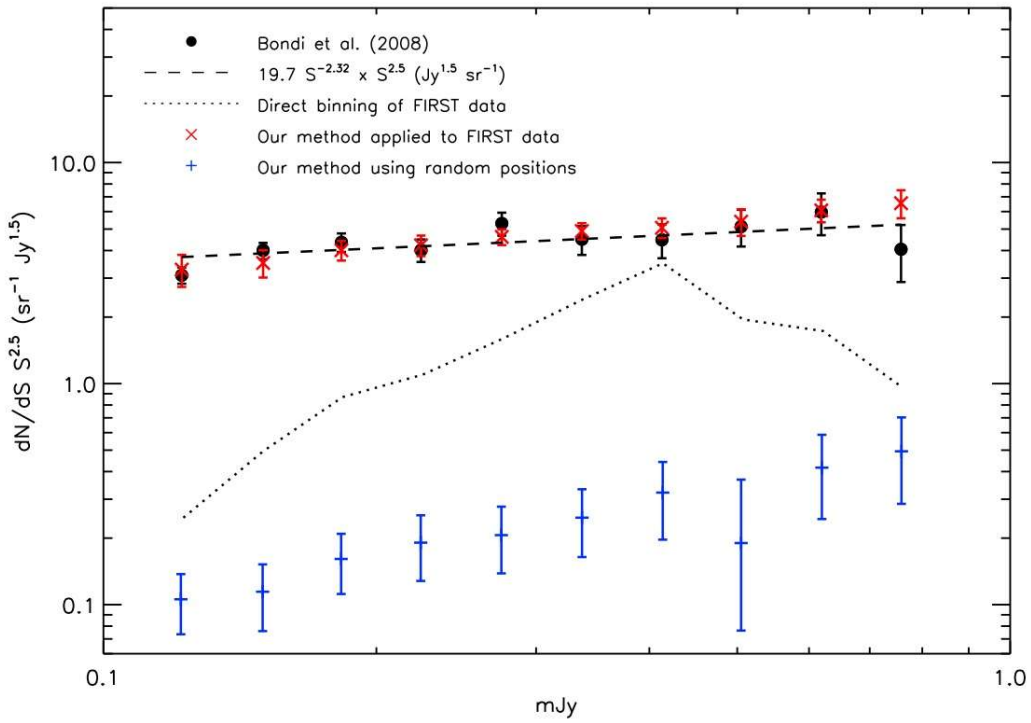

FIGURE 2.1: The source counts in the COSMOS field. The dotted lines represent the FIRST flux densities extracted at the positions of VLA-COSMOS 1.4-GHz sources. The red crosses (x) are the application of the technique to the noisy FIRST flux densities (dotted lines). The blue crosses (+) are the application of the technique on random noisy FIRST flux densities. The black circles are the VLA-COSMOS 1.4-GHz source counts from Bondi et al. (2008) and the dashed line is a fit to the VLA-COSMOS 3-GHz. Credit Mitchell-Wynne et al. (2014)

2013) positions. In both cases they recovered the corrected source counts. However, when confusion is introduced to the SKADs simulation, the recovered source counts are biased. Chen et al. (2017) extended the technique of Zwart et al. (2015b) by including the effects of the point spread function and source confusion, an approach that incorporates some of the reasoning from the $P(D)$ analysis with a Bayesian likelihood model fitting (Patanchon et al., 2009), they were able to successfully recover the correct source counts. Pan et al. (2020) extended upon the work of Zwart et al. (2015b) to measure the HI mass function.

The stacking analysis used in this thesis is based on a Bayesian formalism that can probe the RLF below the detection threshold of a map.

The idea is to start with a model for the RLF for a given redshift bin, which is translated into a source-count model, convolved with the noise and fit to the noisy

source count with the full Bayesian approach of Zwart et al. (2015b). Below is an overview of the technique.

2.2 Bayesian framework for measuring the RLF

The starting point is similar to a standard stacking technique, which is to extract the flux densities ($S_{\rm m}$) at the position of galaxies from data at a different wavelength. Assuming that the extracted flux density is from a single galaxy, it is a combination of the noiseless or intrinsic flux density of that galaxy (S) and the noise (n) at that position,

$$S_m = S + n. \tag{2.1}$$

The total noise (n) at the position of an object is assumed to follow a Gaussian distribution, centered at zero with a variance σ^2. In this thesis I assume that confusion noise is negligible (which holds for the FIRST and VLA-COSMOS 3-GHz surveys). The flux densities are then binned across the full flux density distribution and fit with source count models.

The fitting approach uses Bayes' theorem,

$$\mathcal{P}(\Theta|D,H) = \frac{\mathcal{L}(D|\Theta,H)\Pi(\Theta|H)}{\mathcal{Z}}, \tag{2.2}$$

where $\mathcal{P}$ is the posterior distribution of the parameters Θ, given the data D and model H. $\mathcal{L}$ is the likelihood, the probability distribution of the data given the model, and Π is the prior, the known constraints on the parameters. $\mathcal{Z}$ is the Bayesian evidence, which normalises $\mathcal{P}$ and can be written as an integral of $\mathcal{L}$ and Π over the n-dimensional parameter space Θ,

$$\mathcal{Z} = \int \mathcal{L}\Pi \mathrm{d}^n\Theta. \tag{2.3}$$

A model has high evidence when a large portion of its prior parameter space is likely (i.e. large likelihood), and small evidence when a large portion of its parameter space has a small likelihood, irrespective of how peaked the likelihood function is. This therefore automatically encapsulates Occam's razor (Feroz et al. 2009b).

In order to compute this posterior distribution, one needs to sample from it. Sampling has always been one of the most computationally expensive parts of model

selection because it involves solving the multidimensional integral in Eq. 2.3. Nested sampling (Skilling 2004) was created for its efficiency in calculating the evidence, with an added bonus of producing posterior inferences as a by-product. MULTINEST (Feroz et al., 2009a,b; Buchner et al., 2014) is a robust implementation of nested sampling, returning the full posterior distribution from which the uncertainty analysis can be correctly undertaken.

In Bayesian model selection, one compares the evidences of two models, A and B. This is quantified by considering the ratio of their evidences $\mathcal{Z}_A/\mathcal{Z}_B$, or equivalently, the difference in their log-evidence, $\ln(\mathcal{Z}_A) - \ln(\mathcal{Z}_B)$, known as the Bayes factor. Jeffreys (1961) introduced a way to conclude how much better Model A is compared to B using the Bayes factor: $\Delta \ln \mathcal{Z} < 1$ is 'not significant', $1 < \Delta \ln \mathcal{Z} < 2.5$ is 'significant', $2.5 < \Delta \ln \mathcal{Z} < 5$ is 'strong', and $\Delta \ln \mathcal{Z} > 5$ is 'decisive'. I adopt this scale in my analysis and use it to compare different models for the evolving RLF.

2.2.1 Likelihood function

Since I am dealing with a binned flux density distribution of the galaxies, I assume a Poisson likelihood function. As such, the likelihood of finding k_i objects in the i^{th} flux density bin $[S_{mi}, S_{mi} + \Delta S_m]$ follows a Poisson distribution,

$$\mathcal{L}_i\left(k_i|\boldsymbol{\Theta}\right) = \frac{I_i^{k_i} \mathrm{e}^{-I_i}}{k_i!}, \tag{2.4}$$

where I_i is the theoretically-expected number of sources in the i^{th} measured bin, given by the modified equation taken from Mitchell-Wynne et al. (2014),

$$I_i = \int_{S_{min}}^{S_{max}} dS \frac{dN(S)}{dS} \int_{S_{m_i}}^{S_{m_i}+\Delta S_{m_i}} dS_m \frac{1}{\sigma_n \sqrt{2\pi}} \exp\left(-\frac{(S-S_m)^2}{2\sigma^2}\right). \tag{2.5}$$

Here dN/dS is the source count model (number of sources per flux density bin), σ is the average noise of the data and S is again the intrinsic flux density of the source. In Chapter 3 I apply the technique to FIRST data, where the intrinsic FIRST flux density (S_{F}) of a galaxy is affected by biases (CLEAN and snapshot bias, see Eq. 3.2). Therefore, in order to compare the intrinsic flux (S) to the measured flux density, I need to first apply the expected bias effects of the FIRST observation, e.g. $S_{\mathrm{F}} = \max\{S/1.4, (S - 0.25\,\mathrm{mJy})\}$. This approach naturally takes into account sample variance (at the Poisson level), since it does not fix the total number of

predicted sources to the observed number (other regions of the sky could have a different total number). This will have implications for the allowed minimum and maximum flux density values of the fits. I expect the fits to have large variance at the low flux density level (because of the noise) and at the high flux density level (because of Poisson fluctuations due to the low number of sources).

Solving the second integral, Eq. 2.5 becomes

$$I_i = \int_{S_{min}}^{S_{max}} dS \frac{dN(S)}{dS} \frac{1}{2}\left\{ \mathrm{erf}\left(\frac{S - S_{m_i}}{\sigma\sqrt{2}}\right) - \mathrm{erf}\left(\frac{S - (S_{m_i} + \Delta S_{m_i})}{\sigma\sqrt{2}}\right)\right\}. \tag{2.6}$$

The total likelihood for the N bins is given by,

$$\mathcal{L}\left(\mathbf{k}|\boldsymbol{\Theta}\right) = \prod_{i=1}^{N} \mathcal{L}_i\left(k_i|\boldsymbol{\theta}\right). \tag{2.7}$$

As the aim is to fit models that describe the RLF, the RLF models have to be converted to source counts (dN/dS), and compared to the binned flux densities.

2.2.2 Radio luminosity function models

The spectral luminosity L_ν, at frequency ν of a source at redshift z can be related to the observed flux density at the same frequency, S_ν, through

$$L_\nu = 4\pi D_L^2 (1+z)^{-\alpha-1} S_\nu, \tag{2.8}$$

where D_L is the luminosity distance, α is the spectral index of the source (we assume to be $\alpha = -0.7$), and z is the redshift of the source.

The luminosity function (LF), $\rho(L_\nu)$, is the number density of sources per luminosity density bin, e.g. $\rho(L_\nu) = dN/(dLdV)$ (where dV is comoving volume). Another common definition of the LF (Φ), which I use in this thesis, normalises the RLF per magnitude (as opposed to using per $\log_{10} L$), where $m - m_0 = -2.5\log_{10}(L/L_0)$. The relationship between these two definitions is then

$$\Phi(L_\nu) = \frac{dN}{dV\,dm} = \frac{dN}{dV\,dL_\nu}\frac{dL_\nu}{dm} = \ln(10^{0.4}) L_\nu \rho(L_\nu). \tag{2.9}$$

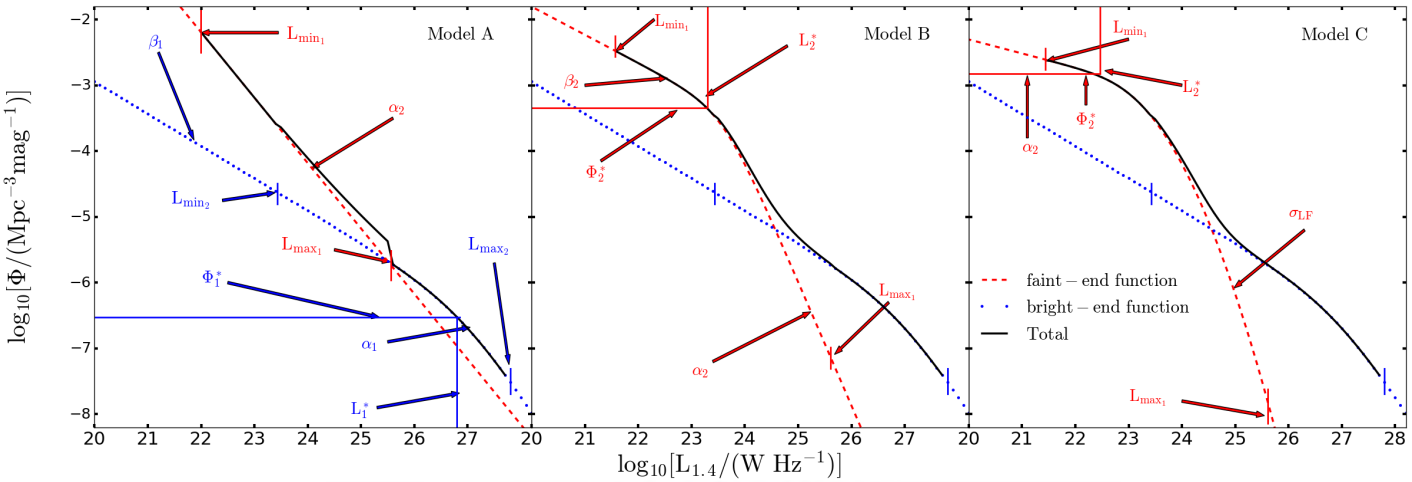

FIGURE 2.2: The three models and their parameters. The bright population is modeled by the blue dots (the bright function, which is the same for all the models) and the faint population is modeled by the red dashed line (faint function). The faint function is different for the three models: Model A has a powerlaw, Model B is a double powelaw and Model C is a lognormal powerlaw.

I define parametric models for the RLF consisting of two functions, one for the luminous sources and the other for faint sources (using subscripts 1 and 2 respectively). The RLF at higher luminosities is dominated by AGN and has been shown to follow a double power law (e.g. Willott et al. 2001; Mauch and Sadler 2007; Prescott et al. 2016), so I parameterise the luminous part of the RLF as a double power law for all the models considered here. The shape of the RLF at low luminosities is dominated by SFGs but also contains radio-quiet AGN (Jarvis and Rawlings, 2004; White et al., 2015, 2017), so for that, three models are considered: a power law, a double power law and a modified Schechter function (log-normal power law) shown in Fig. 2.2. These models are given below.

Model A is the simplest overall form for the RLF – a double power law for the high luminosities (the detected sources) and a single power law to describe the RLF at low luminosities:

$$\Phi(L)_A = \frac{\Phi_1^*}{(L/L_1^*)^{\alpha_1} + (L/L_1^*)^{\beta_1}} + \frac{\Phi_2^*}{(L/L_2^*)^{\alpha_2}}. \tag{2.10}$$

Note that L_2^* and Φ_2^* will be degenerate here, but the model is kept in this form for convenience.

Model B has a double power law for both the high- and low-luminosity sources:

$$\Phi(L)_B = \frac{\Phi_1^*}{(L/L_1^*)^{\alpha_1} + (L/L_1^*)^{\beta_1}} + \frac{\Phi_2^*}{(L/L_2^*)^{\alpha_2} + (L/L_2^*)^{\beta_2}}. \tag{2.11}$$

Model C has a double power law for the luminous sources and a log-normal power law for low-luminosity sources, which has been used for star-forming galaxies (e.g. Tammann et al. 1979):

$$\begin{aligned}\Phi(L)_C =& \frac{\Phi_1^*}{(L/L_1^*)^{\alpha_1} + (L/L_1^*)^{\beta_1}} \\ &+ \Phi_2^* \left(\frac{L}{L_2^*}\right)^{1-\alpha_2} \exp\left[-\frac{1}{2\sigma_{LF}^2} \log_{10}^2\left(1 + \frac{L}{L_2^*}\right)\right].\end{aligned} \tag{2.12}$$

In Chapter 4 I explore a model of fixed functional form that evolves with redshift, and to facilitate comparison with previous work (e.g. McAlpine et al., 2013; Novak et al., 2017, 2018), I also consider '**Model D**', which has a total RLF given by combining local SFG and AGN RLFs. I use the local AGN RLF model and parameters from Mauch and Sadler (2007), where they constrain both the bright and faint ends of the AGN population. They fit their RLF with a double power law (first function of Eq. 2.12), with best-fit parameters, $\phi_1^* = 10^{-5.5}$ Mpc^{-3}mag^{-1}, $L_1^* = 10^{24.59}$ WHz^{-1}, $\alpha_1 = 1.27$ and $\beta_1 = 0.49$.

For modelling SFGs, I use the local SFG RLF from Novak et al. (2017) obtained by fitting a log-normal power law to combined data from Condon et al. (2002), Best et al. (2005), and Mauch and Sadler (2007), which contains low-resolution and deep high-resolution information to constrain both the faint and bright ends of the SFG RLF. Using an analytical function in the form of a log-normal power law (second function of Eq. 2.12) their best-fit parameters are $\Phi_2^* = 1.42 \times 10^{-3}$ Mpc^{-3}mag^{-1} (scaled to my binning), $L_2^* = 1.85 \times 10^{21}$ WHz^{-1}, $\alpha_2 = 1.22$ and $\sigma_{LF} = 0.63$.

In order to fit Model D to galaxy samples at different redshifts I need to evolve the RLF. The most common ways to quantify this evolution are through density and/or luminosity evolution, although I note that the true evolution is probably a mixture of the two (e.g. Yuan et al., 2016). Density evolution is apparent through a vertical shift in the RLF with changing redshift, and luminosity evolution as a horizontal shift (i.e the characteristic luminosity increases or decreases with redshift). The SFGs and AGN are known to evolve differently, hence I adopt two separate evolution models for these two populations . The combined density- and luminosity-evolution

TABLE 2.1: Assumed priors for the SKADS noisy sources.

Parameter	Prior
α_2, β_2	uniform $\in [-5, 5]$
σ_{LF}	Gaussian$\sim$ $(\mu = 0.6, \sigma = 0.1)$
$\log_{10}[L_{\min_2}/(\mathrm{WHz}^{-1})]$	uniform $\in [20, 25]$
$\log_{10}[L_{\max_2}/(\mathrm{WHz}^{-1})]$	uniform $\in [20, 25]$
$\log_{10}[\phi_2^*/(\mathrm{Mpc}^{-3}\mathrm{mag}^{-1})]$	uniform $\in [-12, -2]$
$\log_{10}[L_2^*/(\mathrm{WHz}^{-1})]$	uniform $\in [20, 24.5]$

fit is known to have large degeneracies when the knee (L_2^*) of the RLF for SFGs is not well constrained, and pure density evolution can overestimate sources at low luminosities (e.g. Novak et al. 2017, 2018). Therefore, I only consider a pure luminosity evolution (PLE) of the form,

$$\begin{aligned}\Phi(L, z) =& \Phi_0^{SF}\left[\frac{L}{(1+z)^{\alpha_L^{SF}+z\beta_L^{SF}}}\right] \\ &+ \Phi_0^{AGN}\left[\frac{L}{(1+z)^{\alpha_L^{AGN}+z\beta_L^{AGN}}}\right],\end{aligned} \tag{2.13}$$

where Φ_0^{SF} is the local SFG RLF, Φ_0^{AGN} is the local AGN RLF, and $\alpha_L^{SF,AGN}, \beta_L^{SF,AGN}$ are the evolution parameters.

Finally, it is noted that each of the model functions will be bounded: $L_{\min_1} \leq L \leq L_{\max_1}$ for the low-luminosity end and $L_{\min_2} \leq L \leq L_{\max_2}$ for the high-luminosity end. The boundaries are allowed to overlap since there might be a contribution from both populations.

The likelihood (Eq. 2.6) is computed in flux density space, which means that the LF models, $\Phi(L)$, have to be converted into source-count models, dN/dS:

$$\begin{aligned}\frac{dN}{dS} &= \frac{dN}{dL}\frac{dL}{dS} \\ &= \rho(L)V_i 4\pi D_L^2 (1+z_i)^{-\alpha-1} \\ &= \frac{\Phi(L)V_i}{L\ln(10^{0.4})} 4\pi D_L^2 (1+z_i)^{-\alpha-1},\end{aligned} \tag{2.14}$$

where V_i is the volume of the survey for the redshift bin i and z_i is the mean redshift for that bin.

2.2.3 Priors

Priors play an important role in Bayesian inference as they define the sampled parameter space. A uniform prior is the simplest form, providing an equal weighting of the parameter space. I assign a uniform prior to the power law slopes $\alpha_{1,2}$, $\beta_{1,2}$ and α_2. The parameter σ_{LF} is assigned a Gaussian prior. To avoid degeneracies in the slopes for the double power law, I also impose $\alpha_{1,2} \geq \beta_{1,2}$. The parameters $L^*_{1,2}$, $L_{\min_{1,2}}$, $L_{\max_{1,2}}$ and $\phi^*_{1,2}$ all have uniform priors in log-space. I have an additional prior on the AGN break (L^*_1) that must never be less than 0.5 dex above the detection threshold. I have this prior because the bright end of the RLF is not always well constrained by the COSMOS data (Chapter 4). Furthermore, the prior is justified because the AGN RLF is well explored in the literature and the break is found at luminosities well above the luminosity corresponding to 5σ (e.g Smolčić et al., 2017b; Ceraj et al., 2018).

Combining Eq. 2.7 with the priors, and substituting into Eq. 2.2, one can determine the posterior probability distribution as well as the evidence. I use a Python implementation (Buchner et al. 2014) of MultiNest (PyMultiNest) to fit the models with evidence_tolerence = 0.5 and sampling_efficiency = 0.3.

2.3 Tests on simulated data

I test the technique by applying it to the Square Kilometre Array Design Studies SKA Simulated Skies (SKADS-S^3) simulations (see Wilman et al. 2008, 2010). SKADS is a semi-empirical simulation of the extragalactic radio continuum sky, covering a sky area of 20×20 deg^2 with ≈ 320 million sources out to a redshift of $z = 20$ and flux density of 10 nJy. In the tests below I use $\sim$ 555000 sources contained within a 8 deg^2 patch of the simulation in the redshift range $1.0 < z < 1.3$ [2]. Of those sources, 223 457 have radio luminosities between $20.5 < \log_{10}[L/\mathrm{W\,Hz^{-1}}] < 24.5$ and I call this the full (deep) sample (luminosities are calculated using the mean redshift $z = 1.15$). In order to test how a higher luminosity cut may alter the fits, I also consider a brighter (shallow) sample of 91 458 sources that lie between $21.5 < \log_{10}[L/\mathrm{W\,Hz^{-1}}] < 24.5$[3].

[2] This particular redshift was chosen simply because it is one of the redshift ranges used in Chapter 3.

[3] These luminosity ranges were chosen because they are the similar to those probed in Chapter 3 and Chapter 4.

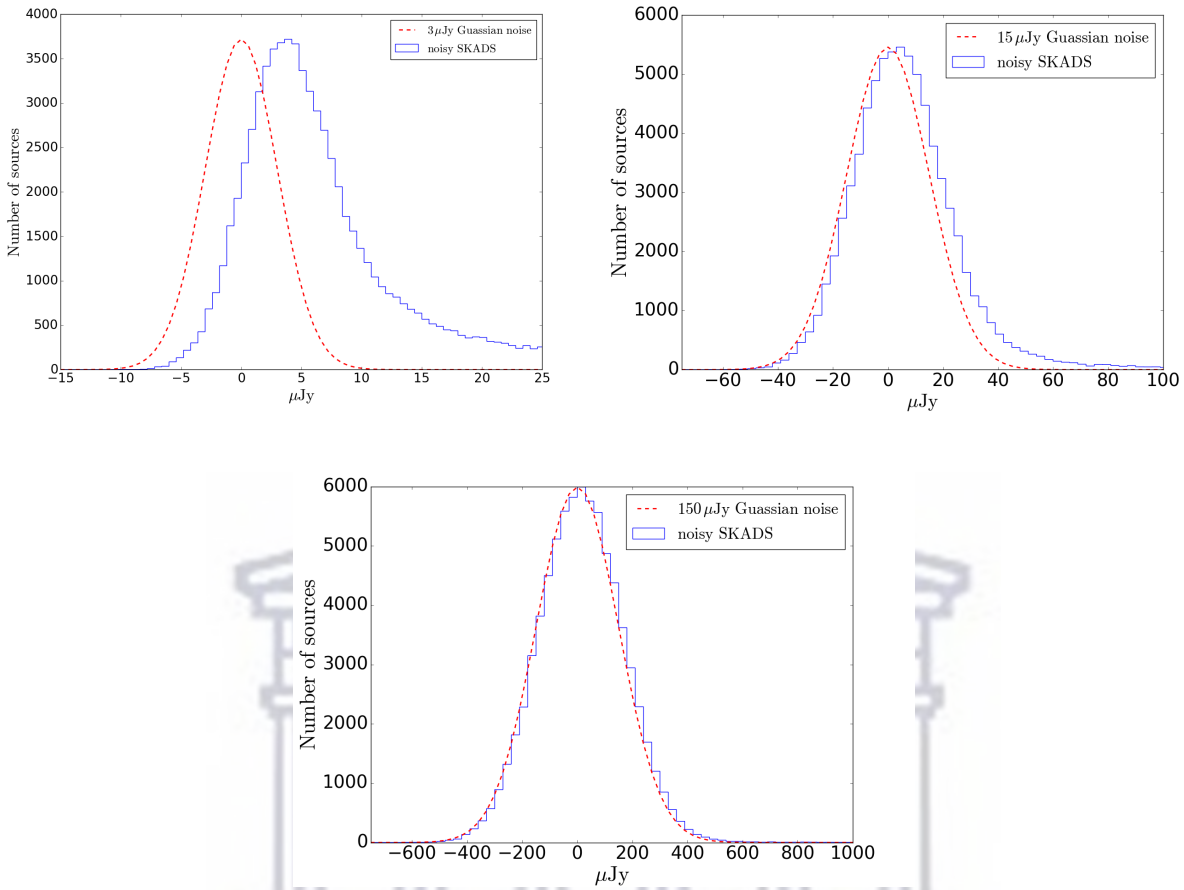

FIGURE 2.3: Histogram of flux density of the SKADS sources with 3 μJy (top left), 15 μJy (top right) and 150 μJy (bottom) random Gaussian noise added (blue solid line). The dashed line is the histogram of the random Gaussian noise.

2.3.1 Shallow sample

I first start with the shallow sample which contains sources with radio luminosities between $21.5 < \log_{10}[L/\mathrm{W\,Hz^{-1}}] < 24.5$. I add noise – generated from a Gaussian distribution, with standard deviation σ of 150 μJy ($S_n = S + N[150\ \mu\mathrm{Jy},\ 0]$) – to the shallow sample, to emulate the observed data (i.e. the 'noisy' sources in FIRST). I repeat this using two noise levels of 15 μJy and 3 μJy. I bin the noisy SKADS sources in the observed flux density, shown in Fig. 2.3. The noisy flux densities closely resemble the Gaussian distribution of the added noise when the added noise is much greater than the average flux density of the sources, as seen in the case where 150 μJy noise is added. In the 15 μJy case where the added noise is comparable to the flux density of the sources the noisy flux density distribution has an offset from the Gaussian distribution of the noise (which is centred at zero). The smaller the added noise is relative to the average flux density then the larger the

TABLE 2.2: The relative log-evidence, $\Delta \log_{10} Z$, for the models using single RLF (Model A', B' and C') relative to the model with the lowest evidence in each case, applied to the deep and shallow SKADS sample with different noise levels. The winning model (model with the highest evidence) for each noise level in both the deep and shallow sample is in bold.

Model	3 μJy	15 μJy	150 μJy
	$\Delta \log_{10} Z$		
$21.5 < \log_{10}[L/(\mathrm{WHz}^{-1})] < 24.5$			
A'	0.0 ± 0.00	0.0 ± 0.00	0.0 ± 0.0
B'	$\mathbf{449.1 \pm 0.23}$	$\mathbf{134.2 \pm 0.22}$	$\mathbf{1.6 \pm 0.17}$
C'	446.7 ± 0.22	102.5 ± 0.21	0.9 ± 0.17
$20.5 < \log_{10}[L/(\mathrm{WHz}^{-1})] < 24.5$			
A'	0.0 ± 0.00	0.0 ± 0.00	0.0 ± 0.00
B'	941.0 ± 0.22	128.7 ± 0.20	0.5 ± 0.15
C'	$\mathbf{989.4 \pm 0.21}$	$\mathbf{134.4 \pm 0.20}$	$\mathbf{1.5 \pm 0.18}$

offset is between the noisy flux densities and the Gaussian noise. I then apply the technique on all three noisy samples using a different set of models, which include only the part used for the low-luminosity region (parameters with subscript '2'). These are defined as **Model** A' (single power-law), **Model** B' (double power-law) and **Model** C' (a log-normal power law). The priors assumed for the simulations are shown in Table 2.1.

MULTINEST returns the Bayesian evidence for the model and the posterior distribution for all the fitted parameters. The 'relative evidence' for a model is the difference between the model evidence and the reference-model evidence (where the reference model is the model with the lowest evidence). The relative evidence for the SKADS samples is shown in Table 2.2, where the winning model, the one with the highest relative evidence, is in bold. From the relative evidence it is clear that the data prefer the double power law function (Model B') for all the noise levels in the shallow sample. The evidence is marginal between models for the 150 μJy noise level. The evidence also suggests that the power law function (Model A') is a significantly poor fit compared to the other models for the 15 μJy and 3 μJy noise levels. The evidence is much more significant because lower-noise is added to the simulated data.

Fig. 2.4 shows the one-dimensional (1D) and two-dimensional (2D) posterior distributions for the fits of the various models to the 'noisy' shallow SKADS sample. The 1D posterior distribution is the marginalization for each parameter, located at the end of each row in Fig. 2.4. The 68% and 95% confidence regions in the 2D

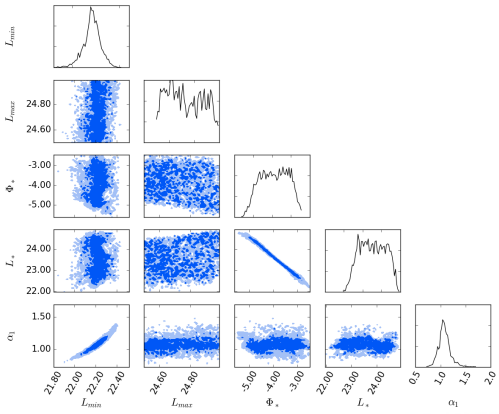

(A) Model A'; 150 μJy

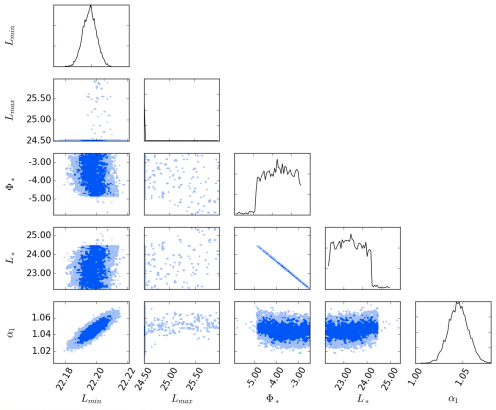

(B) Model A'; 15 μJy

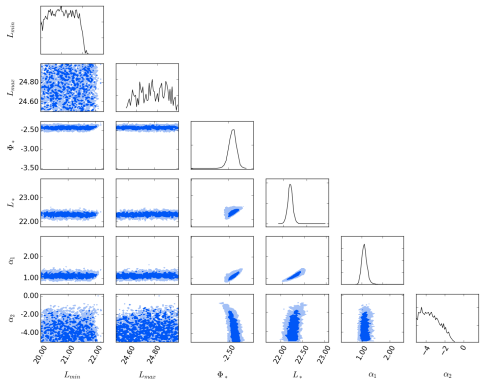

(C) Model B'; 150 μJy

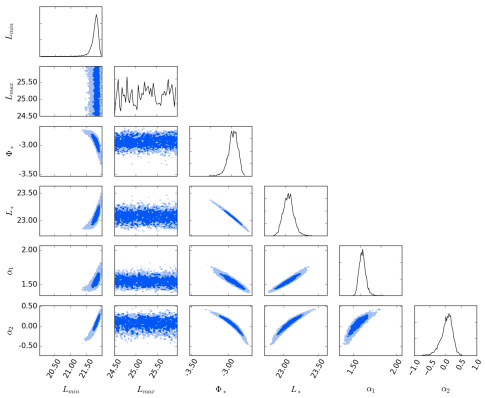

(D) Model B'; 15 μJy

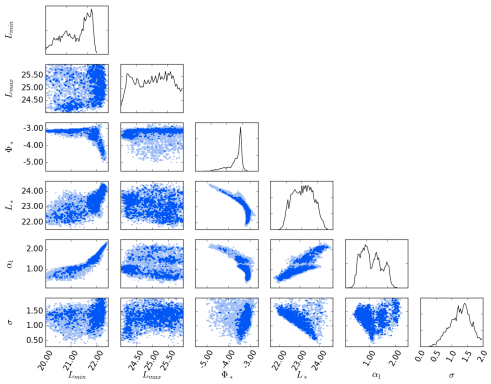

(E) Model C'; 150 μJy

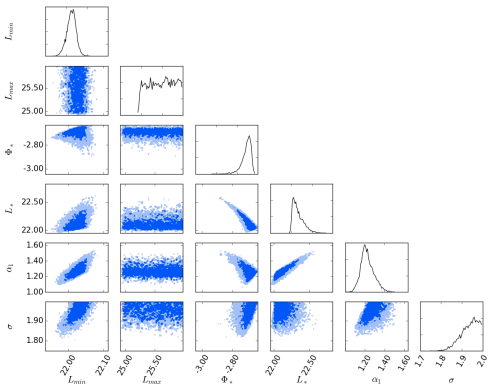

(F) Model C'; 15 μJy

FIGURE 2.4: The posterior distributions for the shallow SKADS sample ($21.5 < \log_{10}[L/(\mathrm{WHz}^{-1})] < 24.5$) with the noise levels of 150 μJy and 15 μJy using Models A', B' and C'. The parameters L_{min_1}, L_{max_1}, Φ_2^* and L_2^* are in logarithmic space ($\log_{10}$). The dark blue and the light blue regions are the 68% and 95% regions.

are the models with the highest likelihood that make up 68% and 95% of the posterior distribution. The peaks in 1D do not always do justice to the 2D posteriors, as the 2D ones are not just simple Gaussians. They show distorted 'banana-like' shapes, with some having long tails. The limits on each plot are the maximum and minimum values from the posterior distribution. Some of these parameters (mainly the boarder parameters $L_{\max_{1,2}}$ and $L_{\min_{1,2}}$) are unconstrained and therefore limited by the assumed priors. Note, however, that this has no effect on the reconstructed RLFs. The is no difference in the posterior distributions for Model A with the 150 μJy and 15 μJy noise levels. This is due, as the evidence shows in Table 2.2, Model A being a poor fit for the data. The posterior distribution for Model B with the two noise models show a different solutions as the parameters Φ^*, L^*, α_1 and α_2 all cover a different parts of the posterior space with little overlap. Furthermore, in the 150 μJy noise level Φ^* is directly proportional to L^* while this relation ship is inversely proportional in the 15 μJy noise level. The posterior distributions for Model C with the 150 μJy noise level show three different solutions which are more evident in the 1D distribution of α_1. The poster distributions for 15 μJy noise level has only one of the three solutions shown in the posterior distributions for the 150 μJy noise level.

Along with the evidence and the posterior distributions, MultiNest returns three values to summarize each parameter: the median, maximum-likelihood and maximum-a-posteriori (MAP, maximizing the product of the likelihood and prior) values. Obtaining a single value for a parameter is straightforward if the 1-D posterior is Gaussian, as the mean, MAP and maximum likelihood are the same or very similar. It is clear that some of the posteriors in Fig. 2.4 are not Gaussian, which would mean that the three summaries are likely to be different from one another. All three parameters are used to reconstruct the LFs in turn. (The maximum likelihood gives the same value as the MAP for models with uniform priors, so I just quote the MAP). Although they are good estimates, they still do not fully describe the complex nature of the posterior, as clearly shown in Fig. 2.4.

In Fig. 2.5 I show the reconstruction of RLFs of the noisy shallow SKADS sample $21.5 < \log_{10}[L_{1.4}/\mathrm{W\,Hz^{-1}}] < 24.5$ using the average, MAP parameters and the 95% confidence interval for each model fit and noise level. Such a choice is not unique, as the models that span the 95% confidence interval do not necessarily give a continuous region in terms of the RLF curves. The 95% region is calculated by reconstructing the RLF in a chosen set of luminosity bins, using all the models in the

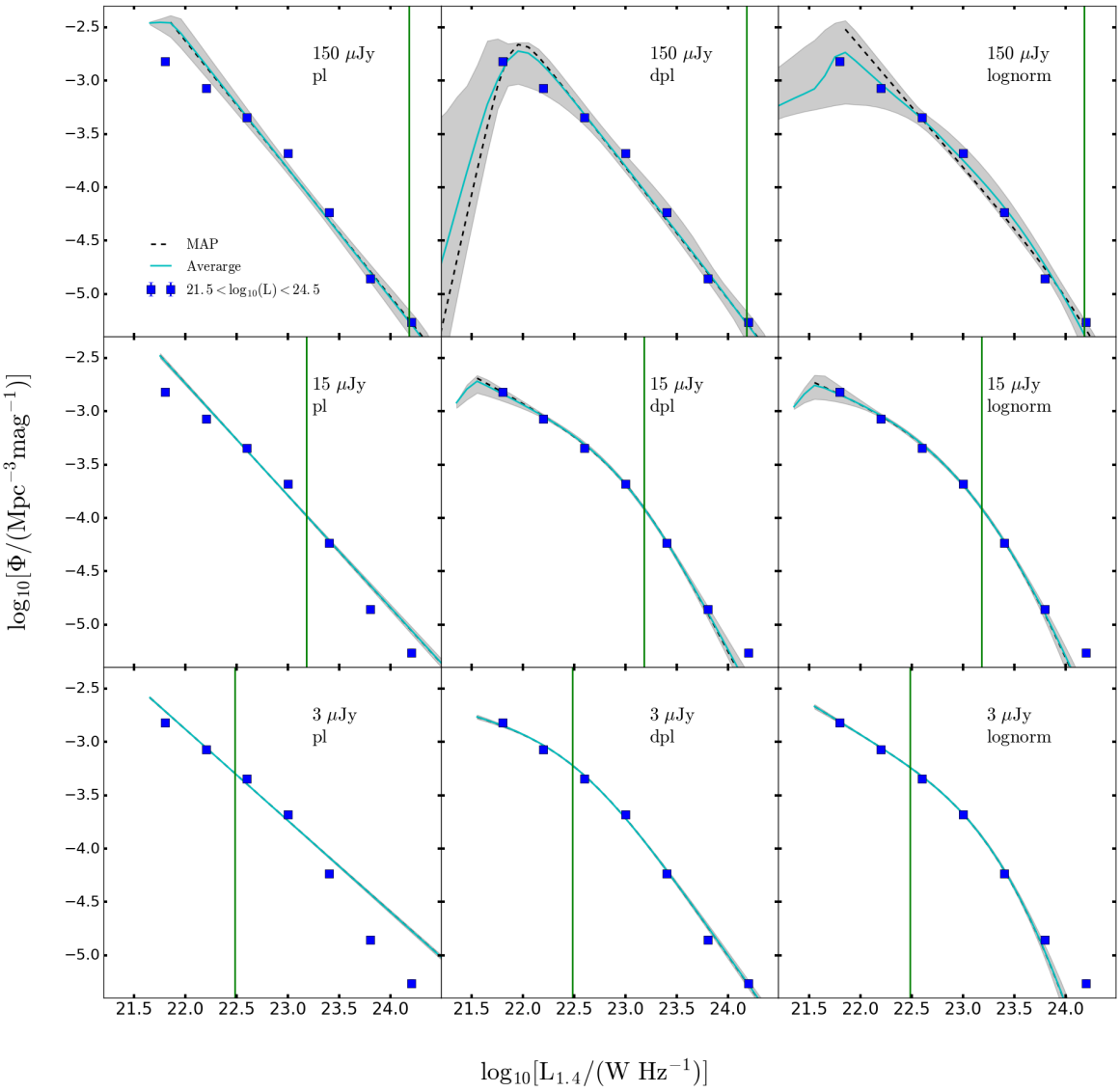

FIGURE 2.5: The SKADS RLF and the reconstruction of the RLF using BAYESTACK for the $21.5 < \log_{10}[L/(\mathrm{WHz}^{-1})] < 24.5$ in the redshift range $1 < z < 1.3$ (the shallow sample). The top, middle and bottom panels are the reconstructions when noise of respectively $150\,\mu$Jy , $15\,\mu$Jy and $3\,\mu$Jy is added to the simulated SKADS sources. The left panels are the power law models ('pl', A'), the middle (vertical) panels are the double power law models ('dpl', B') and the right panels are the log-normal models ('lognorm', C'). The blue squares denote the true SKADS RLFs for the shallow sample obtained using the $1/V_{\mathrm{max}}$ method. The cyan and black dashed curves respectively represent the RLFs reconstructed using the median and MAP parameters. The grey regions represent the 95% confidence intervals for the distribution of model reconstructions in the posterior. The green solid line represents the $5\,\sigma$ noise (using $z = 1.15$) shown in the to the right corner of each panel.

posterior, and determining the 95% limits in each luminosity bin independently. The actual RLF representing the simulated data can be calculated directly by binning the luminosity values from the simulation and normalizing by the comoving volume. Throughout the thesis I use the $1/V_{\rm max}$ method to calculate the RLF (Schmidt, 1968) given by,

$$\Phi(L_\nu) = \frac{1}{\Delta m} \sum_{i=1}^{N} \left(\frac{1}{V_{\rm max}} \right)_i , \tag{2.15}$$

with an uncertainty

$$\sigma(\Phi) = \frac{1}{\Delta m} \left[\sum_{i=1}^{N} \left(\frac{1}{V_{\rm max}} \right)_i^2 \right]^{1/2} , \tag{2.16}$$

where $V_{\rm max}$ is the volume contained by a maximum redshift from the minimum of that from the redshift bin and the flux limits of the surveys involved. The $1/V_{\rm max}$ RLFs are also included in Fig. 2.5. The reconstructed RLFs with 150 μJy noise levels have a large scatter but are in good agreement with the true SKADS RLF up to $\approx$ 2 dex below the detection threshold, except for the power law (model A'), which is unable to reproduce some futures of the $V_{\rm max}$ as is also clear from Table 2.2. As expected, using lower noise levels produces RLF reconstructions with better fits to the SKADS RLF and smaller 95% confidence regions (the 15 μJy and 3 μJy noise level panels in Fig. 2.7). Thus the fitting method works for the current noise levels and for those that will be obtained by future radio surveys. The fit is unbiased, though if the model is quite poor, the fitting will obviously also be poor (as in the case of the power law).

2.3.2 Deep sample

I also add the random noise levels to the deeper sample ($20.5 < \log_{10}[L_{1.4}/\mathrm{W\,Hz^{-1}}] < 24.5$) to see how this affects the fitting. The evidence from running the various noise levels with all three models is shown in the lower part of Table 2.2. In contrast to the shallow sample were Model B' is the preferred, the evidence prefers the log-normal (Model C') in all the noise levels. The single power law (Model A') is again significantly the least preferred model for all the noise levels. The 1D and 2D posterior distributions are shown in Fig. 2.6 and the RLFs are shown in Fig. 2.7. As in the shallow case, the reconstructed RLFs with 150 μJy noise level have a large scatter but are still in good agreement with the true SKADS RLF up to $\approx$ 4 dex below the detection threshold. The lower noise levels also produce better

fits to the SKADS data with smaller posterior distributions (which are a subset of the higher noise levels) that lead to RLF reconstructions with smaller 95% confidence regions. Thus the fitting is not affected when the sample includes sources down to $\log_{10}[L/(W\,Hz^{-1})] = 20.5$, although (as one would expect) the uncertainty increases as one moves to lower luminosities for a given noise level.

2.4 Summary

I have built on the work of Zwart et al. (2015b) by adapting the Bayesian stacking technique (BAYESTACK) to fit RLFs directly to data below the radio detection threshold. I tested the technique by fitting three models to mock SKADS simulation catalogues (Wilman et al. 2008; 2010), with random Gaussian noise of 150 μJy added. I successfully recovered the SKADS RLF over 2 dex below the 5σ detection threshold. I ran further tests using mock catalogues with 15 μJy and 3 μJy Gaussian noise and as expected, reconstructed a better-constrained RLF with respect to the true SKADS RLF. Finally, I ran the 150 μJy, 15 μJy and 3 μJy added noise on deeper simulated data and showed that the fitting is not affected when the sample includes sources down to lower luminosities, although the uncertainty increases towards lower luminosities.

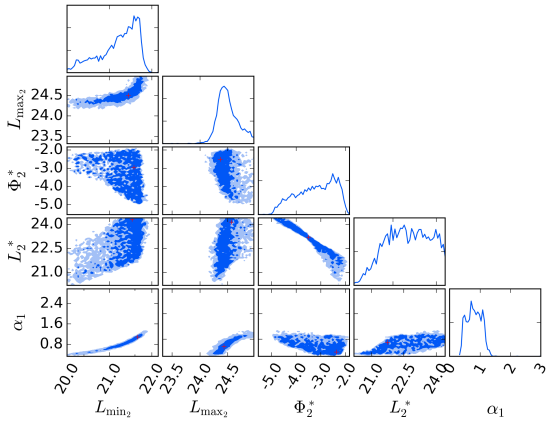

(A) Model A'; 150 μJy

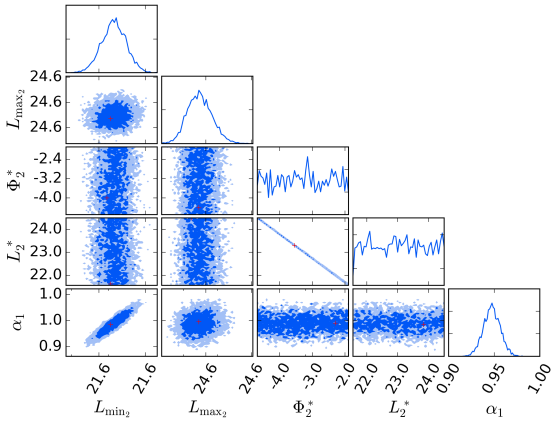

(B) Model A'; 15 μJy

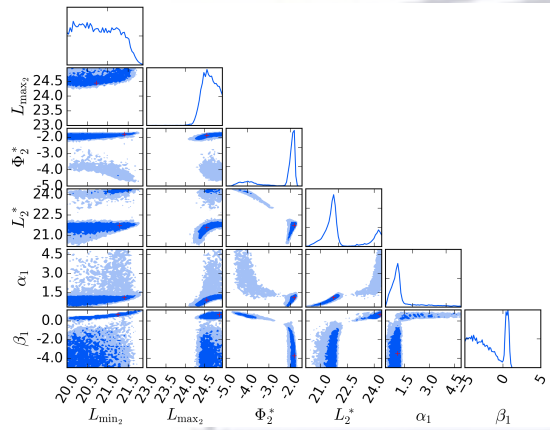

(C) Model B'; 150 μJy

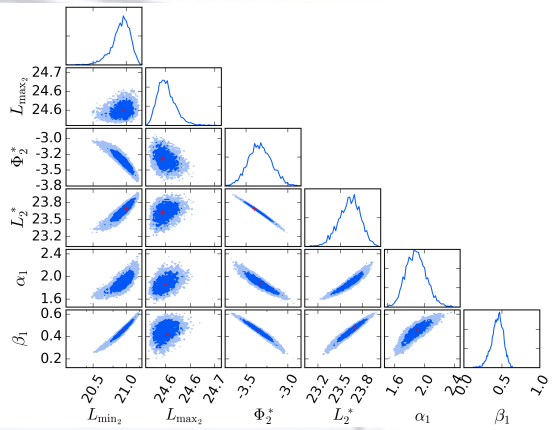

(D) Model B'; 15 μJy

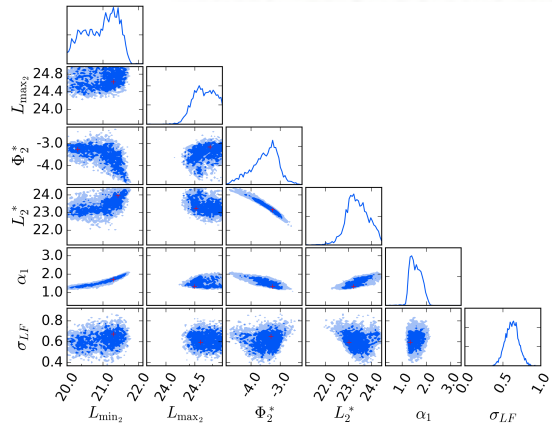

(E) Model C'; 150 μJy

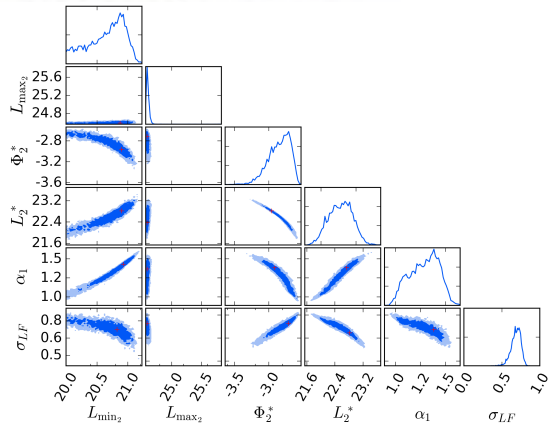

(F) Model C'; 15 μJy

FIGURE 2.6: The posterior distributions for the full SKADS sample ($20.5 < \log_{10}[L/(\mathrm{WHz}^{-1})] < 24.5$) with the noise levels of 150 μJy and 15 μJy using Models A', B' and C'. The parameters $L_{\min_2}$, $L_{\max_2}$, Φ_2^* and L_2^* are in logarithmic space ($\log_{10}$). The dark blue and the light blue regions are the 68% and 95% regions. The red cross represents the point with the highest marginalised likelihood in each individual plot.

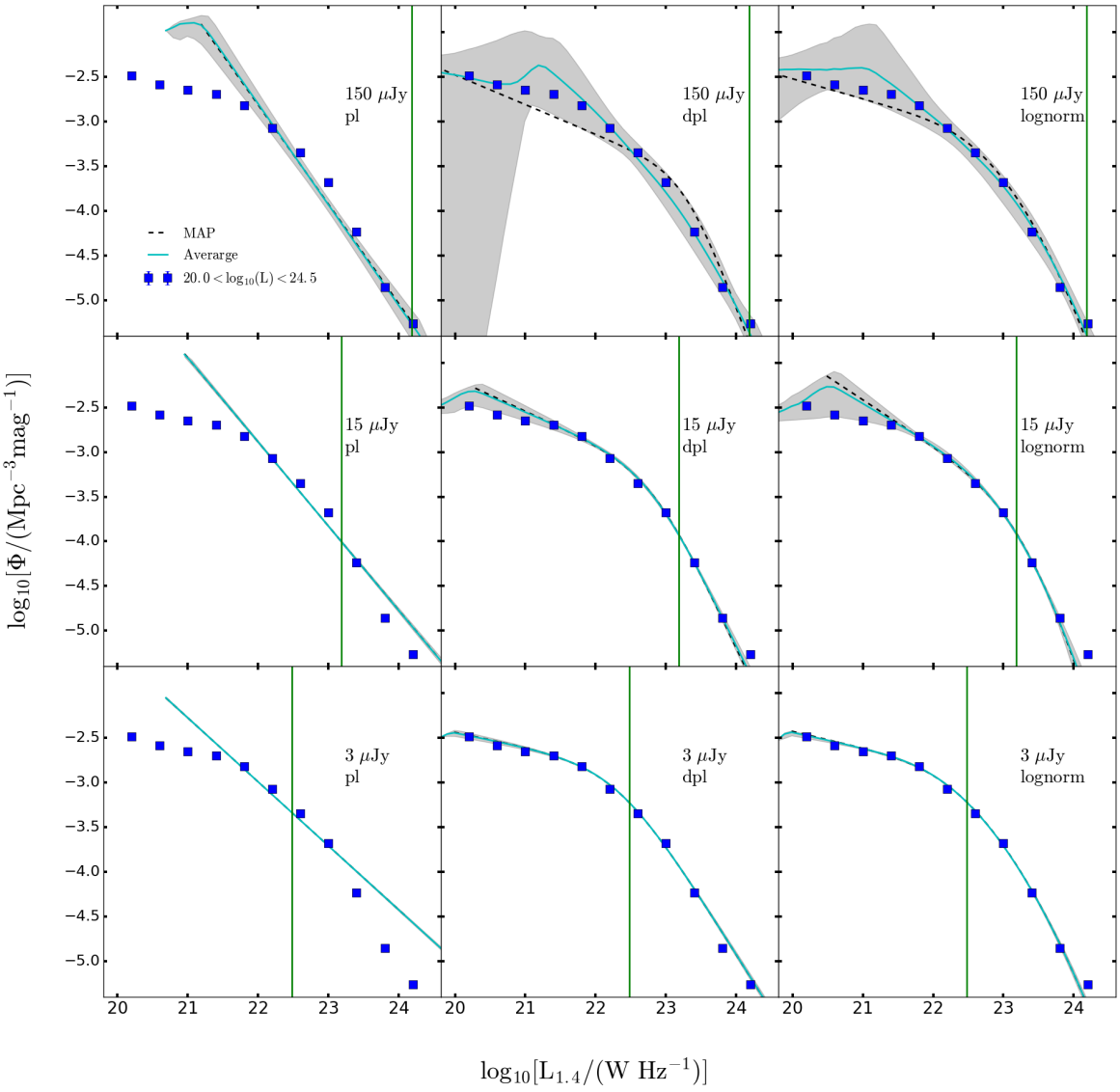

e

FIGURE 2.7: The SKADS RLF and the reconstruction of the RLF using BAYESTACK for the $20.5 < \log_{10}[L/(\mathrm{WHz}^{-1})] < 24.5$ in the redshift range $1 < z < 1.3$ (deep sample). The top, middle and bottom panels are the reconstructions when noise levels of respectively $150\,\mu$Jy , $15\,\mu$Jy and $3\,\mu$Jy are added respectively to the deep SKADS sample. The left panels are the power law models ('pl', A'), the center panels are the double power law models ('dpl', B') and the right panels are the log-normal models ('lognorm', C'). The blue squares and blue stars denote the true SKADS RLFs for the deep sample. The cyan and black dashed curves respectively represent the RLFs reconstructed using the median and MAP parameters. The grey regions represent the 95% confidence intervals for the distribution of model reconstructions in the posterior. The green solid line represents the 5 σ noise (using $z = 1.15$) shown in the top-right corner of each panel.

Chapter 3

The optically selected 1.4-GHz quasar luminosity function below 1 mJy

3.1 Introduction

The evolution of quasars has been a subject of interest ever since their discovery (Schmidt, 1963). Quasars have been of particular interest over the past decade because of the role that they — and AGN in general — play in galaxy evolution. For example, feedback from AGN may expel or heat gas in a galaxy, thereby quenching star formation in the host galaxies (e.g. Granato et al., 2004; Scannapieco and Oh, 2004; Croton et al., 2006; Hopkins et al., 2008; Antonuccio-Delogu and Silk, 2008), or feasibly in the wider environment (e.g. Rawlings and Jarvis, 2004; Hatch et al., 2014). This may be a major contributor to establishing the observed relationship between SMBHs and the central bulge properties in a galaxy (e.g. Ferrarese and Merritt 2000; Hopkins et al. 2006).

The radio emission from radio-loud quasars is known to be mainly dominated by synchrotron radiation from electrons accelerated by powerful jets, while the source of radio-quiet quasars is still debated (see Chapter 1.2.2.2). One suggestion is that the radio emission from radio-quiet quasars is a result of synchrotron radiation from supernova explosions associated with star formation in the host galaxy, rather than

being the result of AGN processes. One of the ways to study quasars and their source of radio emission is through RLFs.

The RLF of radio-loud quasars has been extensively-studied (e.g. Schmidt, 1970; Willott et al., 1998; Jiang et al., 2007), but the faint (radio-quiet) end is not well-explored, as these fainter sources lie below the detection threshold of most wide-area radio surveys. Various methods are used in the literature to study radio-quiet populations. One such method is deep-narrow radio surveys (e.g. Condon et al., 2003; Kellermann et al., 2008; Padovani et al., 2009, 2011; Miller et al., 2013; Ocran et al., 2017; Mauch et al., 2020; Heywood et al., 2020). Such surveys have contributed to our understanding of the radio emission from the radio-quiet population. For instance, Padovani et al. (2015) found that radio emission from radio-quiet AGNs receives a contribution from accretion related activity as well as a contribution related to star formation. However, very few genuinely luminous quasars are detected in these deep-narrow surveys ($\sim$ 15 quasars per deg^2).

In this chapter I apply the Bayesian-stacking technique developed in Chapter 2 to probe the RLF of optically selected quasars below the radio detection threshold. The quasars are from the SDSS (York et al., 2000) DR7 quasar catalogue (Shen et al., 2011), and the radio flux densities are taken from the FIRST (Becker et al., 1995).

In Chapter 3.2 I describe the optical and radio data used in this chapter. In Chapter 3.3 I present the results of applying the Bayesian-stack technique to optically selected quasars in seven redshift bins. I discuss and compare the results to the literature in Chapter 3.4, finally concluding the discussion in Chapter 3.5.

3.2 Data

In a stacking experiment, where the goal is to extract information from undetected sources in a given survey, one needs data from another survey in which the sources have already been identified. In this chapter I use optically selected quasars from the SDSS and radio data from the FIRST survey.

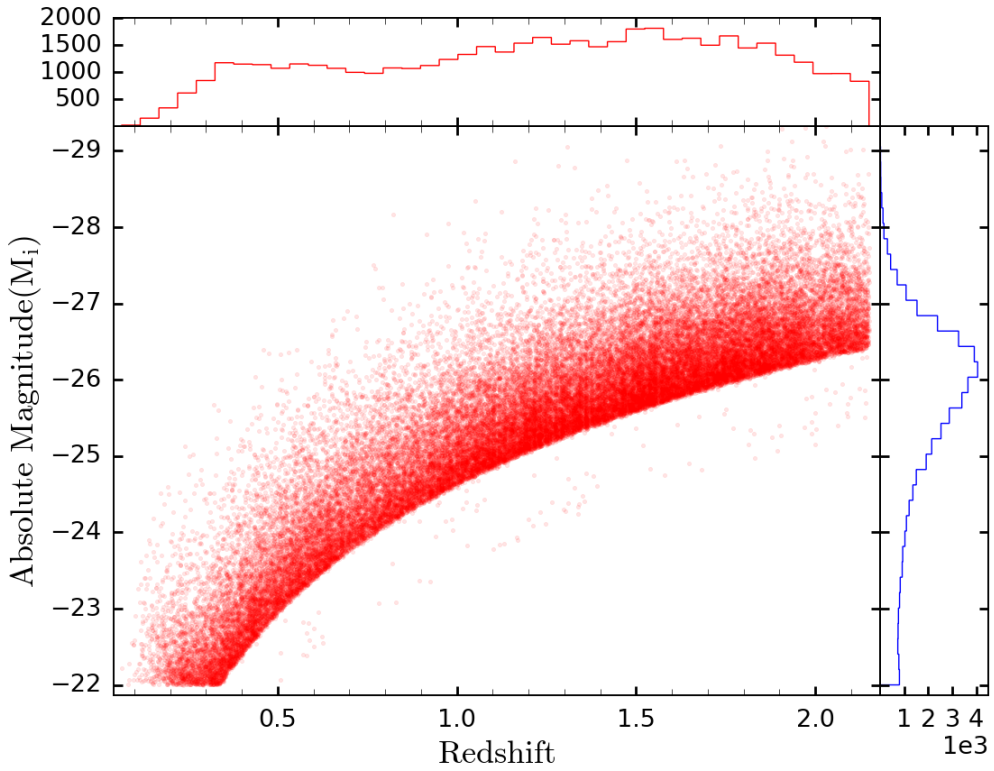

FIGURE 3.1: The redshift–absolute-magnitude distribution of the uniformly-selected SDSS quasars (Richards et al. 2002). The upper and right panels are the histograms of the redshift and K-corrected absolute i-band magnitude respectively, with bin sizes of $\Delta z = 0.05$ and $\Delta\text{mag} = 0.2$.

3.2.1 The optical quasar sample

The optical data are drawn from the quasar catalogue (Schneider et al., 2010) of the SDSS seventh data release (DR7, Abazajian et al. (2009)). In SDSS, quasars are mainly identified using colour selection for objects in the magnitude range $15 < i < 19.1$ (Richards et al., 2002; Richards, 2006). Quasars are then differentiated from galaxies and stars by their unique colours in multi-dimensional colour-colour space (Fan, 1999): SDSS's candidate quasars are primarily outliers from stellar regions in colour-colour space (Richards et al., 2001); the regions having large stellar contamination were avoided. The quasar sample includes additional sources that are selected because they have a FIRST counterpart. A source is targeted for spectroscopic follow-up if it is within 2 arcsec from a source in the FIRST catalogue. The final catalogue contains 105 783 spectroscopically confirmed quasars, all brighter than $M_i = -22$, with at least one emission line with full width at half-maximum greater than 1 000 km/s or a relevant absorption feature.

I use a sample consisting of 59 932 quasars selected across the survey area (purely colour-selected sources with the flag UNIFORM=1 from Shen et al. 2011) for the purpose of having a homogeneous sample of quasars. This sample covers an effective area of 6 248 deg^2 (Shen et al., 2011). Fig. 3.1 shows the distribution of sources in absolute magnitude and redshift for this uniform sample.

The sample is divided into seven redshift bins (from $z = 0.2$ to $z = 2.15$, see Table 3.1), reducing it to 48 046 sources. Since each redshift bin has a non-negligible width, I apply an absolute-magnitude cut to each redshift bin (corresponding to a minimum luminosity cut per bin) to ensure all quasars in the bin are observed within the sensitivity limit of the survey. This reduces the total sample to 24 003. The maximum absolute magnitude in each redshift bin corresponds to the optical flux limit at the highest redshift in that bin given by

$$M_i = m_i - 5\log_{10}[\mathrm{D}_L(z_{\mathrm{up}})/10] - K(z), \tag{3.1}$$

where $m_i = 18.7$ is just above the magnitude completeness limit ($m_i = 19.1$) for DR7, $\mathrm{D_L(z_{up})}$ is the luminosity distance (in pc) at the upper redshift of the bin and $K(z)$ is the K-correction, which accounts for the fact that the absolute magnitudes are affected by the 'redshifting' in the spectrum from the emitted frame to the observed frame (Oke and Sandage, 1968). I use K-corrections from Richards (2006).

3.2.2 Radio data

The FIRST survey (Becker et al. 1995) was carried out with the VLA in its 'B' configuration at 20 cm (1.4 GHz), yielding a synthesized beam size of 5.4″ (FWHM). It covered 8 444 deg^2 in the North Galactic Cap and 2 131 deg^2 in the South Galactic Cap giving a total coverage of 10 575 deg^2. The survey footprint overlaps the area that SDSS covered in the North Galactic Cap, as well as a smaller $\simeq 2.5$ deg^2 wide strip along the celestial equator. The maps have noise of $\approx 150\,\mu$Jy/beam. The survey catalogue contains more than 800,000 sources above the detection limit of 1 mJy, and includes peak and integrated flux densities calculated by fitting a 2D Gaussian to each source. The survey is 95% complete at 2 mJy and 80% complete at 1 mJy. The maps are stored as FITS images and have 1.8″ pixels.

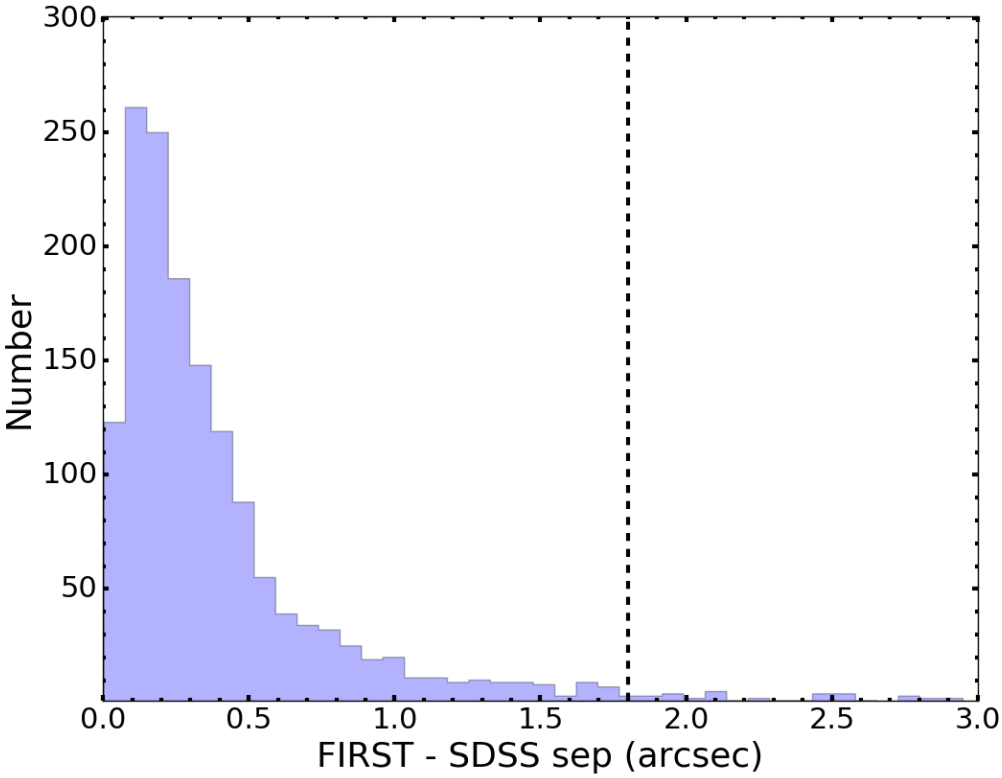

FIGURE 3.2: The distribution of the separation between detected FIRST and SDSS quasar positions with a bin size of 0.07 arcsec. The vertical dashed line at 1.8 arcsec is the cut-off separation between the FIRST and SDSS detected sources that I used in this work.

3.2.3 Cross-matching catalogues

I first matched the SDSS quasars with detected sources from the FIRST catalogue. The separation allowed between the coordinates of the two catalogues should be as small as possible to avoid random matching with other sources, but also large enough to ensure real matches are not omitted because of slight random offsets in position between the optical and radio data.

Fig. 3.2 shows the results of matching the SDSS sample to the FIRST catalogue. I choose a limiting separation of 1.8 arcsec based on Fig. 3.2, which is the pixel size of the FIRST images. From the original 105 783 quasars I made 3 815 matches (∼3%), which is consistent with the low number of optical-to-radio matches found by Pâris et al. (2012) and Pâris et al. (2017). The SDSS and FIRST have a false positively rate of 0.1% within a 2″. I find 2 381 (∼ 10%) matches from my sample of 24 003 SDSS quasars. The fraction of FIRST detected sources in my sample is

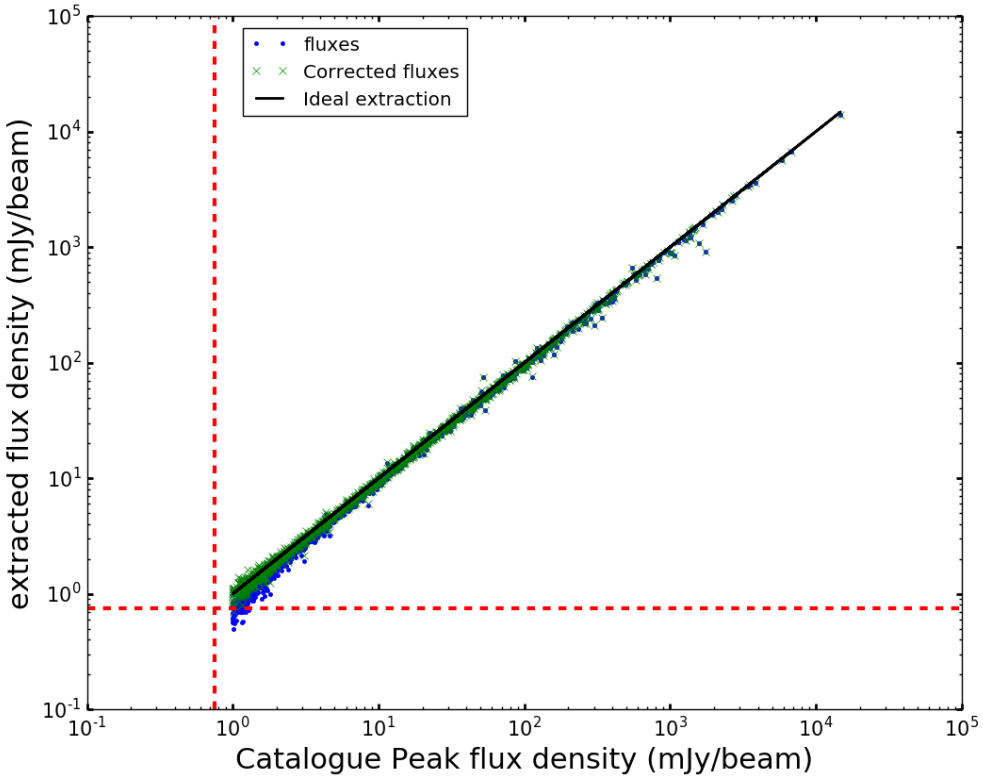

FIGURE 3.3: Comparison between the FIRST-catalogue peak flux densities and map-extracted flux densities, represented by the blue points. The green crosses denote the extracted flux densities after correction for the biases described by Eq 3.2. The solid black line represents the case where the extracted flux densities would be equal to the catalogue flux densities, and the dashed red lines indicate the 5σ threshold.

higher that those in the parent sample due to the absolute magnitude cut which is likely to remove sources with low optical luminosity. This selection introduces a bias to the radio luminosity function due to the correlation between optical and radio luminosity.

The FIRST catalogue only contains sources with flux densities above the detection threshold of ~ 1 mJy. In order to obtain sources with flux densities below the FIRST detection threshold I extracted 11×11 pixel stamps (19.8×19.8 arcsec) from the FIRST maps, centered on the SDSS quasar positions, and used the central pixel value as the radio flux density of the quasar. Consequently 23 490 of the quasars have flux densities, the rest fall outside FIRST coverage.

In Fig 3.3 I compare the catalogued peak flux densities and the extracted flux densities for 2,381 detected sources. Most of the extracted flux densities are in

TABLE 3.1: The redshift bins used to separate the sources, along with the absolute-magnitude cut, the number of sources (N), and the number of sources with extracted FIRST flux densities, $N_{\rm FIRST}$ (most of these sources are undetected in FIRST). The RQF ('radio-quiet' fraction) of the quasars is calculated by integrating over the low-luminosity part of the RLF described in Chapter 2.2.2 and dividing by the integral over the total luminosity function.

Redshift bin	max(M_i)	N	$N_{\rm FIRST}$	RQF (%)
$0.20 < z < 0.45$	-23.0	1234	1222	96.2
$0.45 < z < 0.70$	-24.1	1437	1424	91.8
$0.70 < z < 1.00$	-24.9	2401	2359	86.3
$1.00 < z < 1.30$	-25.4	4534	4472	93.8
$1.30 < z < 1.60$	-25.8	5967	5879	93.7
$1.60 < z < 1.85$	-26.2	4988	4923	91.4
$1.85 < z < 2.15$	-26.6	3250	3211	91.4

good agreement with peak flux densities, with the exception of flux densities below 10 mJy, which underestimate the peak flux densities. There are also about 10 sources with high scatter from the peak flux densities. The difference between the extracted flux densities and peak flux densities at low flux densities will affect the results and therefore needs to be accounted for and understood. Note, however, that there could be a difference in the effect on extraction of high signal-to-noise (detected) sources compared to the undetected ones. For instance, detected sources could be more extended and therefore slightly resolved by the FIRST restoring beam. Other possible contributions to the difference in the flux densities are CLEAN and snapshot biases.

CLEAN bias is a systematic effect that decreases the peak flux density of a source above the detection limit and redistributes it around the map. This phenomenon is associated with the non-linear CLEAN process (Condon et al. 1994) and affects large-area radio surveys such as FIRST and the NRAO VLA Sky Survey (NVSS; Condon et al. 1998). The bias is additive and has an approximately constant magnitude, with a value of 0.25 mJy beam^{-1} for FIRST (Becker et al., 1995). White et al. (2007) discovered another bias that affects sub-threshold sources (which are not CLEANed) and suggested that it is associated with the sidelobes of the beam pattern. This snapshot bias behaves differently from the one associated with CLEAN, as it is multiplicative (i.e. the higher the flux density the higher the bias). The proposed total bias correction summarized by White et al. (2007) is

$$S = \min(1.40\ S_{\rm F}, S_{\rm F} + 0.25\,{\rm mJy}), \tag{3.2}$$

TABLE 3.2: Assumed priors. $L_{5\sigma}$ is the luminosity corresponding to the 5σ flux density cut for a given redshift.

Parameter	Prior
$\alpha_1, \beta_1, \alpha_2, \beta_2$	uniform $\in [-5, 5]$
σ_{LF}	uniform $\in [0.1, 2]$
$\log_{10}[L_{\min_{\{1,2\}}}/(\mathrm{WHz}^{-1})]$	uniform $\in [20, 30]$
$\log_{10}[L_{\max_{\{1,2\}}}/(\mathrm{WHz}^{-1})]$	uniform $\in [20, 30]$
$\log_{10}[\phi^*_{\{1,2\}}/(\mathrm{Mpc}^{-3}\mathrm{mag}^{-1})]$	uniform $\in [-12, -2]$
$\log_{10}[L^*_1/(\mathrm{WHz}^{-1})]$	uniform $\in [\log_{10}(L_{5\sigma}), 30]$
$\log_{10}[L^*_2/(\mathrm{WHz}^{-1})]$	uniform $\in [20, \log_{10}(L_{5\sigma})]$

where S should be the intrinsic flux density of the source and S_{F} is the 'intrinsic' (uncorrected) flux density from FIRST. This is an idealised case, where S_{F} is meant to incorporate the calibration effects in the FIRST data. It is important to note that this correction can only be applied when the noise can be neglected, that is, for the case of detected sources or the stacked median flux as done in White et al. (2007). Applying the correction to the detected sources, I find that the low flux densities are the ones most affected by the correction. I also find that they are in good (better) agreement with the catalogue flux densities (Fig 3.3). Since, in my case, I am also dealing with noise dominated sources, these corrections need to be incorporated directly into the likelihood function. This implies that in Eq. 2.6 the intrinsic flux density S obtained from stacked FIRST flux densities is actually S_{F}, as described in Chapter 2.2.1. Therefore, the measured flux densities from FIRST S_{m}, which will include noise, as opposed to the ideal noiseless case above, are:

$$S_{\mathrm{m}} = S_{\mathrm{F}} + n, \tag{3.3}$$

where n represents the noise distribution. To proceed with the analysis, the sources in each redshift bin in Table 3.1, were further binned in terms of the measured radio flux density (S_{m}, Fig. 4.4). This includes both detected and undetected sources. One can see from the negative side of the flux density distributions that the noise is Gaussian to a good approximation, while there is a tail on the positive side of the distributions, which shows the contribution from faint real sources. There is an offset in the noisy flux densities because the average 'true' flux density of these faint sources is comparable to the noise. The flux density distribution is more Gaussian-like if the noise is much larger than the true flux density of the faint sources. This effect is more pronounced for the higher-redshift bins, where a greater fraction of sources is undetected.

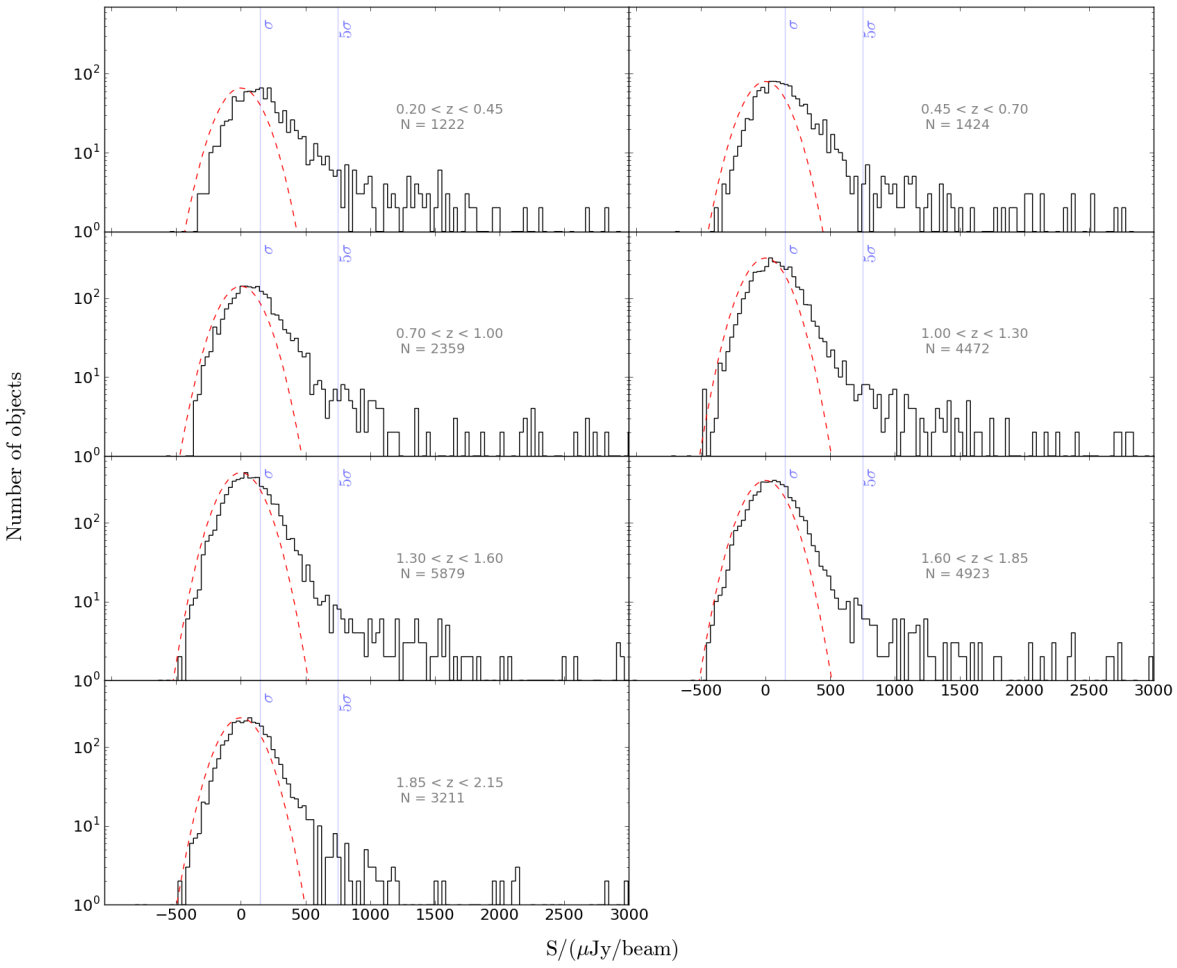

FIGURE 3.4: Histograms of the extracted FIRST flux densities ($S_{\rm m}$) extracted from cut-outs centered at the SDSS quasar positions, with 30μJy bins. The quasars are divided into 7 redshift bins from Legacy (Shen et al., 2011). The two blue lines in each bin represent the FIRST $\sigma = 150\mu$Jy and $5\sigma = 750\mu$Jy. The red dashed curve is a fixed Gaussian distribution, of mean flux density of zero and $\sigma = 150\mu$Jy, which represents the expected flux density distribution if there were no sources in the map.

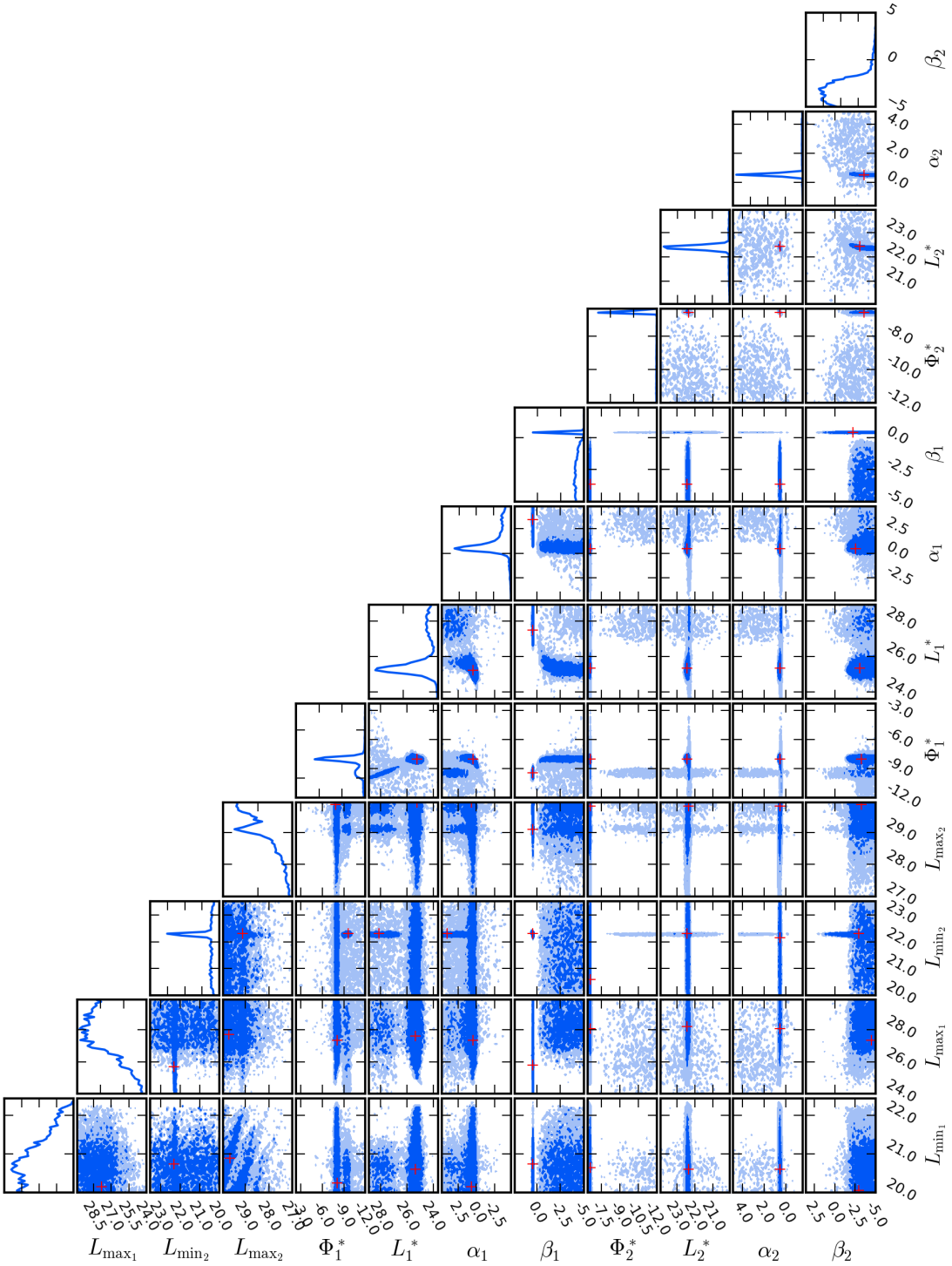

FIGURE 3.5: The posterior distributions for the winning model – model B, the double power-law – in the lowest redshift bin ($0.2 < z < 0.45$). The parameters $L_{\min_{1,2}}$, $L_{\max_{1,2}}$, $L_{1,2*}$ and $\Phi^*_{1,2}$ are presented in logarithmic space ($\log_{10}$). The dark blue and the light blue regions are the 68% and 95% regions. The red cross represents the point with the highest marginalised likelihood in each individual plot.

TABLE 3.3: Relative evidence of the different models for each redshift bin in the FIRST data. The reference evidence is the model with the lowest value for each redshift bin, and the winning model has the highest relative evidence (in bold).

Model	$\triangle \log_{10} \mathcal{Z}$	$\triangle \log_{10} \mathcal{Z}$	$\triangle \log_{10} \mathcal{Z}$	$\triangle \log_{10} \mathcal{Z}$
	$0.20 < z < 0.45$	$0.45 < z < 0.70$	$0.70 < z < 1.00$	$1.00 < z < 1.30$
A	4.4 ± 0.20	0.0 ± 0.00	2.0 ± 0.21	10.1 ± 0.22
B	$\mathbf{5.6 \pm 0.20}$	$\mathbf{0.7 \pm 0.19}$	$\mathbf{2.7 \pm 0.21}$	$\mathbf{11.9 \pm 0.22}$
C	0.0 ± 0.00	0.6 ± 0.19	0.0 ± 0.00	0.0 ± 0.00
	$1.30 < z < 1.60$	$1.60 < z < 1.85$	$1.85 < z < 2.15$	
A	0.1 ± 0.23	0.0 ± 0.00	0.0 ± 0.00	
B	$\mathbf{0.8 \pm 0.23}$	$\mathbf{3.0 \pm 0.22}$	$\mathbf{2.0 \pm 0.22}$	
C	0.0 ± 0.00	1.9 ± 0.22	1.9 ± 0.25	

3.3 Results

I apply BAYESTACK to the observational data from SDSS and FIRST in each of the redshift bins shown in Table 3.1, using the three free models and the priors in Table 3.2.

3.3.1 Quasars at $0.2 < z < 0.45$

I start with the lowest redshift sample because it allows a direct comparison to the work of Kellermann et al. (2016).

I use the Bayesian technique to fit the three RLF models to all the sources (radio detected and undetected) from a volume-limited sample defined by $M_i < -23$ at $0.2 < z < 0.45$. The first column of Table 3.3 shows the relative evidence of the fit to the models. From the relative evidence I conclude that the data significantly prefer Model B, which consists of a double power-law for the luminous sources and a second double power-law for the low-luminosity and undetected sources.

Fig. 3.5 shows the posterior distributions for the winning Model B. As with the SKADS sources, the boundary parameters $L_{\mathrm{max}_{1,2}}$ along with $L_{\mathrm{min}_{1,2}}$ exceed the prior limit and are unconstrained. Note, however, that this has very little impact on the actual observed numbers (and that the uncertainty increases due to noise and/or Poisson fluctuations). The other parameters have at least one well-defined peak and either a secondary peak or a long tail that spans a large range in both the 68% and/or 95% regions. The faint-end slope β_2 only has a long tail, which span a large range below 0.

In Fig. 3.6 I show the optically selected quasar RLF across the full luminosity and redshift range from my sample. The black circles denote the RLF determined using the $1/V_{\rm max}$ method, which is only possible for those detected above a certain flux density threshold (I use 5σ), whereas the lines and shaded regions show the full RLF distribution from the Bayesian modelling. Concentrating on the lowest redshift bin (top-left panel of Fig. 3.6), I find that the number density of radio-bright quasars increases with decreasing radio luminosity, as expected.

I compare my inferred RLFs for optically selected quasars with similar RLFs from the literature, reported by Condon et al. (2013) and Kellermann et al. (2016). The optical data are the same volume-limited sample from SDSS's DR7. The radio data are all from the VLA but each sample was observed with different configurations and depths. My data are from FIRST, which was observed in the 'B' configuration, with a resolution of 5″ and an rms of 0.15 mJy, corresponding to a detection threshold of 1 mJy. The Condon et al. sample is from the NRAO VLA Sky Survey (NVSS; Condon et al. 1998) observed using the compact 'D' and 'DnC' configurations, with a resolution of 45″ and an rms of 0.45 mJy (a detection threshold of 2.4 mJy). Kellermann et al. observed a complete sub-sample of these quasars, over a reduced redshift range ($0.2 < z < 0.3$) at 6 GHz using the VLA in the 'C' configuration, with a resolution of 3.5″ and rms as low as 6 μJy for the fainter sources. In order to enable a direct comparison to the results in my lowest redshift bin, the 6 GHz luminosities of the Kellermann et al. sources are converted to 1.4 GHz luminosities using a spectral index of $\alpha = -0.7$ and their number density is increased by $\log_{10}[\Phi/(\mathrm{Mpc}^{-3}\mathrm{mag}^{-1})] = 0.2$ to correct for evolution (Condon et al. 2013) when comparing the RLF over the redshift range $0.2 < z < 0.3$ with that over $0.2 < z < 0.45$.

The RLF above the nominal 5σ threshold for my sample is in good agreement with the RLFs of both Condon et al. (2013) and Kellermann et al. (2016) between radio luminosities $25 < \log_{10}[L_{1.4}/\mathrm{W\,Hz}^{-1}] < 26$ but is less consistent with the Condon et al. (2013) RLF towards the low-luminosity end where there are direct detections ($23.6 < \log_{10}[L_{1.4}/\mathrm{W\,Hz}^{-1}] < 25$). Furthermore, my RLF has large uncertainties above $\log_{10}[L_{1.4}/\mathrm{W\,Hz}^{-1}] \sim 26$. These are both probably due to the fact that only seven of the 26 sources observed in NVSS above $\log_{10}[L_{1.4}/\mathrm{W\,Hz}^{-1}] \approx 26$ are compact (Condon et al. 2013) and the rest are extended sources that have emission resolved by FIRST (hence the sources occupy lower luminosity bins below

$\log_{10}[L_{1.4}/\mathrm{W\,Hz^{-1}}] \sim 26$), leading to the discrepancy with the Condon et al. (2013) study and reducing the numbers in the highest luminosity bins.

Each of the RLFs in this redshift bin also shows a flattening in the number density between $\log_{10}[L_{1.4}\ /\mathrm{W\,Hz^{-1}}] \approx 25.5$ and $\log_{10}[L_{1.4}/\mathrm{W\,Hz^{-1}}] \approx 24$. Below $\log_{10}[L_{1.4}/\mathrm{W\,Hz^{-1}}] = 24.4$ my RLF is higher than that of Condon et al. but still in good agreement with Kellermann et al.. The difference between my RLF and that from Condon et al. is most probably due to the difference in resolution of the radio data, which results in sources moving into lower-luminosity bins due to some emission being resolved.

Given the likely underestimation of extended emission using the FIRST survey, I use the Condon et al. flux densities for sources found in both NVSS and FIRST in the RLF fit (shown in Fig. 3.5 and Fig. 3.6). However, I note that extended emission may still be resolved out for sources below the flux density limit but I have no way of estimating this. Although I could potentially use the NVSS data here, I would then have to deal with confusion issues due to the larger synthesised beam. I therefore continue to use the FIRST data, but the issue of extended emission should be borne in mind.

The reconstruction of the RLF below the detection threshold continues to follow the slope (of the double power-law) established from $\log_{10}[L_{1.4}/\mathrm{W\,Hz^{-1}}] \geq 24.4$, dropping at $\log_{10}[L_{1.4}/\mathrm{W\,Hz^{-1}}] \approx 22.4$. This therefore measures the RLF ~ 2 dex below $\log_{10}[L_{1.4}/\mathrm{W\,Hz^{-1}}] = 23.4$ ($= 5\sigma$). The steep drop-off in the RLF at $\log_{10}[L_{1.4}/\mathrm{W\,Hz^{-1}}] < 22$ is due to the optical limit of the quasar sample which is a combination of the flux-limit and absolute magnitude cut, meaning that there are no optically selected quasars contributing to this part of the RLF. The 95% region does not allow the possibility of no drop-off as the data has a well pronounced drop-off. It should be noted that the median reconstructed RLF is not always in the middle of the 95% region, this is because the posterior distributions are not all perfect Gaussians. Furthermore, some posterior distributions have double peaks and/or long tails which affects the median.

Comparing the reconstructed RLF to the Kellermann et al. (2016) individually observed sources, I find that the two measurements are in complete agreement.

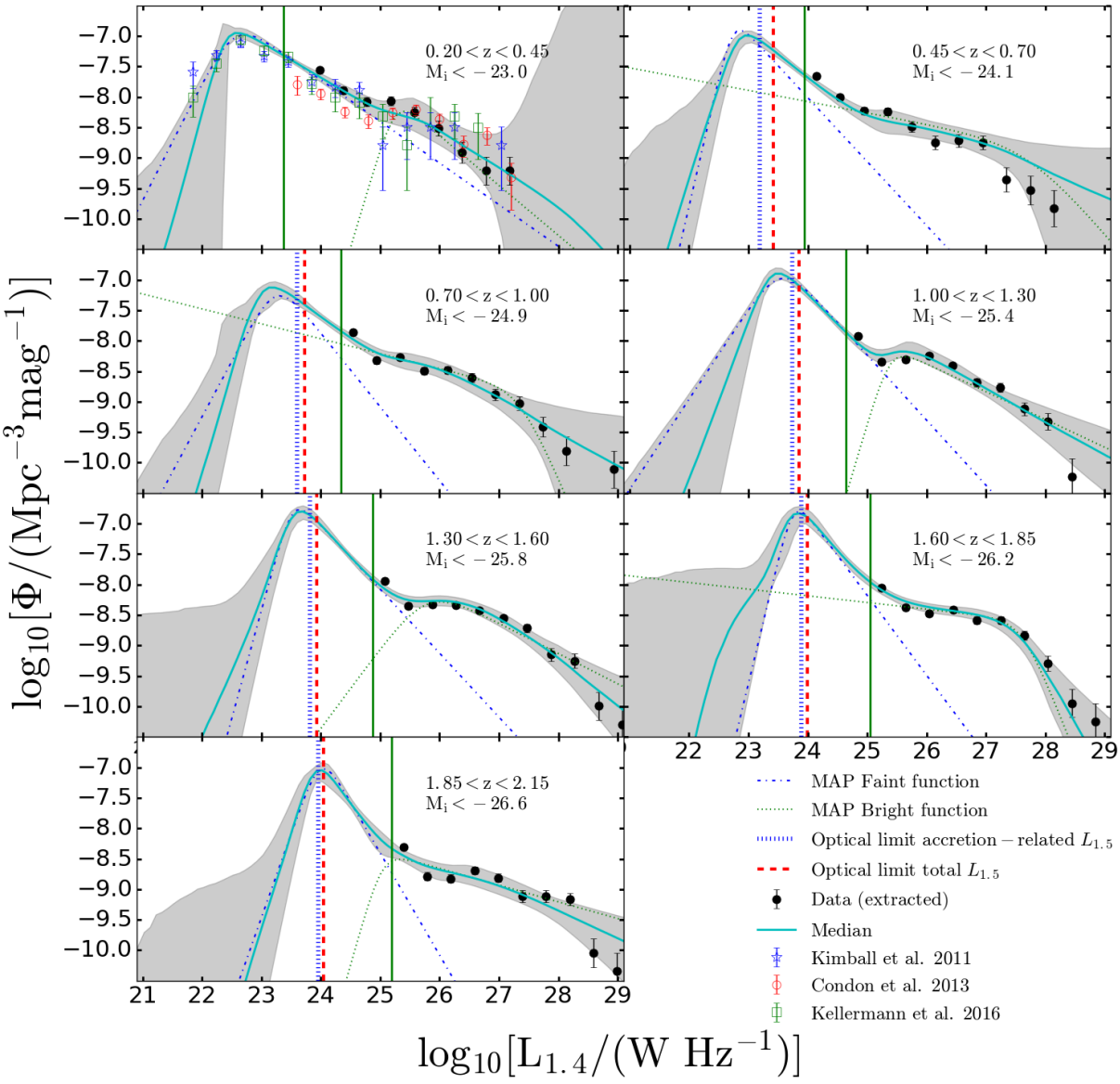

FIGURE 3.6: The optically selected quasar RLF and its evolution with redshift. The black dots are the $1/V_{\rm max}$ RLFs from sources above 5σ. The blue unfilled stars, red unfilled circles and the green unfilled squares respectively represent the RLFs from Kimball et al. (2011), Condon et al. (2013) and Kellermann et al. (2016). The cyan curves represent the RLFs reconstructed from the median parameters of the winning model (Table 3.3) in each redshift bin. The blue dashed-dotted and green dotted lines are the faint and bright functions with their MAP parameters respectively. The grey region represents the 95% confidence interval of the distribution of reconstructions of models in the posterior. The green, vertical line is 5σ computed using the mean redshift for each redshift bin. The blue dotted and red dashed lines are an estimate of the radio-luminosity limit that corresponds to the optical limit, assuming optical–radio correlations for quasars (White et al., 2017) that are based on accretion-related radio emission and total radio emission, respectively.

TABLE 3.4: The MAP posterior parameters for the double power-law – the winning model – for the quasar RLF, in each of the redshift bins and their 2σ. The units of the parameters are as shown in Table 3.2.

Parameter	$0.2 < z < 0.45$	$0.45 < z < 0.7$	$0.7 < z < 1.0$	$1.0 < z < 1.3$	$1.3 < z < 1.6$	$1.6 < z < 1.85$	$1.85 < z < 2.15$
$\log_{10}[L_{\min_1}]$	$20.83^{+1.27}_{-0.79}$	$20.69^{+1.69}_{-0.65}$	$21.94^{+0.85}_{-1.87}$	$20.76^{+1.97}_{-0.71}$	$20.45^{+2.68}_{-0.40}$	$22.00^{+1.38}_{-1.90}$	$22.38^{+0.40}_{-2.35}$
$\log_{10}[L_{\max_1}]$	$28.75^{+1.14}_{-3.82}$	$24.18^{+5.65}_{-0.91}$	$24.69^{+3.25}_{-0.07}$	$29.44^{+0.43}_{-3.98}$	$29.35^{+0.52}_{-3.92}$	$26.30^{+3.57}_{-0.85}$	$25.92^{+3.94}_{-0.29}$
$\log_{10}[L_{\min_2}]$	$20.60^{+2.85}_{-0.44}$	$23.43^{+0.94}_{-3.29}$	$22.69^{+1.67}_{-2.54}$	$21.26^{+3.89}_{-3.05}$	$18.63^{+6.43}_{-0.39}$	$22.31^{+2.54}_{-2.11}$	$22.71^{+2.55}_{-2.51}$
$\log_{10}[L_{\max_2}]$	$29.65^{+0.32}_{-2.18}$	$28.91^{+1.05}_{-1.36}$	$29.03^{+0.94}_{-0.91}$	$29.76^{+0.22}_{-1.49}$	$29.55^{+0.42}_{-1.49}$	$28.12^{+1.83}_{-0.09}$	$29.92^{+0.07}_{-1.26}$
$\log_{10}[\Phi_1^*]$	$-8.01^{+1.57}_{-3.50}$	$-9.02^{+0.68}_{-0.16}$	$-8.79^{+0.72}_{-0.35}$	$-8.10^{+0.26}_{-0.12}$	$-8.03^{+0.10}_{-0.26}$	$-8.58^{+0.42}_{-0.18}$	$-8.39^{+0.16}_{-0.35}$
$\log_{10}[L_1^*]$	$25.25^{+3.52}_{-0.55}$	$27.74^{+0.08}_{-2.72}$	$27.36^{+0.37}_{-2.39}$	$25.38^{+0.70}_{-0.13}$	$25.78^{+1.41}_{-0.08}$	$27.61^{+0.22}_{-0.82}$	$25.04^{+2.29}_{-0.01}$
α_1	$0.82^{+3.80}_{-2.45}$	$1.16^{+2.74}_{-1.10}$	$2.27^{+1.21}_{-2.09}$	$0.46^{+0.39}_{-0.11}$	$0.50^{+0.70}_{-0.08}$	$2.46^{+1.00}_{-1.56}$	$0.27^{+0.70}_{-0.04}$
β_1	$-3.26^{+3.79}_{-1.60}$	$0.18^{+0.01}_{-4.70}$	$0.24^{+0.10}_{-4.90}$	$-3.30^{+2.84}_{-1.45}$	$-1.31^{+1.30}_{-1.19}$	$0.11^{+0.11}_{-0.56}$	$-3.44^{+3.53}_{-1.29}$
$\log_{10}[\Phi_2^*]$	$-6.73^{+0.04}_{-4.91}$	$-6.94^{+0.00}_{-0.16}$	$-6.97^{+0.15}_{-0.12}$	$-6.68^{+0.11}_{-0.02}$	$-6.53^{+0.07}_{-0.09}$	$-6.55^{+0.10}_{-0.12}$	$-6.73^{+0.09}_{-0.19}$
$\log_{10}[L_2^*]$	$22.55^{+0.78}_{-1.36}$	$22.74^{+0.20}_{-0.14}$	$23.25^{+0.22}_{-0.42}$	$23.54^{+0.02}_{-0.27}$	$23.53^{+0.26}_{-0.11}$	$23.76^{+0.23}_{-0.20}$	$24.00^{+0.07}_{-0.32}$
α_2	$0.68^{+3.37}_{-0.24}$	$1.05^{+0.06}_{-0.40}$	$1.21^{+0.54}_{-0.65}$	$1.07^{+0.14}_{-0.22}$	$1.05^{+0.47}_{-0.17}$	$1.31^{+0.47}_{-0.40}$	$1.67^{+0.26}_{-0.80}$
β_2	$-1.92^{+1.92}_{-2.97}$	$-4.21^{+2.67}_{-0.69}$	$-1.82^{+0.42}_{-3.09}$	$-1.48^{+0.06}_{-3.31}$	$-3.56^{+2.22}_{-1.33}$	$-4.05^{+2.67}_{-0.85}$	$-2.75^{+0.96}_{-2.17}$

3.3.2 Higher-redshift bins

In Chapter 3.3.1 I demonstrated that the technique is able to reconstruct the RLF below the detection threshold in the lowest-z sample, for which there are deeper radio data. In this section, I present the result using my algorithm and the three models describing the RLF to the higher redshift bins. The relative evidence of the models for each redshift bin is shown in Table 3.3. The data prefer Model B (a double power-law for the low-luminosity sources) for all the redshift bins and the posterior distributions are shown and discussed in the appendix (Fig. 3.7).

The optically selected quasar RLF mirrors the general shape seen in the lowest redshift bin over all redshifts. In all cases I see that the bright-end of the RLF increases steeply as the radio luminosity decreases towards $L_1^* \sim 10^{25}\,\mathrm{W\,Hz^{-1}}$ and then turns over. Just below this luminosity I see the second (faint-end) double power law starting to dominate the RLF, where I find a steep increase as the radio luminosity decreases towards $\log_{10}[L_{1.4}/\mathrm{W\,Hz^{-1}}] \sim 23$. My reconstructed RLF also follows the $1/V_{\mathrm{max}}$ points very well where I am able to measure them.

This flattening of the bright-end of the RLF and subsequent increase below $\log_{10}[L_{1.4}/\mathrm{W\,Hz^{-1}}] < 26$ are also observed in optically selected quasar RLFs studies (e.g. Condon et al., 2013; Kellermann et al., 2016; Hwang et al., 2018). Similar flattening is observed in the RLF of other optically selected AGN samples (e.g. Rush et al., 1996; Padovani et al., 2015). A clear change of the slope in the number density is also observed in radio-selected AGN RLFs (e.g Willott et al. 2001, Smolčić et al. 2009, McAlpine et al. 2013). Indeed, my fitted values for L_1^* are in good agreement with the RLF derived using the deep VLA-3 GHz survey from Smolčić et al. (2017).

At radio luminosities below where the flattening takes place, the reconstructed RLF steeply increases towards lower luminosities, with a slope established above 5σ for all redshift bins. The preferred model for all redshift bins is Model B (Table 3.3, the double power-law). With this model, the RLF in all redshift bins peaks at L_2^*, dropping below L_2^*. This fall-off is due to the hard absolute magnitude cut-off in the parent sample, and essentially means that there is no significant evidence for any radio continuum emission from my quasar sample below L_2^*.

3.4 Discussion

The definition of radio-loudness varies in the literature, as some objects can be classified as 'radio-quiet' in one definition and 'radio-loud' in another, e.g. either by considering the ratio of optical to radio emission (e.g. Kellermann et al., 1989) or by just using a radio lumninosity threshold (e.g. Miller et al., 1990). In this chapter, I do not explicitly classify quasars as radio-loud or radio-quiet, instead using the shape of the RLF to infer where these populations dominate. In all the RLFs I use, (Fig. 3.6) there is a clear change in behaviour at or around $\log_{10}[L_{1.4}/\mathrm{W\,Hz^{-1}}] \sim 25$. I define the 'radio-loud' population as the quasars that are described by a bright-end double power-law (parameters with subscript '1' in the modelling). The faint end (radio-quiet quasars) is parameterised by the power-law, double power-law or log-normal function. For this study all redshift bins had the double power-law as the winning model (Table 3.3). Due to the optical selection my analysis will miss quasars in dusty or mis-aligned galaxies, were the broad-lines of are not seen. Furthermore, quasars with extended emission will also be missed from my analysis.

3.4.1 Radio-loud quasars

The radio emission from radio-loud quasars is powered by processes associated with the accretion on the central SMBH. Falling within the AGN orientation-based unification model (e.g. Barthel, 1989; Antonucci, 1993; Urry and Padovani, 1995), these radio-loud objects have been shown to require a SMBH of mass $M_{\mathrm{BH}} > 10^8\,\mathrm{M}_\odot$ (McLure and Jarvis, 2004), whereas their radio-quiet counterparts can have lower-mass black holes. By integrating under the two double power-law models, representing the bright and faint ends of the RLF, I find that the radio-loud fraction of quasars makes up $\approx 10\%$ of the total quasar population in the sample at $z > 0.7$ (Table 3.1). However, I find that the radio-loud fraction drops to ≈ 7 and 4% of the total quasars in the two lowest redshift bins (Table 3.1). It should be noted however, that L_{max2} and L_{min2} are not well constrained as the low-luminosity faint slope is positive and the high-luminosity bright end slope is negative, hence increasing the range of integration increase the size of the population covered and hence partly leads to those parameters being so ill constrained. This lower fraction of radio-loud quasars towards lower redshifts reflects the fact that I have a much fainter optical magnitude limit at low redshift, and if radio loudness is linked to the combination of accretion rate and black-hole mass, then lower-optical luminosity quasars are more

likely to be radio quiet. These fractions are in line with previous studies of radio-loud and radio-quiet quasars with a variety of classification schemes (e.g. White et al., 2007; Cirasuolo et al., 2005; Baloković et al., 2012).

However, one of the differences is that I actually find a much more pronounced flattening than the studies based purely on radio-selected samples (e.g. Willott et al., 2001; Smolčić et al., 2009; McAlpine et al., 2013). One reason for this could be that there is a real difference in the physical properties that generate radio emission in optically selected quasars compared to the more-general population of radio-selected AGN. I also cannot rule out the possibility of the optical selection creating a bias in the RLF that artificially flattens, or decreases, the bright-end of the RLF below $\log_{10}[L_{1.4}/\mathrm{W\,Hz^{-1}}] \sim 26$. However, I have been conservative in my optical selection, ensuring that the quasar sample is complete across the full width of all redshift bins. I cannot rule out incompleteness due to the colour selection within the SDSS sample, but I would not expect this to have a significant effect in individual, relatively narrow, redshift bins. A possible explanation could be my sample becoming incomplete in terms of the RLF based on the optically selected sample. This could arise if there is a correlation between the optical emission in these quasars and their radio emission.

Several authors have investigated the link between optical emission and radio emission from quasars (e.g. Serjeant et al., 1998; White et al., 2007, 2017), finding evidence for a correlation. However, one has to be careful when measuring correlations between flux-limited samples. Therefore, in Fig. 3.6 I show the radio luminosity where I expect the optical flux limit to start imposing incompleteness on the RLF, based on the absolute magnitude limits shown in Table 3.1. For this I use the relation between optical luminosity and the star formation subtracted radio luminosity found by White et al. (2017), from their radio-quiet quasar sample at $z \sim 1$. I also show the radio luminosity limit based on the White et al. (2017) optical luminosity versus total radio luminosity, for completeness. One can see that the radio luminosity at which the optical selection may lead to incompleteness in the RLF is just above the radio luminosity at which the drop in the RLF occurs. This supports the argument that the drop/turnover at low luminosities is caused by lack of fainter optical quasars. However, there is significant scatter in the White et al. (2017) optical-radio correlation of around 1 dex in radio luminosity for a given optical luminosity. Therefore, it is certainly possible that some of the flattening could arise from incompleteness in the RLF due to the optical magnitude limit. To test this I

increased the optical magnitude limit for my sample in each redshift bin in order to check if the flattening or downturn become more prominent. In all bins the turnover (i.e. the value of β_1) became more prominent. I therefore suggest that at least some of the flattening is due to incompleteness introduced by the optical magnitude limit of the parent sample, although I note that the uncertainties increase in response to using a smaller quasar sample when a higher optical-luminosity threshold is imposed.

3.4.2 Radio-quiet quasars

This population makes up about 92% (Table 3.1) of the quasar population in my sample, but the origin of the radio emission is not well understood. My reconstructed RLFs increase steeply below $\log_{10}[L_{1.4}/\mathrm{W\,Hz^{-1}}] \sim 24.5$. This steepening could be attributed to an increasing contribution from star formation in the host galaxy (e.g. Terlevich et al. 1987, 1992; Padovani et al. 2011; Kimball et al. 2011; Bonzini et al. 2013; Condon et al. 2013; Kellermann et al. 2016; Stacey et al. 2018; Gürkan et al. 2018a) or is AGN-related with a different scaling relation or different emission associated with the AGN (Herrera Ruiz et al. 2016, Zakamska et al. 2016, White et al. 2015, 2017, Hartley et al. 2019) compared to their radio-loud counterparts. However, I note that the steepening is significantly less pronounced in the two lowest-redshift bins, which may indicate that the optical magnitude limit may play a role in creating an artificially steepening slope in the observed RLF. In such a case, the distinction between radio-loud and radio-quiet would become more difficult, with evidence that the population has a more continuous distribution (e.g. Lacy et al., 2001; Gürkan et al., 2019).

Kimball et al. (2011) suggested that the 'bump' observed at $\log_{10}[L_{1.4}/\mathrm{W\,Hz^{-1}}] \approx 22.7$ in their low-z volume-limited sample (Fig. 3.6) corresponds to star-forming galaxies. Kellermann et al. (2016) tested their hypothesis by using mid-infrared data from WISE to search for a correlation between the 22 μm and 6 GHz flux densities, which is a characteristic of the FIRC. However, they found no strong correlation and so suggest that the 22 μm fluxes do not only measure star formation but can also be contaminated by warm dust heated by the AGN (Polletta et al. 2010). Coziol et al. (2017) tested the star formation hypothesis by also matching the Kellermann et al. sources against WISE. They found counterparts for all but seven sources, created a new diagnostic plane based on WISE colours (Coziol et al.

2015), and found that: (i) there is no separation between the radio-quiet and radio-loud quasars in the colour distribution, and (ii) most of the Kellermann et al. (2016) quasars (like my lowest z sample) have low SFRs.

White et al. (2015) used deep optical and NIR data to identify a sample of quasars across a range of redshifts, and conducted a stacking experiment using deep VLA 1.4 GHz data. Comparing their quasar sample with multiple galaxy samples (matched by stellar mass, having assumed the SMBH mass of the quasar), they provided evidence that the radio emission from these quasars – which lie at much higher redshift but cover similar optical luminosities as the Kellermann et al. (2016) sample – predominantly arises from accretion-related activity. Furthermore, by comparing the SFRs using FIR data of a randomly selected subset of a volume-limited quasar sample at $0.9 < z < 1.1$, White et al. (2017) showed that the radio emission from star formation is sub-dominant.

The only evidence in my modelled RLFs for star formation contributing to the radio emission in quasars comes from the observed strong steepening of the RLF towards low luminosities, below the nominal 5σ detection threshold at $z > 0.7$. However, where my optically selected quasar sample contains the lowest-luminosity quasars ($z < 0.7$), the evidence for this steepening is weaker. On the other hand, comparing the observed upturn in the quasar RLF with the star-forming galaxy RLF at $z > 0.8$ from Novak et al. (2018), I find that the steepening occurs at approximately the same radio luminosity that the star forming galaxies dominate over AGN in radio-selected surveys. This strengthens the suggestion that star formation plays an important role at these low radio luminosities. Indeed, this was used as evidence in favour of the star formation becoming the dominant contribution to radio luminosity in this regime by Kimball et al. (2011) and Condon et al. (2013). Nevertheless, it is clear that the RLF is a relatively blunt tool for disentangling the dominant contribution to the low-luminosity radio emission in quasars. A more productive route may be to explore the bivariate optical and RLF for quasars (e.g. Singal et al., 2011), where the optical selection is naturally accounted for and models that link the optical and radio emission could be incorporated.

A more direct method would be to use high-resolution radio data that can resolve any star formation on the scale of the host galaxy. The VLA has the potential to do this, but would need to move towards a frequency of 6 GHz to achieve the required resolution of $\sim 0.5''$ for the vast majority of quasars that lie at $z > 0.5$. Given the typical spectral index of the synchrotron radiation from both star formation and

AGN-associated emission of $\alpha \sim -0.7$, this would then require longer integration times and may also suffer from contamination from free-free emission, making the results more difficult to interpret. eMERLIN has the potential to carry out similar resolution studies at lower frequencies (e.g. Guidetti et al., 2013; Radcliffe et al., 2018; Jarvis et al., 2019).

3.5 Conclusions

I used FIRST radio flux densities extracted at the positions of optical quasars from a uniformly selected (homogeneous) sample of SDSS DR7 divided into seven volume-limited redshift bins. I parameterized the high-luminosity RLF using a double power-law. For my lowest-z sample I found that the $1/V_{\rm max}$ and double power-law RLF for luminous sources were in agreement with those from Kellermann et al., but marginally inconsistent with those of Condon et al. at the luminous and faint ends of the detected RLF. Some of the difference at the faint end is probably due to the different resolution of NVSS and FIRST. In the other redshift bins, I found that each of the bright ends of the RLFs, which broadly represent radio-loud quasars, is described by a double power law. This double power-law generally flattens towards low luminosities. A similar drop/flattening is observed for extremely red quasars (Hwang et al., 2018) and in AGN RLFs (e.g Smolčić et al. 2009). I suggest that some of this flattening could also be due to the optical flux limit of the sample reducing the number of quasars that could contribute radio data to these radio luminosities, although this would need to be tested thoroughly with a deeper optical selection or by considering a bivariate model of the optical and RLFs.

With BAYESTACK I probe the RLF down to 2 dex below the detection threshold of FIRST (1 mJy). The difference in how deep I can probe compared to the simulation is related to the lack of low luminosity radio sources in the sample compared to SKADS. At low redshift ($z < 0.7$) I see a continuous distribution from the bright to the faint end of the RLF, whereas at $z > 0.7$, the RLF steeply increases towards fainter luminosities $\log_{10}[L_{1.4}/\mathrm{W\,Hz^{-1}}] < 24.5$. This could be due to the source population changing or to the biased flattening of the RLF because of the optical flux limit described previously. I note, however, that the steep increase coincides with the measured steepening in the RLF from radio-selected samples of star-forming galaxies (e.g. Novak et al., 2018). In order to determine whether this steepening

is indeed due to star formation, higher-resolution radio imaging would be ideal, to resolve the radio emission from star formation in the host galaxy.

Finally, the RLF peaks between $\log_{10}[L_{1.4}/\mathrm{W\,Hz^{-1}}] \sim 22.5$ and $\log_{10}[L_{1.4}/\mathrm{W\,Hz^{-1}}] \sim 24$ (depending on the redshift) and drops rather abruptly after that. This is due to the parent sample containing no quasars that are generating radio emission below this luminosity and is not an astrophysical effect.

3.6 Appendix

3.6.1 Triangle plots

Fig. 3.7 show the 1-D and 2-D posterior distributions for all of the winning models for each redshift bin. The 1-D posterior distribution is the marginalization of each parameter shown at the end of each row. The parameters have well-defined peaks, except for the boundary parameters (L_{min_1}, L_{max_1}, L_{min_2} and L_{max_2}) and the second slope β_2 (the faint-end slope for the faint-quasar function in Models A and B), which are not well constrained. The upper limit of the fitted L_{max_1} is unconstrained or (even) truncated, but this does not significantly affect the fit in my areas of interest.

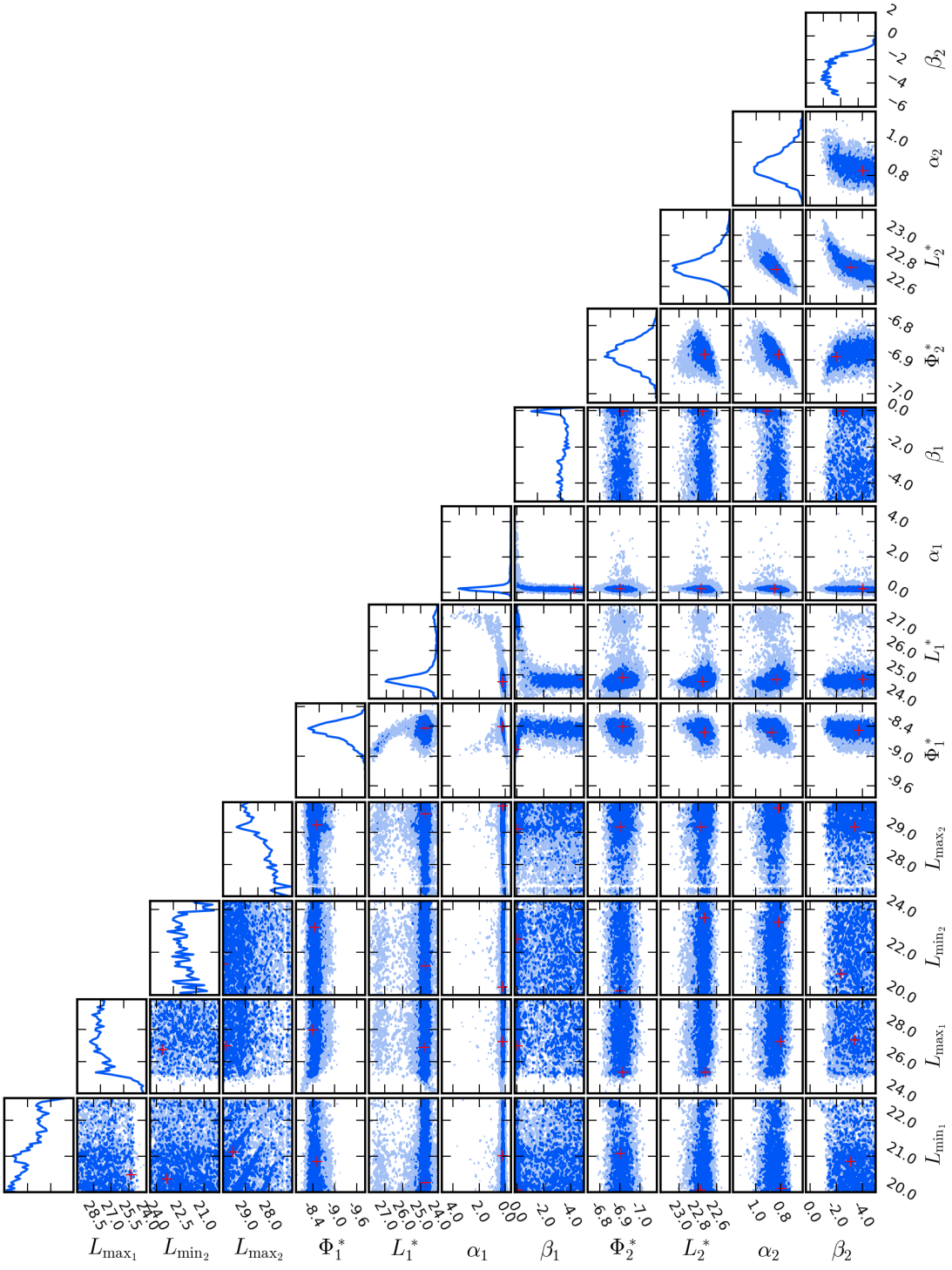

FIGURE 3.7: The posterior distributions of the winning models (Table 3.3) for each redshift bin. The inner plots are the 2-D posterior distributions for the various combinations of the parameters, and the last plots on each row give the 1-D marginalized probability distribution for each parameter. The parameters $L_{\mathrm{min}_{1,2}}$, $L_{\mathrm{max}_{1,2}}$, $L_{1,2*}$ and $\Phi^*_{1,2}$ are presented in logarithmic space ($\log_{10}$). The dark blue and the light blue regions are the 68% and 95% regions. The red cross represents the point with the highest marginalised likelihood in each individual plot. The above is for the $0.45 < z < 0.70$ bin.

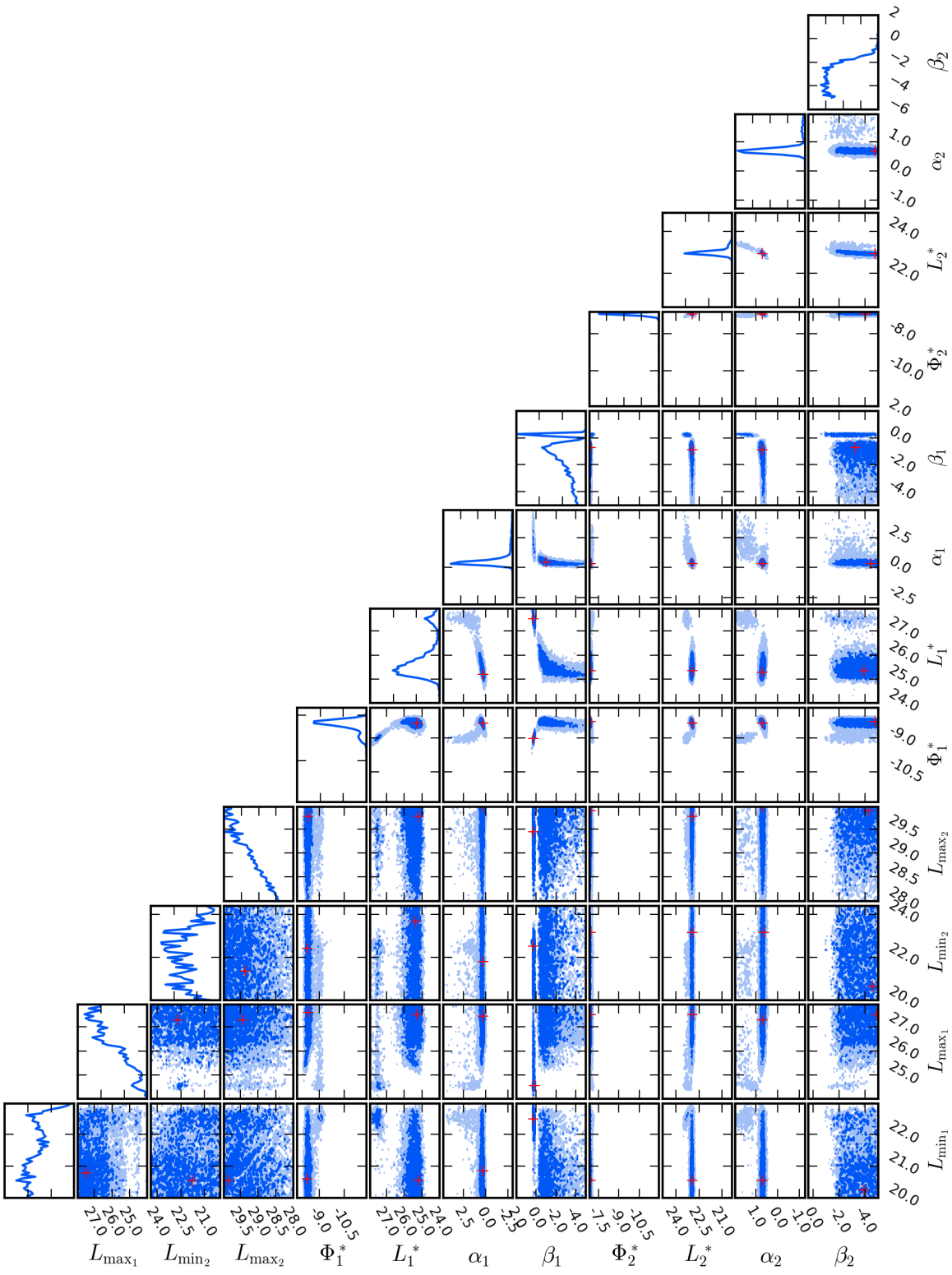

FIGURE 3.7: The posterior distributions, continued. The above is for the $0.70 < z < 1.00$ bin.

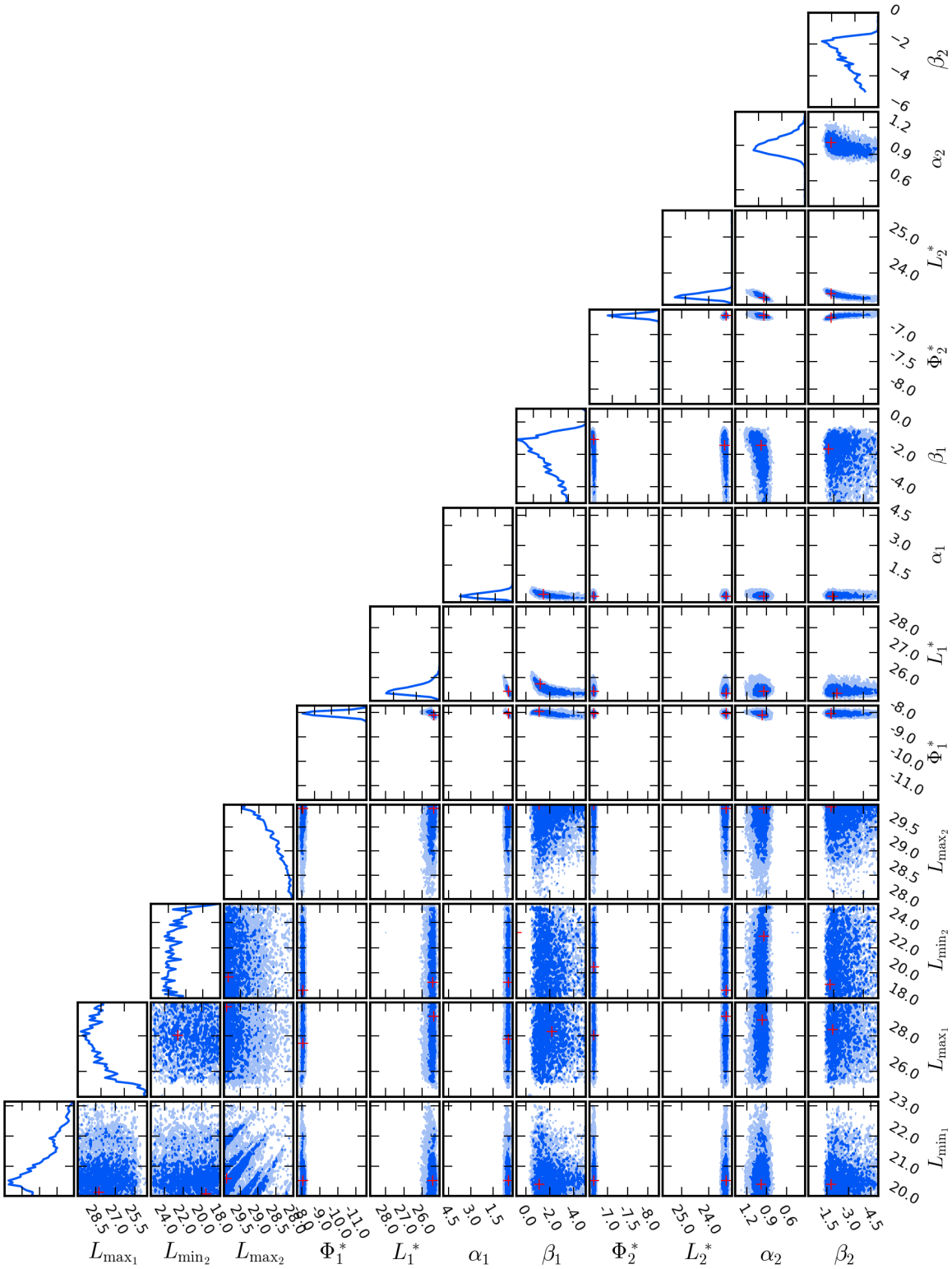

FIGURE 3.7: The posterior distributions, continued. The above is for the $1.00 < z < 1.30$ bin.

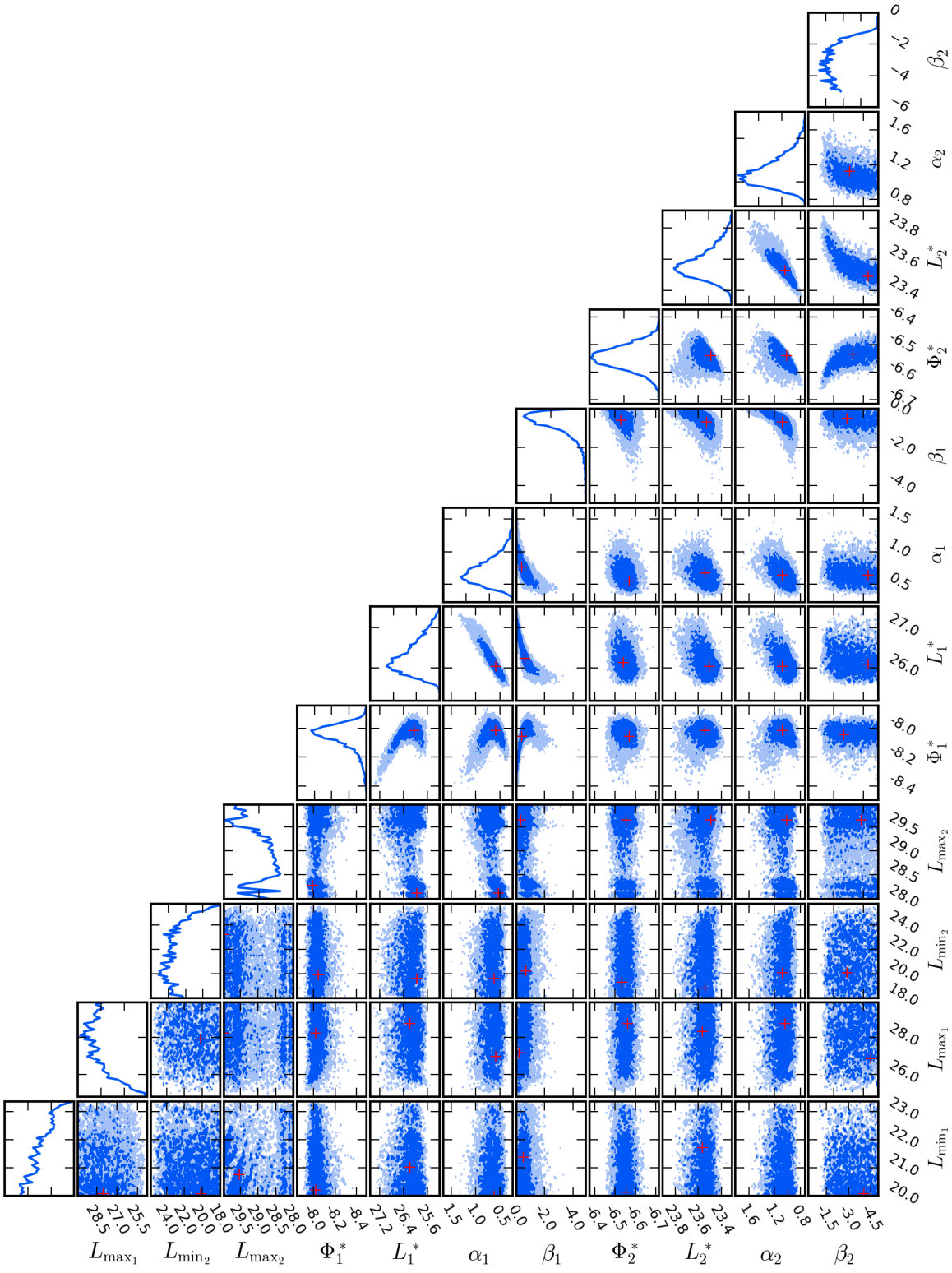

FIGURE 3.7: The posterior distributions, continued. The above is for the $1.30 < z < 1.60$ bin.

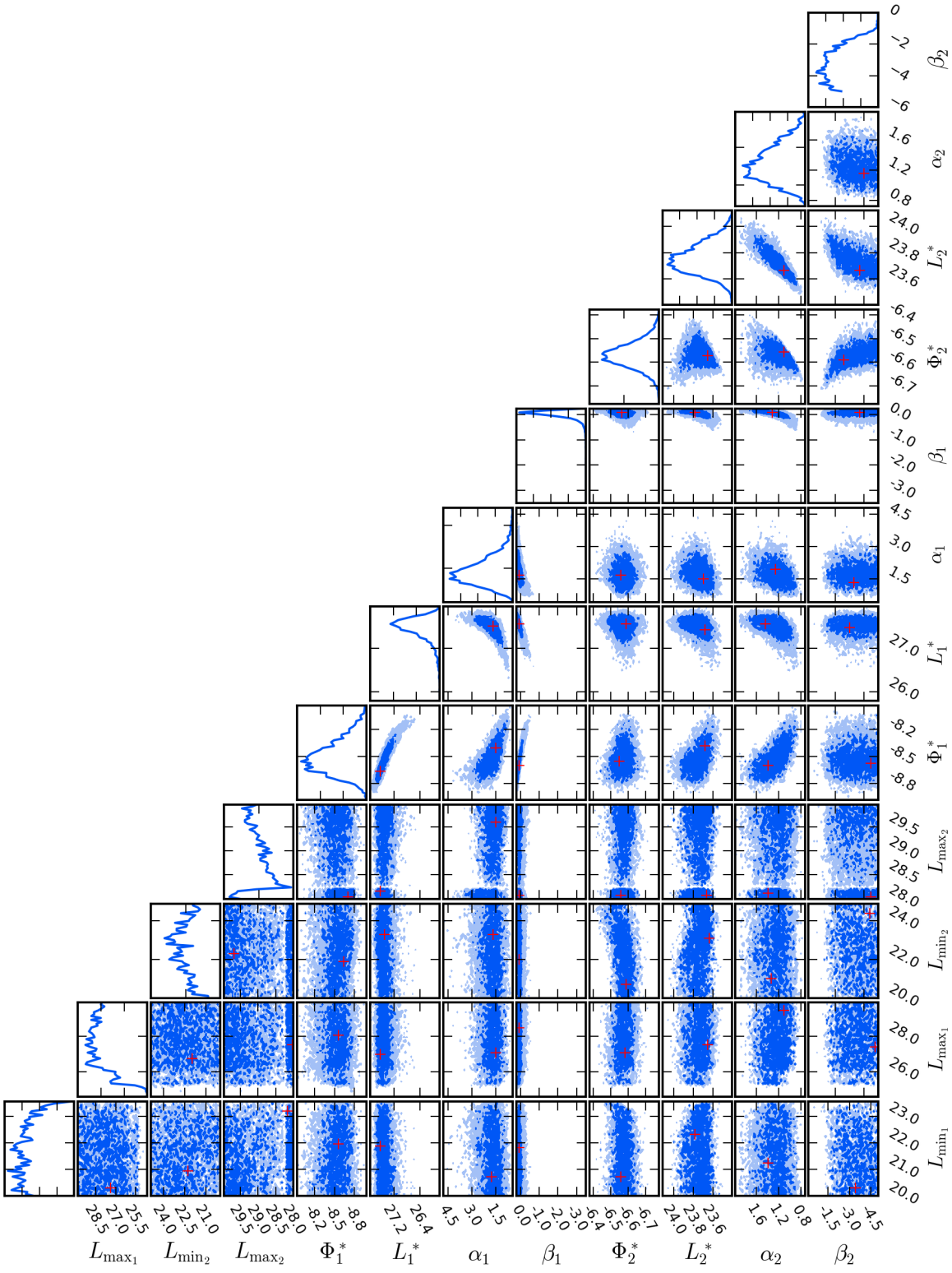

FIGURE 3.7: The posterior distributions, continued. The above is for the $1.60 < z < 1.85$ bin.

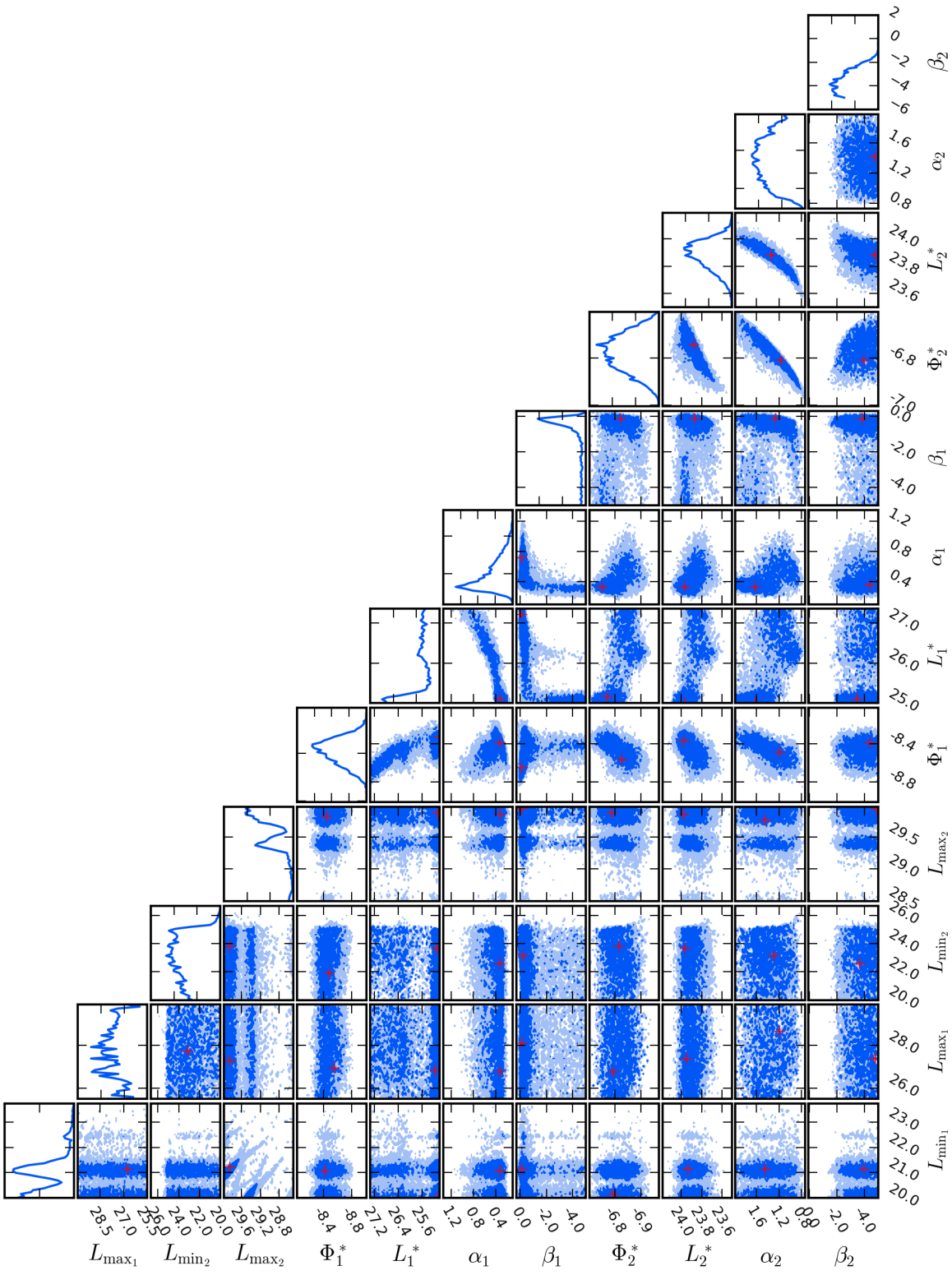

FIGURE 3.7: The posterior distributions, continued. The above is for the $1.85 < z < 2.15$ bin.

Chapter 4

A deep radio view of the evolution of the cosmic star-formation rate density from stellar-mass selected samples in VLA-COSMOS

4.1 Introduction

Understanding the evolution of star formation in galaxies over the history of the Universe is a key aspect of galaxy-formation studies. It has the potential to tell us how, when and where, star formation happened from the onset of the first galaxies within the epoch of reionisation, through to the present day. Measuring the SFR in galaxies can be done at a variety of wavelengths (see Chapter 1.2.1.4).

However, the most reliable estimates for the star-formation rate based on radio emission tend to be for those where the contribution from an SMBH is thought to be negligible. One way to do this, is to select galaxies based on their optical properties, rather than using a radio-selected sample. This mitigates against the inevitable bias for 'normal' galaxies with low-level AGN-related radio emission to be boosted above the flux-density limit of the radio survey, whereas those galaxies with the same SFR but no AGN-related emission fall below the same flux limit.

Therefore, in this chapter I measure the RLF of NIR selected galaxies below the nominal flux limit by applying the technique developed in Chapter 2. I use a set

of SFG and AGN models for the RLF and fit directly to the radio data using a full Bayesian approach. In Chapter 4.2 I describe the radio, optical and NIR survey data I use, along with the photometric redshifts and the derived stellar masses. In Chapter 4.3 I present the results of the various RLF model forms and in Chapter 4.4 I use the most appropriate RLF models to calculate the evolution of the cosmic star formation rate density, and compare this with other studies in the literature. Chapter 4.5 summarises my conclusions.

4.2 Data

4.2.1 Near-infrared data

In order to select the galaxies for this study, I use the NIR imaging in Y, J, H and K_s bands taken with the VIRCAM (Emerson and Sutherland, 2010) as part of the ultra deep survey on the VISTA telescope, UltraVISTA (McCracken et al., 2012) and the deep optical data from Canada-France-Hawaii-Telescope Legacy Survey (CFHTLS) as well as the HyperSuprimeCam Strategic Survey Programme (HSC; Aihara et al., 2018a,b) over the COSMOS field. In the fourth UltraVISTA data release (DR4) the survey covers a total area of $\sim 1.9\,\mathrm{deg}^2$, which is reduced to an effective area of $\sim 1.8\,\mathrm{deg}^2$ when masked regions (saturated by stars, regions of high noise) are excluded [1]. The overlapping effective area between DR4 and CFHTLS or HSC is $1.52\ \mathrm{deg}^2$. The flux densities were extracted from a $2''$-diameter aperture in each band using the K_s-band as the detection image (a rough proxy for stellar mass over the redshift range in which I am interested), and extracting the flux at these positions across the other NIR and optical data (following Bowler et al., 2020; Adams et al., 2020). The catalogue has a non-uniform 5σ detection threshold with a minimum of $K_s = 24.5$.

4.2.1.1 Photometric redshifts and stellar masses

The photometric redshifts are the same as those used by Adams et al 2020b (in prep) and are measured by fitting the multi-band data available in the COSMOS field to a synthetic library of galaxy templates using LePHARE (Arnouts et al.,

[1] http://ultravista.org/release4/dr4_release.pdf

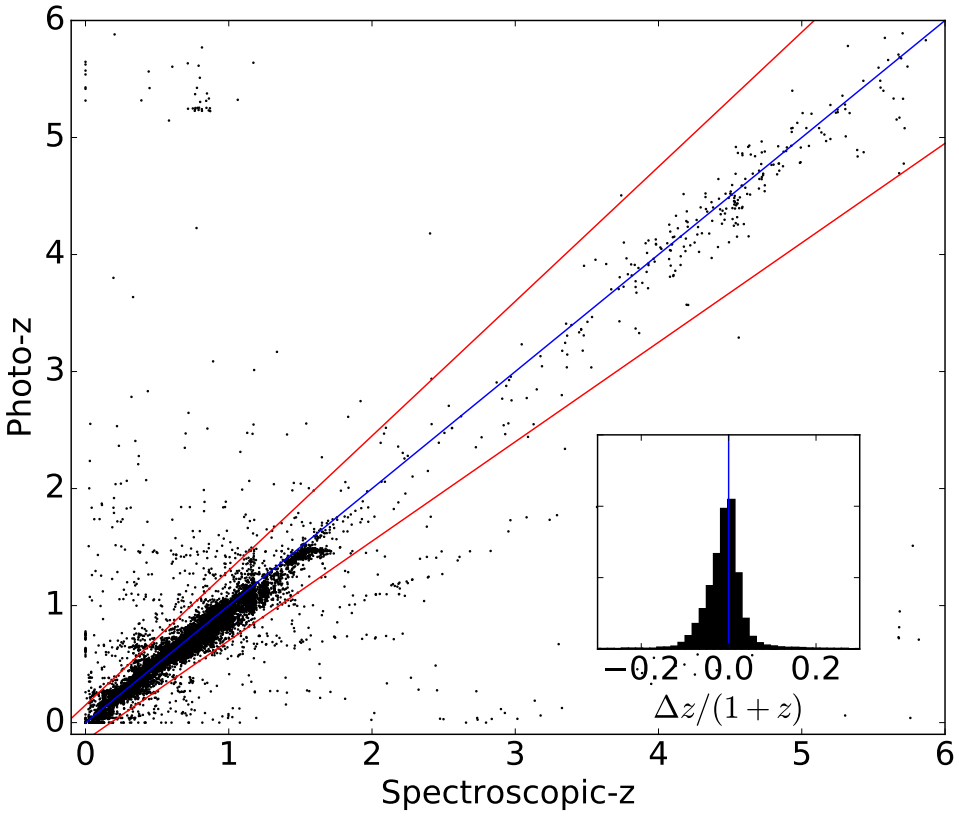

FIGURE 4.1: Comparison between the photometric redshifts to the 22 409 spectroscopic redshifts available in the literature over our sample area. Credit: Adams et al. 2021 (in prep)

2002; Ilbert et al., 2009). In summary, they follow Ilbert et al. (2013), using several synthetic galaxy multi-band templates from Bruzual and Charlot (2003) and Polletta et al. (2007) [generated using the stellar population synthesis model of Bruzual and Charlot (2003) assuming a Chabrier (2003) IMF] to compare with the observed photometry.

A comparison of the photometric redshifts to the spectroscopic redshifts available in the literature (Lilly et al., 2009; Coil et al., 2011; Cool et al., 2013; Le Fèvre et al., 2013; Alam et al., 2015; Hasinger et al., 2018) shown in Fig. 4.1, Adams et al 2020b (in prep) reports an outlier rate of 828/19 752 (4.2%) and a normalised mean absolute deviation (NMAD) of 0.0312.

The stellar masses are computed again using LEPHARE to compare the multi-band data with templates, but with the redshift fixed at the best-fit photometric redshift. χ^2 minimisation is again used to find the best fit template from the Bruzual and Charlot (2003) models.

TABLE 4.1: This table shows the redshift bins along with the median redshift of the data in each bin. $N_{\rm Tot}$ is the total number of galaxies in each bin. I show the stellar-mass completeness limit that contains 90% of the galaxy's stellar mass completeness. I also present the number of galaxies with stellar mass above the stellar-mass completeness limit (N, my sample) and the number of sources in my sample that have VLA-COSMOS 3-GHz counterparts ($N_{\rm VLA}$).

Redshift bin	$z_{\rm Med}$	$N_{\rm Tot}$	$\log(M_{\rm lim}/M_{\odot})$	N	$N_{\rm VLA}$
$0.1 < z < 0.4$	0.32	34695	8.1	20497	588
$0.4 < z < 0.6$	0.53	27591	8.7	18035	688
$0.6 < z < 0.8$	0.7	41125	8.9	25593	839
$0.8 < z < 1.0$	0.89	43649	9.1	28803	930
$1.0 < z < 1.3$	1.11	50713	9.3	27068	1003
$1.3 < z < 1.6$	1.45	35315	9.5	17883	766
$1.6 < z < 2.0$	1.75	38456	9.6	15621	783
$2.0 < z < 2.5$	2.23	13504	10.0	5496	413
$2.5 < z < 3.2$	2.83	24476	9.9	8961	269
$3.2 < z < 4.0$	3.44	10288	10.2	3664	50

4.2.1.2 Sample

My goal in this chapter is to measure the evolution of the RLF and thus the cosmic SFRD using SFGs, which means removing contamination from stars and emission from AGN. Sources are classified as a star if, 1) the best-fit star template has higher probability than the best-fit galaxy template; and 2) the source does not meet the BzK colour–colour selection criteria from Daddi et al. (2004), which combines the B and z optical bands with NIR K band to identify stars. Passive galaxies are traditionally identified using colour–colour plots with $(U-V)$ vs $(V-J)$, usually referred to as UVJ (e.g. Wuyts et al., 2007; Williams et al., 2009). However, several studies have shown that $\sim 10-20\%$ of passive sources have significant SF in the host galaxy (e.g. Belli et al., 2017; Merlin et al., 2018; Leja et al., 2019).

Therefore, I choose not to separate the galaxies in my sample into quiescent and SF, and instead aim to detect radio emission from star formation for all galaxies that lie above the flux/mass limit in this study.

4.2.1.3 Completeness

In a magnitude-limited survey, the stellar mass completeness is a function of the mass-to-light ratio (which depends on a galaxy template) and redshift. In light of this, I divide the data into ten redshift bins (from $z = 0.1$ to $z = 4$, ensuring that

the redshift bins are large enough not to be compromised by photometric-redshift uncertainties [i.e. the photometric redshift uncertainty $\ll$ redshift bin width]) and estimate a conservative stellar-mass completeness limit ($M_{\rm lim}$) in each redshift. To estimate this stellar-mass completeness limit I follow Ilbert et al. (2013). I start by computing the stellar-mass limit ($M_{\rm min}$) for each galaxy. The stellar-mass limit is the stellar mass that a galaxy at a certain redshift with stellar mass (M) would have if observed at the 5σ flux limit ($K_s = 24.5$),

$$\log(M_{\rm min}) = \log(M) + 0.4(K_S - 24.5). \tag{4.1}$$

The stellar-mass completeness limit is then given by the stellar-mass limit that is above 90% of the stellar-mass limits in the redshift bin (Table 4.1, Fig 4.2). This stellar mass completeness limit takes into account the different galaxy templates (and their corresponding mass-to-light ratio), which then ensures that not more than 10% of the low-mass galaxies are missing in the sample. Applying the stellar-mass cut results in a total galaxy sample size of 171 621, over the redshift range $0.1 < z < 4$.

4.2.2 Radio data

I use radio data from the VLA-COSMOS 3-GHz survey (Smolčić et al., 2017). The survey covers 2.6 deg^2 with a resolution of 0.75″ and a noise with a median value of 2.3 μJy. 10,830 detected sources were extracted in the central 2 deg^2 using BLOBCAT (Hales et al. 2012) with 67 found to be multi-component. The multi-component sources were visually confirmed. Most of them were galaxies with resolved structures such as jet/lobe/core. A small portion of the multi-component sources were SFGs with disk-like structures (Smolčić et al. 2017).

4.2.3 Flux-density extraction

For sources that lie significantly above the noise limit of the data, flux densities are usually extracted by running a source finder that identifies a source lying significantly above the noise and then aims to quantify the integrated flux-density of the sources, either by using the fitting of multiple Gaussians (e.g. PyBDSF; Mohan and Rafferty, 2015) or by flood filling to a certain level above the background noise

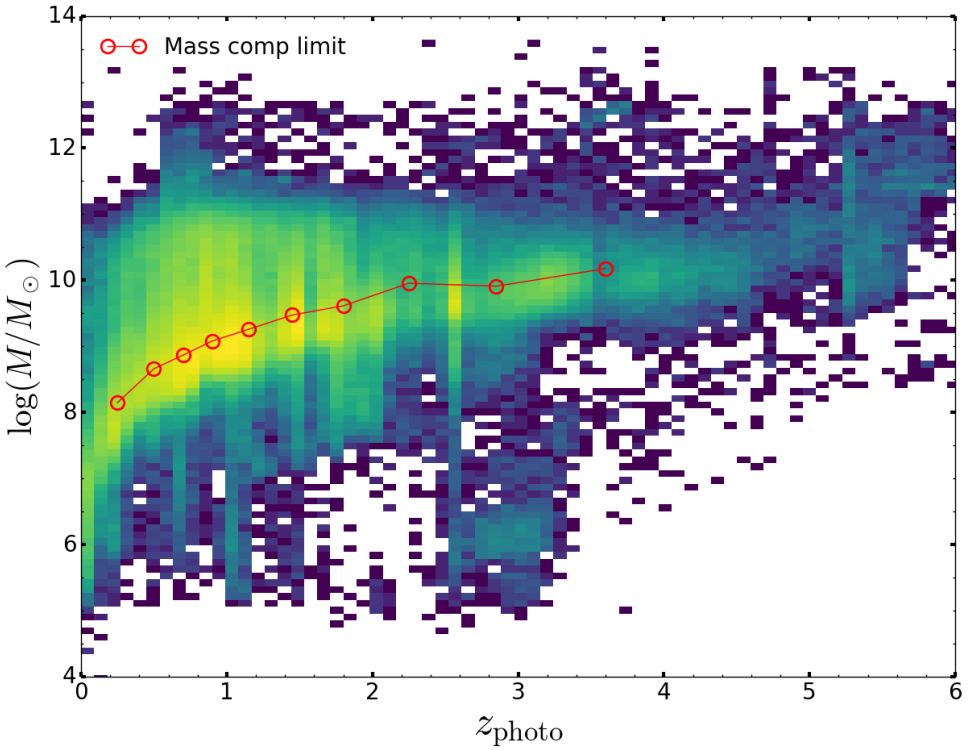

FIGURE 4.2: The stellar mass of the galaxies in the UltraVISTA DR4 sample as a function of photometric redshifts. The red circles connected by lines represents the stellar mass completeness limit.

[e.g. BLOBCAT (Hales et al., 2012) and PROFOUND (Robotham et al., 2018; Hale et al., 2019)].

The challenge here is that most of the NIR sources do not have a radio counterpart above the detection threshold. The simplest approach would be to use a square centered at the NIR position and measure total flux density by summing the individual flux densities per pixel, accounting for the beam area. The size of the aperture plays an important role because if it is too big compared to the projected size of the galaxy, there will be increased contribution from noise and there is also a greater chance that the measured flux will include a contribution from nearby objects. If the size is too small, the flux density of the galaxy might be underestimated. The extraction "stamp" should therefore be as close as possible to the expected size of the galaxies. In this chapter I use a square with a size of 7×7 pixels ($1.4'' \times 1.4''$), which is large enough to contain the average size of galaxies, based on several studies on radio-continuum sizes of μJy galaxies (e.g. Murphy et al., 2017; Guidetti et al., 2017; Bondi et al., 2018; Cotton et al., 2018; Jiménez-Andrade et al., 2019), and

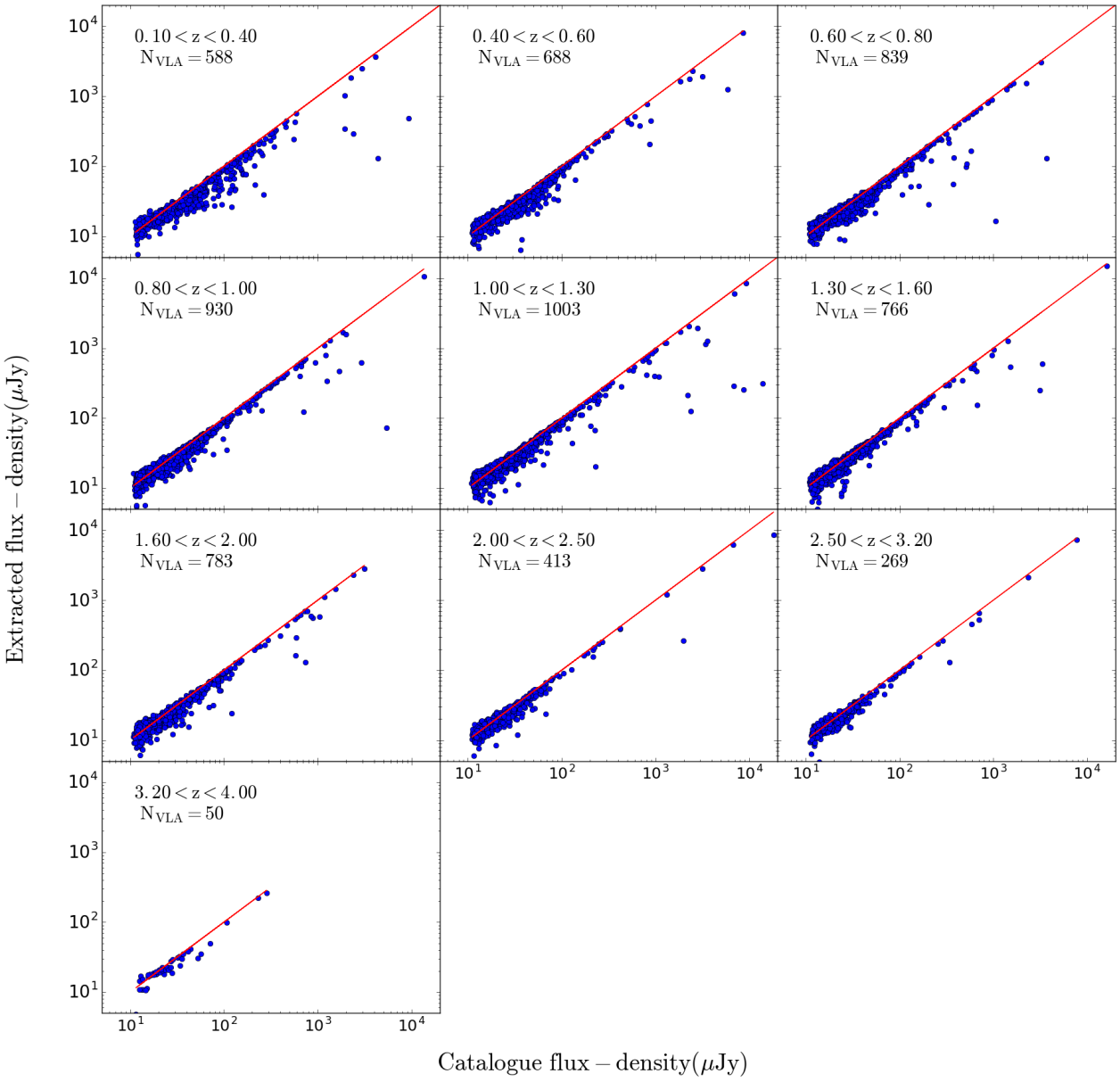

FIGURE 4.3: Comparison between the VLA-COSMOS 3-GHz flux densities extracted around the NIR position and VLA-COSMOS 3-GHz-COSMOS2015 matched flux densities from Smolčić et al. (2017a), represented by the blue points. I matched the UltraVISTA sources with Smolčić et al. (2017a) sources using their COSMOS2015 ID.

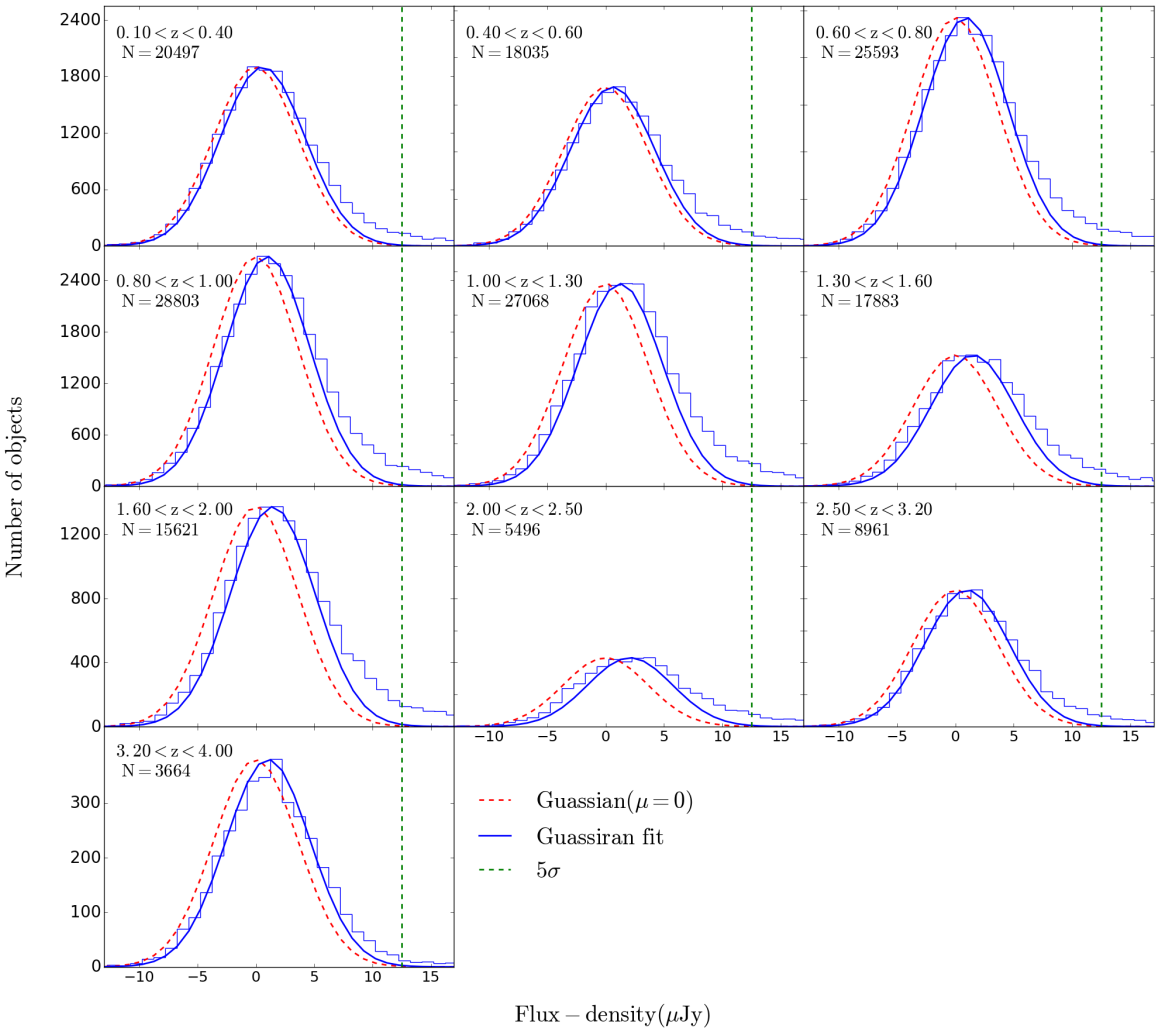

FIGURE 4.4: The histograms of the VLA-COSMOS 3 GHz integrated flux density extracted from apertures (7×7 pixels) centered at the NIR positions. The red dashed curve centred at zero is a Gaussian fit to the flux densities extracted from apertures centered $50''$ from the NIR positions in each redshift bin. The Gaussians have mean of $\sigma = 2.32 \pm 0.167\mu$Jy over all the redshift bins. The blue line represents a shift in the red dashed line to fit by eye the Gaussian part of the source flux densities. The green, vertical dashed line in each panel represents the $5\sigma = 18.37\mu$Jy limit of the VLA-COSMOS data.

small enough to avoid contamination from background sources. I note that as the flux density in the images is per beam area, the unresolved (or marginally resolved) galaxies will have all of their flux accounted for using this aperture size. The mean noise from the 7×7 aperture is $\sigma = 2.32 \pm 0.167\mu$Jy at 3 GHz.

TABLE 4.2: Assumed priors. $L_{5\sigma}$ is the luminosity corresponding to the $5\sigma_n$ flux-density cut for a given redshift.

Parameter	Prior
$\alpha_1, \beta_1, \alpha_2, \beta_2, \delta$	uniform $\in [-5, 5]$
σ_{LF}	Gaussian$\sim (\mu = 0.6, \sigma = 0.1)$
$\log_{10}[L_{\min_{\{1,2\}}}/(\mathrm{WHz}^{-1})]$	uniform $\in [18, 30]$
$\log_{10}[L_{\max_{\{1,2\}}}/(\mathrm{WHz}^{-1})]$	uniform $\in [18, 30]$
$\log_{10}[\phi^*_{\{1,2\}}/(\mathrm{Mpc}^{-3}\mathrm{mag}^{-1})]$	uniform $\in [-12, -2]$
$\log_{10}[L^*_1/(\mathrm{WHz}^{-1})]$	uniform $\in [\log_{10}(L_{5\sigma}) + 0.5, 30]$
$\log_{10}[L^*_2/(\mathrm{WHz}^{-1})]$	uniform $\in \left[18, \log_{10}(L^*_1)\right]$

In Fig 4.3 I compare the flux densities I extracted with the detected VLA-COSMOS 3-GHz Smolčić et al. (2017) sources matched to the Laigle et al. (2016) COSMOS2015 multi-wavelength catalogue based on UltraVISTA DR2 (Smolčić et al., 2017a). The measured flux densities I measured scatter around the 1-to-1 line at faint flux densities (i.e. $S_{3\ \mathrm{GHz}} < 30\,\mu$Jy). Above $S_{3\ \mathrm{GHz}} \sim 40\,\mu$Jy the flux densities I extracted underestimate the VLA-COSMOS 3-GHz flux densities. The underestimation is due to the large sources (predominantly large low-redshift star-forming galaxies and more distant extended AGN) that are larger than the aperture size.

Since my focus in this thesis is on sources below the nominal detection threshold I use the 7×7 pixel aperture and for sources above 500 μJy I use the flux densities of Smolčić et al. (2017). This accounts for source with high flux-densities which are likely to be underestimated because either the source is larger than the aperture or it is a multi-component source. Fig 4.4 shows the flux densities extracted from a 7x7 aperture for all the sources in each redshift bin. The extracted flux densities follow a Gaussian distribution with an offset from zero. From Chapter 2.3.1 I found that an offset occurs when the majority of the sources have flux densities comparable to the noise. The offset is smaller at the lower redshifts and seems to increase with redshift. An increase in the offset means that the majority of flux densities are higher than the noise (see Fig. 2.3). This suggests that at higher redshifts most of undetected sources have on average higher flux densities than at lower redshifts. The flux densities have a positive tail that represents real detected sources. This tail becomes less pronounced at high redshift, which is caused by the lack of sources with high flux densities at these redshifts.

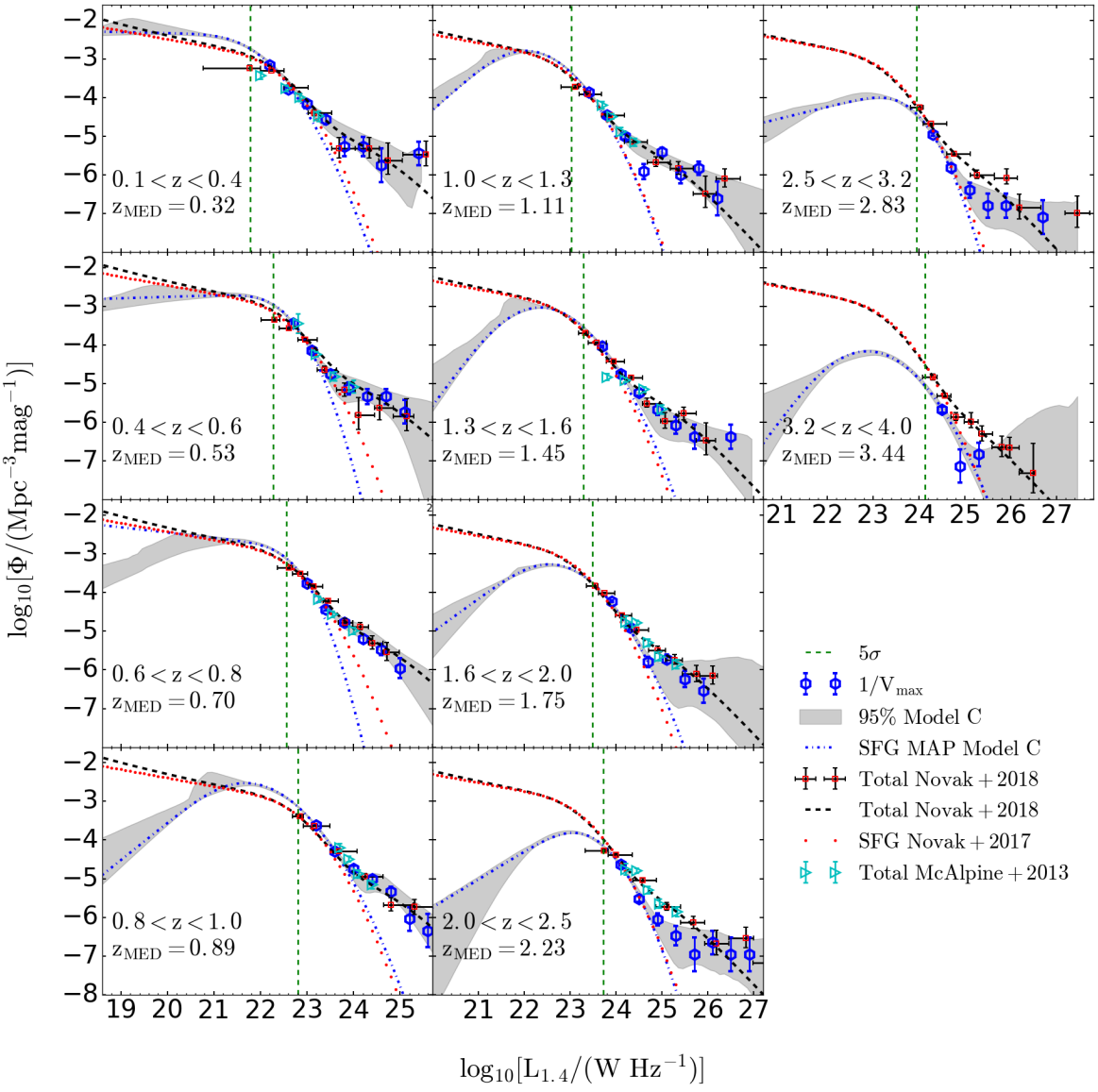

FIGURE 4.5: The rest-frame 1.4 GHz RLF of both AGN and SFGs in the COSMOS field. The blue dash-dotted curve is the SF RLF reconstructed using MAP parameters from the lognormal power law (Model C) fit to each redshift bin. The grey region represents the 95% confidence interval of the distribution of reconstructions of models in the posterior. The blue hexagons represent $1/V_{\mathrm{max}}$ estimations for the detected sources. The red squares are radio-selected RLF data points from Novak et al. (2018), with the curved black, dashed line showing a pure luminosity evolution fit to them. The cyan triangles represent the total RLF from McAlpine et al. (2013). The red dots show a PLE fit to SFGs from Novak et al. (2017). The vertical, green dashed lines correspond to the detection threshold (5σ) computed using the median redshift for each redshift bin.

4.3 Results

In this section I provide a binned RLF for the radio-detected sources in my mass-selected sample, based on the $1/V_{\rm max}$ statistic, and then present the results of the RLF modelling described in Chapter 2.2.2 using the priors in Table 4.2.

4.3.1 The binned RLF

Fig 4.5 includes the $1/V_{\rm max}$ measurements for the stellar mass-selected sources above the nominal 5σ detection threshold. Due to the stellar-mass selection the RLFs are not expected to be exactly the same as the RLF determined using a purely radio-selected sample. However, I note that the VLA-COSMOS 3-GHz sources all have optical/NIR counterparts up to $z \sim 1.5$, and $\sim 95\%$ completeness at $z \sim 4$ (Smolčić et al., 2017a). Given that the main goal of this thesis is to measure the RLF for the fainter population of SFGs and how they evolve, this does not affect the results.

The $1/V_{\rm max}$ data points (dark-blue data points in Fig 4.5) are in good agreement with McAlpine et al. (2013) and Novak et al. (2018) measurements for $z < 2$. At $z > 2$ my $1/V_{\rm max}$ points lie below the volume density found in these studies at the intermediate luminosities between $24 < \log_{10}[L_{1.4}/{\rm W\,Hz^{-1}}] < 26$. This is mainly due to my mass selection, rather than using the full optical/NIR data and the associated photometric redshifts. The uncertainty associated with photomoetric redshift has not been accounted for throughout this chapter. This is because the uncertainties from photometric redshifts are averaged out when there are sufficient sources in each bin. Furthermore, my redshift bins are large enough to minimize the uncertainties. There is also uncertainty from the spectral index, which is associated with the imperfect radio K-correction and the fact that we assume an average spectral index $\alpha = -0.7$ for all our sources. The spectral index can deviate by as much as ~ 0.4 from the mean spectral index (e.g. Kimball and Ivezić, 2008; Zinn et al., 2012) which can lead to a maximum shift of $\Delta \log_{10}(L) = 0.32$ and $\Delta \log_{10}(L) = 0.41$ at $z = 2$ and $z = 4$ respectively (see Novak et al. 2018 for an in-depth discussion). The effects of the spectral index average out when a bin has sufficient number of sources in the bin which is not the case at higher luminosities. However, as I note above, all these have little effect on my main results.

Model	$\triangle \log_{10} \mathcal{Z}$	$\triangle \log_{10} \mathcal{Z}$	$\triangle \log_{10} \mathcal{Z}$	$\triangle \log_{10} \mathcal{Z}$
	$0.10 < z < 0.40$	$0.40 < z < 0.60$	$0.60 < z < 0.80$	$0.80 < z < 1.00$
B	$\mathbf{47.9 \pm 0.26}$	$\mathbf{16.0 \pm 0.27}$	42.4 ± 0.27	52.3 ± 0.27
C	$\mathbf{47.9 \pm 0.25}$	13.2 ± 0.21	$\mathbf{42.7 \pm 0.26}$	$\mathbf{57.4 \pm 0.25}$
D	0.0 ± 0.00	0.0 ± 0.00	0.0 ± 0.00	0.0 ± 0.00
	0.0 ± 0.00	$1.30 < z < 1.60$	$1.60 < z < 2.00$	$2.00 < z < 2.50$
B	0.0 ± 0.00	19.1 ± 0.26	91.4 ± 0.27	58.4 ± 0.25
C	$\mathbf{3.2 \pm 0.31}$	$\mathbf{21.8 \pm 0.25}$	$\mathbf{97.4 \pm 0.25}$	$\mathbf{62.3 \pm 0.23}$
D	0.8 ± 0.26	0.0 ± 0.00	0.0 ± 0.00	0.0 ± 0.00
	$2.50 < z < 3.20$	$3.20 < z < 4.00$		
B	69.0 ± 0.26	10.9 ± 0.23		
C	$\mathbf{71.1 \pm 0.24}$	$\mathbf{13.5 \pm 0.21}$		
D	0.0 ± 0.00	0.0 ± 0.00		

TABLE 4.3: The relative evidence for the different models (Chapter 2.2.2) in each redshift bin of the NIR-selected radio data. In each redshift bin the reference evidence is from the model with the lowest log-evidence and the winning model is in bold.

4.3.2 The free RLF models

I use BAYESTACK to determine the best-fit parameters for the RLF of the mass-selected sample using Models B and C (Chapter 2.2.2) in each redshift bin. For each redshift bin I record the Bayesian evidence, posterior distributions for each parameter along with the median, maximum-likelihood and MAP values for each parameter (shown in Table 4.5). The Bayes factors for each redshift bin are shown in Table 4.3, where the reference evidence is for the model with the lowest evidence and the model with the highest evidence is in bold text. I find that the data mostly prefers Model C, the model with a log-normal power-law describing the faint sources (dominated by SFGs) and a double power-law describing the bright-end sources.

In Fig 4.5 I show the stellar-mass-selected RLF, reconstructed using the MAP parameters from Model C along with the 95% confidence interval. The 95% region is calculated by reconstructing the RLF in a chosen set of luminosity bins, using all the models in the posterior, and determining the 95% limits in each luminosity bin independently. The MAP reconstruction follows the $1/V_{\rm max}$ data points very well and also follows the Novak et al. (2018) extrapolated evolution fit well, for at least an order of magnitude below the detection threshold, to $z \sim 1.6$. Similar to the intermediate luminosities, the faint-end of the reconstructed RLF underestimates the extrapolated evolution fit from Novak et al. (2018) at higher redshifts ($z > 1.6$). This is due to the Novak et al. (2018) RLF having a fixed faint-end slope that

extends below their detection threshold (and is essential fixed by the low redshift data). Instead, I am using a mass-selected sample with the aim of probing this regime, and so in Models B and C, I allow the faint-end slope of the SFG RLF to vary freely.

I also see that the reconstructed RLF, at much lower luminosities (two or more orders of magnitude below the detection threshold, noticeably above $z \sim 0.4$), falls off steeply. This is due to the mass selection, in that I am approaching a point in the RLF where there are not any galaxies at low stellar mass to populate this part of the RLF (owing to the relationship between galaxy mass and SFR; Noeske et al., 2007; Daddi et al., 2007; Whitaker et al., 2014; Johnston et al., 2015). I have checked this by including all NIR-detected sources (rather than using the mass-limited sample) and find that the luminosity where the fall-off occurs moves to lower luminosities, as expected. This shows that it is not a feature of the RLF, but a feature of the parent sample, because of the lack of low-stellar-mass sources in my sample, and this stellar mass limit obviously increases with redshift due to the flux limit of the NIR data.

4.3.3 The fixed RLF model

My main goal is to constrain the RLF to low radio luminosities to obtain a measurement of the cosmic SFRD from a stellar-mass-selected sample. Through the BAYESTACK technique I am able to constrain the RLF to luminosities below the 5σ detection threshold. However, as shown in Chapter 4.3.2, my mass selection causes the free-fitting models to fall off towards lower radio luminosities. This is not an underlying feature of the SFG RLF, and will therefore affect the cosmic SFRD estimation. To address this, I follow the work of McAlpine et al. (2013) and Novak et al. (2017, 2018) in fixing the shape of the RLF to that of the local RLF (Chapter 2.2.2).

I start by modelling the individual redshift bins using the fixed model, Model D, with $\beta_{LF}^{SF,AGN} = 0$ (i.e. only allowing a re-normalisation of the RLF in each redshift bin, with a single luminosity evolution term). The resulting RLF is shown in Fig. 4.6. Table 4.3 shows that Model D is (almost) always the least preferred model (having the lowest log-evidence). This is because Model D *enforces* a fixed faint-end slope. Whereas, the mass-selected sample has a cut at the low-mass end, which corresponds to a gradual fall-off at low radio luminosity (and a different faint-end slope). This

means that the fixed slope will struggle to produce a fit as good as the models with more freedom, as it assumes that the (missing) lower-mass galaxies are in the sample. Thus, formally it is the worst fitting model (given the selection effects), even though it may accurately represent the underlying RLF.

I also run BAYESTACK simultaneously over all of the redshift bins using the pure PLE. The PLE for my AGN and SFG galaxies is given by the following MAP values and 95% confidence limits,

$$L_{\rm AGN} \propto (1+z)^{1.82\pm0.2-(0.47\pm0.10)z}$$

and

$$L_{\rm SFG} \propto (1+z)^{4.04\pm0.04-(0.85\pm0.02)z}.$$

In Fig. 4.6 I show the RLF fits and 95% confidence intervals for the individual redshift bins, alongside the PLE RLF model fits, both with the fixed RLF shape. The PLE RLF model fits agrees with the $1/V_{\rm max}$ data points across all redshifts up to $z \sim 2$. At the highest redshifts ($z > 2$) I find some differences between my model (plus my binned data) and the models of Novak et al. (2017, 2018). At the high radio luminosities, small number statistics, coupled with slight differences in the photometric redshifts used by myself and Novak et al. (2017), offer some explanation as to why my RLF lies below theirs. Furthermore, I note that my data are also becoming increasingly incomplete at these redshifts, and sources that are relatively bright at radio wavelengths could have lower-mass/faint host galaxies (e.g. Jarvis et al., 2009; Norris et al., 2011; Collier et al., 2014). However, more relevant to the focus of this work are the differences in the evolution of the lower-luminosity component of the RLF, which I assume to be dominated by SFGs. There is contribution from low-luminosity AGN to lower-luminosity component of the RLF. However, it is impossible to determine with current surveys, as such faint AGN would be faint at all wavelengths. What I care about is the dominant emission mechanism, which is star formation at this flux levels. Furthermore, even some contamination from AGN would not greatly affect the main results.

The SFG component of my RLF model evolves with similar strength to that of Novak et al. (2017) up to $z \sim 1.6$, with the degeneracy between α_L^{SF} and β_L^{SF} (see Fig. 4.10) across this redshift range explaining the apparent difference in the evolutionary parameters (Table 4.4). However, beyond $z \sim 2$, the Novak et al. (2017) RLF continues to evolve, whereas I find that the SFG RLF from my model

TABLE 4.4: Comparison with determinations in the literature of the pure luminosity evolution of the RLF.

Reference	$\alpha_L^{\rm SF}$	$\beta_L^{\rm SF}$	$\alpha_L^{\rm AGN}$	$\beta_L^{\rm AGN}$
This work	4.04 ± 0.04	-0.85 ± 0.02	1.82 ± 0.20	-0.47 ± 0.10
Novak et al. 2018	2.95 ± 0.04	-0.29 ± 0.02	2.86 ± 0.16	-0.70 ± 0.06
Novak et al., Smolčić et al.*	3.16 ± 0.04	-0.32 ± 0.02	2.88 ± 0.17	-0.84 ± 0.07
McAlpine et al. 2013	2.47 ± 0.12**		1.18 ± 0.21**	

* Novak et al. (2017) is the SFG-only PLE and Smolčić et al. (2017b) an AGN-only PLE fit

** McAlpine et al. (2013) fit only one evolutionary term each for the SF and AGN

reaches a steady state and then begins to decline (for the Novak et al. (2017) PLE model, this decline does not take effect until $z > 3.5$).

I note that this decline coincides with the decrease in low stellar-mass sources in my stellar-mass-limited sample at these redshifts. However, it is also worth mentioning that the total RLF (AGN + SFGs) does remain a reasonable fit to the binned $1/V_{\rm max}$ points of Novak et al. (2018) out to $z \sim 2.5$, suggesting that some of the deficit in the low-luminosity RLF is compensated for by the evolving high-luminosity RLF that I associate with AGN.

4.4 Cosmic history of star formation

Although NIR observations cannot be used directly to measure the SFR of a galaxy, they are dominated by emission from solar-mass type stars that are a significant fraction of a galaxy's stellar mass. These observations, therefore, contain potential SFGs and are not as affected by dust as optical/UV data. However, I use the *radio* data to measure the SFR; these do not require any corrections for dust. The stellar-mass-selected RLF of SFGs, obtained from Model D, provides a good estimate of the RLF of SFGs (based on Fig. 4.6), and from this I can obtain the SFRD by integrating under it, i.e.

$$SFRD = \int_{\rm Lmin}^{\rm Lmax} SFR(L_{1.4})\Phi(L_{1.4})dL, \tag{4.2}$$

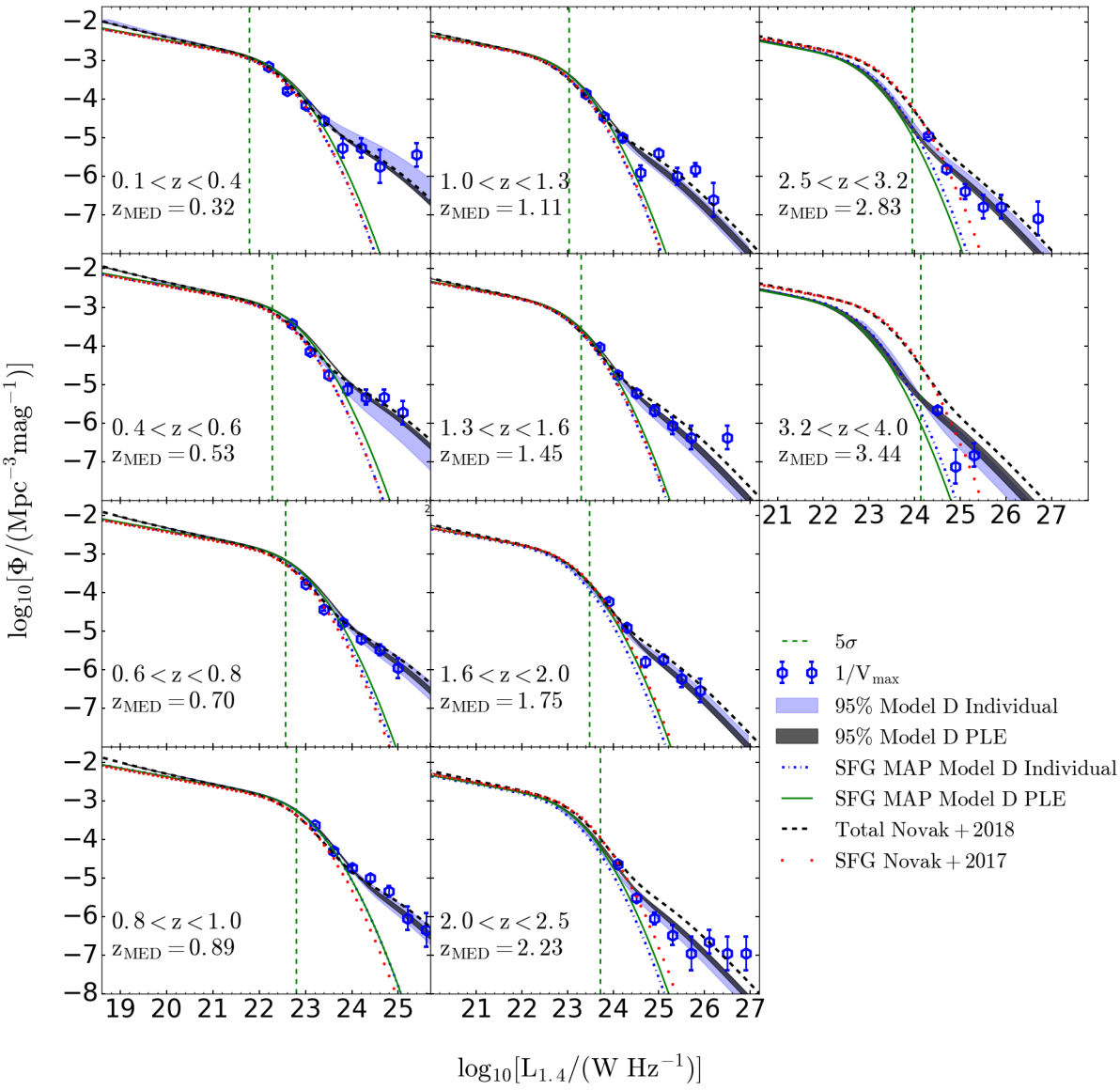

FIGURE 4.6: The rest-frame RLF of both AGN and SFGs in the COSMOS field. The blue hexagons represent $1/V_{\mathrm{max}}$ estimations for the UltraVISTA sources with VLA-COSMOS 3-GHz detected sources. The dark grey and blue regions represents the 95% confidence interval of the distribution of reconstructions for Model D PLE fit and Model D individual fit to each redshift bin respectively. The green and blue dashed-dotted lines represent the SFG components of the total RLF of the Model D PLE fit and Model D Individual fit to each redshift bin respectively. The curved, black, dashed line represents the PLE fit to the radio-selected RLF from Novak et al. (2018). The red dots are a PLE fit to the SFGs from (Novak et al., 2017). The vertical, green dashed lines correspond to the detection threshold (5σ) computed using the median redshift for each redshift bin.

where $\Phi(L_{1.4})$ is my RLF for SFGs and $SFR(L_{1.4})$ is the SFR associated with 1.4-GHz radio luminosities. This relies on the infrared–SFR relation. Using the Kennicutt (1998) calibration, the total infrared luminosity ($L_{\rm TIR}$) is related to the SFR by,

$$\frac{SFR}{\rm M_{\odot}yr^{-1}} = 4.5 \times 10^{-37} \frac{L_{\rm TIR}}{W}, \tag{4.3}$$

where L_{TIR} is the total infrared luminosity. The radio luminosity can be converted to the total infrared luminosity and linked to SFR using the IRRC; (Delhaize et al., 2017),

$$\frac{SFR}{\rm M_{\odot}yr^{-1}} = f_{\rm IMF} \times 10^{q_{\rm TIR}-24} \frac{L_{\rm 1.4GHz}}{\rm WHz^{-1}}, \tag{4.4}$$

where $f_{\rm IMF}$ is the IMF (equal to 1 for a Chabrier IMF; Chabrier 2003) and $q_{\rm TIR}$ is a parameter that quantifies the IRRC given by,

$$q_{\rm TIR} = \log\left(\frac{L_{\rm TIR}}{3.75 \times 10^{12}\rm W}\right) - \log\left(\frac{L_{\rm 1.4GHz}}{\rm WHz^{-1}}\right). \tag{4.5}$$

I adopt a $q_{\rm TIR}$ value that evolves with redshift, given by $q_{\rm TIR}(z) = 2.78 \pm 0.02(1+z)^{-0.14\pm0.01}$ (Novak et al., 2017), although I note that the evolution may be due to mass dependence of the IRRC (e.g. Gürkan et al., 2018b). I then obtain the SFRD by numerically integrating the product of the RLF and the SFR over 1.4-GHz radio luminosities (Eq. 4.2). For this, it is ideal to ensure that the integral covers all radio luminosities and not just the range dictated by my fitted values of $L_{\rm min}$ and $L_{\rm max}$. Although I note that this makes little difference in the derived cosmic SFRD, due to the shallowness of the faint-end slope for low SFRs, and the steep exponential decline at high SFRs. With this in mind I use $\log_{10}(L_{\rm min}) = 21$ in all redshift bins and SFG models

In Fig. 4.7 I present the cosmic SFRDs obtained using the SFG component [2] from various models. As would be expected, the different models used in fitting the RLF result in different determinations of the cosmic SFRD. Here I present cosmic SFRDs obtained using Model C (blue data points) and Model D, both from fitting individual redshift bins (blue shading[3]) and from the PLE fit (magenta shading).

The SFRD from Model D individual redshift bins steadily increases with redshift out to $z \sim 1$, flattens until $z \sim 1.4$, and steadily decreases towards higher redshifts.

[2] I assume that the AGN component also accounts for emission from faint AGN. If there is contamination from AGN however, it is negligible at low radio luminosities where SFG dominates.

[3] The 95% region is calculated using the 95% confidence interval from the RLF.The conversion error associated with the q value (Novak et al., 2017) has not been accounted for in this calculation.

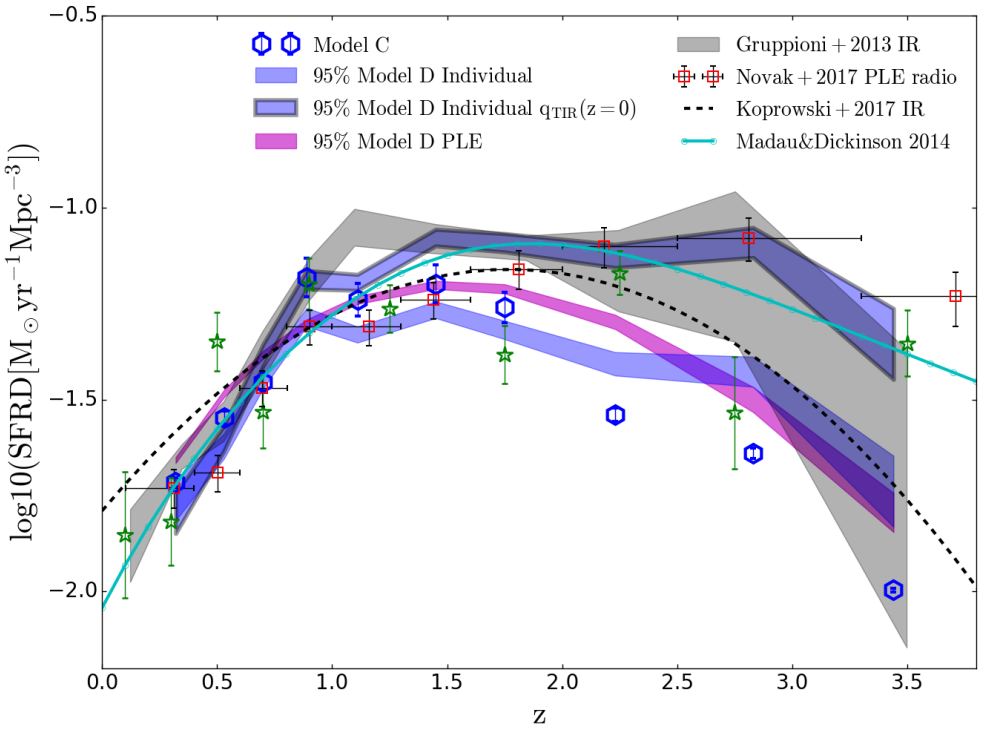

FIGURE 4.7: The cosmic SFRD. The blue hexagons are generated from the SFG MAP values for the Model C fit to each individual redshift bin. The blue shading corresponds to the 95% confidence region of the SFG component of the Model D fit to each redshift bin (individually). The blue region with borders also corresponds to the 95% confidence region of the individual Model D fit but is calculated assuming a non-evolving $q_{TIR}(z = 0) = 2.64 \pm -0.02$ (Bell, 2003). The magenta shading corresponds to the 95% confidence region of the SFG component of the Model D PLE fit to the combined redshift bins. The green stars are the combined uncorrected IR and UV data from Liu et al. (2018) and the red squares are from the SFG RLF of Novak et al. (2017), using a PLE fit. The black, dashed line is from Koprowski et al. (2017) and the connected, cyan dots represent a fit by Madau and Dickinson (2014) to various cosmic SFRD measurements in the literature. The gray, shaded region is the cosmic SFRD generated from the infrared LF of Gruppioni et al. (2013).

The SFRD based on the Model C individual redshift bins is in good agreement with that based on the individual Model D bins below $z \sim 1$. However, between $1 < z < 1.7$ Model C has higher SFR because the faint-end slope remains high to around 1 dex below the knee in the SFG RLF. Above $z \sim 2$, Model C gives a lower SFRDs compared to Model D individual SFRDs. This is because of the downturn in the faint end of the SFG RLF caused by the rising incompleteness due to the stellar-mass-selection. The SFRD based on the Model-D PLE RLF behaves similar to Model C but gives a higher SFRD than the other models between

$1.6 < z < 2.5$, where the stellar-mass selection still enables the knee in the SFG RLF to be constrained well, and the fixed faint end slope ensures that the SFRD remains high. At $z > 2.5$ the stellar-mass limit starts imposing on my ability to constrain the position of the knee in the SFG RLF, and the best-fit evolutionary terms force the position of the knee to lower radio luminosities in order to fit the incomplete parent sample. All my SFRDs estimations start to decline steadily between $1.5 < z < 2$ because of the rising stellar-mass limit with redshift.

I have mentioned that my sample misses low stellar-mass galaxies at high redshift. However, there are other galaxies that are missing from my sample, including dusty starburst galaxies such as sub-mm galaxies and star forming galaxies at low redshifts ($z < 0.5$). Recent studies have found that $\sim 10 - 30\%$ of sub-mm galaxies, which peak in the redshift range $1.8 < z < 3.4$ (Chapman et al., 2005; Simpson et al., 2014; Dudzevičiūtė et al., 2020b; Simpson et al., 2020), are missing from NIR surveys (Simpson et al., 2014; Brisbin et al., 2017; Cowie et al., 2018; Dudzevičiūtė et al., 2020b). The low-redshift star forming galaxies are diffused sources with sizes larger than the radio extraction aperture I have used. However, these low-redshift sources are too rare compared to the sources that are observed.

4.4.1 Comparison to the literature

In this subsection I compare my cosmic SFRD determinations, which are based on NIR-selected RLFs of SFGs (constrained below the nominal detection threshold using the Bayesian-stacking technique), to literature measurements of the cosmic SFRD using a variety of SFR tracers.

4.4.1.1 Comparison with the radio-selected cosmic SFRD

I first compare my cosmic SFRDs to the cosmic SFRD determined by Novak et al. (2017), which is based on COSMOS2015 photometry and SED fits (Laigle et al., 2016; Delvecchio et al., 2017) and VLA-COSMOS 3-GHz data. My results are in good agreement with those of Novak et al. (2017) at $z < 1.6$, and the lower uncertainties I found occur because I constrain the RLF using sources that lie below $5\,\sigma$ in the radio data better. However, my SFRDs deviate from those of Novak et al. (2017) at $z > 1.6$ as a result of my stellar-mass selection and possibly the assumed extrapolation to faint luminosities and completeness corrections implemented by

Novak et al. (2017). The impact of this is most apparent in Fig. 4.6, where the discrepancy between the SF component(s) of my 'Model D' RLF(s) and that of the Novak et al. (2017) RLF increases with redshift. Furthermore, although not shown in Fig. 4.7, at $z > 1.6$, my results are in broad agreement with other radio-based estimates of the cosmic SFRD in the literature (e.g. Smolčić et al., 2009; Karim et al., 2011; Ocran et al., 2020). Thus, my results should be regarded as complementary to those that use radio selection to measure the RLF. In this study, the incompleteness arises from the stellar-mass selection only, but I am able to constrain the faint-end slope to higher redshifts directly than the pure radio-selection. Completeness corrections for radio-selected samples are required for both the radio data (e.g. Eddington bias, which is relatively straightforward to account for) *and* in terms of the ability to identify a host galaxy and measure a redshift (which is less of a problem for fields with excellent ancillary data, such as COSMOS).

4.4.1.2 Comparison to other studies

Next, I compare my cosmic SFRDs to the dust-obscured cosmic SFRD from Gruppioni et al. (2013). For this they use a total-IR LF based on deep *Herschel* data, from the PACS Evolutionary Probe (PEP; Lutz et al. 2011) and the complementary *Herschel* Multi-tiered Extragalactic Survey (HerMES; Oliver et al. 2012), out to $z \sim 4$. I convert their L_{TIR} density (where the L_{TIR} is obtained from an integral over the whole thermal IR spectrum) to the SFRD using Eq. 4.3. In Fig. 4.7 I also plot the IR-based cosmic SFRD from Koprowski et al. (2017), who used *Herschel* (FIR) flux densities for their LFs, extracted at the positions of sub-mm sources identified using the James Clerk Maxwell Telescope's SCUBA-2 Cosmology Legacy Survey (S2CLS; Geach et al. 2017) and the Atacama Large Millimeter/Sub-mm Array (ALMA; Dunlop et al. 2017) in the COSMOS and UKIDSS-UDS fields. My results are in good agreement with those of Gruppioni et al. (2013) below $z \sim 1$, but then deviate towards higher redshifts where the IR SFRD continues to increase (before flattening and then falling around $z \sim 3$). It should be noted that there are many uncertainties in measuring L_{TIR} from a few data points. There are also k-correction effects, since, as one goes to higher redshifts one moves away from the peak of the thermal emission (far-IR bump) at $\sim 100\mu$m in the rest frame. At these high redshifts the L_{TIR} becomes dominated by hotter dust systems, which are more likely to have AGN contributions. This implies that converting from L_{TIR} to SFRD for these systems may lead to an overestimation of the cosmic SFRD. The SFRD

by Koprowski et al. (2017) is higher than both of my SFRD determinations at most redshifts, except around $z \sim 1$ where my results overlap. I note that Gruppioni and Pozzi (2019) attributed the discrepancies between the two IR-SFRD functions (Gruppioni et al., 2013; Koprowski et al., 2017) to selection bias, incompleteness effects, and the choice of SED in the SCUBA-selected data from Koprowski et al. (2017), which highlights some of the issues I mention above.

I also compare my results with the cosmic SFRDs from Liu et al. (2018), which represent the total cosmic SFRDs (a combination of the dust-obscured and unobscured cosmic SFRD measurements). Liu et al. (2018) derived their SFRD using super-deblended FIR to sub-mm *Herschel* photometry from confused galaxies in the northern field of the Great Observatories Origins Deep Survey (GOODS). The FIR/sub-mm photometry is extracted based on fitting SEDs to sources selected from the deep *Spitzer Space Telescope* (Werner et al., 2004) Multiband Imaging Photometer (MIPS; Rieke et al. 2004) and 1.4 GHz VLA (Morrison et al., 2010; Owen, 2018) data. The SFRD derived from Liu et al. (2018) is in good agreement with my results until $z \sim 3$ with minor deviations. They agree with the decline above $z \sim 1.6$ because the sample is also limited by stellar mass, due to their optical/NIR selections.

I also show the Madau and Dickinson (2014) cosmic SFRD, which is a fit to various cosmic SFRDs in literature. My results are again in good agreement below $z \sim 1$. However, my results deviate at $z > 1$, which is certainly influenced by my stellar-mass selection. Assuming a IRRC form that evolves negatively with increasing redshift, meaning that for a given radio luminosity, the SFR would be lower at high redshift, than at low redshift. This could obviously result in a false decrease in the SFRD if the real IRRC did not evolve with redshift, which other studies have suggested, depending on how the galaxies have been selected (e.g. Molnár et al., 2018). For example, one aspect of this is that Gürkan et al. (2018b); Delvecchio et al. (2020) all find that the IRRC has a dependence on the stellar mass of the galaxy, and this may be responsible for the observed evolution of the IRRC, as higher-redshift samples are inevitably dominated by more massive galaxies due to the nature of flux-limited samples. However, mass is unlikely to be the only extra parameter that needs to be considered when using the IRRC to convert a radio luminosity to star-formation rate, with Smith et al. (2014) and Read et al. (2018) showing that dust temperature, and how one includes sensible k-corrections for a range of dust temperatures at different redshifts, can be crucial to measure the SFR.

Furthermore, as we move beyond $z \sim 1$, inverse Compton scattering of the Cosmic Microwave Background photons may reduce the level of radio emission from star-forming galaxies observed at a given (relatively high) frequency (e.g. Murphy, 2009). All of these issues result in my understanding of any evolution in $q_{\rm TIR}$ being uncertain. In Fig. 4.7 I therefore also show how the SFRD evolves when adopting a constant of $q_{\rm TIR} = 2.64$ (Bell, 2003). One can see that this has a dramatic effect on the high-redshift evolution of the SFRD, with the cosmic SFRD derived from the RLFs determined in this thesis remaining high by a factor of 2-3 at $z \sim 3.5$.

4.4.2 Contribution from different stellar mass populations

As noted previously, the stellar-mass selection I have applied to my sample to ensure completeness (Chapter 4.2.1.3) means that I miss low-stellar mass ($M < 10^9$ M$_\odot$) sources at high redshift ($z \gtrsim 1.5$).

To further investigate the effects of stellar mass on the total RLF I divide my sources into low ($10^{8.5} \leq M \leq 10^{10}$ M$_\odot$) and high ($M > 10^{10}$ M$_\odot$) stellar-mass galaxies, shown in Fig 4.8 for Models C and D. It should be noted that I am using a stellar mass of $M = 10^{10}$ M$_\odot$ due to the fact that my NIR sample is complete to $M \sim 10^{10}$ M$_\odot$ in the highest redshift bin (Fig. 4.2). Galaxies with high stellar mass typically have high radio luminosities, as expected, and host a large proportion of the detected radio sources. The low stellar-mass galaxies typically have low radio luminosities and dominate the RLF below the 5σ detection threshold, for $z < 1.5$. Above $z > 1.5$, the contribution from the low stellar-mass sources decreases rapidly due to my stellar-mass completeness limit (see Fig 4.2). It is clear that the bulk of the RLF that I am able to measure at $z > 0.4$ is dominated by galaxies with stellar-mass $M > 10^{10}$ M$_\odot$.

In Fig 4.9 I show the contribution from the low ($10^{8.5} \leq M/{\rm M}_\odot \leq 10^{10}$) and high ($M > 10^{10}$ M$_\odot$) stellar mass sources to the total cosmic SFRD. The RLF for low stellar mass sources (orange and purple shades in Fig 4.8) shows that they are not the dominant population contributing to the SFRD at any redshift. However, they are important to include, as they are crucial to determine the position of the knee in the LF (L^*), where the bulk of the SFRD is concentrated, and the steepness of the faint-end slope (with a steep slope resulting in a higher contribution to the SFRD from these faint sources). The fact that they are missing in my sample at high redshifts, means that this may affect my cosmic SFRD estimate.

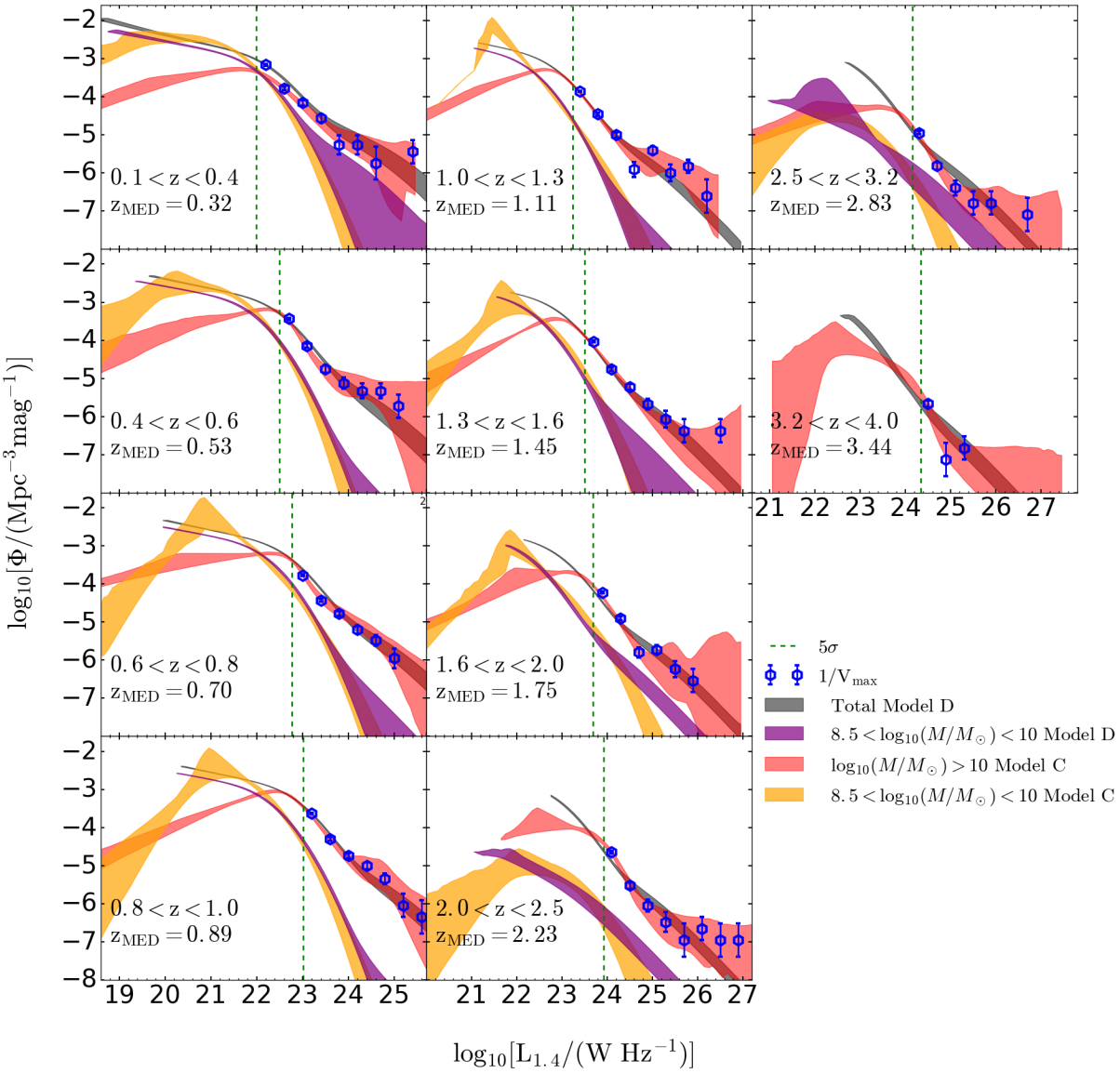

FIGURE 4.8: The contribution to the total rest-frame 1.4-GHz RLF from sources with different stellar masses in the COSMOS field. Low stellar mass ($10^{8.5} < M/\mathrm{M}_{\odot} < 10^{10}$) is represented by the purple and orange shaded regions, corresponding to the 95% confidence interval of the distribution of reconstructions of models in the posteriors. The contribution from sources with high stellar mass ($M > 10^{10}$ $\mathrm{M}_{\odot}$) is represented by the 95% region. The total RLFs based on Model-D fit to each redshift bin are represented by the grey shading which corresponds to the 95% region. The blue hexagons represent $1/V_{\mathrm{max}}$ estimations for my detected sources. The vertical, green dotted lines correspond to the detection threshold (5σ) computed using the median redshift for each redshift bin.

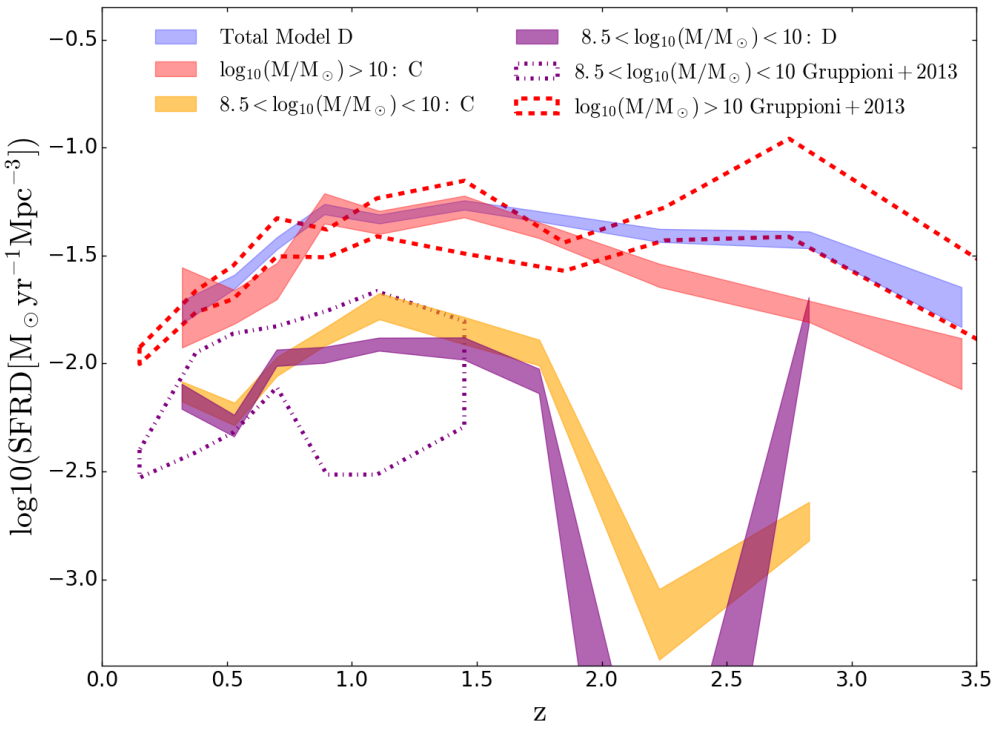

FIGURE 4.9: Contribution from different stellar mass populations to the cosmic SFRD. The blue shading represents 95% confidence region associated with the total cosmic SFRD from Model C fit to each redshift bin (individually). The orange and purple shading is the 95% confidence region from sources with low stellar masses ($10^{8.5} \leq M \leq 10^{10}$ M$_\odot$) from Model C and Model D respectively. The red shading is the 95% confidence region from sources with high stellar masses ($M > 10^{10}$ M$_\odot$). The red dashed and purple dashed-dotted lines are the high ($10^{10} \leq M \leq 10^{12}$ M$_\odot$) and low ($M < 10^{10}$ M$_\odot$) stellar-mass contributions from Gruppioni et al. (2013).

The contribution from low stellar masses decreases from the lowest redshift bin to the second redshift bin and increases with redshift up to $z \sim 1$ (for Model C and $z \sim 1.5$ for Model D), where it peaks and falls towards higher redshifts (owing to the NIR selection). The shape of the low stellar mass sources is similar to the total SFRD below $z \sim 1$. The contribution from high stellar mass dominates the total SFRD at all redshift bins and hence has a shape almost identical to the total (with minor differences).

I compare my results to the cosmic SFRDs from Gruppioni et al. (2013), who divided their sources into three stellar mass (low, mid and high) bins. Their low stellar mass contribution, $M < 10^{10}$ M$_\odot$, shows larger error bars but is fully in agreement with my results. I compare my high stellar mass contribution with the combination of

their mid ($10^{10} \leq M/\mathrm{M}_{\odot} \leq 10^{11}$) and high stellar masses ($10^{11} \leq M/\mathrm{M}_{\odot} \leq 10^{12}$), which are in good agreement below $z \sim 2$. Above $z \sim 2$ the Gruppioni et al. (2013) (high stellar mass) sources result in a higher SFRD, with an increasing contribution from dusty starburst galaxies and SF AGN. This might imply that I am missing these sources in my stellar-mass selection, or it is possible that they are instead contribute to the total RLF through the high-luminosity art which we do not use to determine the SFRD.

4.5 Conclusions

My main goal is to constrain the RLF to low radio luminosities and then obtain a measurement of the cosmic sta SFRD from my stellar mass-limited sample. Using BAYESTACK I probe the stellar-mass selected RLF orders of magnitude below the nominal 5σ detection by fitting parametric models to the RLF for both SFGs (low-luminosity radio source) and AGN (high-luminosity radio sources). The reconstructed RLF follows the $1/V_{\mathrm{max}}$-points very well above the detection limit. I find that my models also follow the Novak et al. (2018) extrapolated pure luminosity evolution fit well, for at least an order of magnitude below the detection threshold, to $z \sim 1.6$.

However, due to my stellar mass limit, the (free mode; Model C) faint-end slope of my SFG RLF, obtained using the Bayesian-stacking technique, falls off towards low radio luminosities, particularly at the higher redshifts ($z > 1.5$). This fall-off is not an underlying feature of the RLF of SFGs but is the result of a lack of fainter radio sources in the parent stellar-mass selected sample. This is due to the known relation between stellar mass and star-formation rates (e.g. Noeske et al., 2007; Daddi et al., 2007; Johnston et al., 2015), where the stellar-mass selected sample imposes a natural limit on the level of star formation in galaxies I am able to probe. As the stellar-mass limit increases with redshift, due to the flux limit of the optical/NIR data, this means I do not have the radio-fainter SFGs in my sample.

I address this by fixing the shape of the RLF to that of the local RLF and allowing it to evolve with redshift. I start by obtaining the RLF in each individual redshift bin, by allowing the knee in both the SFG and AGN RLFs to be a free parameter. Next I use a pure luminosity evolution fit (with two luminosity evolution terms)

to fit the RLF with a prescribed functional form over all the redshift bins. I find that the best fit PLE model gives $L_{\rm AGN} \propto (1+z)^{1.82\pm0.2-(0.47\pm0.10)z}$ and $L_{\rm SFG} \propto (1+z)^{4.04\pm0.04-(0.85\pm0.02)z}$. The evolution strength is similar to that of Novak et al. (2017) up to $z \sim 1.6$. However, beyond $z \sim 2$, the Novak et al. (2017) RLF continues to evolve, whereas I find that my RLF does not evolve as strongly beyond $z > 2.5$. The lack of strong evolution coincides with the decrease of low stellar-mass sources in my stellar mass-limited sample at these redshifts. This results in the position of the knee in the RLF moving to lower luminosities for the SFG population, at $z > 2.5$.

I use my RLF models to determine the radio-derived SFRD by numerically integrating the product of the 1.4 GHz RLF of SFGs and the SFR associated with the 1.4 GHz luminosity based on the IRRC. I found my SFRD to be consistent with the established behaviour at low redshift, where it increases strongly with redshift out to $z \sim 1$ (e.g Gruppioni et al., 2013; Madau and Dickinson, 2014; Koprowski et al., 2017; Novak et al., 2017). Beyond $z \sim 1$ the SFRD determined from radio observations depends strongly on the assumed conversion from radio luminosity to SFR. Assuming an evolving IRRC results in the SFRD decreasing at high redshift. Whereas, if I assume that the IRRC is constant with redshift then the SFRD remains relatively flat out to the limit the sample at $z \sim 3.5$. Clearly, if we are to use radio emission as a tracer of star-formation rate across cosmic time, the relationship between the radio luminosity and the SFRs needs to be better understood and expanded to include other factors, such as inverse Compton scattering of CMB photons (e.g. Murphy, 2009), stellar-mass dependence (e.g. Gürkan et al., 2018b) and morphology (e.g. Molnár et al., 2018).

I also investigate the effects of stellar mass on the total RLF by splitting my sample into low ($10^{8.5} \leq M/\mathrm{M}_{\odot} \leq 10^{10}$) and high ($M > 10^{10}$ $\mathrm{M}_{\odot}$) stellar mass. I find that the low stellar mass sources dominate the faint end of the RLF and the high stellar mass sources are usually associated with the radio-detected sources, as expected given the relationship between stellar mass and SFR. I find that the SFRD is dominated by sources with high stellar masses ($> 10^{10}$ $\mathrm{M}_{\odot}$) at all redshifts, and that the missing low stellar mass sources in the NIR flux limit will not be enough to make up for the decline of my SFRD compared to the findings of Madau and Dickinson (2014) and Novak et al. (2017) using the evolving IRRC relation.

4.6 Appendix

Fig 4.10 shows the 1-D and 2-D posterior distributions for the PLE Model C to the data at all the redshift bins. The 1-D posterior distribution is the marginalization of each parameter shown at the end of each row. The parameters have well-defined peaks, and parameters $L_{\rm min1}$ and $L_{\rm max}$ have two peaks.

Fig 4.11 show the 1-D and 2-D posterior distributions for Model C applied to all the redshift bins. The boundary parameters are mostly do not have a well defined peak and also hit the prior range. This does not affect the fit as long as the prior space is large enough. L_1^* (the AGN break) also hit the prior edge however, this prior is motivated by literature data.

Fig 4.16 show the posterior distribution for Model D applied to all the redshift bins individually. Table 4.5 show the MAP parameters obtained from the various models applied to the each individual redshift bin.

Table 4.6 are the MAP parameters for the various models applied to the low and high stellar mass galaxies in each redshift bin.

TABLE 4.5: The MAP posterior parameters of Models B, C and D for the NIR-selected RLF, in each of the redshift bins and their σ. The units of the parameters are as shown in Table 4.2.

Parameter	$0.1 < z < 0.4$	$0.4 < z < 0.6$	$0.6 < z < 0.8$	$0.8 < z < 1.0$	$1.0 < z < 1.3$	$1.3 < z < 1.6$	$1.6 < z < 2.0$	$2.0 < z < 2.5$	$2.5 < z < 3.2$	$3.2 < z < 4.0$
					Model B					
$\log_{10}[L_{\min_1}]$	$17.42^{+0.75}_{-0.31}$	$19.44^{+0.49}_{-1.86}$	$20.21^{+0.22}_{-0.48}$	$19.80^{+0.85}_{-1.37}$	$20.99^{+0.26}_{-1.66}$	$19.12^{+0.41}_{-0.43}$	$21.72^{+0.07}_{-0.12}$	$22.13^{+0.14}_{-0.28}$	$20.44^{+0.90}_{-0.74}$	$22.18^{+0.16}_{-0.31}$
$\log_{10}[L_{\max_1}]$	$24.65^{+0.09}_{-0.10}$	$25.68^{+0.54}_{-0.57}$	$25.40^{+0.13}_{-0.13}$	$26.50^{+0.32}_{-0.32}$	$26.20^{+0.13}_{-0.13}$	$26.52^{+0.33}_{-0.34}$	$26.50^{+0.33}_{-0.34}$	$26.98^{+0.67}_{-0.64}$	$26.74^{+0.48}_{-0.48}$	$26.74^{+0.50}_{-0.50}$
$\log_{10}[L_{\min_2}]$	$19.70^{+0.95}_{-0.99}$	$19.69^{+0.88}_{-1.02}$	$20.88^{+0.46}_{-0.44}$	$20.41^{+0.38}_{-0.39}$	$22.54^{+0.16}_{-0.16}$	$22.54^{+0.17}_{-0.16}$	$21.57^{+0.82}_{-0.85}$	$21.66^{+0.89}_{-0.90}$	$22.63^{+0.23}_{-0.21}$	$22.64^{+0.23}_{-0.22}$
$\log_{10}[L_{\max_6}]$	$25.00^{+0.15}_{-0.11}$	$26.27^{+0.19}_{-0.51}$	$25.20^{+0.40}_{-0.14}$	$27.20^{+0.22}_{-0.39}$	$26.22^{+0.19}_{-0.18}$	$26.86^{+0.10}_{-0.21}$	$26.50^{+0.35}_{-0.33}$	$26.27^{+0.73}_{-0.16}$	$26.16^{+0.33}_{-0.11}$	$26.83^{+0.46}_{-0.51}$
$\log_{10}[\Phi_1^*]$	$-4.74^{+0.24}_{-0.28}$	$-4.88^{+0.45}_{-0.50}$	$-4.08^{+0.26}_{-0.33}$	$-4.51^{+0.18}_{-0.30}$	$-5.02^{+0.18}_{-0.25}$	$-5.82^{+0.36}_{-0.48}$	$-5.02^{+0.17}_{-0.22}$	$-5.87^{+0.40}_{-0.53}$	$-6.09^{+0.41}_{-0.69}$	$-6.58^{+0.42}_{-0.58}$
$\log_{10}[L_1^*]$	$24.54^{+0.31}_{-0.30}$	$24.95^{+0.71}_{-0.76}$	$23.56^{+0.75}_{-0.29}$	$24.48^{+0.33}_{-0.25}$	$25.03^{+0.63}_{-0.27}$	$25.94^{+0.54}_{-0.60}$	$25.42^{+0.14}_{-0.17}$	$24.97^{+0.94}_{-0.63}$	$24.82^{+0.95}_{-1.26}$	$25.61^{+0.77}_{-0.68}$
α_1	$1.48^{+1.27}_{-1.00}$	$2.04^{+2.07}_{-1.22}$	$0.92^{+0.61}_{-0.23}$	$1.32^{+0.92}_{-0.44}$	$0.99^{+0.97}_{-0.48}$	$0.35^{+0.91}_{-0.83}$	$3.02^{+1.64}_{-1.45}$	$0.60^{+0.93}_{-0.57}$	$0.39^{+1.59}_{-0.63}$	$1.15^{+0.44}_{-0.35}$
β_1	$-0.26^{+0.40}_{-0.43}$	$0.23^{+0.28}_{-0.82}$	$-1.78^{+1.47}_{-1.96}$	$-2.06^{+1.34}_{-1.79}$	$-1.73^{+1.63}_{-2.10}$	$-1.86^{+1.24}_{-1.36}$	$-2.59^{+1.60}_{-1.61}$	$-1.49^{+1.54}_{-2.26}$	$-2.13^{+1.54}_{-1.80}$	$-0.04^{+0.44}_{-0.44}$
$\log_{10}[\Phi_2^*]$	$-1.97^{+0.05}_{-0.06}$	$-2.51^{+0.23}_{-0.27}$	$-2.45^{+0.24}_{-0.22}$	$-2.10^{+0.08}_{-0.28}$	$-2.43^{+0.20}_{-0.35}$	$-2.44^{+0.04}_{-0.03}$	$-3.41^{+0.21}_{-0.17}$	$-3.74^{+0.32}_{-0.34}$	$-3.58^{+0.07}_{-0.12}$	$-4.62^{+0.44}_{-0.33}$
$\log_{10}[L_2^*]$	$21.71^{+0.08}_{-0.08}$	$22.54^{+0.19}_{-0.20}$	$22.68^{+0.16}_{-0.24}$	$22.49^{+0.28}_{-0.12}$	$22.80^{+0.32}_{-0.21}$	$22.89^{+0.06}_{-0.06}$	$23.80^{+0.13}_{-0.16}$	$23.97^{+0.22}_{-0.25}$	$23.86^{+0.10}_{-0.09}$	$24.30^{+0.17}_{-0.31}$
α_2	$1.38^{+0.09}_{-0.08}$	$2.37^{+1.10}_{-0.47}$	$2.15^{+0.63}_{-0.43}$	$1.59^{+0.20}_{-0.12}$	$1.62^{+0.24}_{-0.12}$	$1.52^{+0.07}_{-0.07}$	$2.23^{+0.30}_{-0.24}$	$2.52^{+1.17}_{-0.51}$	$2.16^{+0.27}_{-0.23}$	$3.35^{+1.05}_{-1.16}$
β_2	$-0.04^{+0.07}_{-0.03}$	$0.17^{+0.20}_{-0.24}$	$0.24^{+0.17}_{-0.23}$	$-0.17^{+0.40}_{-0.13}$	$0.07^{+0.35}_{-0.46}$	$-0.44^{+0.05}_{-0.06}$	$0.47^{+0.11}_{-0.16}$	$0.37^{+0.26}_{-0.37}$	$-0.10^{+0.19}_{-0.07}$	$0.61^{+0.23}_{-0.37}$
					Model C					
$\log_{10}[L_{\min_1}]$	$18.47^{+0.33}_{-0.26}$	$17.68^{+1.16}_{-0.51}$	$19.61^{+0.33}_{-1.10}$	$18.68^{+1.03}_{-0.53}$	$19.46^{+0.76}_{-0.35}$	$19.43^{+1.24}_{-0.29}$	$19.65^{+0.74}_{-0.50}$	$20.14^{+0.88}_{-0.73}$	$18.88^{+1.16}_{-0.58}$	$17.43^{+2.34}_{-1.55}$
$\log_{10}[L_{\max_1}]$	$24.65^{+0.10}_{-0.10}$	$24.72^{+0.85}_{-0.86}$	$25.40^{+0.13}_{-0.13}$	$26.49^{+0.33}_{-0.32}$	$26.73^{+0.49}_{-0.45}$	$26.51^{+0.32}_{-0.32}$	$26.50^{+0.29}_{-0.31}$	$26.97^{+0.66}_{-0.62}$	$26.76^{+0.47}_{-0.48}$	$26.71^{+0.49}_{-0.47}$
$\log_{10}[L_{\min_2}]$	$19.09^{+0.60}_{-0.65}$	$19.02^{+0.64}_{-0.68}$	$19.50^{+0.74}_{-0.86}$	$20.07^{+0.77}_{-0.83}$	$20.89^{+0.71}_{-0.93}$	$20.88^{+0.62}_{-0.88}$	$20.54^{+0.78}_{-0.80}$	$20.70^{+0.85}_{-0.88}$	$20.38^{+0.80}_{-0.77}$	$22.92^{+0.36}_{-0.39}$
$\log_{10}[L_{\max_6}]$	$24.94^{+0.18}_{-0.11}$	$25.54^{+0.16}_{-0.29}$	$26.04^{+0.27}_{-0.03}$	$26.72^{+0.18}_{-0.29}$	$27.60^{+0.29}_{-0.18}$	$26.85^{+0.08}_{-0.14}$	$27.16^{+0.25}_{-0.16}$	$26.37^{+1.22}_{-0.24}$	$27.29^{+0.13}_{-0.15}$	$26.99^{+0.37}_{-0.49}$
$\log_{10}[\Phi_1^*]$	$-4.12^{+0.27}_{-0.35}$	$-4.39^{+0.22}_{-0.33}$	$-4.39^{+0.16}_{-0.26}$	$-4.47^{+0.15}_{-0.20}$	$-4.68^{+0.26}_{-0.76}$	$-5.53^{+0.28}_{-0.35}$	$-5.57^{+0.32}_{-0.30}$	$-5.93^{+0.27}_{-0.34}$	$-5.99^{+0.35}_{-0.42}$	$-6.73^{+0.70}_{-1.07}$
$\log_{10}[L_1^*]$	$23.49^{+0.69}_{-0.36}$	$23.62^{+1.08}_{-0.38}$	$24.30^{+0.31}_{-0.21}$	$24.60^{+0.26}_{-0.14}$	$24.49^{+1.47}_{-0.58}$	$25.71^{+0.62}_{-0.48}$	$25.65^{+0.73}_{-0.61}$	$25.00^{+0.63}_{-0.55}$	$24.96^{+0.75}_{-0.87}$	$25.53^{+0.87}_{-0.89}$
α_1	$0.97^{+0.41}_{-0.32}$	$0.73^{+1.08}_{-0.31}$	$1.45^{+0.33}_{-0.33}$	$1.47^{+0.29}_{-0.30}$	$0.81^{+0.62}_{-0.24}$	$0.92^{+0.49}_{-0.37}$	$0.81^{+0.54}_{-0.41}$	$0.43^{+0.50}_{-0.39}$	$0.54^{+0.52}_{-0.37}$	$0.68^{+0.79}_{-0.78}$
β_1	$-0.17^{+0.41}_{-1.13}$	$-1.37^{+1.39}_{-2.35}$	$0.03^{+0.29}_{-0.50}$	$-0.53^{+0.57}_{-0.94}$	$-0.06^{+0.45}_{-1.48}$	$0.20^{+0.20}_{-0.38}$	$-0.75^{+0.64}_{-0.70}$	$-1.97^{+1.50}_{-1.89}$	$-1.91^{+1.56}_{-1.93}$	$-1.36^{+1.10}_{-1.03}$
$\log_{10}[\Phi_2^*]$	$-2.00^{+0.04}_{-0.06}$	$-2.24^{+0.03}_{-0.04}$	$-2.23^{+0.03}_{-0.04}$	$-2.36^{+0.13}_{-0.23}$	$-2.61^{+0.10}_{-0.11}$	$-3.39^{+0.36}_{-0.36}$	$-3.19^{+0.19}_{-0.35}$	$-3.78^{+0.28}_{-1.02}$	$-3.52^{+0.02}_{-0.02}$	$-4.69^{+0.74}_{-0.61}$
$\log_{10}[L_2^*]$	$21.11^{+0.20}_{-0.18}$	$21.73^{+0.16}_{-0.16}$	$21.65^{+0.24}_{-0.30}$	$20.93^{+0.37}_{-0.35}$	$21.33^{+0.19}_{-0.17}$	$21.11^{+0.31}_{-0.25}$	$21.65^{+0.35}_{-0.37}$	$22.10^{+0.39}_{-0.69}$	$22.92^{+0.21}_{-0.28}$	$21.55^{+0.76}_{-0.36}$
α_2	$1.08^{+0.09}_{-0.06}$	$0.89^{+0.10}_{-0.04}$	$0.88^{+0.14}_{-0.16}$	$0.31^{+0.21}_{-0.25}$	$0.22^{+0.15}_{-0.14}$	$-0.32^{+0.34}_{-0.26}$	$0.12^{+0.25}_{-0.32}$	$-0.12^{+0.35}_{-0.83}$	$0.66^{+0.07}_{-0.10}$	$-0.46^{+0.73}_{-0.42}$
σ_{LF}	$0.66^{+0.06}_{-0.06}$	$0.51^{+0.05}_{-0.05}$	$0.56^{+0.07}_{-0.06}$	$0.67^{+0.02}_{-0.04}$	$0.62^{+0.02}_{-0.02}$	$0.63^{+0.01}_{-0.02}$	$0.64^{+0.02}_{-0.03}$	$0.56^{+0.02}_{-0.03}$	$0.53^{+0.06}_{-0.05}$	$0.61^{+0.03}_{-0.03}$
					Model D					
$\log_{10}[L_{\min}]$	$18.62^{+0.05}_{-0.06}$	$19.70^{+0.02}_{-0.02}$	$20.01^{+0.02}_{-0.02}$	$20.37^{+0.02}_{-0.02}$	$21.18^{+0.01}_{-0.01}$	$21.81^{+0.01}_{-0.01}$	$22.17^{+0.01}_{-0.01}$	$22.74^{+0.02}_{-0.02}$	$22.72^{+0.02}_{-0.02}$	$22.76^{+0.04}_{-0.05}$
$\log_{10}[L_{\max}]$	$25.70^{+0.13}_{-0.12}$	$26.07^{+0.55}_{-0.38}$	$26.73^{+0.19}_{-0.29}$	$26.33^{+0.40}_{-0.41}$	$26.53^{+0.31}_{-0.31}$	$26.63^{+0.24}_{-0.25}$	$26.47^{+0.37}_{-0.37}$	$27.28^{+0.15}_{-0.17}$	$26.92^{+0.06}_{-0.07}$	$26.81^{+0.13}_{-0.17}$
α_{SF}	$3.03^{+0.19}_{-0.20}$	$2.91^{+0.08}_{-0.08}$	$3.20^{+0.06}_{-0.06}$	$3.34^{+0.04}_{-0.04}$	$2.83^{+0.03}_{-0.03}$	$2.64^{+0.03}_{-0.03}$	$2.31^{+0.03}_{-0.03}$	$1.93^{+0.03}_{-0.03}$	$1.75^{+0.03}_{-0.04}$	$1.20^{+0.06}_{-0.08}$
α_{AGN}	$4.29^{+1.21}_{-1.41}$	$0.35^{+0.77}_{-0.77}$	$1.64^{+0.50}_{-0.47}$	$1.56^{+0.36}_{-0.40}$	$1.34^{+0.24}_{-0.25}$	$0.96^{+0.21}_{-0.26}$	$1.12^{+0.17}_{-0.17}$	$0.47^{+0.16}_{-0.16}$	$0.49^{+0.12}_{-0.13}$	$-0.36^{+0.17}_{-0.20}$

TABLE 4.6: The MAP posterior parameters of the low (using Model C and Model D) and high (using Model C) stellar mass contribution to NIR-selected RLF, in each of the redshift bins and their σ. The Model C and Model D units of the parameters are as shown in Table 4.2.

Parameter	$0.1\|z\|0.4$	$0.4 < z < 0.6$	$0.6 < z < 0.8$	$0.8 < z < 1.0$	$1.0 < z < 1.3$	$1.3 < z < 1.6$	$1.6 < z < 2.0$	$2.0 < z < 2.5$	$2.5 < z < 3.2$	$3.2 < z < 4.0$
					High stellar mass Model C fit					
$\log_{10}[L_{\min_1}]$	$17.88^{+1.01}_{-0.71}$	$17.64^{+1.17}_{-0.41}$	$19.10^{+0.72}_{-0.72}$	$18.80^{+0.70}_{-0.50}$	$19.11^{+0.97}_{-0.96}$	$19.03^{+0.40}_{-0.86}$	$18.70^{+2.84}_{-0.51}$	$22.17^{+0.15}_{-0.22}$	$20.78^{+0.82}_{-0.93}$	$22.18^{+0.16}_{-0.31}$
$\log_{10}[L_{\max_1}]$	$24.66^{+0.10}_{-0.10}$	$25.63^{+0.54}_{-0.53}$	$25.40^{+0.13}_{-0.13}$	$26.50^{+0.31}_{-0.33}$	$26.19^{+0.13}_{-0.13}$	$26.53^{+0.31}_{-0.35}$	$26.50^{+0.33}_{-0.32}$	$26.99^{+0.67}_{-0.63}$	$26.75^{+0.47}_{-0.47}$	$26.74^{+0.50}_{-0.50}$
$\log_{10}[L_{\min_2}]$	$19.68^{+1.01}_{-1.05}$	$19.75^{+0.84}_{-1.00}$	$20.95^{+0.41}_{-0.48}$	$20.40^{+0.38}_{-0.39}$	$22.54^{+0.16}_{-0.16}$	$22.55^{+0.17}_{-0.17}$	$21.58^{+0.77}_{-0.82}$	$21.66^{+0.86}_{-0.90}$	$22.64^{+0.23}_{-0.22}$	$22.64^{+0.23}_{-0.22}$
$\log_{10}[L_{\max_6}]$	$25.03^{+0.29}_{-0.15}$	$26.29^{+0.17}_{-0.41}$	$25.46^{+0.46}_{-0.32}$	$27.18^{+0.23}_{-0.50}$	$26.23^{+0.16}_{-0.18}$	$26.84^{+0.11}_{-0.29}$	$26.70^{+0.10}_{-0.32}$	$26.26^{+0.61}_{-0.15}$	$26.17^{+0.33}_{-0.12}$	$26.83^{+0.46}_{-0.51}$
$\log_{10}[\Phi_1^*]$	$-4.82^{+0.25}_{-0.32}$	$-4.71^{+0.35}_{-0.44}$	$-4.02^{+0.22}_{-0.27}$	$-4.53^{+0.23}_{-0.28}$	$-5.03^{+0.19}_{-0.25}$	$-6.20^{+0.50}_{-0.66}$	$-5.25^{+0.33}_{-0.63}$	$-5.83^{+0.39}_{-0.49}$	$-6.19^{+0.36}_{-0.67}$	$-6.58^{+0.42}_{-0.58}$
$\log_{10}[L_1^*]$	$24.58^{+0.35}_{-0.33}$	$24.77^{+0.71}_{-0.82}$	$23.50^{+0.55}_{-0.31}$	$24.63^{+0.34}_{-0.34}$	$25.05^{+0.63}_{-0.30}$	$25.94^{+0.56}_{-0.60}$	$25.50^{+0.57}_{-0.26}$	$24.87^{+0.98}_{-0.57}$	$25.11^{+0.75}_{-1.21}$	$25.61^{+0.77}_{-0.68}$
α_1	$1.39^{+1.48}_{-1.10}$	$1.69^{+2.16}_{-1.03}$	$0.95^{+0.44}_{-0.20}$	$1.89^{+1.58}_{-0.84}$	$0.98^{+0.98}_{-0.48}$	$0.49^{+0.91}_{-0.92}$	$2.32^{+2.04}_{-1.89}$	$0.60^{+0.87}_{-0.50}$	$0.37^{+1.66}_{-0.64}$	$1.15^{+0.44}_{-0.35}$
β_1	$-0.42^{+0.42}_{-0.37}$	$0.04^{+0.28}_{-0.86}$	$-1.72^{+1.43}_{-1.99}$	$-1.39^{+1.17}_{-2.01}$	$-1.50^{+1.41}_{-2.25}$	$-1.90^{+1.38}_{-1.41}$	$-2.53^{+1.44}_{-1.50}$	$-1.56^{+1.50}_{-2.15}$	$-2.22^{+1.59}_{-1.72}$	$-0.04^{+0.44}_{-0.44}$
$\log_{10}[\Phi_2^*]$	$-2.65^{+0.04}_{-0.05}$	$-2.61^{+0.03}_{-0.04}$	$-2.69^{+0.05}_{-0.06}$	$-2.41^{+0.03}_{-0.03}$	$-2.65^{+0.03}_{-0.03}$	$-2.77^{+0.03}_{-0.03}$	$-3.05^{+0.03}_{-0.11}$	$-3.70^{+0.18}_{-0.30}$	$-3.74^{+0.07}_{-0.11}$	$-4.62^{+0.44}_{-0.33}$
$\log_{10}[L_2^*]$	$22.03^{+0.11}_{-0.11}$	$22.54^{+0.05}_{-0.05}$	$22.77^{+0.05}_{-0.05}$	$22.65^{+0.06}_{-0.06}$	$22.88^{+0.05}_{-0.05}$	$23.06^{+0.06}_{-0.06}$	$23.42^{+0.11}_{-0.06}$	$23.93^{+0.21}_{-0.15}$	$23.89^{+0.11}_{-0.10}$	$24.30^{+0.17}_{-0.31}$
α_2	$1.22^{+0.15}_{-0.12}$	$2.23^{+0.31}_{-0.25}$	$2.47^{+0.49}_{-0.36}$	$1.58^{+0.12}_{-0.10}$	$1.59^{+0.10}_{-0.08}$	$1.49^{+0.08}_{-0.08}$	$1.80^{+0.16}_{-0.11}$	$2.50^{+0.88}_{-0.41}$	$2.05^{+0.28}_{-0.24}$	$3.35^{+1.05}_{-1.16}$
β_2	$-0.31^{+0.07}_{-0.05}$	$-0.34^{+0.04}_{-0.04}$	$-0.17^{+0.09}_{-0.05}$	$-0.47^{+0.04}_{-0.05}$	$-0.49^{+0.05}_{-0.05}$	$-0.62^{+0.06}_{-0.07}$	$-0.45^{+0.29}_{-0.05}$	$0.17^{+0.30}_{-0.25}$	$-0.23^{+0.18}_{-0.08}$	$0.61^{+0.23}_{-0.37}$
					low stellar mass Model C' fit					
$\log_{10}[L_{\min}]$	$18.20^{+0.68}_{-0.15}$	$18.37^{+1.05}_{-0.91}$	$20.76^{+0.04}_{-0.08}$	$20.76^{+0.14}_{-1.62}$	$21.41^{+0.03}_{-0.03}$	$21.48^{+0.12}_{-1.36}$	$21.78^{+0.05}_{-0.06}$	$20.64^{+0.83}_{-1.06}$	$19.79^{+1.09}_{-1.13}$	-
$\log_{10}[L_{\max}]$	$25.22^{+0.08}_{-0.12}$	$25.38^{+0.26}_{-0.24}$	$26.26^{+0.16}_{-0.17}$	$26.53^{+0.29}_{-0.32}$	$27.03^{+0.64}_{-0.67}$	$26.74^{+0.17}_{-0.15}$	$26.76^{+0.48}_{-0.53}$	$26.92^{+0.65}_{-0.59}$	$27.26^{+0.15}_{-0.17}$	-
$\log_{10}[\Phi_1^*]$	$-2.05^{+0.02}_{-0.04}$	$-2.27^{+0.08}_{-0.68}$	$-3.41^{+0.69}_{-0.40}$	$-2.39^{+0.35}_{-0.72}$	$-4.41^{+0.67}_{-0.46}$	$-3.13^{+0.47}_{-0.41}$	$-4.50^{+0.71}_{-0.36}$	$-4.83^{+0.22}_{-0.58}$	$-4.46^{+0.26}_{-0.63}$	-
$\log_{10}[L_1^*]$	$20.54^{+0.25}_{-0.33}$	$20.35^{+0.61}_{-0.97}$	$22.54^{+0.28}_{-0.58}$	$21.29^{+0.61}_{-1.14}$	$23.38^{+0.28}_{-0.41}$	$22.07^{+0.73}_{-0.97}$	$23.57^{+0.24}_{-0.50}$	$21.88^{+0.74}_{-0.62}$	$21.57^{+0.58}_{-0.53}$	-
α_1	$0.83^{+0.11}_{-0.13}$	$0.52^{+0.37}_{-0.80}$	$2.14^{+0.09}_{-0.22}$	$1.36^{+0.50}_{-1.88}$	$2.45^{+0.06}_{-0.10}$	$1.53^{+0.53}_{-1.81}$	$2.26^{+0.09}_{-0.18}$	$0.34^{+0.64}_{-0.80}$	$0.10^{+0.46}_{-0.59}$	-
σ_{LF}	$0.67^{+0.05}_{-0.05}$	$0.64^{+0.03}_{-0.06}$	$0.67^{+0.08}_{-0.09}$	$0.62^{+0.08}_{-0.05}$	$0.63^{+0.09}_{-0.10}$	$0.60^{+0.10}_{-0.05}$	$0.64^{+0.09}_{-0.09}$	$0.59^{+0.06}_{-0.07}$	$0.62^{+0.05}_{-0.06}$	-
					Low stellar mass Model D fit					
$\log_{10}[L_{\min}]$	$18.80^{+0.07}_{-0.04}$	$19.40^{+0.02}_{-0.02}$	$19.95^{+0.02}_{-0.02}$	$20.27^{+0.02}_{-0.02}$	$21.05^{+0.01}_{-0.01}$	$21.55^{+0.02}_{-0.02}$	$21.78^{+0.02}_{-0.02}$	$21.61^{+0.11}_{-0.12}$	$22.08^{+0.12}_{-0.76}$	-
$\log_{10}[L_{\max}]$	$26.39^{+0.23}_{-0.75}$	$26.27^{+0.51}_{-0.52}$	$26.24^{+0.51}_{-0.51}$	$26.22^{+0.52}_{-0.49}$	$26.26^{+0.51}_{-0.52}$	$26.25^{+0.53}_{-0.51}$	$26.26^{+0.49}_{-0.53}$	$26.50^{+0.34}_{-0.33}$	$26.51^{+0.33}_{-0.34}$	-
α_{SF}	$0.04^{+0.02}_{-0.02}$	$-0.04^{+0.02}_{-0.02}$	$0.26^{+0.02}_{-0.02}$	$0.30^{+0.02}_{-0.02}$	$0.38^{+0.01}_{-0.01}$	$0.41^{+0.02}_{-0.03}$	$0.31^{+0.02}_{-0.02}$	$-5.69^{+3.17}_{-2.97}$	$-0.09^{+0.14}_{-4.26}$	-
α_{AGN}	$-2.19^{+1.39}_{-5.05}$	$-5.91^{+2.89}_{-2.72}$	$-5.60^{+3.42}_{-3.11}$	$-5.74^{+2.86}_{-2.89}$	$-5.24^{+3.31}_{-3.32}$	$-1.17^{+0.37}_{-5.34}$	$-0.55^{+0.11}_{-0.12}$	$-1.14^{+0.11}_{-0.12}$	$-0.69^{+0.22}_{-0.19}$	-

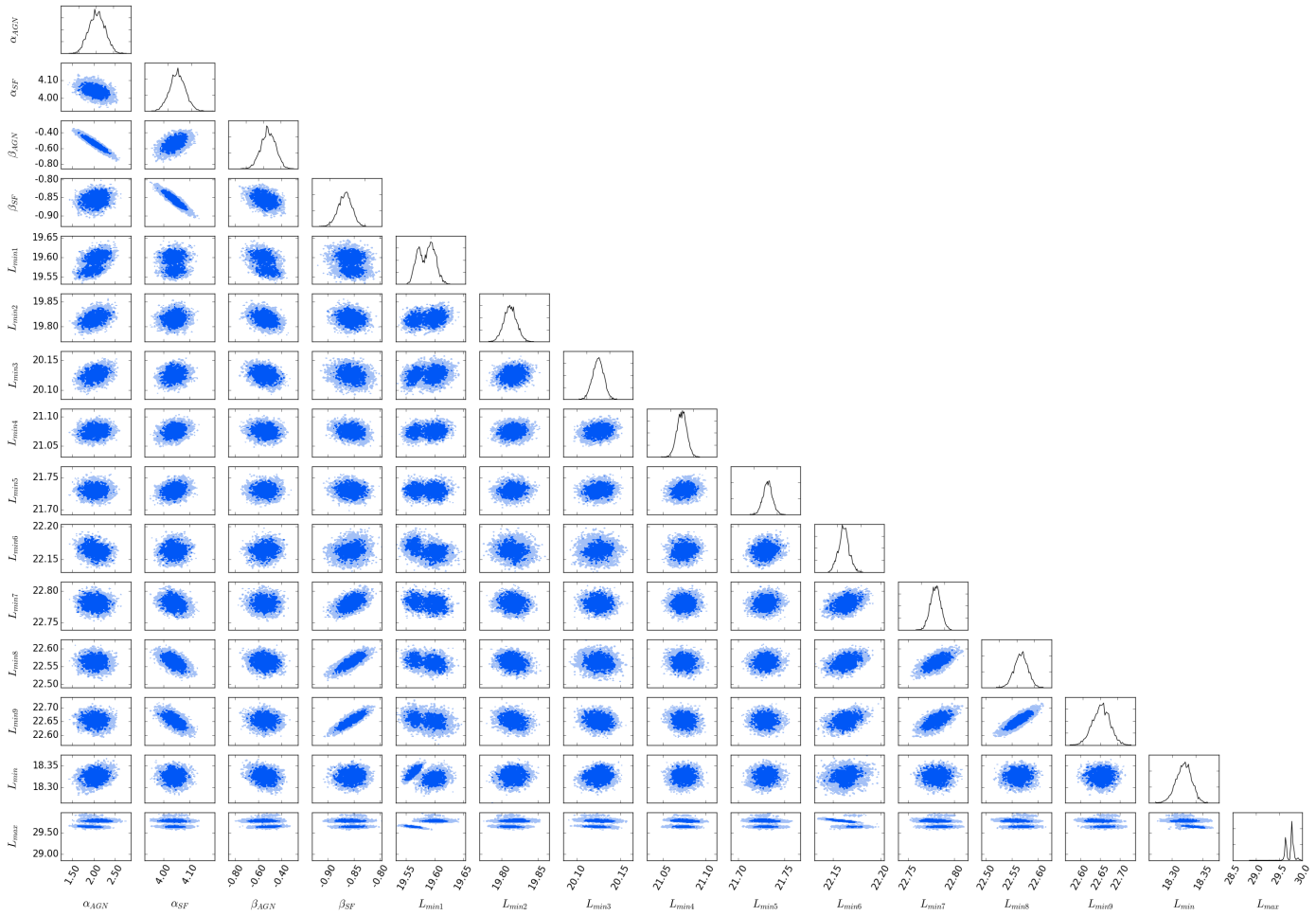

FIGURE 4.10: The triangle plot of Model D pure luminosity evolution to all the redshift bins.

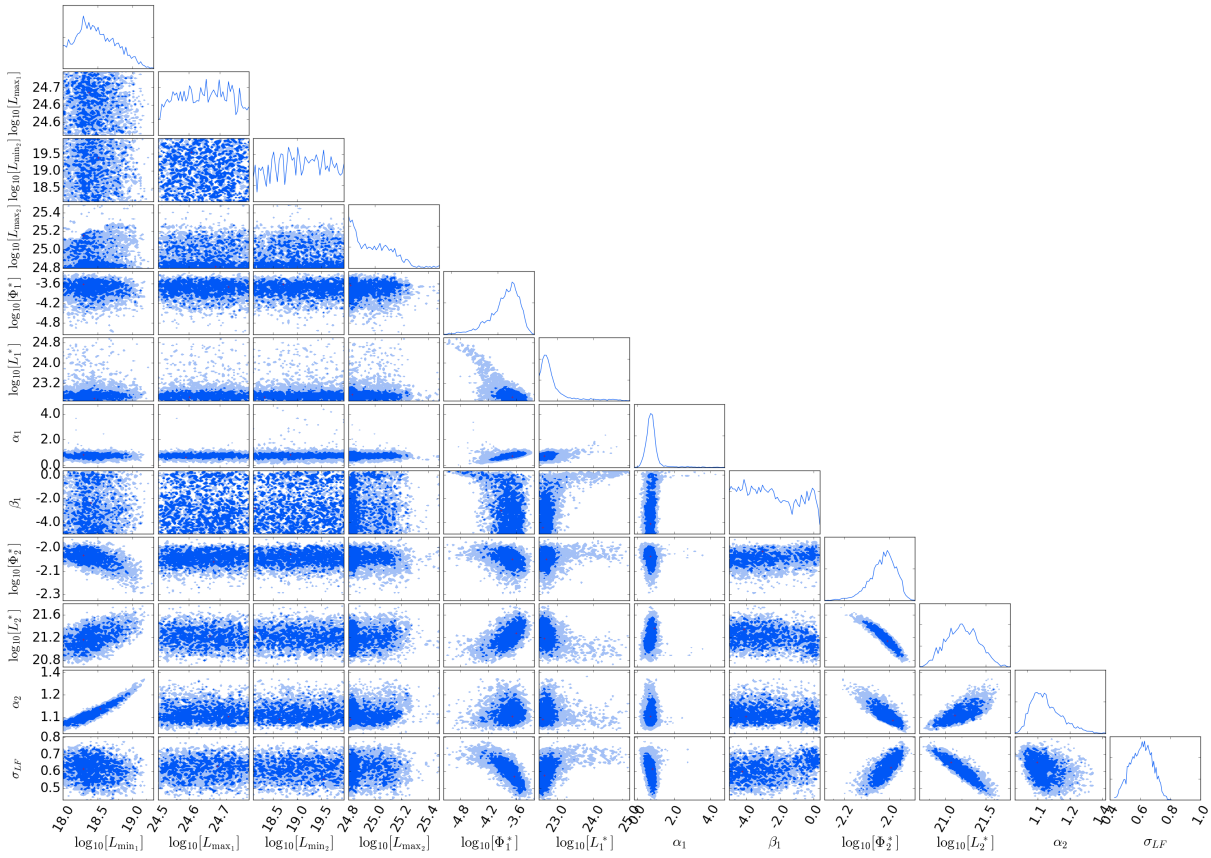

(A) $0.1 < z < 0.4$

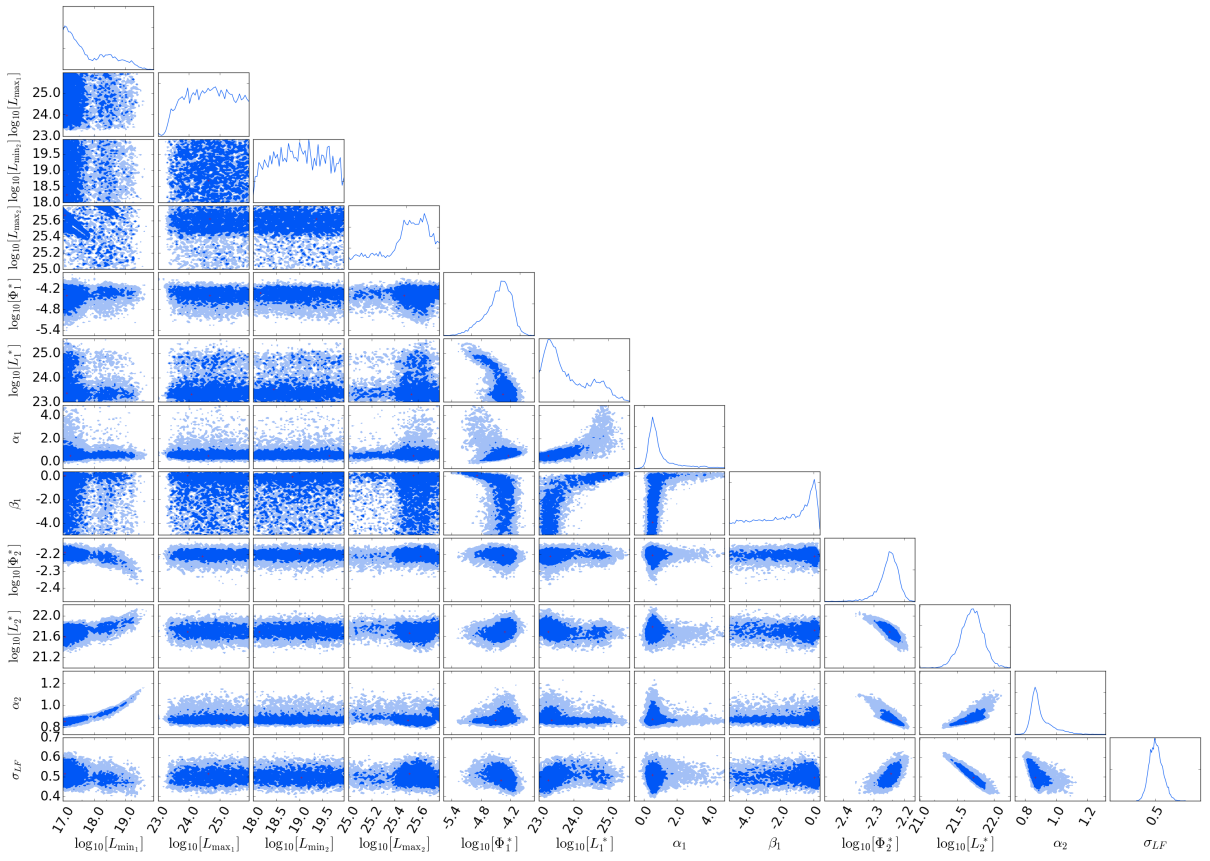

(B) $0.4 < z < 0.6$

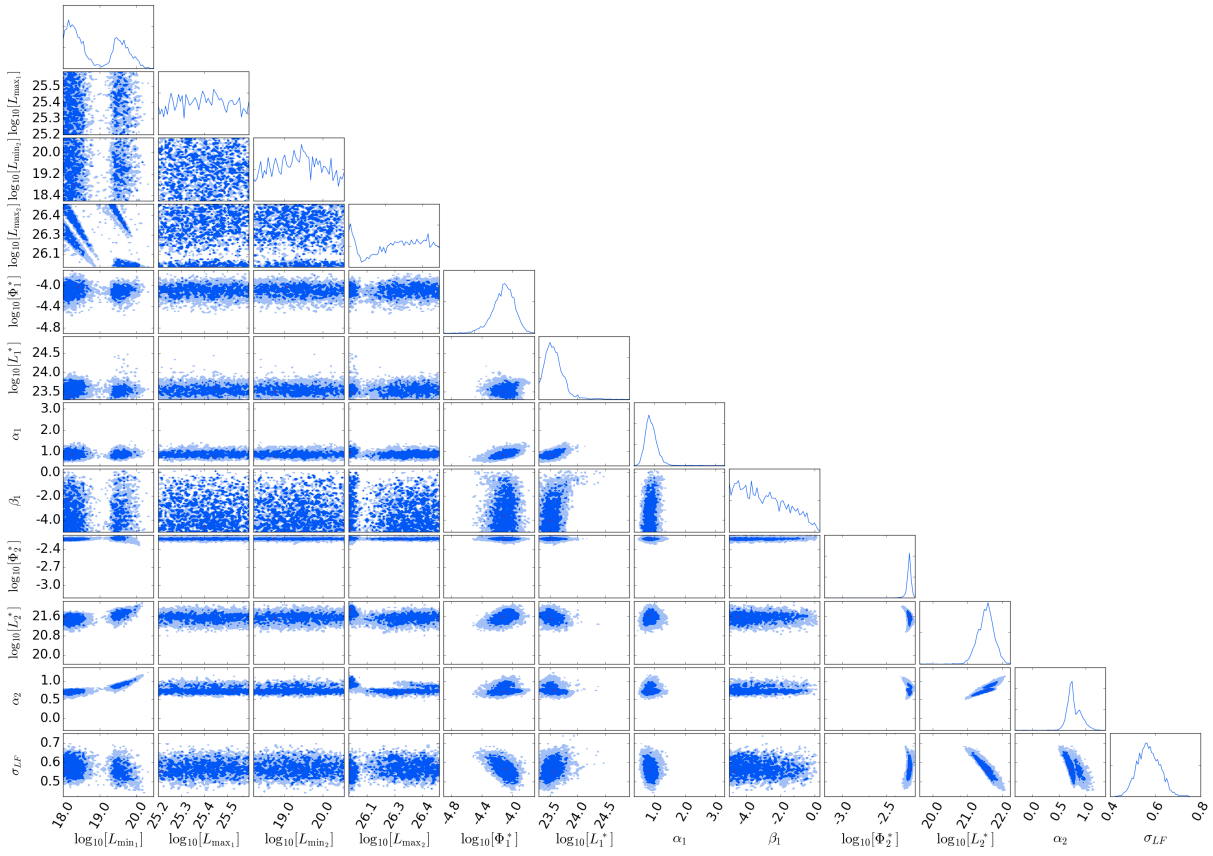

(A) $0.6 < z < 0.8$

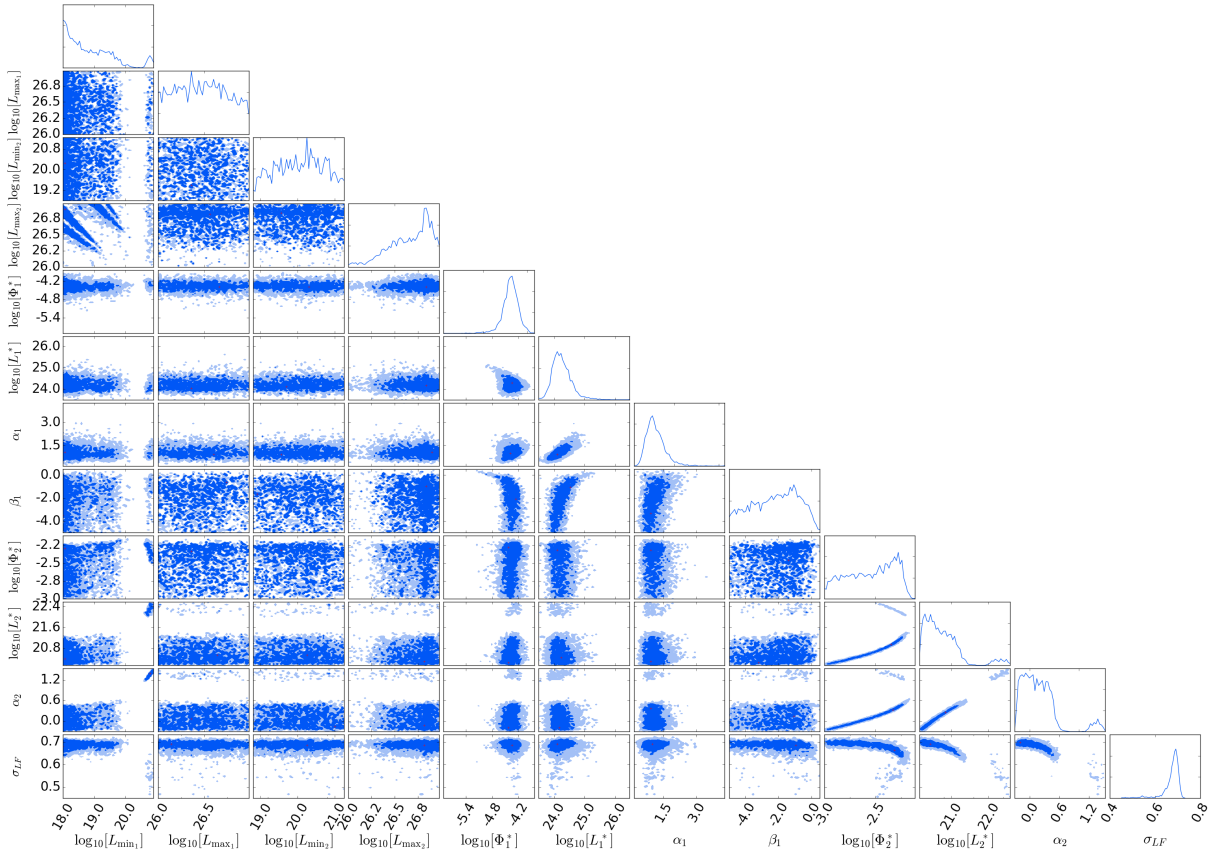

(B) $0.8 < z < 1.0$

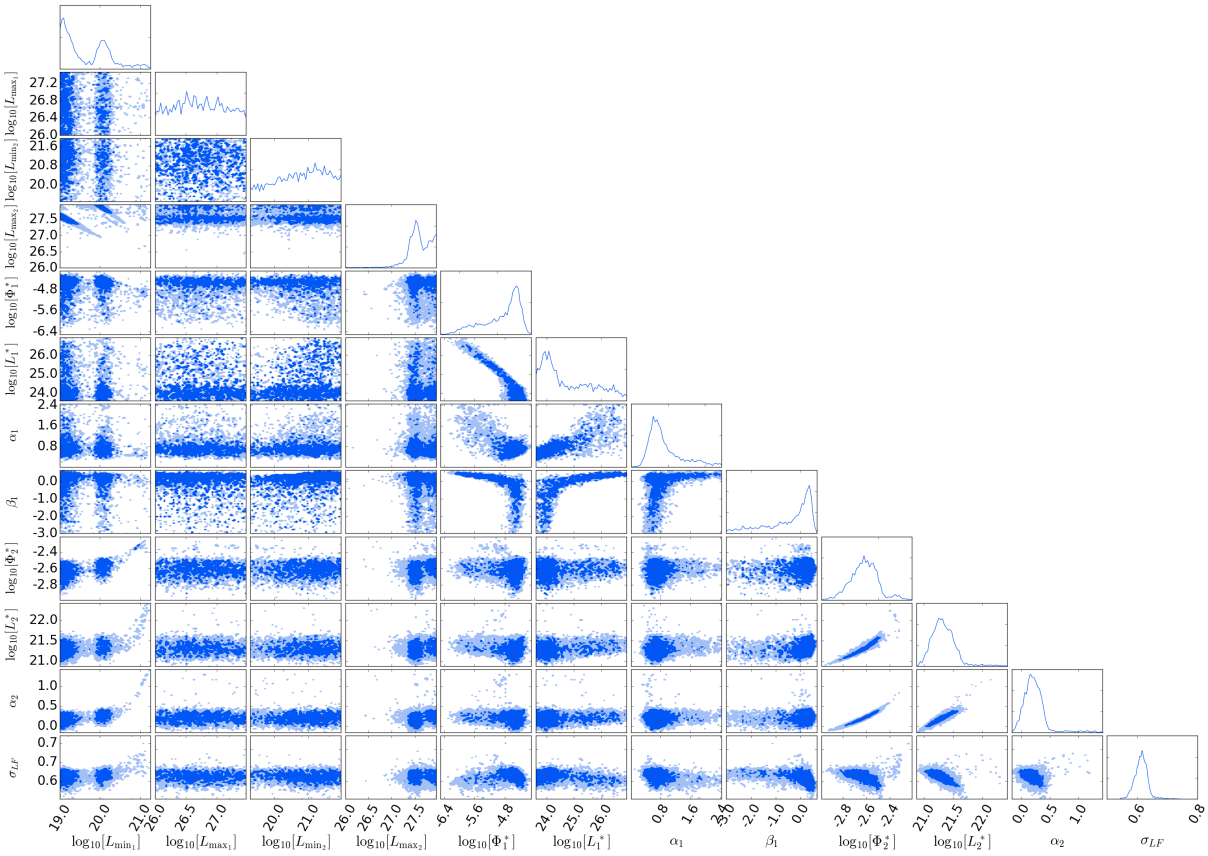

(A) $1.0 < z < 1.3$

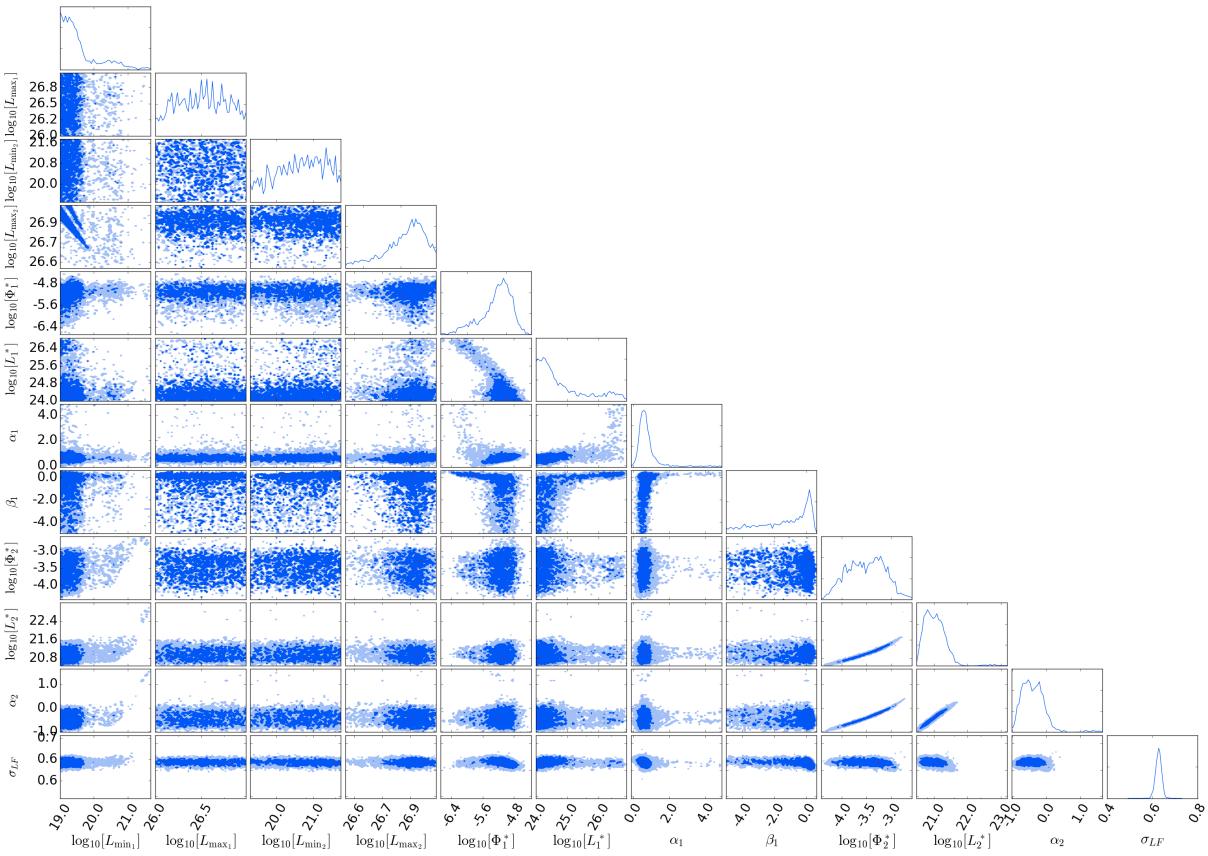

(B) $1.3 < z < 1.6$

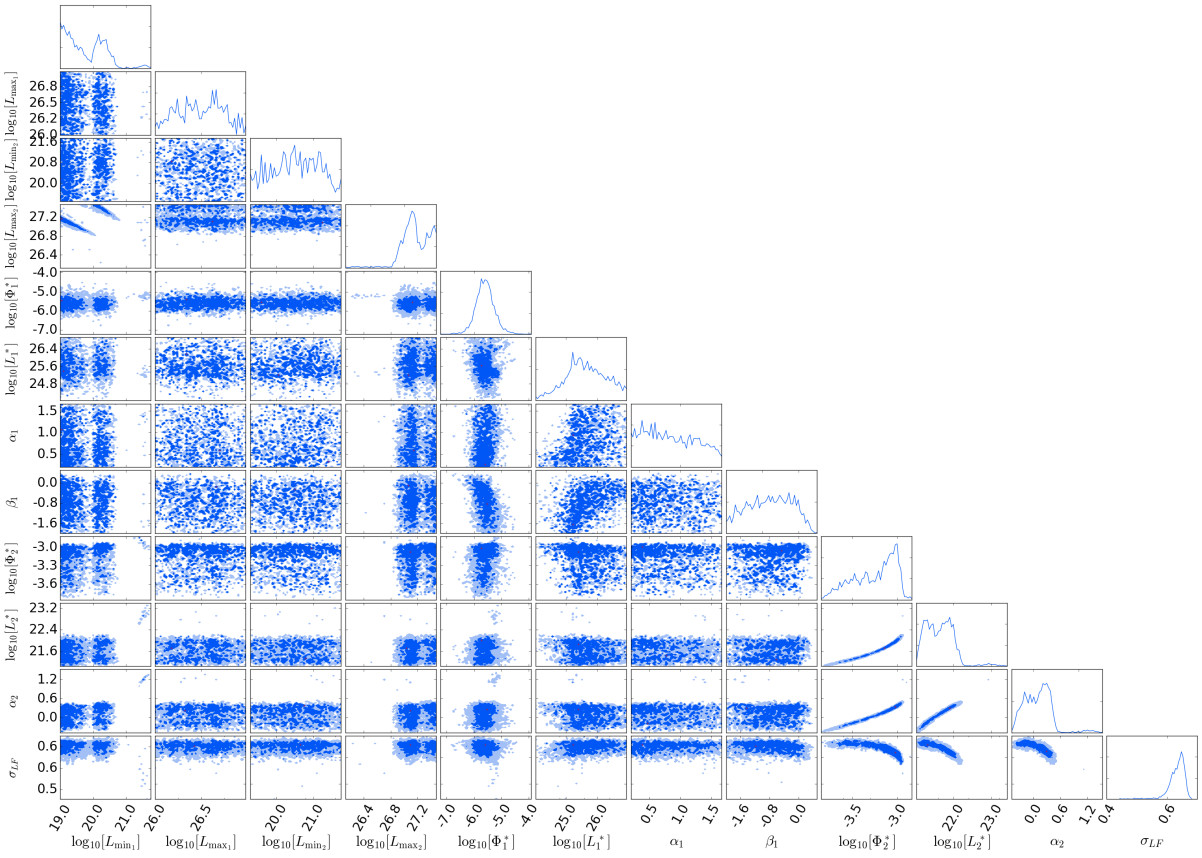

(A) $1.6 < z < 2.0$

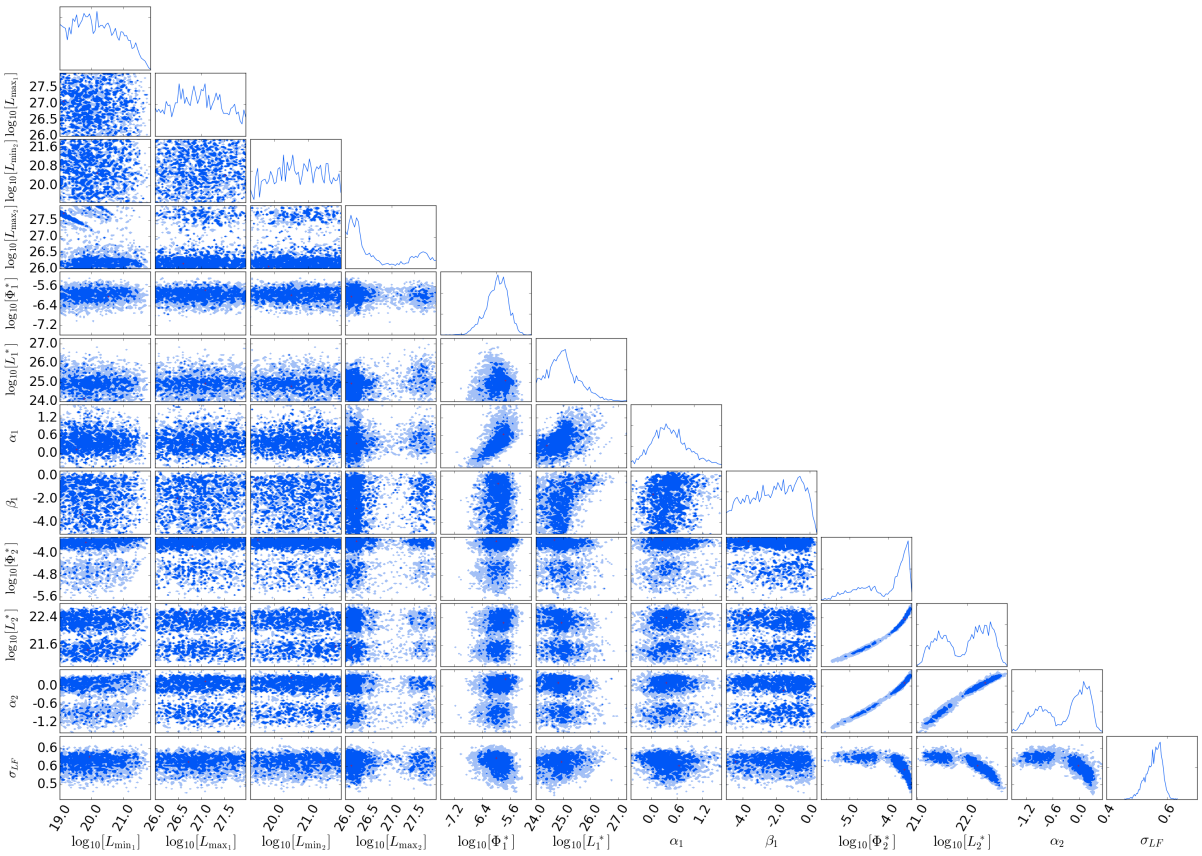

(B) $2.0 < z < 2.$

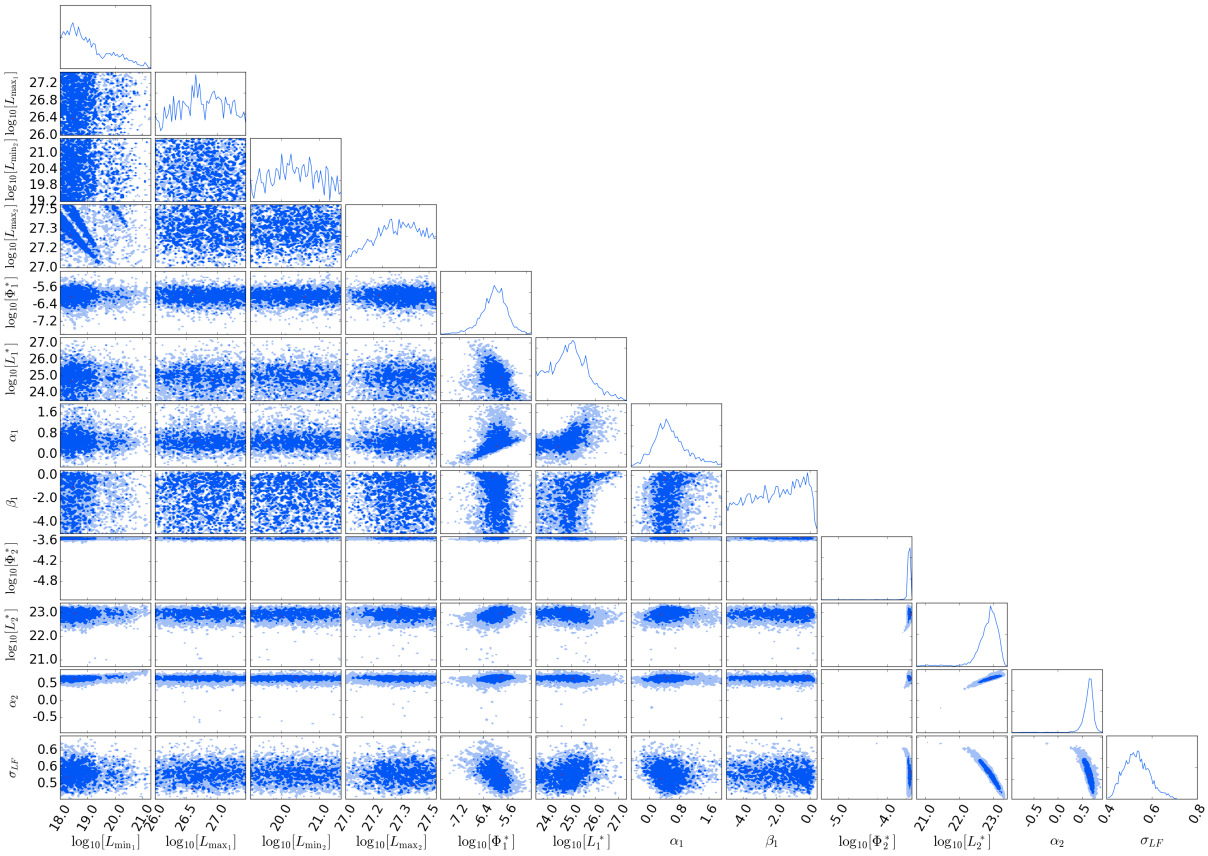

(A) $2.5 < z < 3.2$

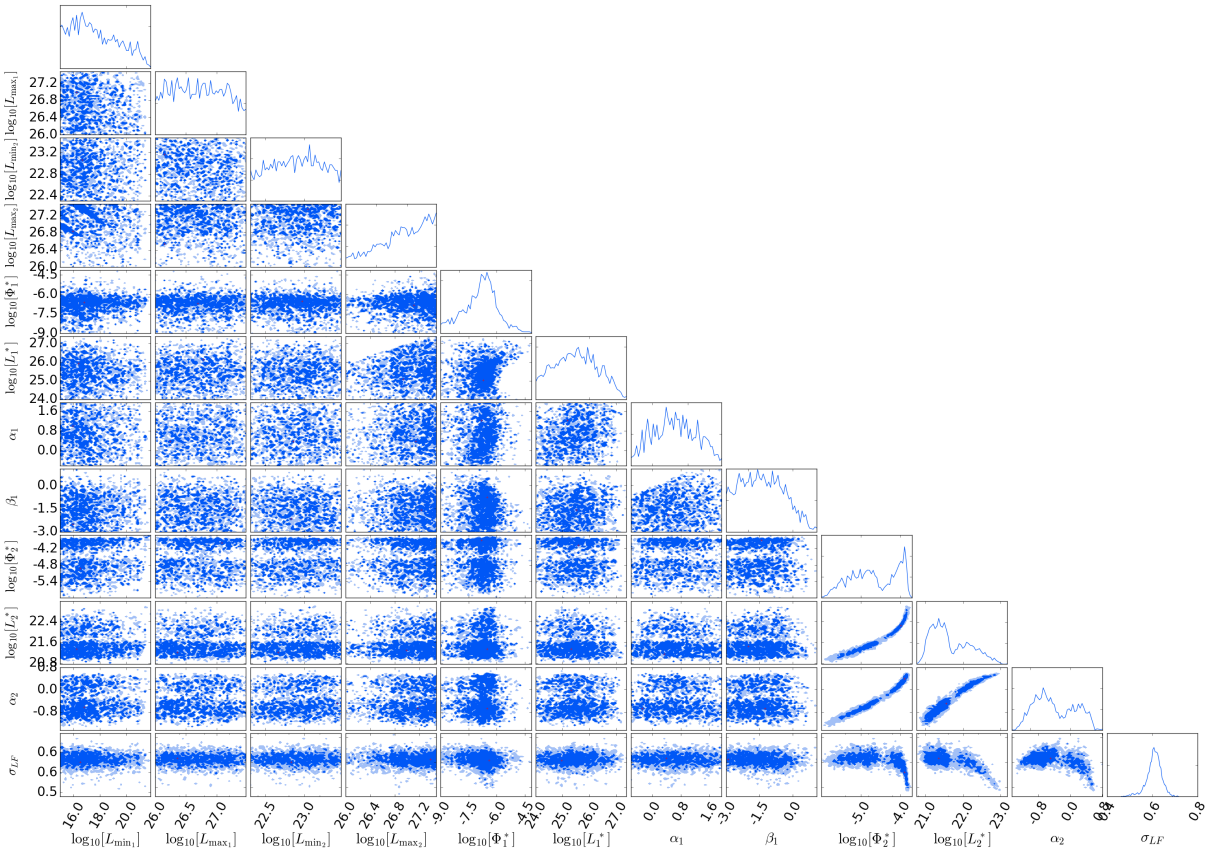

(B) $3.2 < z < 4.0$

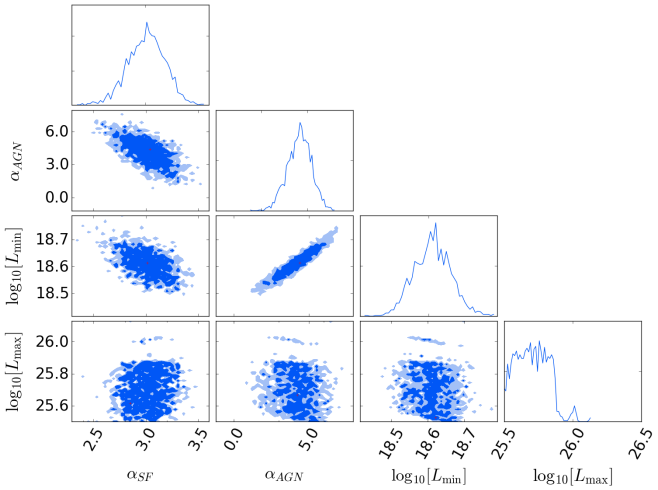

(A) $0.1 < z < 0.4$

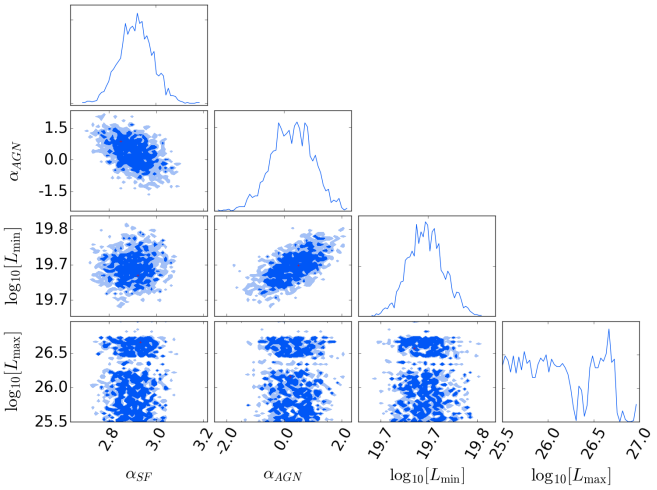

(B) $0.4 < z < 0.6$

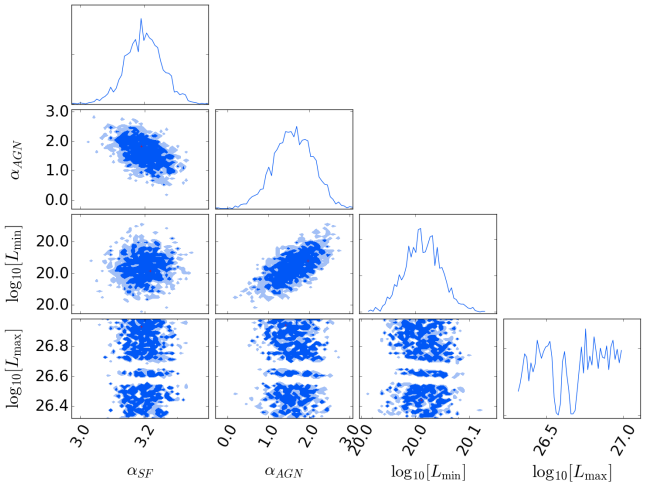

(C) $0.6 < z < 0.8$

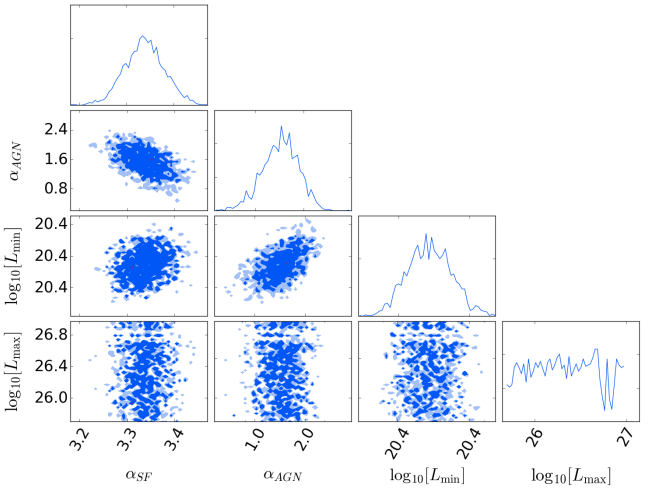

(D) $0.8 < z < 1.0$

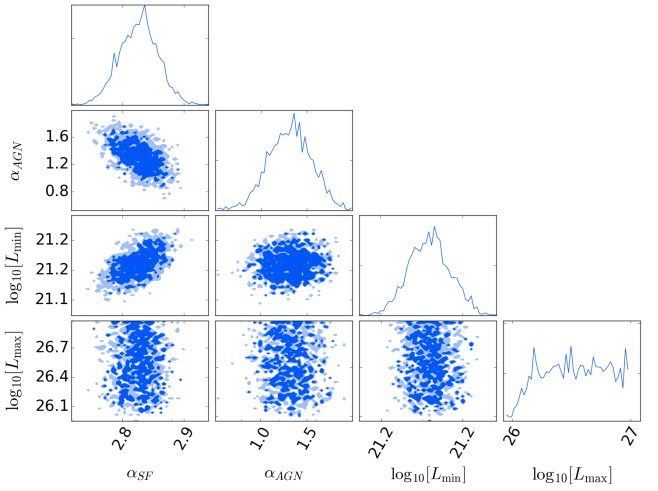

(E) $1.0 < z < 1.3$

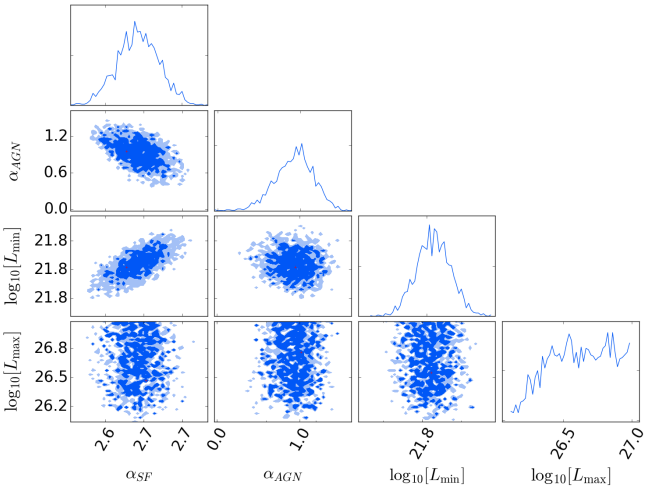

(F) $1.3 < z < 1.6$

FIGURE 4.16: The triangle plots for model D fit to the the individual redshift bins.

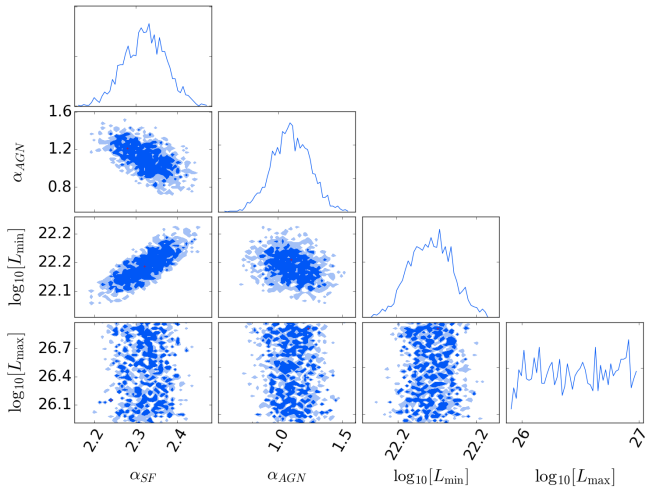

(A) $1.6 < z < 2.0$

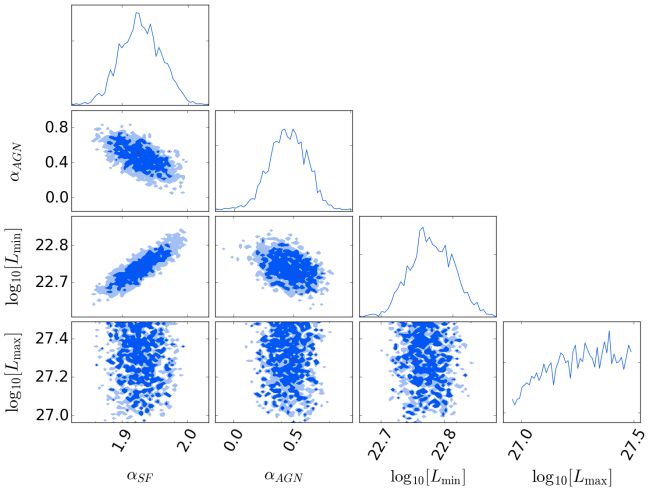

(B) $2.0 < z < 2.$

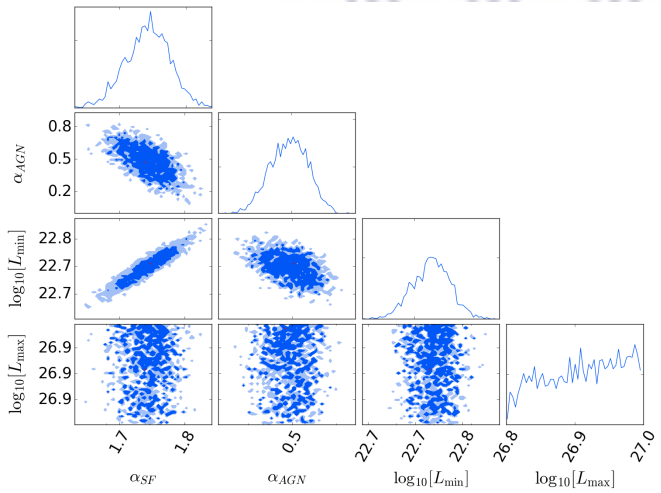

(C) $2.5 < z < 3.2$

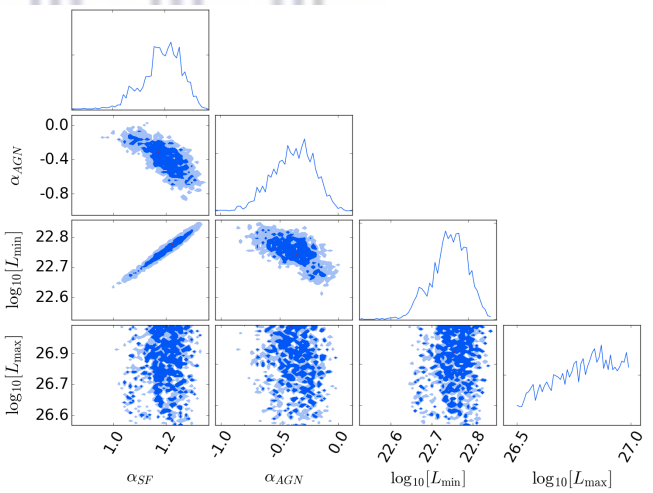

(D) $3.2 < z < 4.0$

FIGURE 4.17: Continued.

Chapter 5

Conclusions

In this thesis I investigate the nature of faint radio population which consists of star froming galaxies (SFG) and radio-quiet active galactic nuclei (AGN). Radio quiet AGN are very important to the study of galaxy evolution as they contain two of fundamental processes in the universe, star formation and AGN accretion. The interply between the two processes leads to an observed co-evolution between the super massive black hole (SMBH) and the host galaxy properties. Radio observations provide an unbiased view of these processes as they are not affected by dust. The questions I try to address are: 1) what is the main source of radio emission in radio-quiet AGN that lack powerful jets and 2) What is the evolution of the cosmic star formation rate density (SFRD) measured through unbiased radio observations.

I address both problems through probing the radio luminosity function (RLF) below the detection threshold because 1) Radio-quiet quasars are below the detection threshold of large radio surveys and there are too few of them in deep surveys; and 2) the bulk of SFG that populate the faint-end slope of the SFG RLF are also below the detection threshold of most deep surveys and they are required to estimate the SFRD. Most studies extrapolate the measure of the RLF to the faint-end to compute the SFRD. For these reasons, I extended a Bayesian stacking technique to probe the RLF below the radio detection threshold given prior positional information of the AGN or SFG at a different wavelength.

5.1 Summary of results

In Chapter 2 I test the technique by adding Gaussian noise (σ) to simulated data. The technique correctly reconstructs RLFs model that are in agreement with the simulated data for up to three orders of magnitude (3 dex) below the detection threshold (5σ).

In Chapter 3 I apply the Bayesian stacking technique to 1.4-GHz flux densities from Faint Images of the Radio Sky at twenty-cm (FIRST), extracted at the positions of optical quasars from the Sloan Digital Sky Survey (SDSS) over seven redshift bins up to $z = 2.15$ and measure the RLF down to two orders of magnitude below the FIRST detection threshold. I do not divide the quasars into radio-loud and radio-quiet using traditional optical-radio ratios but on the basis of the shape of the RLF. I found that each of the bright ends of the RLFs, which broadly represent radio-loud quasars, is described by a double power law. This double power-law generally flattens towards low luminosities. A similar drop/flattening is observed for extremely red quasars and in AGN RLFs. I suggest that some of this flattening could also be due to the optical flux limit of the sample reducing the number of quasars that could contribute radio data to these radio luminosities, although this would need to be tested thoroughly with a deeper optical selection or by considering a bivariate model of the optical and RLFs.

I find that the radio luminosity where radio-quiet quasars emerge (assuming that the faint end of the RLF is the radio-quiet population) coincides with the luminosity where SFGs are expected to start to dominate the radio galaxy RLF. This implies that there could be a significant contribution from star formation in the host galaxies, but to confirm such a scenario additional data such as higher-resolution radio imaging would be ideal, in order to resolve the radio emission from star formation in the host galaxy.

In Chapter 4 I then applied the Bayesian stacking technique again to probe the total RLF of stellar mass-limited near-IR (NIR) selected galaxies in the COSMOS field orders of magnitude below the 5σ detection threshold by fitting parametric models to the RLF for both SFGs and AGNs. However, because of stellar mass limit, the SFG RLF falls off towards low radio luminosities, particularly at the higher redshifts ($z > 1.5$). This fall-off is the result of a lack of fainter radio sources in the parent stellar-mass selected sample. This is due to the known relation between stellar mass and SFRs, where the stellar-mass selected sample imposes a natural limit

on the level of star-formation in galaxies I am able to probe. As the stellar-mass limit increases with redshift, owing to the flux limit of the NIR data, this means that I do not have the radio-fainter SFGs in my sample. I address this by fitting a fixed local RLF model, which is a combination of AGN and SFG, with a pure luminosity evolution (PLE) model. From the RLF for SFGs, I determine the cosmic star formation rate density (SFRD), using an evolving infrared-radio correlation (IRRC). My results are an improvement to the literature as my extrapolations are constrained to much lower luminosities due to the Bayesian-stacking technique.. The cosmic SFRD is consistent with the established behaviour in literature from the lowest redshift $z \sim 0$ to $z \sim 1.5$. My results deviate at $z > 1.5$, which is influenced by my stellar-mass selection and the uncertainty of the IRRC at higher redshifts.

I investigate the effects of stellar mass on the total RLF by splitting my sample into low ($10^{8.5} \leq \mathrm{M/M_{\odot}} \leq 10^{10}$) and high ($\mathrm{M} > 10\,\mathrm{M_{\odot}}$) stellar-mass subsets. I find that the low stellar-mass sources dominate the faint end of the RLF. I find that the SFRD is dominated by sources in the high stellar mass bin, at all redshifts.

I investigate the uncertainty in the IRRC by adopting a constant IRRC measured in the nearby universe. I find that the cosmic SFRD becomes flat and a factor of 2-3 higher at $z \sim 3.5$ than the SFRD obtained with an evolving IRRC. This illustrated that the relationship between the radio luminosity and SFR needs to be better understood and expanded to include other factors, such as inverse Compton scattering of CMB photons at higher redshifts (due to denser environment), stellar-mass dependence and morphology.

Clearly, there is much more work to be done to understand the evolution of the SFRD, with various wavelengths suffering from different selection issues and radio measurements that rely on extrapolations. Here, I have used a method to determine the evolution of the RLF based on the radio emission from a stellar-mass selected sample in the COSMOS field. However, uncertainties in the conversion from radio luminosity to SFR, and how it may or may not evolve with redshift, means it is difficult to make strong claims about the evolution beyond $z \sim 1$.

In both applications of above, I have demonstrated that the Bayesian-stacking technique is a powerful method to probe the RLF at least 2 dex below the detection threshold. However, the RLF obtained from the technique contain selection effects from the optical/NIR parent sample. With the limitations, it is not straightforward

to compare the optically/NIR selected RLF with radio-selected RLF. Furthermore, it is crucial to understand the correlation of the optical/NIR and radio fluxes to fully understand how these selection effects manifests in the RLF.

5.2 Future work

To minimize the effects of the stellar mass cut imposed on my COSMOS sample I fixed the faint-end slope of my SFG RLF. However, the selection effects still affected the high redshift bins. An alternative approach would be to estimate the incompleteness from stellar mass by comparing our stellar mass functions to those in the literature. The stellar mass incompleteness can be converted into a SFR by using the main sequence of SFG (Chapter 1.2.1.6). There will be uncertainty in the SFR correction due to uncertainties in the both the stellar-mass function and the main sequence.

One can extend the SFRD study to other radio frequency data to overcome some of the issues raised in this thesis. For example, the level of inverse Compton scattering of CMB photons and the contribution from free-free emission from HII regions will have a greater impact on higher frequency emission than on low frequency. This is obviously more of an issue at high redshifts, where the rest-frame frequency is $>$ 9 GHz for sources at $z > 2$ in the 3 GHz data I use here. Thus, undertaking a similar study as I have done here over the deep fields observed by the LOFAR (Tasse et al. submitted, Sabater et al. submitted) at an observed frequency of 150 MHz, and the MeerKAT International Giga-Hertz Tiered Extragalactic Exploration (MIGHTEE; Jarvis et al. 2016, Heywood et al. in prep) Survey at 856-1712 MHz, would provide crucial information necessary to advance our understanding of the cosmic SFRD further.

The deeper data from the new generation of radio telescopes will allow fainter detections above the threshold but using stacking techniques such as the one presented in this thesis puts us a step ahead in respect of much fainter RLF. For example, MIGHTEE aims to reach the 1 μJy rms level over 20 deg^2 . If there are $\sim$ 2000 quasars over the area, then one can reach 100 nJy levels using this technique. However, MIGHTEE or MeerKAT observations in general will be confusion-limited owing to the relatively small baselines. Application of the Bayesian-stacking technique to MIGTHEE will require the confusion noise to be accounted for. A P(D) analysis

on MIGHTEE similar to Mauch et al. (2020), would also have the advantage that it does not rely on multiwavelength observations.

The main limitation of measuring the SFRD with radio data is the radio to SFR conversion. An interesting avenue would be to use multiwavelength data to improve this relation. MIGTHEE is ideal to conduct such a study as it contains multiwavelength data from X-ray through to FIR and radio. The multiwavelength data will firstly lead to reliable counterparts, photometric redshifts and stellar masses. Furthermore, the multiwavelenght data will allow for a study of the factors that affect the radio luminosity-SFR relation.

Detailed studies of local galaxies are require to understand the radio emission processes and how they relate to star-formation better. This includes free-free emission which becomes a more dominant component in the rest-frame at higher redshifts.

The next-generation telescopes will reach lower flux levels down to μJy with the SKA pathfinders and nJy with the SKA. The SKA will directly probe the radio luminosities that I achieve using the Bayesian-stacking technique. This will provide more data to investigate dominant emission in radio-quiet AGN further, since most of the population will be detected. However, since redshifts are required to study these sources, all studies will be fundamentally limited by the optical/NIR. This implies that the deeper radio data does not necessarily give better results than those presented here. The advantage of the deep data however, is that it has higher resolution and it is not as confused. This will then allow for one to conduct a stacking technique such as the one I present in this thesis to even lower depths using prior data from deeper future optical/NIR surveys such as the Large Synoptic Survey Telescope (LSST) and EUCLID .

Bibliography

K. N. Abazajian, J. K. Adelman-McCarthy, M. A. Agüeros, S. S. Allam, C. Allende Prieto, D. An, K. S. J. Anderson, S. F. Anderson, J. Annis, N. A. Bahcall, and et al. The Seventh Data Release of the Sloan Digital Sky Survey. *ApJS*, 182:543-558, June 2009. doi: 10.1088/0067-0049/182/2/543.

Marek A. Abramowicz and P. Chris Fragile. Foundations of Black Hole Accretion Disk Theory. *Living Reviews in Relativity*, 16(1):1, January 2013. doi: 10.12942/lrr-2013-1.

N. J. Adams, R. A. A. Bowler, M. J. Jarvis, B. Häußler, R. J. McLure, A. Bunker, J. S. Dunlop, and A. Verma. The rest-frame UV luminosity function at z 4: a significant contribution of AGNs to the bright end of the galaxy population. *MNRAS*, 494(2):1771–1783, March 2020. doi: 10.1093/mnras/staa687.

Thomas F. Adams. A Survey of the Seyfert Galaxies Based on Large-Scale Image-Tube Plates. *ApJS*, 33:19, January 1977. doi: 10.1086/190416.

Hiroaki Aihara, Nobuo Arimoto, Robert Armstrong, Stéphane Arnouts, Neta A. Bahcall, Steven Bickerton, James Bosch, Kevin Bundy, Peter L. Capak, James H. H. Chan, Masashi Chiba, Jean Coupon, Eiichi Egami, Motohiro Enoki, Francois Finet, Hiroki Fujimori, Seiji Fujimoto, Hisanori Furusawa, Junko Furusawa, Tomotsugu Goto, Andy Goulding, Johnny P. Greco, Jenny E. Greene, James E. Gunn, Takashi Hamana, Yuichi Harikane, Yasuhiro Hashimoto, Takashi Hattori, Masao Hayashi, Yusuke Hayashi, Krzysztof G. Hełminiak, Ryo Higuchi, Chiaki Hikage, Paul T. P. Ho, Bau-Ching Hsieh, Kuiyun Huang, Song Huang, Hiroyuki Ikeda, Masatoshi Imanishi, Akio K. Inoue, Kazushi Iwasawa, Ikuru Iwata, Anton T. Jaelani, Hung-Yu Jian, Yukiko Kamata, Hiroshi Karoji, Nobunari Kashikawa, Nobuhiko Katayama, Satoshi Kawanomoto, Issha Kayo, Jin Koda, Michitaro Koike, Takashi Kojima, Yutaka Komiyama, Akira Konno, Shintaro Koshida, Yusei Koyama, Haruka Kusakabe, Alexie Leauthaud, Chien-Hsiu Lee, Lihwai Lin, Yen-Ting Lin, Robert H. Lupton, Rachel Mand elbaum, Yoshiki Matsuoka, Elinor Medezinski, Sogo Mineo, Shoken Miyama, Hironao Miyatake, Satoshi Miyazaki, Rieko Momose, Anupreeta More, Surhud More, Yuki Moritani, Takashi J. Moriya, Tomoki Morokuma, Shiro Mukae, Ryoma Murata, Hitoshi Murayama, Tohru Nagao, Fumiaki Nakata, Mana Niida, Hiroko Niikura, Atsushi J. Nishizawa, Yoshiyuki Obuchi, Masamune Oguri, Yukie Oishi, Nobuhiro Okabe, Sakurako Okamoto, Yuki Okura, Yoshiaki Ono, Masato Onodera, Masafusa Onoue, Ken Osato, Masami Ouchi, Paul A. Price, Tae-Soo Pyo, Masao Sako, Marcin Sawicki, Takatoshi Shibuya, Kazuhiro Shimasaku, Atsushi Shimono, Masato Shirasaki, John D. Silverman, Melanie Simet, Joshua Speagle, David N. Spergel, Michael A. Strauss, Yuma Sugahara, Naoshi Sugiyama, Yasushi Suto, Sherry H. Suyu, Nao Suzuki, Philip J. Tait, Masahiro Takada, Tadafumi Takata, Naoyuki Tamura, Manobu M. Tanaka, Masaomi Tanaka, Masayuki Tanaka, Yoko Tanaka, Tsuyoshi Terai, Yuichi Terashima, Yoshiki Toba, Nozomu Tominaga, Jun Toshikawa, Edwin L. Turner, Tomohisa Uchida, Hisakazu Uchiyama, Keiichi Umetsu, Fumihiro Uraguchi, Yuji Urata, Tomonori Usuda, Yousuke Utsumi, Shiang-Yu Wang, Wei-Hao Wang, Kenneth C. Wong, Kiyoto Yabe, Yoshihiko Yamada, Hitomi Yamanoi, Naoki Yasuda, Sherry Yeh, Atsunori Yonehara, and Suraphong Yuma. The Hyper Suprime-Cam SSP Survey: Overview and survey design. *PASJ*, 70:S4, January 2018a. doi: 10.1093/pasj/psx066.

Hiroaki Aihara, Robert Armstrong, Steven Bickerton, James Bosch, Jean Coupon, Hisanori Furusawa, Yusuke Hayashi, Hiroyuki Ikeda, Yukiko Kamata, Hiroshi Karoji, Satoshi Kawanomoto, Michitaro Koike, Yutaka Komiyama, Dustin Lang, Robert H. Lupton, Sogo Mineo, Hironao Miyatake, Satoshi Miyazaki, Tomoki Morokuma, Yoshiyuki Obuchi, Yukie Oishi, Yuki Okura, Paul A. Price, Tadafumi Takata, Manobu M. Tanaka, Masayuki Tanaka, Yoko Tanaka, Tomohisa Uchida, Fumihiro Uraguchi, Yousuke Utsumi, Shiang-Yu Wang, Yoshihiko Yamada, Hitomi Yamanoi, Naoki Yasuda, Nobuo Arimoto, Masashi Chiba, Francois Finet, Hiroki Fujimori, Seiji Fujimoto, Junko Furusawa, Tomotsugu Goto, Andy Goulding, James E. Gunn, Yuichi Harikane, Takashi Hattori, Masao Hayashi, Krzysztof G. Hełminiak, Ryo Higuchi, Chiaki Hikage, Paul T. P. Ho, Bau-Ching Hsieh, Kuiyun Huang, Song Huang, Masatoshi Imanishi, Ikuru Iwata, Anton T. Jaelani, Hung-Yu Jian, Nobunari Kashikawa, Nobuhiko Katayama, Takashi Kojima, Akira Konno, Shintaro Koshida, Haruka Kusakabe, Alexie Leauthaud, Chien-Hsiu Lee, Lihwai Lin, Yen-Ting Lin, Rachel Mandelbaum, Yoshiki Matsuoka, Elinor Medezinski, Shoken Miyama, Rieko Momose, Anupreeta More, Surhud More, Shiro Mukae, Ryoma Murata, Hitoshi Murayama, Tohru Nagao, Fumiaki Nakata, Mana Niida, Hiroko Niikura, Atsushi J. Nishizawa, Masamune Oguri, Nobuhiro Okabe, Yoshiaki Ono, Masato Onodera, Masafusa Onoue, Masami Ouchi, Tae-Soo Pyo, Takatoshi Shibuya, Kazuhiro Shimasaku, Melanie Simet, Joshua Speagle, David N. Spergel, Michael A. Strauss, Yuma Sugahara, Naoshi Sugiyama, Yasushi Suto, Nao Suzuki, Philip J. Tait, Masahiro Takada, Tsuyoshi Terai, Yoshiki Toba, Edwin L. Turner, Hisakazu Uchiyama, Keiichi Umetsu, Yuji Urata, Tomonori Usuda, Sherry Yeh, and Suraphong Yuma. First data release of the Hyper Suprime-Cam Subaru Strategic Program. *PASJ*, 70:S8, January 2018b. doi: 10.1093/pasj/psx081.

J. Aird, A. L. Coil, and A. Georgakakis. X-rays across the galaxy population - I. Tracing the main sequence of star formation. *MNRAS*, 465(3):3390–3415, March 2017. doi: 10.1093/mnras/stw2932.

Shadab Alam, Franco D. Albareti, Carlos Allende Prieto, F. Anders, Scott F. Anderson, Timothy Anderton, Brett H. Andrews, Eric Armengaud, Éric Aubourg, Stephen Bailey, Sarbani Basu, Julian E. Bautista, Rachael L. Beaton, Timothy C. Beers, Chad F. Bender, Andreas A. Berlind, Florian Beutler, Vaishali Bhardwaj, Jonathan C. Bird, Dmitry Bizyaev, Cullen H. Blake, Michael R. Blanton, Michael Blomqvist, John J. Bochanski, Adam S. Bolton, Jo Bovy, A. Shelden Bradley, W. N. Brandt, D. E. Brauer, J. Brinkmann, Peter J. Brown, Joel R. Brownstein, Angela Burden, Etienne Burtin, Nicolás G. Busca, Zheng Cai, Diego Capozzi, Aurelio Carnero Rosell, Michael A. Carr, Ricardo Carrera, K. C. Chambers, William James Chaplin, Yen-Chi Chen, Cristina Chiappini, S. Drew Chojnowski, Chia-Hsun Chuang, Nicolas Clerc, Johan Comparat, Kevin Covey, Rupert A. C. Croft, Antonio J. Cuesta, Katia Cunha, Luiz N. da Costa, Nicola Da Rio, James R. A. Davenport, Kyle S. Dawson, Nathan De Lee, Timothée Delubac, Rohit Deshpande, Saurav Dhital, Letícia Dutra-Ferreira, Tom Dwelly, Anne Ealet, Garrett L. Ebelke, Edward M. Edmondson, Daniel J. Eisenstein, Tristan Ellsworth, Yvonne Elsworth, Courtney R. Epstein, Michael Eracleous, Stephanie Escoffier, Massimiliano Esposito, Michael L. Evans, Xiaohui Fan, Emma Fernández-Alvar, Diane Feuillet, Nurten Filiz Ak, Hayley Finley, Alexis Finoguenov, Kevin Flaherty, Scott W. Fleming, Andreu Font-Ribera, Jonathan Foster, Peter M. Frinchaboy, J. G. Galbraith-Frew, Rafael A. García, D. A. García-Hernández, Ana E. García Pérez, Patrick Gaulme, Jian Ge, R. Génova-Santos, A. Georgakakis, Luan Ghezzi, Bruce A. Gillespie, Léo Girardi, Daniel Goddard, Satya Gontcho A Gontcho, Jonay I. González Hernández, Eva K. Grebel, Paul J. Green, Jan Niklas Grieb, Nolan Grieves, James E. Gunn, Hong Guo, Paul Harding, Sten Hasselquist, Suzanne L. Hawley, Michael Hayden, Fred R. Hearty, Saskia Hekker, Shirley Ho, David W. Hogg, Kelly Holley-Bockelmann, Jon A. Holtzman, Klaus Honscheid, Daniel Huber, Joseph Huehnerhoff, Inese I. Ivans, Linhua Jiang, Jennifer A. Johnson, Karen Kinemuchi, David Kirkby, Francisco Kitaura, Mark A. Klaene, Gillian R. Knapp, Jean-Paul Kneib, Xavier P. Koenig, Charles R. Lam, Ting-Wen Lan, Dustin Lang, Pierre Laurent, Jean-Marc Le Goff, Alexie Leauthaud, Khee-Gan Lee, Young Sun Lee, Timothy C. Licquia, Jian Liu, Daniel C. Long, Martín López-Corredoira, Diego Lorenzo-Oliveira, Sara Lucatello, Britt Lundgren, Robert H. Lupton, Claude E. Mack III, Suvrath Mahadevan, Marcio A. G. Maia, Steven R. Majewski, Elena Malanushenko, Viktor Malanushenko, A. Manchado, Marc Manera, Qingqing Mao, Claudia Maraston, Robert C. Marchwinski, Daniel

Margala, Sarah L. Martell, Marie Martig, Karen L. Masters, Savita Mathur, Cameron K. McBride, Peregrine M. McGehee, Ian D. McGreer, Richard G. McMahon, Brice Ménard, Marie-Luise Menzel, Andrea Merloni, Szabolcs Mészáros, Adam A. Miller, Jordi Miralda-Escudé, Hironao Miyatake, Antonio D. Montero-Dorta, Surhud More, Eric Morganson, Xan Morice-Atkinson, Heather L. Morrison, Beno
it Mosser, Demitri Muna, Adam D. Myers, Kirpal Nandra, Jeffrey A. Newman, Mark Neyrinck, Duy Cuong Nguyen, Robert C. Nichol, David L. Nidever, Pasquier Noterdaeme, Sebastián E. Nuza, Julia E. O'Connell, Robert W. O'Connell, Ross O'Connell, Ricardo L. C. Ogando, Matthew D. Olmstead, Audrey E. Oravetz, Daniel J. Oravetz, Keisuke Osumi, Russell Owen, Deborah L. Padgett, Nikhil Padmanabhan, Martin Paegert, Nathalie Palanque-Delabrouille, Kaike Pan, John K. Parejko, Isabelle Pâris, Changbom Park, Petchara Pattarakijwanich, M. Pellejero-Ibanez, Joshua Pepper, Will J. Percival, Ismael Pérez-Fournon, Ignasi Perez-Rafols, Patrick Petitjean, Matthew M. Pieri, Marc H. Pinsonneault, Gustavo F. Porto de Mello, Francisco Prada, Abhishek Prakash, Adrian M. Price-Whelan, Pavlos Protopapas, M. Jordan Raddick, Mubdi Rahman, Beth A. Reid, James Rich, Hans-Walter Rix, Annie C. Robin, Constance M. Rockosi, Thaíse S. Rodrigues, Sergio Rodríguez-Torres, Natalie A. Roe, Ashley J. Ross, Nicholas P. Ross, Graziano Rossi, John J. Ruan, J. A. Rubiño-Martín, Eli S. Rykoff, Salvador Salazar-Albornoz, Mara Salvato, Lado Samushia, Ariel G. Sánchez, Basílio Santiago, Conor Sayres, Ricardo P. Schiavon, David J. Schlegel, Sarah J. Schmidt, Donald P. Schneider, Mathias Schultheis, Axel D. Schwope, C. G. Scóccola, Caroline Scott, Kris Sellgren, Hee-Jong Seo, Aldo Serenelli, Neville Shane, Yue Shen, Matthew Shetrone, Yiping Shu, V. Silva Aguirre, Thirupathi Sivarani, M. F. Skrutskie, Anže Slosar, Verne V. Smith, Flávia Sobreira, Diogo Souto, Keivan G. Stassun, Matthias Steinmetz, Dennis Stello, Michael A. Strauss, Alina Streblyanska, Nao Suzuki, Molly E. C. Swanson, Jonathan C. Tan, Jamie Tayar, Ryan C. Terrien, Aniruddha R. Thakar, Daniel Thomas, Neil Thomas, Benjamin A. Thompson, Jeremy L. Tinker, Rita Tojeiro, Nicholas W. Troup, Mariana Vargas-Magaña, Jose A. Vazquez, Licia Verde, Matteo Viel, Nicole P. Vogt, David A. Wake, Ji Wang, Benjamin A. Weaver, David H. Weinberg, Benjamin J. Weiner, Martin White, John C. Wilson, John P. Wisniewski, W. M. Wood-Vasey, Christophe Yeche, Donald G. York, Nadia L. Zakamska, O. Zamora, Gail Zasowski, Idit Zehavi, Gong-Bo Zhao, Zheng Zheng, Xu Zhou (), Zhimin Zhou (), Hu Zou (), and Guangtun Zhu. THE ELEVENTH AND TWELFTH DATA RELEASES OF THE SLOAN DIGITAL SKY SURVEY: FINAL DATA FROM SDSS-III. *The Astrophysical Journal Supplement Series*, 219(1):12, jul 2015. doi: 10.1088/0067-0049/219/1/12. URL https://doi.org/10.1088%2F0067-0049%2F219%2F1%2F12.

Ph. André, A. Men'shchikov, S. Bontemps, V. Könyves, F. Motte, N. Schneider, P. Didelon, V. Minier, P. Saraceno, D. Ward-Thompson, J. di Francesco, G. White, S. Molinari, L. Testi, A. Abergel, M. Griffin, Th. Henning, P. Royer, B. Merín, R. Vavrek, M. Attard, D. Arzoumanian, C. D. Wilson, P. Ade, H. Aussel, J. P. Baluteau, M. Benedettini, J. Ph. Bernard, J. A. D. L. Blommaert, L. Cambrésy, P. Cox, A. di Giorgio, P. Hargrave, M. Hennemann, M. Huang, J. Kirk, O. Krause, R. Launhardt, S. Leeks, J. Le Pennec, J. Z. Li, P. G. Martin, A. Maury, G. Olofsson, A. Omont, N. Peretto, S. Pezzuto, T. Prusti, H. Roussel, D. Russeil, M. Sauvage, B. Sibthorpe, A. Sicilia-Aguilar, L. Spinoglio, C. Waelkens, A. Woodcraft, and A. Zavagno. From filamentary clouds to prestellar cores to the stellar IMF: Initial highlights from the Herschel Gould Belt Survey. *A&A*, 518:L102, July 2010. doi: 10.1051/0004-6361/201014666.

Robert Antonucci. Unified models for active galactic nuclei and quasars. *ARA&A*, 31:473–521, Jan 1993. doi: 10.1146/annurev.aa.31.090193.002353.

V. Antonuccio-Delogu and J. Silk. Active galactic nuclei jet-induced feedback in galaxies - I. Suppression of star formation. *MNRAS*, 389:1750–1762, October 2008. doi: 10.1111/j.1365-2966.2008.13663.x.

S. Arnouts, L. Moscardini, E. Vanzella, S. Colombi, S. Cristiani, A. Fontana, E. Giallongo, S. Matarrese, and P. Saracco. Measuring the redshift evolution of clustering: the Hubble Deep Field South. *MNRAS*, 329(2):355–366, Jan 2002. doi: 10.1046/j.1365-8711.2002.04988.x.

Eduardo Bañados, Bram P. Venemans, Chiara Mazzucchelli, Emanuele P. Farina, Fabian Walter, Feige Wang, Roberto Decarli, Daniel Stern, Xiaohui Fan, Frederick B. Davies, Joseph F. Hennawi, Robert A. Simcoe, Monica L. Turner, Hans-Walter Rix, Jinyi Yang, Daniel D. Kelson, Gwen C. Rudie, and Jan Martin Winters. An 800-million-solar-mass black hole in a significantly neutral Universe at a redshift of 7.5. *Nature*, 553(7689):473–476, January 2018. doi: 10.1038/nature25180.

Steven A. Balbus and John F. Hawley. A Powerful Local Shear Instability in Weakly Magnetized Disks. I. Linear Analysis. *ApJ*, 376:214, July 1991. doi: 10.1086/170270.

M. Baloković, V. Smolčić, Ž. Ivezić, G. Zamorani, E. Schinnerer, and B. C. Kelly. Disclosing the Radio Loudness Distribution Dichotomy in Quasars: An Unbiased Monte Carlo Approach Applied to the SDSS-FIRST Quasar Sample. *ApJ*, 759(1):30, Nov 2012. doi: 10.1088/0004-637X/759/1/30.

X. Barcons and A. C. Fabian. A fluctuation analysis of the X-ray background in the Einstein Observatory IPC. *MNRAS*, 243:366–371, April 1990.

J. M. Bardeen, J. R. Bond, N. Kaiser, and A. S. Szalay. The Statistics of Peaks of Gaussian Random Fields. *ApJ*, 304:15, May 1986. doi: 10.1086/164143.

M. Bartelmann and S. D. M. White. Stacking clusters in the ROSAT All-Sky Survey. *A&A*, 407: 845–854, September 2003. doi: 10.1051/0004-6361:20030991.

Peter D. Barthel. Is Every Quasar Beamed? *ApJ*, 336:606, Jan 1989. doi: 10.1086/167038.

Richard Barvainis. Hot Dust and the Near-Infrared Bump in the Continuum Spectra of Quasars and Active Galactic Nuclei. *ApJ*, 320:537, September 1987. doi: 10.1086/165571.

Nate Bastian, Michael Meyer, Julia Greissl, and Anil Seth. Testing IMF universality through the direct detection of low mass stars in starburst galaxies. NOAO Proposal, August 2010.

R. H. Becker, R. L. White, and D. J. Helfand. The FIRST Survey: Faint Images of the Radio Sky at Twenty Centimeters. *ApJ*, 450:559, September 1995. doi: 10.1086/176166.

Eric F. Bell. Estimating Star Formation Rates from Infrared and Radio Luminosities: The Origin of the Radio-Infrared Correlation. *ApJ*, 586(2):794–813, April 2003. doi: 10.1086/367829.

Sirio Belli, Reinhard Genzel, Natascha M. Förster Schreiber, Emily Wisnioski, David J. Wilman, Stijn Wuyts, J. Trevor Mendel, Alessandra Beifiori, Ralf Bender, Gabriel B. Brammer, Andreas Burkert, Jeffrey Chan, Rebecca L. Davies, Ric Davies, Maximilian Fabricius, Matteo Fossati, Audrey Galametz, Philipp Lang, Dieter Lutz, Ivelina G. Momcheva, Erica J. Nelson, Roberto P. Saglia, Linda J. Tacconi, Ken-ichi Tadaki, Hannah Übler, and Pieter van Dokkum. KMOS^{3D} Reveals Low-level Star Formation Activity in Massive Quiescent Galaxies at 0.7 < z < 2.7. *ApJ*, 841(1):L6, May 2017. doi: 10.3847/2041-8213/aa70e5.

A. J. Benson, R. G. Bower, C. S. Frenk, C. G. Lacey, C. M. Baugh, and S. Cole. What Shapes the Luminosity Function of Galaxies? *ApJ*, 599(1):38–49, December 2003. doi: 10.1086/379160.

S. Berta, D. Lutz, P. Santini, S. Wuyts, D. Rosario, D. Brisbin, A. Cooray, A. Franceschini, C. Gruppioni, E. Hatziminaoglou, H. S. Hwang, E. Le Floc'h, B. Magnelli, R. Nordon, S. Oliver, M. J. Page, P. Popesso, L. Pozzetti, F. Pozzi, L. Riguccini, G. Rodighiero, I. Roseboom, D. Scott, M. Symeonidis, I. Valtchanov, M. Viero, and L. Wang. Panchromatic spectral energy distributions of Herschel sources. *A&A*, 551:A100, March 2013. doi: 10.1051/0004-6361/201220859.

P. S. Bessiere, C. N. Tadhunter, C. Ramos Almeida, and M. Villar Martín. The importance of galaxy interactions in triggering type II quasar activity. *MNRAS*, 426:276–295, October 2012. doi: 10.1111/j.1365-2966.2012.21701.x.

P. N. Best. Radio-Loud AGN Heating in Elliptical Galaxies and Clusters. In H. Böhringer, G. W. Pratt, A. Finoguenov, and P. Schuecker, editors, *Heating versus Cooling in Galaxies and Clusters of Galaxies*, page 166, 2007. doi: 10.1007/978-3-540-73484-0_31.

P. N. Best, G. Kauffmann, T. M. Heckman, and Ž. Ivezić. A sample of radio-loud active galactic nuclei in the Sloan Digital Sky Survey. *MNRAS*, 362(1):9–24, September 2005. doi: 10.1111/j.1365-2966.2005.09283.x.

R. J. Beswick, T. W. B. Muxlow, H. Thrall, A. M. S. Richards, and S. T. Garrington. An evolution of the infrared-radio correlation at very low flux densities? *MNRAS*, 385(3):1143–1154, April 2008. doi: 10.1111/j.1365-2966.2008.12931.x.

R. D. Blandford and D. G. Payne. Hydromagnetic flows from accretion disks and the production of radio jets. *MNRAS*, 199:883–903, June 1982. doi: 10.1093/mnras/199.4.883.

R. D. Blandford and R. L. Znajek. Electromagnetic extraction of energy from Kerr black holes. *MNRAS*, 179:433–456, May 1977. doi: 10.1093/mnras/179.3.433.

M. Bondi, P. Ciliegi, E. Schinnerer, V. Smolčić, K. Jahnke, C. Carilli, and G. Zamorani. The VLA-COSMOS Survey. III. Further Catalog Analysis and the Radio Source Counts. *ApJ*, 681: 1129–1135, July 2008. doi: 10.1086/589324.

M. Bondi, G. Zamorani, P. Ciliegi, V. Smolčić, E. Schinnerer, I. Delvecchio, E. F. Jiménez-Andrade, D. Liu, P. Lang, B. Magnelli, E. J. Murphy, and E. Vardoulaki. Linear radio size evolution of μJy populations. *A&A*, 618:L8, Oct 2018. doi: 10.1051/0004-6361/201834243.

I. A. Bonnell, M. R. Bate, C. J. Clarke, and J. E. Pringle. Accretion and the stellar mass spectrum in small clusters. *MNRAS*, 285(1):201–208, February 1997. doi: 10.1093/mnras/285.1.201.

Ian A. Bonnell and Matthew R. Bate. Accretion in stellar clusters and the collisional formation of massive stars. *MNRAS*, 336(2):659–669, October 2002. doi: 10.1046/j.1365-8711.2002.05794.x.

Ian A. Bonnell and Matthew R. Bate. Star formation through gravitational collapse and competitive accretion. *MNRAS*, 370(1):488–494, July 2006. doi: 10.1111/j.1365-2966.2006.10495.x.

M. Bonzini, P. Padovani, V. Mainieri, K. I. Kellermann, N. Miller, P. Rosati, P. Tozzi, and S. Vattakunnel. The sub-mJy radio sky in the Extended Chandra Deep Field-South: source population. *MNRAS*, 436:3759–3771, December 2013. doi: 10.1093/mnras/stt1879.

Leindert A. Boogaard, Roberto Decarli, Jorge González-López, Paul van der Werf, Fabian Walter, Rychard Bouwens, Manuel Aravena, Chris Carilli, Franz Erik Bauer, Jarle Brinchmann, Thierry Contini, Pierre Cox, Elisabete da Cunha, Emanuele Daddi, Tanio Díaz-Santos, Jacqueline Hodge, Hanae Inami, Rob Ivison, Michael Maseda, Jorryt Matthee, Pascal Oesch, Gergö Popping, Dominik Riechers, Joop Schaye, Sander Schouws, Ian Smail, Axel Weiss, Lutz Wisotzki, Roland Bacon, Paulo C. Cortes, Hans-Walter Rix, Rachel S. Somerville, Mark Swinbank, and Jeff Wagg. The ALMA Spectroscopic Survey in the HUDF: Nature and Physical Properties of Gas-mass Selected Galaxies Using MUSE Spectroscopy. *ApJ*, 882(2):140, September 2019. doi: 10.3847/1538-4357/ab3102.

N. Bourne, S. J. Maddox, L. Dunne, R. Auld, M. Baes, I. K. Baldry, D. G. Bonfield, A. Cooray, S. M. Croom, A. Dariush, G. de Zotti, S. P. Driver, S. Dye, S. Eales, H. L. Gomez, J. González-Nuevo, A. M. Hopkins, E. Ibar, M. J. Jarvis, A. Lapi, B. Madore, M. J. Michałowski, M. Pohlen, C. C. Popescu, E. E. Rigby, M. Seibert, D. J. B. Smith, R. J. Tuffs, P. van der Werf, S. Brough, S. Buttiglione, A. Cava, D. L. Clements, C. J. Conselice, J. Fritz, R. Hopwood, R. J. Ivison, D. H. Jones, L. S. Kelvin, J. Liske, J. Loveday, P. Norberg, A. S. G. Robotham, G. Rodighiero, and P. Temi. Herschel-ATLAS/GAMA: a census of dust in optically selected galaxies from stacking at submillimetre wavelengths. *MNRAS*, 421:3027–3059, April 2012. doi: 10.1111/j.1365-2966.2012.20528.x.

R. J. Bouwens, G. D. Illingworth, P. A. Oesch, M. Trenti, I. Labbé, L. Bradley, M. Carollo, P. G. van Dokkum, V. Gonzalez, B. Holwerda, M. Franx, L. Spitler, R. Smit, and D. Magee. UV Luminosity Functions at Redshifts z 4 to z 10: 10,000 Galaxies from HST Legacy Fields. *ApJ*, 803(1):34, April 2015. doi: 10.1088/0004-637X/803/1/34.

R. A. A. Bowler, M. J. Jarvis, J. S. Dunlop, R. J. McLure, D. J. McLeod, N. J. Adams, B. Milvang-Jensen, and H. J. McCracken. A lack of evolution in the very bright end of the galaxy luminosity function from z 8 to 10. *MNRAS*, 493(2):2059–2084, April 2020. doi: 10.1093/mnras/staa313.

B. J. Boyle and Roberto J. Terlevich. The cosmological evolution of the QSO luminosity density and of the star formation rate. *MNRAS*, 293(2):L49–L51, January 1998. doi: 10.1046/j.1365-8711.1998.01264.x.

B. J. Boyle, T. J. Cornwell, E. Middelberg, R. P. Norris, P. N. Appleton, and Ian Smail. Extending the infrared radio correlation. *MNRAS*, 376(3):1182–1188, April 2007. doi: 10.1111/j.1365-2966.2007.11509.x.

A. Brandenburg and A. Lazarian. Astrophysical Hydromagnetic Turbulence. *Space Sci. Rev.*, 178 (2-4):163–200, October 2013. doi: 10.1007/s11214-013-0009-3.

W. N. Brandt and Chandra Deep Field North Team. The Chandra Deep Field North Survey: Multiwavelength Source Properties, Stacking Results, and Future Plans. In *American Astronomical Society Meeting Abstracts*, volume 199 of *American Astronomical Society Meeting Abstracts*, page 140.02, December 2001.

Drew Brisbin, Oskari Miettinen, Manuel Aravena, Vernesa Smolčić, Ivan Delvecchio, Chunyan Jiang, Benjamin Magnelli, Marcus Albrecht, Alejandra Muñoz Arancibia, Hervé Aussel, Nikola Baran, Frank Bertoldi, Matthieu Béthermin, Peter Capak, Caitlin M. Casey, Francesca Civano, Christopher C. Hayward, Olivier Ilbert, Alexander Karim, Olivier Le Fevre, Stefano Marchesi, Henry Joy McCracken, Felipe Navarrete, Mladen Novak, Dominik Riechers, Nelson Padilla, Mara Salvato, Kimberly Scott, Eva Schinnerer, Kartik Sheth, and Lidia Tasca. An ALMA survey of submillimeter galaxies in the COSMOS field: Multiwavelength counterparts and redshift distribution. *A&A*, 608:A15, December 2017. doi: 10.1051/0004-6361/201730558.

Simcha Brownson, Francesco Belfiore, Roberto Maiolino, Lihwai Lin, and Stefano Carniani. What drives galaxy quenching? resolving molecular gas and star formation in the green valley. *Monthly Notices of the Royal Astronomical Society: Letters*, 498(1):L66–L71, Jul 2020. ISSN 1745-3933. doi: 10.1093/mnrasl/slaa128. URL http://dx.doi.org/10.1093/mnrasl/slaa128.

G. Bruzual and S. Charlot. Stellar population synthesis at the resolution of 2003. *MNRAS*, 344 (4):1000–1028, Oct 2003. doi: 10.1046/j.1365-8711.2003.06897.x.

J. Buchner, A. Georgakakis, K. Nandra, L. Hsu, C. Rangel, M. Brightman, A. Merloni, M. Salvato, J. Donley, and D. Kocevski. X-ray spectral modelling of the AGN obscuring region in the CDFS: Bayesian model selection and catalogue. *A&A*, 564:A125, April 2014. doi: 10.1051/0004-6361/201322971.

D. Burgarella, V. Buat, and J. Iglesias-Páramo. Star formation and dust attenuation properties in galaxies from a statistical ultraviolet-to-far-infrared analysis. *MNRAS*, 360(4):1413–1425, July 2005. doi: 10.1111/j.1365-2966.2005.09131.x.

D. Burgarella, P. Levacher, S. Vives, K. Dohlen, and S. Pascal. The FLARE mission: deep and wide-field 1-5um imaging and spectroscopy for the early universe: a proposal for M5 cosmic vision call. In *Space Telescopes and Instrumentation 2016: Optical, Infrared, and Millimeter Wave*, volume 9904 of *Society of Photo-Optical Instrumentation Engineers (SPIE) Conference Series*, page 99042N, July 2016. doi: 10.1117/12.2234622.

Adam Burrows, W. B. Hubbard, J. I. Lunine, and James Liebert. The theory of brown dwarfs and extrasolar giant planets. *Reviews of Modern Physics*, 73(3):719–765, July 2001. doi: 10.1103/RevModPhys.73.719.

J. P. Caillault and D. J. Helfand. The Einstein soft X-ray survey of the Pleiades. *ApJ*, 289: 279–299, February 1985. doi: 10.1086/162888.

Bradley W. Carroll and Dale A. Ostlie. *An Introduction to Modern Astrophysics*. 2nd (international) edition, 2007.

L. Ceraj, V. Smolčić, I. Delvecchio, M. Novak, G. Zamorani, J. Delhaize, E. Schinnerer, E. Vardoulaki, and N. Herrera Ruiz. The VLA-COSMOS 3 GHz Large Project: Star formation properties and radio luminosity functions of AGN with moderate-to-high radiative luminosities out to z
6. *A&A*, 620:A192, December 2018. doi: 10.1051/0004-6361/201833935.

Gilles Chabrier. Galactic Stellar and Substellar Initial Mass Function. *PASP*, 115(809):763–795, Jul 2003. doi: 10.1086/376392.

Gilles Chabrier. *The Initial Mass Function: From Salpeter 1955 to 2005*, volume 327 of *Astrophysics and Space Science Library*, page 41. 2005. doi: 10.1007/978-1-4020-3407-7_5.

S. C. Chapman, A. W. Blain, Ian Smail, and R. J. Ivison. A Redshift Survey of the Submillimeter Galaxy Population. *ApJ*, 622(2):772–796, April 2005. doi: 10.1086/428082.

S. Chen, J. T. L. Zwart, and M. G. Santos. Fully-Bayesian stacking in the presence of confusion. *ArXiv e-prints*, September 2017.

M. Cirasuolo, M. Magliocchetti, and A. Celotti. Faint radio-loud quasars: clues to their evolution. *MNRAS*, 357:1267–1280, March 2005. doi: 10.1111/j.1365-2966.2005.08729.x.

Alison L. Coil, Michael R. Blanton, Scott M. Burles, Richard J. Cool, Daniel J. Eisenstein, John Moustakas, Kenneth C. Wong, Guangtun Zhu, James Aird, Rebecca A. Bernstein, Adam S. Bolton, and David W. Hogg. THE PRISM MULTI-OBJECT SURVEY (PRIMUS). i. SURVEY OVERVIEW AND CHARACTERISTICS. *The Astrophysical Journal*, 741(1):8, oct 2011. doi: 10.1088/0004-637x/741/1/8. URL https://doi.org/10.1088%2F0004-637x%2F741%2F1%2F8.

J. D. Collier, J. K. Banfield, R. P. Norris, D. H. F. M. Schnitzeler, A. E. Kimball, M. D. Filipović, T. H. Jarrett, C. J. Lonsdale, and N. F. H. Tothill. Infrared-faint radio sources: a new population of high-redshift radio galaxies. *MNRAS*, 439(1):545–565, March 2014. doi: 10.1093/mnras/stt2485.

J. J. Condon. Confusion and Flux-Density Error Distributions. *ApJ*, 188:279–286, March 1974. doi: 10.1086/152714.

J. J. Condon. Cosmological evolution of radio sources. *ApJ*, 287:461–474, December 1984. doi: 10.1086/162705.

J. J. Condon and K. J. Mitchell. 4C 29.47 - Quasi-periodic outbursts recorded by precessing jets? *ApJ*, 276:472–475, January 1984. doi: 10.1086/161634.

J. J. Condon, M. L. Anderson, and G. Helou. Correlations between Far-Infrared, Radio, and Blue Luminosities of Spiral Galaxies. *ApJ*, 376:95, July 1991. doi: 10.1086/170258.

J. J. Condon, W. D. Cotton, E. W. Greisen, Q. F. Yin, R. A. Perley, and J. J. Broderick. The NRAO VLA Sky Survey. In D. R. Crabtree, R. J. Hanisch, and J. Barnes, editors, *Astronomical Data Analysis Software and Systems III*, volume 61 of *Astronomical Society of the Pacific Conference Series*, page 155, 1994.

J. J. Condon, W. D. Cotton, E. W. Greisen, Q. F. Yin, R. A. Perley, G. B. Taylor, and J. J. Broderick. The NRAO VLA Sky Survey. *AJ*, 115:1693–1716, May 1998. doi: 10.1086/300337.

J. J. Condon, W. D. Cotton, and J. J. Broderick. Radio Sources and Star Formation in the Local Universe. *AJ*, 124(2):675–689, August 2002. doi: 10.1086/341650.

J. J. Condon, W. D. Cotton, Q. F. Yin, D. L. Shupe, L. J. Storrie-Lombardi, G. Helou, B. T. Soifer, and M. W. Werner. The SIRTF First-Look Survey. I. VLA Image and Source Catalog. *AJ*, 125:2411–2426, May 2003. doi: 10.1086/374633.

J. J. Condon, W. D. Cotton, E. B. Fomalont, K. I. Kellermann, N. Miller, R. A. Perley, D. Scott, T. Vernstrom, and J. V. Wall. Resolving the Radio Source Background: Deeper Understanding through Confusion. *ApJ*, 758:23, October 2012. doi: 10.1088/0004-637X/758/1/23.

J. J. Condon, K. I. Kellermann, A. E. Kimball, Ž. Ivezić, and R. A. Perley. Active Galactic Nucleus and Starburst Radio Emission from Optically Selected Quasi-stellar Objects. *ApJ*, 768:37, May 2013. doi: 10.1088/0004-637X/768/1/37.

Richard J. Cool, John Moustakas, Michael R. Blanton, Scott M. Burles, Alison L. Coil, Daniel J. Eisenstein, Kenneth C. Wong, Guangtun Zhu, James Aird, Rebecca A. Bernstein, Adam S. Bolton, David W. Hogg, and Alexander J. Mendez. THE PRISM MULTI-OBJECT SURVEY (PRIMUS). II. DATA REDUCTION AND REDSHIFT FITTING. *The Astrophysical Journal*, 767(2):118, apr 2013. doi: 10.1088/0004-637x/767/2/118. URL https://doi.org/10.1088%2F0004-637x%2F767%2F2%2F118.

W. D. Cotton, J. J. Condon, K. I. Kellermann, M. Lacy, R. A. Perley, A. M. Matthews, T. Vernstrom, Douglas Scott, and J. V. Wall. The Angular Size Distribution of μJy Radio Sources. *ApJ*, 856(1):67, Mar 2018. doi: 10.3847/1538-4357/aaaec4.

L. L. Cowie, J. González-López, A. J. Barger, F. E. Bauer, L. Y. Hsu, and W. H. Wang. A Submillimeter Perspective on the GOODS Fields (SUPER GOODS). III. A Large Sample of ALMA Sources in the GOODS-S. *ApJ*, 865(2):106, October 2018. doi: 10.3847/1538-4357/aadc63.

R. Coziol, J. P. Torres-Papaqui, and H. Andernach. Comparing Narrow- and Broad-line AGNs in a New Diagnostic Diagram for Emission-line Galaxies Based on WISE Data. *AJ*, 149:192, June 2015. doi: 10.1088/0004-6256/149/6/192.

Roger Coziol, Heinz Andernach, Juan Pablo Torres-Papaqui, René Alberto Ortega-Minakata, and Froylan Moreno del Rio. What sparks the radio-loud phase of nearby quasars? *MNRAS*, 466: 921–944, April 2017. doi: 10.1093/mnras/stw3164.

D. J. Croton, V. Springel, S. D. M. White, G. De Lucia, C. S. Frenk, L. Gao, A. Jenkins, G. Kauffmann, J. F. Navarro, and N. Yoshida. The many lives of active galactic nuclei: cooling flows, black holes and the luminosities and colours of galaxies. *MNRAS*, 365:11–28, January 2006. doi: 10.1111/j.1365-2966.2005.09675.x.

Elisabete da Cunha, Stéphane Charlot, and David Elbaz. A simple model to interpret the ultraviolet, optical and infrared emission from galaxies. *MNRAS*, 388(4):1595–1617, August 2008. doi: 10.1111/j.1365-2966.2008.13535.x.

E. Daddi, A. Cimatti, A. Renzini, A. Fontana, M. Mignoli, L. Pozzetti, P. Tozzi, and G. Zamorani. A New Photometric Technique for the Joint Selection of Star-forming and Passive Galaxies at 1.4 <~z <~2.5. *ApJ*, 617(2):746–764, December 2004. doi: 10.1086/425569.

E. Daddi, M. Dickinson, G. Morrison, R. Chary, A. Cimatti, D. Elbaz, D. Frayer, A. Renzini, A. Pope, D. M. Alexander, F. E. Bauer, M. Giavalisco, M. Huynh, J. Kurk, and M. Mignoli. Multiwavelength Study of Massive Galaxies at z~2. I. Star Formation and Galaxy Growth. *ApJ*, 670(1):156–172, November 2007. doi: 10.1086/521818.

Romeel Davé, Daniel Anglés-Alcázar, Desika Narayanan, Qi Li, Mika H. Rafieferantsoa, and Sarah Appleby. SIMBA: Cosmological simulations with black hole growth and feedback. *MNRAS*, 486(2):2827–2849, June 2019. doi: 10.1093/mnras/stz937.

M. Davis, G. Efstathiou, C. S. Frenk, and S. D. M. White. The evolution of large-scale structure in a universe dominated by cold dark matter. *ApJ*, 292:371–394, May 1985. doi: 10.1086/163168.

Pratika Dayal and Andrea Ferrara. Early galaxy formation and its large-scale effects. *Phys. Rep.*, 780:1–64, December 2018. doi: 10.1016/j.physrep.2018.10.002.

T. de Jong, U. Klein, R. Wielebinski, and E. Wunderlich. Radio continuum and far-infrared emission from spiral galaxies : a close correlation. *A&A*, 147:L6–L9, June 1985.

J. Delhaize, V. Smolčić, I. Delvecchio, M. Novak, M. Sargent, N. Baran, B. Magnelli, G. Zamorani, E. Schinnerer, E. J. Murphy, M. Aravena, S. Berta, M. Bondi, P. Capak, C. Carilli, P. Ciliegi, F. Civano, O. Ilbert, A. Karim, C. Laigle, O. Le Fèvre, S. Marchesi, H. J. McCracken, M. Salvato, N. Seymour, and L. Tasca. The VLA-COSMOS 3 GHz Large Project: The infrared-radio correlation of star-forming galaxies and AGN to z $\lesssim$ 6. *A&A*, 602:A4, Jun 2017. doi: 10.1051/0004-6361/201629430.

I. Delvecchio, V. Smolčić, G. Zamorani, C. Del P. Lagos, S. Berta, J. Delhaize, N. Baran, D. M. Alexander, D. J. Rosario, V. Gonzalez-Perez, O. Ilbert, C. G. Lacey, O. Le Fèvre, O. Miettinen, M. Aravena, M. Bondi, C. Carilli, P. Ciliegi, K. Mooley, M. Novak, E. Schinnerer, P. Capak, F. Civano, N. Fanidakis, N. Herrera Ruiz, A. Karim, C. Laigle, S. Marchesi, H. J. McCracken, E. Middleberg, M. Salvato, and L. Tasca. The VLA-COSMOS 3 GHz Large Project: AGN and host-galaxy properties out to z $\lesssim$ 6. *A&A*, 602:A3, June 2017. doi: 10.1051/0004-6361/201629367.

I. Delvecchio, E. Daddi, M. T. Sargent, M. J. Jarvis, D. Elbaz, S. Jin, D. Liu, I. H. Whittam, H. Algera, R. Carraro, C. D'Eugenio, J. Delhaize, B. Kalita, S. Leslie, D. Cs. Molnar, M. Novak, I. Prandoni, V. Smolcic, Y. Ao, M. Aravena, F. Bournaud, J. D. Collier, S. M. Randriamampandry, Z. Randriamanakoto, G. Rodighiero, J. Schober, S. V. White, and G. Zamorani. The infrared-radio correlation of star-forming galaxies is strongly $M_\star$-dependent but nearly redshift-invariant since z$\sim$4. *arXiv e-prints*, art. arXiv:2010.05510, October 2020.

M. Dietrich, S. Mathur, D. M. Terndrup, P. B. Hall, K. M. Leighly, and S. D. Barber. Absorption-Line Variability of Broad-Absorption Line Quasars. In G. Chartas, F. Hamann, and K. M. Leighly, editors, *AGN Winds in Charleston*, volume 460 of *Astronomical Society of the Pacific Conference Series*, page 101, August 2012.

H. Dole, G. Lagache, J. L. Puget, K. I. Caputi, N. Fernández-Conde, E. Le Floc'h, C. Papovich, P. G. Pérez-González, G. H. Rieke, and M. Blaylock. The cosmic infrared background resolved by Spitzer. Contributions of mid-infrared galaxies to the far-infrared background. *A&A*, 451 (2):417–429, May 2006. doi: 10.1051/0004-6361:20054446.

Alyssa B. Drake, Chris Simpson, Chris A. Collins, Phil A. James, Ivan K. Baldry, Masami Ouchi, Matt J. Jarvis, David G. Bonfield, Yoshiaki Ono, Philip N. Best, Gavin B. Dalton, James S. Dunlop, Ross J. McLure, and Daniel J. B. Smith. Evolution of star formation in the UKIDSS Ultra Deep Survey field - I. Luminosity functions and cosmic star formation rate out to z = 1.6. *MNRAS*, 433(1):796–811, July 2013. doi: 10.1093/mnras/stt775.

U. Dudzevičiūtė, Ian Smail, A. M. Swinbank, S. M. Stach, O. Almaini, E. da Cunha, Fang Xia An, V. Arumugam, J. Birkin, A. W. Blain, S. C. Chapman, C. C. Chen, C. J. Conselice, K. E. K. Coppin, J. S. Dunlop, D. Farrah, J. E. Geach, B. Gullberg, W. G. Hartley, J. A. Hodge, R. J. Ivison, D. T. Maltby, D. Scott, C. J. Simpson, J. M. Simpson, A. P. Thomson, F. Walter, J. L. Wardlow, A. Weiss, and P. van der Werf. An ALMA survey of the SCUBA-2 CLS UDS field: physical properties of 707 sub-millimetre galaxies. *MNRAS*, 494(3):3828–3860, April 2020a. doi: 10.1093/mnras/staa769.

U. Dudzevičiūtė, Ian Smail, A. M. Swinbank, S. M. Stach, O. Almaini, E. da Cunha, Fang Xia An, V. Arumugam, J. Birkin, A. W. Blain, S. C. Chapman, C. C. Chen, C. J. Conselice, K. E. K. Coppin, J. S. Dunlop, D. Farrah, J. E. Geach, B. Gullberg, W. G. Hartley, J. A. Hodge, R. J. Ivison, D. T. Maltby, D. Scott, C. J. Simpson, J. M. Simpson, A. P. Thomson, F. Walter, J. L. Wardlow, A. Weiss, and P. van der Werf. An ALMA survey of the SCUBA-2 CLS UDS field: physical properties of 707 sub-millimetre galaxies. *MNRAS*, 494(3):3828–3860, May 2020b. doi: 10.1093/mnras/staa769.

J. S. Dunlop, R. J. McLure, M. J. Kukula, S. A. Baum, C. P. O'Dea, and D. H. Hughes. Quasars, their host galaxies and their central black holes. *MNRAS*, 340:1095–1135, April 2003. doi: 10.1046/j.1365-8711.2003.06333.x.

J. S. Dunlop, R. J. McLure, A. D. Biggs, J. E. Geach, M. J. Michałowski, R. J. Ivison, W. Rujopakarn, E. van Kampen, A. Kirkpatrick, A. Pope, D. Scott, A. M. Swinbank, T. A. Targett, I. Aretxaga, J. E. Austermann, P. N. Best, V. A. Bruce, E. L. Chapin, S. Charlot, M. Cirasuolo, K. Coppin, R. S. Ellis, S. L. Finkelstein, C. C. Hayward, D. H. Hughes, E. Ibar, P. Jagannathan, S. Khochfar, M. P. Koprowski, D. Narayanan, K. Nyland, C. Papovich, J. A. Peacock, G. H. Rieke, B. Robertson, T. Vernstrom, P. P. van der Werf, G. W. Wilson, and M. Yun. A deep ALMA image of the Hubble Ultra Deep Field. *MNRAS*, 466(1):861–883, April 2017. doi: 10.1093/mnras/stw3088.

L. Dunne, R. J. Ivison, S. Maddox, M. Cirasuolo, A. M. Mortier, S. Foucaud, E. Ibar, O. Almaini, C. Simpson, and R. McLure. The star formation history of K-selected galaxies. *MNRAS*, 394: 3–20, March 2009. doi: 10.1111/j.1365-2966.2008.13900.x.

D. J. Eisenstein, D. H. Weinberg, E. Agol, H. Aihara, C. Allende Prieto, S. F. Anderson, J. A. Arns, É. Aubourg, S. Bailey, E. Balbinot, and et al. SDSS-III: Massive Spectroscopic Surveys of the Distant Universe, the Milky Way, and Extra-Solar Planetary Systems. *AJ*, 142:72, September 2011. doi: 10.1088/0004-6256/142/3/72.

F. R. Elder, A. M. Gurewitsch, R. V. Langmuir, and H. C. Pollock. Radiation from Electrons in a Synchrotron. *Physical Review*, 71:829–830, June 1947. doi: 10.1103/PhysRev.71.829.5.

J. Emerson and W. Sutherland. The Visible and Infrared Survey Telescope for Astronomy (VISTA): Looking Back at Commissioning. *The Messenger*, 139:2–5, March 2010.

H. I. Ewen and E. M. Purcell. Observation of a Line in the Galactic Radio Spectrum: Radiation from Galactic Hydrogen at 1,420 Mc./sec. *Nature*, 168(4270):356, September 1951. doi: 10.1038/168356a0.

H. Falcke and P. L. Biermann. The jet-disk symbiosis. I. Radio to X-ray emission models for quasars. *A&A*, 293:665–682, January 1995.

X. Fan. Simulation of Stellar Objects in SDSS Color Space. *AJ*, 117:2528–2551, May 1999. doi: 10.1086/300848.

Xiaohui Fan, Vijay K. Narayanan, Robert H. Lupton, Michael A. Strauss, Gillian R. Knapp, Robert H. Becker, Richard L. White, Laura Pentericci, S. K. Leggett, Zoltán Haiman, James E. Gunn, Željko Ivezić, Donald P. Schneider, Scott F. Anderson, J. Brinkmann, Neta A. Bahcall, Andrew J. Connolly, István Csabai, Mamoru Doi, Masataka Fukugita, Tom Geballe, Eva K. Grebel, Daniel Harbeck, Gregory Hennessy, Don Q. Lamb, Gajus Miknaitis, Jeffrey A. Munn, Robert Nichol, Sadanori Okamura, Jeffrey R. Pier, Francisco Prada, Gordon T. Richards, Alex Szalay, and Donald G. York. A Survey of z>5.8 Quasars in the Sloan Digital Sky Survey. I. Discovery of Three New Quasars and the Spatial Density of Luminous Quasars at z˜6. *AJ*, 122:2833–2849, December 2001. doi: 10.1086/324111.

B. L. Fanaroff and J. M. Riley. The morphology of extragalactic radio sources of high and low luminosity. *MNRAS*, 167:31P–36P, May 1974. doi: 10.1093/mnras/167.1.31P.

A. Feoli and L. Mancini. A Hertzsprung-Russell-like Diagram for Galaxies: The M $_{\text{ffl}}$ Versus M $_{G}\sigma^2$ Relation. *ApJ*, 703:1502–1510, October 2009. doi: 10.1088/0004-637X/703/2/1502.

C. A. C. Fernandes, M. J. Jarvis, S. Rawlings, A. Martínez-Sansigre, E. Hatziminaoglou, M. Lacy, M. J. Page, J. A. Stevens, and E. Vardoulaki. Evidence for a maximum jet efficiency for the most powerful radio galaxies. *MNRAS*, 411:1909–1916, March 2011. doi: 10.1111/j.1365-2966.2010.17820.x.

F. Feroz, M. P. Hobson, and M. Bridges. MULTINEST: an efficient and robust Bayesian inference tool for cosmology and particle physics. *MNRAS*, 398:1601–1614, October 2009a. doi: 10.1111/j.1365-2966.2009.14548.x.

F. Feroz, M. P. Hobson, J. T. L. Zwart, R. D. E. Saunders, and K. J. B. Grainge. Bayesian modelling of clusters of galaxies from multifrequency-pointed Sunyaev-Zel'dovich observations. *MNRAS*, 398:2049–2060, October 2009b. doi: 10.1111/j.1365-2966.2009.15247.x.

L. Ferrarese and D. Merritt. A Fundamental Relation between Supermassive Black Holes and Their Host Galaxies. *ApJ*, 539:L9–L12, August 2000. doi: 10.1086/312838.

E. B. Fomalont, K. I. Kellermann, J. V. Wall, and D. Weistrop. A Deep 6-Centimeter Radio Source Survey. *Science*, 225(4657):23–28, July 1984. doi: 10.1126/science.225.4657.23.

M. Franco, D. Elbaz, L. Zhou, B. Magnelli, C. Schreiber, L. Ciesla, M. Dickinson, N. Nagar, G. Magdis, D. M. Alexander, M. Béthermin, R. Demarco, E. Daddi, T. Wang, J. Mullaney, M. Sargent, H. Inami, X. Shu, F. Bournaud, R. Chary, H. Ferguson, S. L. Finkelstein, M. Giavalisco, C. Gómez-Guijarro, D. Iono, S. Juneau, G. Lagache, L. Lin, K. Motohara, K. Okumura, M. Pannella, C. Papovich, A. Pope, W. Rujopakarn, J. Silverman, and M. Xiao. GOODS-ALMA: The slow downfall of star-formation in z = 2-3 massive galaxies. *arXiv e-prints*, art. arXiv:2005.03043, May 2020.

T. M. O. Franzen, C. A. Jackson, A. R. Offringa, R. D. Ekers, R. B. Wayth, G. Bernardi, J. D. Bowman, F. Briggs, R. J. Cappallo, A. A. Deshpand e, B. M. Gaensler, L. J. Greenhill, B. J. Hazelton, M. Johnston-Hollitt, D. L. Kaplan, C. J. Lonsdale, S. R. McWhirter, D. A. Mitchell, M. F. Morales, E. Morgan, J. Morgan, D. Oberoi, S. M. Ord, T. Prabu, N. Seymour, N. Udaya Shankar, K. S. Srivani, R. Subrahmanyan, S. J. Tingay, C. M. Trott, R. L. Webster, A. Williams, and C. L. Williams. The 154 MHz radio sky observed by the Murchison Widefield Array: noise, confusion, and first source count analyses. *MNRAS*, 459(3):3314–3325, July 2016. doi: 10.1093/mnras/stw823.

Yasmin Friedmann and François Bouchet. Fluctuation analysis of the far-infrared background - information from the confusion. *MNRAS*, 348(3):737–744, March 2004. doi: 10.1111/j.1365-2966.2004.07323.x.

Timothy Garn and Paul Alexander. Radio source stacking and the infrared/radio correlation at μJy flux densities. *MNRAS*, 394(1):105–116, March 2009. doi: 10.1111/j.1365-2966.2008.14296.x.

Eric Gawiser, Harold Francke, Kamson Lai, Kevin Schawinski, Caryl Gronwall, Robin Ciardullo, Ryan Quadri, Alvaro Orsi, L. Felipe Barrientos, Guillermo A. Blanc, Giovanni Fazio, John J. Feldmeier, Jia-sheng Huang, Leopoldo Infante, Paulina Lira, Nelson Padilla, Edward N. Taylor, Ezequiel Treister, C. Megan Urry, Pieter G. van Dokkum, and Shanil N. Virani. Lyα-Emitting Galaxies at z = 3.1: L* Progenitors Experiencing Rapid Star Formation. *ApJ*, 671(1):278–284, December 2007. doi: 10.1086/522955.

J. E. Geach, J. S. Dunlop, M. Halpern, Ian Smail, P. van der Werf, D. M. Alexander, O. Almaini, I. Aretxaga, V. Arumugam, V. Asboth, M. Banerji, J. Beanlands, P. N. Best, A. W. Blain, M. Birkinshaw, E. L. Chapin, S. C. Chapman, C. C. Chen, A. Chrysostomou, C. Clarke, D. L. Clements, C. Conselice, K. E. K. Coppin, W. I. Cowley, A. L. R. Danielson, S. Eales, A. C. Edge, D. Farrah, A. Gibb, C. M. Harrison, N. K. Hine, D. Hughes, R. J. Ivison, M. Jarvis, T. Jenness, S. F. Jones, A. Karim, M. Koprowski, K. K. Knudsen, C. G. Lacey, T. Mackenzie, G. Marsden, K. McAlpine, R. McMahon, R. Meijerink, M. J. Michałowski, S. J. Oliver, M. J. Page, J. A. Peacock, D. Rigopoulou, E. I. Robson, I. Roseboom, K. Rotermund, Douglas Scott, S. Serjeant, C. Simpson, J. M. Simpson, D. J. B. Smith, M. Spaans, F. Stanley, J. A. Stevens, A. M. Swinbank, T. Targett, A. P. Thomson, E. Valiante, D. A. Wake, T. M. A. Webb, C. Willott, J. A. Zavala, and M. Zemcov. The SCUBA-2 Cosmology Legacy Survey: 850 μm maps, catalogues and number counts. *MNRAS*, 465(2):1789–1806, February 2017. doi: 10.1093/mnras/stw2721.

K. Gebhardt, R. Bender, G. Bower, A. Dressler, S. M. Faber, A. V. Filippenko, R. Green, C. Grillmair, L. C. Ho, J. Kormendy, T. R. Lauer, J. Magorrian, J. Pinkney, D. Richstone, and S. Tremaine. A Relationship between Nuclear Black Hole Mass and Galaxy Velocity Dispersion. *ApJ*, 539:L13–L16, August 2000. doi: 10.1086/312840.

Gabriele Ghisellini, Paul W. Guilbert, and Roland Svensson. The Synchrotron Boiler. *ApJ*, 334: L5, November 1988. doi: 10.1086/185300.

V. L. Ginzburg and S. I. Syrovatskii. Cosmic Magnetobremsstrahlung (synchrotron Radiation). *ARA&A*, 3:297, January 1965. doi: 10.1146/annurev.aa.03.090165.001501.

Philipp Girichidis, Stella S. R. Offner, Alexei G. Kritsuk, Ralf S. Klessen, Patrick Hennebelle, J. M. Diederik Kruijssen, Martin G. H. Krause, Simon C. O. Glover, and Marco Padovani. Physical Processes in Star Formation. *Space Sci. Rev.*, 216(4):68, June 2020. doi: 10.1007/s11214-020-00693-8.

M. Glowacki, E. Elson, and R. Davé. The baryonic Tully-Fisher relation in the SIMBA simulation. *MNRAS*, August 2020. doi: 10.1093/mnras/staa2616.

Gopal-Krishna and P. J. Wiita. Extragalactic radio sources with hybrid morphology: implications for the Fanaroff-Riley dichotomy. *A&A*, 363:507–516, November 2000.

G. L. Granato, G. De Zotti, L. Silva, A. Bressan, and L. Danese. A Physical Model for the Coevolution of QSOs and Their Spheroidal Hosts. *ApJ*, 600:580–594, January 2004. doi: 10.1086/379875.

J. E. Greene, L. C. Ho, and A. J. Barth. Black Holes in Pseudobulges and Spheroidals: A Change in the Black Hole-Bulge Scaling Relations at Low Mass. *ApJ*, 688:159–179, November 2008. doi: 10.1086/592078.

C. Gruppioni, F. Pozzi, G. Rodighiero, I. Delvecchio, S. Berta, L. Pozzetti, G. Zamorani, P. Andreani, A. Cimatti, O. Ilbert, E. Le Floc'h, D. Lutz, B. Magnelli, L. Marchetti, P. Monaco, R. Nordon, S. Oliver, P. Popesso, L. Riguccini, I. Roseboom, D. J. Rosario, M. Sargent, M. Vaccari, B. Altieri, H. Aussel, A. Bongiovanni, J. Cepa, E. Daddi, H. Domínguez-Sánchez, D. Elbaz, N. Förster Schreiber, R. Genzel, A. Iribarrem, M. Magliocchetti, R. Maiolino, A. Poglitsch, A. Pérez García, M. Sanchez-Portal, E. Sturm, L. Tacconi, I. Valtchanov, A. Amblard, V. Arumugam, M. Bethermin, J. Bock, A. Boselli, V. Buat, D. Burgarella, N. Castro-Rodríguez, A. Cava, P. Chanial, D. L. Clements, A. Conley, A. Cooray, C. D. Dowell, E. Dwek, S. Eales, A. Franceschini, J. Glenn, M. Griffin, E. Hatziminaoglou, E. Ibar, K. Isaak, R. J. Ivison, G. Lagache, L. Levenson, N. Lu, S. Madden, B. Maffei, G. Mainetti, H. T. Nguyen, B. O'Halloran, M. J. Page, P. Panuzzo, A. Papageorgiou, C. P. Pearson, I. Pérez-Fournon, M. Pohlen, D. Rigopoulou, M. Rowan-Robinson, B. Schulz, D. Scott, N. Seymour, D. L. Shupe, A. J. Smith, J. A. Stevens, M. Symeonidis, M. Trichas, K. E. Tugwell, L. Vigroux, L. Wang, G. Wright, C. K. Xu, M. Zemcov, S. Bardelli, M. Carollo, T. Contini, O. Le Févre, S. Lilly, V. Mainieri, A. Renzini, M. Scodeggio, and E. Zucca. The Herschel PEP/HerMES luminosity function - I. Probing the evolution of PACS selected Galaxies to z 4. *MNRAS*, 432(1):23–52, Jun 2013. doi: 10.1093/mnras/stt308.

C. Gruppioni, M. Bethermin, F. Loiacono, O. Le Fevre, P. Capak, P. Cassata, A. L. Faisst, D. Schaerer, J. Silverman, L. Yan, S. Bardelli, M. Boquien, R. Carraro, A. Cimatti, M. Dessauges-Zavadsky, M. Ginolfi, S. Fujimoto, N. P. Hathi, G. C. Jones, Y. Khusanova, A. M. Koekemoer, G. Lagache, B. C. Lemaux, P. Oesch, F. Pozzi, D. A. Riechers, G. Rodighiero, M. Romano, M. Talia, L. Vallini, D. Vergani, G. Zamorani, and E. Zucca. The ALPINE-ALMA [CII] Survey: nature, luminosity function and star formation history of continuum non-target galaxies up to z~6. *arXiv e-prints*, art. arXiv:2006.04974, June 2020.

Carlotta Gruppioni and Francesca Pozzi. On the existence of bright IR galaxies at z > 2: tension between Herschel and SCUBA-2 results? *MNRAS*, 483(2):1993–1999, February 2019. doi: 10.1093/mnras/sty3278.

D. Guidetti, M. Bondi, I. Prandoni, R. J. Beswick, T. W. B. Muxlow, N. Wrigley, I. Smail, and I. McHardy. e-MERLIN observations at 5 GHz of the GOODS-N region: pinpointing AGN cores in high-redshift galaxies. *MNRAS*, 432(4):2798–2807, Jul 2013. doi: 10.1093/mnras/stt633.

D. Guidetti, M. Bondi, I. Prandoni, T. W. B. Muxlow, R. Beswick, N. Wrigley, I. Smail, I. McHardy, A. P. Thomson, J. Radcliffe, and M. K. Argo. The eMERGE Survey - I: Very Large Array 5.5 GHz observations of the GOODS-North Field. *MNRAS*, 471(1):210–226, Oct 2017. doi: 10.1093/mnras/stx1162.

G. Gürkan, M. Hardcastle, P. Best, L. Morabito, I. Prandoni, M. Jarvis, K. Duncan, G. Calistro Rivera, J. Callingham, R. Cochrane, J. Croston, G. Heald, B. Mingo, S. Mooney, J. Sabater, H. Röttgering, T. Shimwell, D. Smith, C. Tasse, and W. Williams. LoTSS/HETDEX: Optical quasars I. Low-frequency radio properties of optically selected quasars. *arXiv e-prints*, November 2018a.

G. Gürkan, M. J. Hardcastle, D. J. B. Smith, P. N. Best, N. Bourne, G. Calistro-Rivera, G. Heald, M. J. Jarvis, I. Prandoni, H. J. A. Röttgering, J. Sabater, T. Shimwell, C. Tasse, and W. L. Williams. LOFAR/H-ATLAS: the low-frequency radio luminosity-star formation rate relation. *MNRAS*, 475(3):3010–3028, April 2018b. doi: 10.1093/mnras/sty016.

Gülay Gürkan, M. J. Hardcastle, P. N. Best, L. K. Morabito, I. Prandoni, M. J. Jarvis, K. J. Duncan, G. Calistro Rivera, J. R. Callingham, R. K. Cochrane, J. H. Croston, G. Heald, B. Mingo, S. Mooney, J. Sabater, H. J. A. Röttgering, T. W. Shimwell, D. J. B. Smith, C. Tasse, and W. L. Williams. LoTSS/HETDEX: Optical quasars. I. Low-frequency radio properties of optically selected quasars. *A&A*, 622:A11, Feb 2019. doi: 10.1051/0004-6361/201833892.

C. L. Hale, A. S. G. Robotham, L. J. M. Davies, M. J. Jarvis, S. P. Driver, and I. Heywood. Radio source extraction with PROFOUND. *MNRAS*, 487(3):3971–3989, August 2019. doi: 10.1093/mnras/stz1462.

C. A. Hales, T. Murphy, J. R. Curran, E. Middelberg, B. M. Gaensler, and R. P. Norris. BLOBCAT: software to catalogue flood-filled blobs in radio images of total intensity and linear polarization. *MNRAS*, 425(2):979–996, September 2012. doi: 10.1111/j.1365-2966.2012.21373.x.

Martin Hardcastle. The X-ray nuclei of FRII radio galaxies: unification and accretion modes. XMM-Newton Proposal, October 2007.

P. Hartley, N. Jackson, D. Sluse, H. R. Stacey, and H. Vives-Arias. Strong lensing reveals jets in a sub-microJy radio-quiet quasar. *MNRAS*, 485(3):3009–3023, May 2019. doi: 10.1093/mnras/stz510.

Jeremy J. Harwood, Tessa Vernstrom, and Andra Stroe. Unveiling the cause of hybrid morphology radio sources (HyMoRS). *MNRAS*, 491(1):803–822, January 2020. doi: 10.1093/mnras/stz3069.

G. Hasinger, P. Capak, M. Salvato, A. J. Barger, L. L. Cowie, A. Faisst, S. Hemmati, Y. Kakazu, J. Kartaltepe, D. Masters, B. Mobasher, H. Nayyeri, D. Sanders, N. Z. Scoville, H. Suh, C. Steinhardt, and Fengwei Yang. The DEIMOS 10K Spectroscopic Survey Catalog of the COSMOS Field. *ApJ*, 858(2):77, May 2018. doi: 10.3847/1538-4357/aabacf.

N. A. Hatch, D. Wylezalek, J. D. Kurk, D. Stern, C. De Breuck, M. J. Jarvis, A. Galametz, A. H. Gonzalez, W. G. Hartley, A. Mortlock, N. Seymour, and J. A. Stevens. Why z > 1 radio-loud galaxies are commonly located in protoclusters. *MNRAS*, 445(1):280–289, Nov 2014. doi: 10.1093/mnras/stu1725.

E. Haug. Electron-positron bremsstrahlung in thermal plasmas - Simple analytical FITS. *A&A*, 178(1-2):292, May 1987.

E. Haug. Efficient computation of electron-electron bremsstrahlung emission in a hot thermal plasma. *A&A*, 218(1-2):330–333, July 1989.

Christopher C. Hayward, Lauranne Lanz, Matthew L. N. Ashby, Giovanni Fazio, Lars Hernquist, Juan Rafael Martínez-Galarza, Kai Noeske, Howard A. Smith, Stijn Wuyts, and Andreas Zezas. The total infrared luminosity may significantly overestimate the star formation rate of quenching and recently quenched galaxies. *MNRAS*, 445(2):1598–1604, December 2014. doi: 10.1093/mnras/stu1843.

N. Herrera Ruiz, E. Middelberg, R. P. Norris, and A. Maini. Unveiling the origin of the radio emission in radio-quiet quasars. *A&A*, 589:L2, May 2016. doi: 10.1051/0004-6361/201628302.

A. Hewish. Extrapolation of the number-flux density relation of radio stars by Scheuer's statistical methods. *MNRAS*, 123:167, January 1961. doi: 10.1093/mnras/123.2.167.

A. Hewish, S. J. Bell, J. D. H. Pilkington, P. F. Scott, and R. A. Collins. Observation of a Rapidly Pulsating Radio Source. *Nature*, 217(5130):709–713, February 1968. doi: 10.1038/217709a0.

Mark Heyer and T. M. Dame. Molecular Clouds in the Milky Way. *ARA&A*, 53:583–629, August 2015. doi: 10.1146/annurev-astro-082214-122324.

I. Heywood, C. L. Hale, M. J. Jarvis, S. Makhathini, J. A. Peters, M. L. L. Sebokolodi, and O. M. Smirnov. VLA imaging of the XMM-LSS/VIDEO deep field at 1-2 GHz. *MNRAS*, 496(3):3469–3481, June 2020. doi: 10.1093/mnras/staa1770.

J. A. Hodge, R. H. Becker, R. L. White, and W. H. de Vries. Radio Detection of Radio-Quiet Galaxies. *AJ*, 136:1097–1109, September 2008. doi: 10.1088/0004-6256/136/3/1097.

David W. Hogg, G. Neugebauer, Lee Armus, K. Matthews, Michael A. Pahre, B. T. Soifer, and A. J. Weinberger. Near Infrared Imaging of the Hubble Deep Field with the Keck Telescope. *AJ*, 113:474–482, February 1997. doi: 10.1086/118269.

E. J. Hooper, C. D. Impey, C. B. Foltz, and P. C. Hewett. The Radio Properties of Optically Selected Quasars. III. Comparison between Optical and X-Ray Selected Samples. *ApJ*, 473:746, December 1996. doi: 10.1086/178186.

A. M. Hopkins, N. M. McClure-Griffiths, and B. M. Gaensler. Linked Evolution of Gas and Star Formation in Galaxies Over Cosmic History. *ApJ*, 682:L13, July 2008. doi: 10.1086/590494.

P. F. Hopkins, L. Hernquist, T. J. Cox, T. Di Matteo, B. Robertson, and V. Springel. A Unified, Merger-driven Model of the Origin of Starbursts, Quasars, the Cosmic X-Ray Background, Supermassive Black Holes, and Galaxy Spheroids. *ApJS*, 163:1–49, March 2006. doi: 10.1086/499298.

E. P. Hubble. NGC 6822, a remote stellar system. *ApJ*, 62, December 1925. doi: 10.1086/142943.

Edwin Hubble, S Rosseland, J. M., and R. C. J. A. Astronomy. (Scientific Books: The Realm of the Nebulae; Theoretical Astrophysics). *Science*, 84:509–510, December 1936. doi: 10.1126/science.84.2188.509.

Minh T. Huynh, Carole A. Jackson, Ray P. Norris, and Alberto Fernand ez-Soto. Radio Observations of the Hubble Deep Field-South Region. Iv. Optical Properties of the Faint Radio Population. *AJ*, 135(6):2470–2495, June 2008. doi: 10.1088/0004-6256/135/6/2470.

H.-C. Hwang, N. L. Zakamska, R. M. Alexandroff, F. Hamann, J. E. Greene, S. Perrotta, and G. T. Richards. Winds as the origin of radio emission in z = 2.5 radio-quiet extremely red quasars. *MNRAS*, 477:830–844, June 2018. doi: 10.1093/mnras/sty742.

E. Ibar, R. J. Ivison, A. D. Biggs, D. V. Lal, P. N. Best, and D. A. Green. Deep multi-frequency radio imaging in the Lockman Hole using the GMRT and VLA - I. The nature of the sub-mJy radio population. *MNRAS*, 397:281–298, July 2009. doi: 10.1111/j.1365-2966.2009.14866.x.

O. Ilbert, P. Capak, M. Salvato, H. Aussel, H. J. McCracken, D. B. Sanders, N. Scoville, J. Kartaltepe, S. Arnouts, E. Le Floc'h, B. Mobasher, Y. Taniguchi, F. Lamareille, A. Leauthaud, S. Sasaki, D. Thompson, M. Zamojski, G. Zamorani, S. Bardelli, M. Bolzonella, A. Bongiorno, M. Brusa, K. I. Caputi, C. M. Carollo, T. Contini, R. Cook, G. Coppa, O. Cucciati, S. de la Torre, L. de Ravel, P. Franzetti, B. Garilli, G. Hasinger, A. Iovino, P. Kampczyk, J. P. Kneib, C. Knobel, K. Kovac, J. F. Le Borgne, V. Le Brun, O. Le Fèvre, S. Lilly, D. Looper, C. Maier, V. Mainieri, Y. Mellier, M. Mignoli, T. Murayama, R. Pellò, Y. Peng, E. Pérez-Montero, A. Renzini, E. Ricciardelli, D. Schiminovich, M. Scodeggio, Y. Shioya, J. Silverman, J. Surace, M. Tanaka, L. Tasca, L. Tresse, D. Vergani, and E. Zucca. Cosmos Photometric Redshifts with 30-Bands for 2-deg^2. *ApJ*, 690(2):1236–1249, January 2009. doi: 10.1088/0004-637X/690/2/1236.

O. Ilbert, H. J. McCracken, O. Le Fèvre, P. Capak, J. Dunlop, A. Karim, M. A. Renzini, K. Caputi, S. Boissier, S. Arnouts, H. Aussel, J. Comparat, Q. Guo, P. Hudelot, J. Kartaltepe, J. P. Kneib, J. K. Krogager, E. Le Floc'h, S. Lilly, Y. Mellier, B. Milvang-Jensen, T. Moutard, M. Onodera, J. Richard, M. Salvato, D. B. Sanders, N. Scoville, J. D. Silverman, Y. Taniguchi, L. Tasca, R. Thomas, S. Toft, L. Tresse, D. Vergani, M. Wolk, and A. Zirm. Mass assembly in quiescent and star-forming galaxies since z 4 from UltraVISTA. *A&A*, 556:A55, August 2013. doi: 10.1051/0004-6361/201321100.

Ž. Ivezić, R. H. Becker, M. Blanton, X. Fan, K. Finlator, J. E. Gunn, P. Hall, R. S. J. Kim, G. R. Knapp, J. Loveday, R. H. Lupton, K. Menou, V. Narayanan, G. R. Richards, C. M. Rockosi, D. Schlegel, D. P. Schneider, I. Strateva, M. A. Strauss, D. vanden Berk, W. Voges, B. Yanny, and SDSS Collaboration. The Optical, Infrared and Radio Properties of Extragalactic Sources Observed by SDSS, 2MASS and FIRST Surveys. In R. F. Green, E. Y. Khachikian, and D. B. Sanders, editors, *IAU Colloq. 184: AGN Surveys*, volume 284 of *Astronomical Society of the Pacific Conference Series*, page 137, 2002.

Knud Jahnke and Andrea V. Macciò. The non-causal origin of the black-hole-galaxy scaling relations. *The Astrophysical Journal*, 734(2):92, 2011. URL http://stacks.iop.org/0004-637X/734/i=2/a=92.

Karl G. Jansky. Radio Waves from Outside the Solar System. *Nature*, 132(3323):66, July 1933. doi: 10.1038/132066a0.

M. Jarvis, N. Seymour, J. Afonso, P. Best, R. Beswick, I. Heywood, M. Huynh, E. Murphy, I. Prandoni, E. Schinnerer, C. Simpson, M. Vaccari, and S. White. The star-formation history of the Universe with the SKA. In *Advancing Astrophysics with the Square Kilometre Array (AASKA14)*, page 68, April 2015.

M. Jarvis, R. Taylor, I. Agudo, J. R. Allison, R. P. Deane, B. Frank, N. Gupta, I. Heywood, N. Maddox, K. McAlpine, M. Santos, A. M. M. Scaife, M. Vaccari, J. T. L. Zwart, E. Adams, D. J. Bacon, A. J. Baker, B. A. Bassett, P. N. Best, R. Beswick, S. Blyth, M. L. Brown, M. Bruggen, M. Cluver, S. Colafrancesco, G. Cotter, C. Cress, R. Davé, C. Ferrari, M. J. Hardcastle, C. L. Hale, I. Harrison, P. W. Hatfield, H. R. Klockner, S. Kolwa, E. Malefahlo, T. Marubini, T. Mauch, K. Moodley, R. Morganti, R. P. Norris, J. A. Peters, I. Prand oni, M. Prescott, S. Oliver, N. Oozeer, H. J. A. Rottgering, N. Seymour, C. Simpson, O. Smirnov, and D. J. B. Smith. The MeerKAT International GHz Tiered Extragalactic Exploration (MIGHTEE) Survey. In *MeerKAT Science: On the Pathway to the SKA*, page 6, January 2016.

M. E. Jarvis, C. M. Harrison, A. P. Thomson, C. Circosta, V. Mainieri, D. M. Alexander, A. C. Edge, G. B. Lansbury, S. J. Molyneux, and J. R. Mullaney. Prevalence of radio jets associated with galactic outflows and feedback from quasars. *MNRAS*, 485(2):2710–2730, May 2019. doi: 10.1093/mnras/stz556.

M. J. Jarvis and S. Rawlings. The accretion history of the universe with the SKA. *New Astron. Rev.*, 48:1173–1185, December 2004. doi: 10.1016/j.newar.2004.09.006.

M. J. Jarvis, D. G. Bonfield, V. A. Bruce, J. E. Geach, K. McAlpine, R. J. McLure, E. González-Solares, M. Irwin, J. Lewis, A. K. Yoldas, S. Andreon, N. J. G. Cross, J. P. Emerson, G. Dalton, J. S. Dunlop, S. T. Hodgkin, F. O. Le, M. Karouzos, K. Meisenheimer, S. Oliver, S. Rawlings, C. Simpson, I. Smail, D. J. B. Smith, M. Sullivan, W. Sutherland, S. V. White, and J. T. L. Zwart. The VISTA Deep Extragalactic Observations (VIDEO) survey. *MNRAS*, 428:1281–1295, January 2013. doi: 10.1093/mnras/sts118.

Matt J. Jarvis, Hanifa Teimourian, Chris Simpson, Daniel J. B. Smith, Steve Rawlings, and David Bonfield. The discovery of a typical radio galaxy at z = 4.88. *MNRAS*, 398(1):L83–L87, September 2009. doi: 10.1111/j.1745-3933.2009.00715.x.

Matt J. Jarvis, D. J. B. Smith, D. G. Bonfield, M. J. Hardcastle, J. T. Falder, J. A. Stevens, R. J. Ivison, R. Auld, M. Baes, I. K. Baldry, S. P. Bamford, N. Bourne, S. Buttiglione, A. Cava, A. Cooray, A. Dariush, G. de Zotti, J. S. Dunlop, L. Dunne, S. Dye, S. Eales, J. Fritz, D. T. Hill, R. Hopwood, D. H. Hughes, E. Ibar, D. H. Jones, L. Kelvin, A. Lawrence, L. Leeuw, J. Loveday, S. J. Maddox, M. J. Michałowski, M. Negrello, P. Norberg, M. Pohlen, M. Prescott, E. E. Rigby, A. Robotham, G. Rodighiero, D. Scott, R. Sharp, P. Temi, M. A. Thompson, P. van der Werf, E. van Kampen, C. Vlahakis, and G. White. Herschel-ATLAS: the far-infrared-radio correlation at z < 0.5. *MNRAS*, 409(1):92–101, November 2010. doi: 10.1111/j.1365-2966.2010.17772.x.

H. Jeffreys. *Theory of Probability*. Oxford: Clarendon Press, 1961.

L. Jiang, X. Fan, W. N. Brandt, C. L. Carilli, E. Egami, D. C. Hines, J. D. Kurk, G. T. Richards, Y. Shen, M. A. Strauss, M. Vestergaard, and F. Walter. Dust-free quasars in the early Universe. *Nature*, 464:380–383, March 2010. doi: 10.1038/nature08877.

Linhua Jiang, Xiaohui Fan, Željko Ivezić, Gordon T. Richards, Donald P. Schneider, Michael A. Strauss, and Brandon C. Kelly. The Radio-Loud Fraction of Quasars is a Strong Function of Redshift and Optical Luminosity. *ApJ*, 656(2):680–690, Feb 2007. doi: 10.1086/510831.

E. F. Jiménez-Andrade, B. Magnelli, A. Karim, G. Zamorani, M. Bondi, E. Schinnerer, M. Sargent, E. Romano-Díaz, M. Novak, P. Lang, F. Bertoldi, E. Vardoulaki, S. Toft, V. Smolčić, K. Harrington, S. Leslie, J. Delhaize, D. Liu, C. Karoumpis, J. Kartaltepe, and A. M. Koekemoer. Radio continuum size evolution of star-forming galaxies over 0.35 < z < 2.25. *A&A*, 625:A114, May 2019. doi: 10.1051/0004-6361/201935178.

Russell Johnston, Mattia Vaccari, Matt Jarvis, Mathew Smith, Elodie Giovannoli, Boris Häußler, and Matthew Prescott. The evolving relation between star formation rate and stellar mass in the VIDEO survey since z = 3. *MNRAS*, 453(3):2540–2557, November 2015. doi: 10.1093/mnras/stv1715.

J. Jonas and MeerKAT Team. The MeerKAT Radio Telescope. In *MeerKAT Science: On the Pathway to the SKA*, page 1, January 2016.

P. M. W. Kalberla and J. Kerp. Anisotropies in the HI gas distribution toward 3C 196. *A&A*, 595:A37, October 2016. doi: 10.1051/0004-6361/201629113.

E. Kalfountzou, J. A. Stevens, M. J. Jarvis, M. J. Hardcastle, D. J. B. Smith, N. Bourne, L. Dunne, E. Ibar, S. Eales, R. J. Ivison, S. Maddox, M. W. L. Smith, E. Valiante, and G. de Zotti. Herschel-ATLAS: far-infrared properties of radio-loud and radio-quiet quasars. *MNRAS*, 442: 1181–1196, August 2014. doi: 10.1093/mnras/stu782.

A. Karim, E. Schinnerer, A. Martínez-Sansigre, M. T. Sargent, A. van der Wel, H.-W. Rix, O. Ilbert, V. Smolčić, C. Carilli, M. Pannella, A. M. Koekemoer, E. F. Bell, and M. Salvato. The Star Formation History of Mass-selected Galaxies in the COSMOS Field. *ApJ*, 730:61, April 2011. doi: 10.1088/0004-637X/730/2/61.

W. J. Karzas and R. Latter. Electron Radiative Transitions in a Coulomb Field. *ApJS*, 6:167, May 1961. doi: 10.1086/190063.

K. I. Kellermann, R. Sramek, M. Schmidt, D. B. Shaffer, and R. Green. VLA observations of objects in the Palomar Bright Quasar Survey. *AJ*, 98:1195–1207, October 1989. doi: 10.1086/115207.

K. I. Kellermann, E. B. Fomalont, V. Mainieri, P. Padovani, P. Rosati, P. Shaver, P. Tozzi, and N. Miller. The VLA Survey of the Chandra Deep Field-South. I. Overview and the Radio Data. *ApJS*, 179:71–94, November 2008. doi: 10.1086/591055.

K. I. Kellermann, J. J. Condon, A. E. Kimball, R. A. Perley, and Ž. Ivezić. Radio-loud and Radio-quiet QSOs. *ApJ*, 831:168, November 2016. doi: 10.3847/0004-637X/831/2/168.

Jr. Kennicutt, Robert C. Star Formation in Galaxies Along the Hubble Sequence. *ARA&A*, 36: 189–232, Jan 1998. doi: 10.1146/annurev.astro.36.1.189.

Robert C. Kennicutt and Neal J. Evans. Star Formation in the Milky Way and Nearby Galaxies. *ARA&A*, 50:531–608, September 2012. doi: 10.1146/annurev-astro-081811-125610.

Eh. E. Khachikian and D. W. Weedman. A spectroscopic study of luminous galactic nuclei. *Astrofizika*, 7:389–406, January 1971.

A. E. Kimball, K. I. Kellermann, J. J. Condon, Ž. Ivezić, and R. A. Perley. The Two-component Radio Luminosity Function of Quasi-stellar Objects: Star Formation and Active Galactic Nucleus. *ApJ*, 739:29, September 2011. doi: 10.1088/2041-8205/739/1/L29.

Amy E. Kimball and Željko Ivezić. A Unified Catalog of Radio Objects Detected by NVSS, First, WENSS, GB6, and SDSS. *AJ*, 136(2):684–712, August 2008. doi: 10.1088/0004-6256/136/2/684.

M. P. Koprowski, J. S. Dunlop, M. J. Michałowski, K. E. K. Coppin, J. E. Geach, R. J. McLure, D. Scott, and P. P. van der Werf. The evolving far-IR galaxy luminosity function and dust-obscured star formation rate density out to z5. *MNRAS*, 471(4):4155–4169, November 2017. doi: 10.1093/mnras/stx1843.

J. Kormendy and D. Richstone. Inward Bound—The Search For Supermassive Black Holes In Galactic Nuclei. *ARA&A*, 33:581, 1995. doi: 10.1146/annurev.aa.33.090195.003053.

Pavel Kroupa. On the variation of the initial mass function. *MNRAS*, 322(2):231–246, April 2001. doi: 10.1046/j.1365-8711.2001.04022.x.

J. M. Diederik Kruijssen. On the fraction of star formation occurring in bound stellar clusters. *MNRAS*, 426(4):3008–3040, November 2012. doi: 10.1111/j.1365-2966.2012.21923.x.

H. Kubo, T. Takahashi, G. Madejski, M. Tashiro, F. Makino, S. Inoue, and F. Takahara. ASCA Observations of Blazars and Multiband Analysis. *ApJ*, 504(2):693–701, September 1998. doi: 10.1086/306125.

Peter Kurczynski and Eric Gawiser. A Simultaneous Stacking and Deblending Algorithm for Astronomical Images. *AJ*, 139(4):1592–1599, April 2010. doi: 10.1088/0004-6256/139/4/1592.

M. Lacy, S. A. Laurent-Muehleisen, S. E. Ridgway, R. H. Becker, and R. L. White. The Radio Luminosity-Black Hole Mass Correlation for Quasars from the FIRST Bright Quasar Survey and a "Unification Scheme" for Radio-loud and Radio-quiet Quasars. *ApJ*, 551:L17–L21, April 2001. doi: 10.1086/319836.

C. Laigle, H. J. McCracken, O. Ilbert, B. C. Hsieh, I. Davidzon, P. Capak, G. Hasinger, J. D. Silverman, C. Pichon, J. Coupon, H. Aussel, D. Le Borgne, K. Caputi, P. Cassata, Y.-Y. Chang, F. Civano, J. Dunlop, J. Fynbo, J. S. Kartaltepe, A. Koekemoer, O. Le Fèvre, E. Le Floc'h, A. Leauthaud, S. Lilly, L. Lin, S. Marchesi, B. Milvang-Jensen, M. Salvato, D. B. Sanders, N. Scoville, V. Smolcic, M. Stockmann, Y. Taniguchi, L. Tasca, S. Toft, M. Vaccari, and J. Zabl. The COSMOS2015 Catalog: Exploring the 1 z 6 Universe with Half a Million Galaxies. *ApJS*, 224:24, June 2016. doi: 10.3847/0067-0049/224/2/24.

R. A. Laing, J. M. Riley, and M. S. Longair. Bright radio sources at 178 MHz : flux densities, optical identifications and the cosmological evolution of powerful radio galaxies. *MNRAS*, 204: 151–187, July 1983. doi: 10.1093/mnras/204.1.151.

A. Laor and E. Behar. On the origin of radio emission in radio-quiet quasars. *MNRAS*, 390: 847–862, October 2008. doi: 10.1111/j.1365-2966.2008.13806.x.

A. Laor, R. D. Baldi, and E. Behar. What drives the radio slopes in radio-quiet quasars? *MNRAS*, 482:5513–5523, February 2019. doi: 10.1093/mnras/sty3098.

Richard B. Larson. Dynamical models for the formation and evolution of spherical galaxies. *MNRAS*, 166:585–616, March 1974. doi: 10.1093/mnras/166.3.585.

Gregory Laughlin and Peter Bodenheimer. Luminosity Functions for Very Low Mass Stars and Brown Dwarfs. *ApJ*, 403:303, January 1993. doi: 10.1086/172203.

A. Lawrence, S. J. Warren, O. Almaini, A. C. Edge, N. C. Hambly, R. F. Jameson, P. Lucas, M. Casali, A. Adamson, S. Dye, J. P. Emerson, S. Foucaud, P. Hewett, P. Hirst, S. T. Hodgkin, M. J. Irwin, N. Lodieu, R. G. McMahon, C. Simpson, I. Smail, D. Mortlock, and M. Folger. The UKIRT Infrared Deep Sky Survey (UKIDSS). *MNRAS*, 379(4):1599–1617, August 2007. doi: 10.1111/j.1365-2966.2007.12040.x.

O. Le Fèvre, G. Vettolani, B. Garilli, L. Tresse, D. Bottini, V. Le Brun, D. Maccagni, J. P. Picat, R. Scaramella, M. Scodeggio, A. Zanichelli, C. Adami, M. Arnaboldi, S. Arnouts, S. Bardelli, M. Bolzonella, A. Cappi, S. Charlot, P. Ciliegi, T. Contini, S. Foucaud, P. Franzetti, I. Gavignaud, L. Guzzo, O. Ilbert, A. Iovino, H. J. McCracken, B. Marano, C. Marinoni, G. Mathez, A. Mazure, B. Meneux, R. Merighi, S. Paltani, R. Pellò, A. Pollo, L. Pozzetti, M. Radovich, G. Zamorani, E. Zucca, M. Bondi, A. Bongiorno, G. Busarello, F. Lamareille, Y. Mellier, P. Merluzzi, V. Ripepi, and D. Rizzo. The VIMOS VLT deep survey. First epoch VVDS-deep survey: 11 564 spectra with 17.5 $\leq$ IAB $\leq$ 24, and the redshift distribution over 0 $\leq$ z $\leq$ 5. *A&A*, 439 (3):845–862, September 2005. doi: 10.1051/0004-6361:20041960.

O. Le Fèvre, P. Cassata, O. Cucciati, B. Garilli, O. Ilbert, V. Le Brun, D. Maccagni, C. Moreau, M. Scodeggio, L. Tresse, G. Zamorani, C. Adami, S. Arnouts, S. Bardelli, M. Bolzonella, M. Bondi, A. Bongiorno, D. Bottini, A. Cappi, S. Charlot, P. Ciliegi, T. Contini, S. de la Torre, S. Foucaud, P. Franzetti, I. Gavignaud, L. Guzzo, A. Iovino, B. Lemaux, C. López-Sanjuan, H. J. McCracken, B. Marano, C. Marinoni, A. Mazure, Y. Mellier, R. Merighi, P. Merluzzi, S. Paltani, R. Pellò, A. Pollo, L. Pozzetti, R. Scaramella, L. Tasca, D. Vergani, G. Vettolani, A. Zanichelli, and E. Zucca. The VIMOS VLT Deep Survey final data release: a spectroscopic sample of 35 016 galaxies and AGN out to z ~6.7 selected with 17.5 $\leq$ i_{AB} $\leq$ 24.75. *A&A*, 559: A14, November 2013. doi: 10.1051/0004-6361/201322179.

Joel Leja, Sandro Tacchella, and Charlie Conroy. Beyond UVJ: More Efficient Selection of Quiescent Galaxies with Ultraviolet/Mid-infrared Fluxes. *ApJ*, 880(1):L9, July 2019. doi: 10.3847/2041-8213/ab2f8c.

Simon J. Lilly, Vincent Le Brun, Christian Maier, Vincenzo Mainieri, Marco Mignoli, Marco Scodeggio, Gianni Zamorani, Marcella Carollo, Thierry Contini, Jean-Paul Kneib, Olivier Le Fèvre, Alvio Renzini, Sandro Bardelli, Micol Bolzonella, Angela Bongiorno, Karina Caputi, Graziano Coppa, Olga Cucciati, Sylvain de la Torre, Loic de Ravel, Paolo Franzetti, Bianca Garilli, Angela Iovino, Pawel Kampczyk, Katarina Kovac, Christian Knobel, Fabrice Lamareille, Jean-Francois Le Borgne, Roser Pello, Yingjie Peng, Enrique Pérez-Montero, Elena Ricciardelli, John D. Silverman, Masayuki Tanaka, Lidia Tasca, Laurence Tresse, Daniela Vergani, Elena Zucca, Olivier Ilbert, Mara Salvato, Pascal Oesch, Umi Abbas, Dario Bottini, Peter Capak, Alberto Cappi, Paolo Cassata, Andrea Cimatti, Martin Elvis, Marco Fumana, Luigi Guzzo, Gunther Hasinger, Anton Koekemoer, Alexei Leauthaud, Dario Maccagni, Christian Marinoni, Henry McCracken, Pierdomenico Memeo, Baptiste Meneux, Cristiano Porciani, Lucia Pozzetti, David Sanders, Roberto Scaramella, Claudia Scarlata, Nick Scoville, Patrick Shopbell, and

Yoshiaki Taniguchi. The zCOSMOS 10k-Bright Spectroscopic Sample. *ApJS*, 184(2):218–229, October 2009. doi: 10.1088/0067-0049/184/2/218.

Daizhong Liu, Emanuele Daddi, Mark Dickinson, Frazer Owen, Maurilio Pannella, Mark Sargent, Matthieu Béthermin, Georgios Magdis, Yu Gao, Xinwen Shu, Tao Wang, Shuowen Jin, and Hanae Inami. "Super-deblended" Dust Emission in Galaxies. I. The GOODS-North Catalog and the Cosmic Star Formation Rate Density out to Redshift 6. *ApJ*, 853(2):172, February 2018. doi: 10.3847/1538-4357/aaa600.

D. Lutz, A. Poglitsch, B. Altieri, P. Andreani, H. Aussel, S. Berta, A. Bongiovanni, D. Brisbin, A. Cava, J. Cepa, A. Cimatti, E. Daddi, H. Dominguez-Sanchez, D. Elbaz, N. M. Förster Schreiber, R. Genzel, A. Grazian, C. Gruppioni, M. Harwit, E. Le Floc'h, G. Magdis, B. Magnelli, R. Maiolino, R. Nordon, A. M. Pérez García, P. Popesso, F. Pozzi, L. Riguccini, G. Rodighiero, A. Saintonge, M. Sanchez Portal, P. Santini, L. Shao, E. Sturm, L. J. Tacconi, I. Valtchanov, M. Wetzstein, and E. Wieprecht. PACS Evolutionary Probe (PEP) - A Herschel key program. *A&A*, 532:A90, August 2011. doi: 10.1051/0004-6361/201117107.

Mordecai-Mark Mac Low and Ralf S. Klessen. Control of star formation by supersonic turbulence. *Reviews of Modern Physics*, 76(1):125–194, January 2004. doi: 10.1103/RevModPhys.76.125.

Piero Madau and Mark Dickinson. Cosmic Star-Formation History. *ARA&A*, 52:415–486, August 2014. doi: 10.1146/annurev-astro-081811-125615.

Eliab Malefahlo, Mario G. Santos, Matt J. Jarvis, Sarah V. White, and Jonathan T. L. Zwart. The optically selected 1.4-GHz quasar luminosity function below 1 mJy. *MNRAS*, 492(4):5297–5312, March 2020a. doi: 10.1093/mnras/staa112.

Eliab D. Malefahlo, Matt J. Jarvis, Mario G. Santos, Sarah V. White, Nathan J. Adams, and Rebecca A. A. Bowler. A deep radio view of the evolution of the cosmic star-formation rate density from a stellar-mass selected sample in VLA-COSMOS. *arXiv e-prints*, art. arXiv:2012.09797, December 2020b.

D. Christopher Martin, Ted K. Wyder, David Schiminovich, Tom A. Barlow, Karl Forster, Peter G. Friedman, Patrick Morrissey, Susan G. Neff, Mark Seibert, Todd Small, Barry Y. Welsh, Luciana Bianchi, José Donas, Timothy M. Heckman, Young-Wook Lee, Barry F. Madore, Bruno Milliard, R. Michael Rich, Alex S. Szalay, and Sukyoung K. Yi. The UV-Optical Galaxy Color-Magnitude Diagram. III. Constraints on Evolution from the Blue to the Red Sequence. *ApJS*, 173(2):342–356, December 2007. doi: 10.1086/516639.

Philip Massey and K. A. G. Olsen. The Evolution of Massive Stars. I. Red Supergiants in the Magellanic Clouds. *AJ*, 126(6):2867–2886, December 2003. doi: 10.1086/379558.

J. S. Mathis, W. Rumpl, and K. H. Nordsieck. The size distribution of interstellar grains. *ApJ*, 217:425–433, October 1977. doi: 10.1086/155591.

Thomas A. Matthews and Allan R. Sandage. Optical Identification of 3C 48, 3C 196, and 3C 286 with Stellar Objects. *ApJ*, 138:30, July 1963. doi: 10.1086/147615.

T. Mauch, W. D. Cotton, J. J. Condon, A. M. Matthews, T. D. Abbott, R. M. Adam, M. A. Aldera, K. M. B. Asad, E. F. Bauermeister, T. G. H. Bennett, H. Bester, D. H. Botha, L. R. S. Brederode, Z. B. Brits, S. J. Buchner, J. P. Burger, F. Camilo, J. M. Chalmers, T. Cheetham, D. de Villiers, M. S. de Villiers, M. A. Dikgale-Mahlakoana, L. J. du Toit, S. W. P. Esterhuyse, G. Fadana, B. L. Fanaroff, S. Fataar, S. February, B. S. Frank, R. R. G. Gamatham, M. Geyer, S. Goedhart, S. Gounden, S. C. Gumede, I. Heywood, M. J. Hlakola, J. M. G. Horrell, B. Hugo, A. R. Isaacson, G. I. G. Józsa, J. L. Jonas, R. P. M. Julie, F. B. Kapp, V. A. Kasper, J. S. Kenyon, P. P. A. Kotzé, N. Kriek, H. Kriel, T. W. Kusel, R. Lehmensiek, A. Loots, R. T. Lord, B. M. Lunsky, K. Madisa, L. G. Magnus, J. P. L. Main, J. A. Malan, J. R. Manley, S. J. Marais, A. Martens, B. Merry, R. Millenaar, N. Mnyandu, I. P. T. Moeng, O. J. Mokone, T. E. Monama, M. C. Mphego, W. S. New, B. Ngcebetsha, K. J. Ngoasheng, M. T. O. Ockards, N. Oozeer,

A. J. Otto, A. A. Patel, A. Peens-Hough, S. J. Perkins, A. J. T. Ramaila, Z. R. Ramudzuli, R. Renil, L. L. Richter, A. Robyntjies, S. Salie, C. T. G. Schollar, L. C. Schwardt, M. Serylak, R. Siebrits, S. K. Sirothia, O. M. Smirnov, L. Sofeya, G. Stone, B. Taljaard, C. Tasse, I. P. Theron, A. J. Tiplady, O. Toruvanda, S. N. Twum, T. J. van Balla, A. van der Byl, C. van der Merwe, V. Van Tonder, B. H. Wallace, M. G. Welz, L. P. Williams, and B. Xaia. The 1.28 GHz MeerKAT DEEP2 Image. *ApJ*, 888(2):61, January 2020. doi: 10.3847/1538-4357/ab5d2d.

Tom Mauch and Elaine M. Sadler. Radio sources in the 6dFGS: local luminosity functions at 1.4GHz for star-forming galaxies and radio-loud AGN. *MNRAS*, 375(3):931–950, March 2007. doi: 10.1111/j.1365-2966.2006.11353.x.

M. Stephen Maxon and E. Gary Corman. Electron-Electron Bremsstrahlung from a Quantum Plasma (Z=1). *Physical Review*, 163(1):156–161, November 1967. doi: 10.1103/PhysRev.163.156.

K. McAlpine, M. J. Jarvis, and D. G. Bonfield. Evolution of faint radio sources in the VIDEO-XMM3 field. *MNRAS*, 436(2):1084–1095, Dec 2013. doi: 10.1093/mnras/stt1638.

K. McAlpine, I. Prandoni, M. Jarvis, N. Seymour, P. Padovani, P. Best, C. Simpson, D. Guidetti, E. Murphy, M. Huynh, M. Vaccari, S. White, R. Beswick, J. Afonso, M. Magliocchetti, and M. Bondi. The SKA view of the Interplay between SF and AGN Activity and its role in Galaxy Evolution. *Advancing Astrophysics with the Square Kilometre Array (AASKA14)*, art. 83, April 2015.

H. J. McCracken, B. Milvang-Jensen, J. Dunlop, M. Franx, J. P. U. Fynbo, O. Le Fèvre, J. Holt, K. I. Caputi, Y. Goranova, F. Buitrago, J. P. Emerson, W. Freudling, P. Hudelot, C. López-Sanjuan, F. Magnard, Y. Mellier, P. Møller, K. K. Nilsson, W. Sutherland, L. Tasca, and J. Zabl. UltraVISTA: a new ultra-deep near-infrared survey in COSMOS. *A&A*, 544:A156, August 2012. doi: 10.1051/0004-6361/201219507.

Andrew McKellar. Molecular Lines from the Lowest States of Diatomic Molecules Composed of Atoms Probably Present in Interstellar Space. *Publications of the Dominion Astrophysical Observatory Victoria*, 7:251, January 1941.

R. J. McLure, J. S. Dunlop, R. A. A. Bowler, E. Curtis-Lake, M. Schenker, R. S. Ellis, B. E. Robertson, A. M. Koekemoer, A. B. Rogers, Y. Ono, M. Ouchi, S. Charlot, V. Wild, D. P. Stark, S. R. Furlanetto, M. Cirasuolo, and T. A. Targett. A new multifield determination of the galaxy luminosity function at z = 7-9 incorporating the 2012 Hubble Ultra-Deep Field imaging. *MNRAS*, 432(4):2696–2716, July 2013. doi: 10.1093/mnras/stt627.

R. J. McLure, L. Pentericci, A. Cimatti, J. S. Dunlop, D. Elbaz, A. Fontana, K. Nandra, R. Amorin, M. Bolzonella, A. Bongiorno, A. C. Carnall, M. Castellano, M. Cirasuolo, O. Cucciati, F. Cullen, S. De Barros, S. L. Finkelstein, F. Fontanot, P. Franzetti, M. Fumana, A. Gargiulo, B. Garilli, L. Guaita, W. G. Hartley, A. Iovino, M. J. Jarvis, S. Juneau, W. Karman, D. Maccagni, F. Marchi, E. Mármol-Queraltó, E. Pompei, L. Pozzetti, M. Scodeggio, V. Sommariva, M. Talia, O. Almaini, I. Balestra, S. Bardelli, E. F. Bell, N. Bourne, R. A. A. Bowler, M. Brusa, F. Buitrago, K. I. Caputi, P. Cassata, S. Charlot, A. Citro, G. Cresci, S. Cristiani, E. Curtis-Lake, M. Dickinson, G. G. Fazio, H. C. Ferguson, F. Fiore, M. Franco, J. P. U. Fynbo, A. Galametz, A. Georgakakis, M. Giavalisco, A. Grazian, N. P. Hathi, I. Jung, S. Kim, A. M. Koekemoer, Y. Khusanova, O. Le Fèvre, J. M. Lotz, F. Mannucci, D. T. Maltby, K. Matsuoka, D. J. McLeod, H. Mendez-Hernandez, J. Mendez-Abreu, M. Mignoli, M. Moresco, A. Mortlock, M. Nonino, M. Pannella, C. Papovich, P. Popesso, D. P. Rosario, M. Salvato, P. Santini, D. Schaerer, C. Schreiber, D. P. Stark, L. A. M. Tasca, R. Thomas, T. Treu, E. Vanzella, V. Wild, C. C. Williams, G. Zamorani, and E. Zucca. The VANDELS ESO public spectroscopic survey. *MNRAS*, 479(1):25–42, September 2018. doi: 10.1093/mnras/sty1213.

Ross J. McLure and Matt J. Jarvis. The relationship between radio luminosity and black hole mass in optically selected quasars. *MNRAS*, 353(4):L45–L49, Oct 2004. doi: 10.1111/j.1365-2966.2004.08305.x.

E. Merlin, A. Fontana, M. Castellano, P. Santini, M. Torelli, K. Boutsia, T. Wang, A. Grazian, L. Pentericci, C. Schreiber, L. Ciesla, R. McLure, S. Derriere, J. S. Dunlop, and D. Elbaz. Chasing passive galaxies in the early Universe: a critical analysis in CANDELS GOODS-South. *MNRAS*, 473(2):2098–2123, January 2018. doi: 10.1093/mnras/stx2385.

L. Miller, J. A. Peacock, and A. R. G. Mead. The bimodal radio luminosity function of quasars. *MNRAS*, 244:207–213, May 1990.

N. A. Miller, M. Bonzini, E. B. Fomalont, K. I. Kellermann, V. Mainieri, P. Padovani, P. Rosati, P. Tozzi, and S. Vattakunnel. The Very Large Array 1.4 GHz Survey of the Extended Chandra Deep Field South: Second Data Release. *ApJS*, 205:13, April 2013. doi: 10.1088/0067-0049/205/2/13.

B. Mingo, J. H. Croston, M. J. Hardcastle, P. N. Best, K. J. Duncan, R. Morganti, H. J. A. Rottgering, J. Sabater, T. W. Shimwell, W. L. Williams, M. Brienza, G. Gurkan, V. H. Mahatma, L. K. Morabito, I. Prandoni, M. Bondi, J. Ineson, and S. Mooney. Revisiting the Fanaroff-Riley dichotomy and radio-galaxy morphology with the LOFAR Two-Metre Sky Survey (LoTSS). *MNRAS*, 488(2):2701–2721, September 2019. doi: 10.1093/mnras/stz1901.

K. J. Mitchell and J. J. Condon. A confusion-limited 1.49-GHz VLA survey centered on alpha = 13 H 00 M 37 s, delta = + 30 deg 34 arcmin. *AJ*, 90:1957–1966, October 1985. doi: 10.1086/113899.

K. Mitchell-Wynne, M. G. Santos, J. Afonso, and M. J. Jarvis. Beyond stacking: a maximum-likelihood method to constrain radio source counts below the detection threshold. *MNRAS*, 437:2270–2278, January 2014. doi: 10.1093/mnras/stt2035.

Niruj Mohan and David Rafferty. PyBDSF: Python Blob Detection and Source Finder, February 2015.

Dániel Cs Molnár, Mark T. Sargent, Jacinta Delhaize, Ivan Delvecchio, Vernesa Smolčić, Mladen Novak, Eva Schinnerer, Giovanni Zamorani, Marco Bondi, Noelia Herrera-Ruiz, Eric J. Murphy, Eleni Vardoulaki, Alexander Karim, Sarah Leslie, Benjamin Magnelli, C. Marcella Carollo, and Enno Middelberg. The infrared-radio correlation of spheroid- and disc-dominated star-forming galaxies to z $\sim$ 1.5 in the COSMOS field. *MNRAS*, 475(1):827–838, March 2018. doi: 10.1093/mnras/stx3234.

E. Momjian, C. L. Carilli, F. Walter, and B. Venemans. The Highest Redshift Quasar at z = 7.085: A Radio-quiet Source. *AJ*, 147:6, January 2014. doi: 10.1088/0004-6256/147/1/6.

R. Morganti, J. Fogasy, Z. Paragi, T. Oosterloo, and M. Orienti. Radio Jets Clearing the Way Through a Galaxy: Watching Feedback in Action. *Science*, 341:1082–1085, September 2013. doi: 10.1126/science.1240436.

Glenn E. Morrison, Frazer N. Owen, Mark Dickinson, Rob J. Ivison, and Edo Ibar. Very Large Array 1.4 GHz Observations of the GOODS-North Field: Data Reduction and Analysis. *ApJS*, 188(1):178–186, May 2010. doi: 10.1088/0067-0049/188/1/178.

Eric J. Murphy. The Far-Infrared-Radio Correlation at High Redshifts: Physical Considerations and Prospects for the Square Kilometer Array. *ApJ*, 706(1):482–496, November 2009. doi: 10.1088/0004-637X/706/1/482.

Eric J. Murphy, Emmanuel Momjian, James J. Condon, Ranga-Ram Chary, Mark Dickinson, Hanae Inami, Andrew R. Taylor, and Benjamin J. Weiner. The GOODS-n jansky VLA 10 GHz pilot survey: Sizes of star-formingJY radio sources. *The Astrophysical Journal*, 839(1):35, apr 2017. doi: 10.3847/1538-4357/aa62fd. URL https://doi.org/10.3847%2F1538-4357%2Faa62fd.

RENDONG NAN, DI LI, CHENGJIN JIN, QIMING WANG, LICHUN ZHU, WENBAI ZHU, HAIYAN ZHANG, YOULING YUE, and LEI QIAN. The five-hundred-meter aperture spherical radio telescope (fast) project. *International Journal of Modern Physics D*, 20 (06):989–1024, 2011. doi: 10.1142/S0218271811019335. URL https://doi.org/10.1142/S0218271811019335.

K. G. Noeske, B. J. Weiner, S. M. Faber, C. Papovich, D. C. Koo, R. S. Somerville, K. Bundy, C. J. Conselice, J. A. Newman, D. Schiminovich, E. Le Floch, A. L. Coil, G. H. Rieke, J. M. Lotz, J. R. Primack, P. Barmby, M. C. Cooper, M. Davis, R. S. Ellis, G. G. Fazio, P. Guhathakurta, J. Huang, S. A. Kassin, D. C. Martin, A. C. Phillips, R. M. Rich, T. A. Small, C. N. A. Willmer, and G. Wilson. Star formation in AEGIS field galaxies since z =1.1: The dominance of gradually declining star formation, and the main sequence of star-forming galaxies. *The Astrophysical Journal*, 660(1):L43–L46, apr 2007. doi: 10.1086/517926. URL https://doi.org/10.1086%2F517926.

R. P. Norris, A. M. Hopkins, J. Afonso, S. Brown, J. J. Condon, L. Dunne, I. Feain, R. Hollow, M. Jarvis, M. Johnston-Hollitt, E. Lenc, E. Middelberg, P. Padovani, I. Prandoni, L. Rudnick, N. Seymour, G. Umana, H. Andernach, D. M. Alexander, P. N. Appleton, D. Bacon, J. Banfield, W. Becker, M. J. I. Brown, P. Ciliegi, C. Jackson, S. Eales, A. C. Edge, B. M. Gaensler, G. Giovannini, C. A. Hales, P. Hancock, M. T. Huynh, E. Ibar, R. J. Ivison, R. Kennicutt, A. E. Kimball, A. M. Koekemoer, B. S. Koribalski, Á. R. López-Sánchez, M. Y. Mao, T. Murphy, H. Messias, K. A. Pimbblet, A. Raccanelli, K. E. Randall, T. H. Reiprich, I. G. Roseboom, H. Röttgering, D. J. Saikia, R. G. Sharp, O. B. Slee, I. Smail, M. A. Thompson, J. S. Urquhart, J. V. Wall, and G.-B. Zhao. EMU: Evolutionary Map of the Universe. *Publ. Astron. Soc. Australia*, 28:215–248, August 2011. doi: 10.1071/AS11021.

M. Novak, V. Smolčić, J. Delhaize, I. Delvecchio, G. Zamorani, N. Baran, M. Bondi, P. Capak, C. L. Carilli, P. Ciliegi, F. Civano, O. Ilbert, A. Karim, C. Laigle, O. Le Fèvre, S. Marchesi, H. McCracken, O. Miettinen, M. Salvato, M. Sargent, E. Schinnerer, and L. Tasca. The VLA-COSMOS 3 GHz Large Project: Cosmic star formation history since z 5. *A&A*, 602:A5, June 2017. doi: 10.1051/0004-6361/201629436.

M. Novak, V. Smolčić, E. Schinnerer, G. Zamorani, I. Delvecchio, M. Bondi, and J. Delhaize. Constraints on submicrojansky radio number counts based on evolving VLA-COSMOS luminosity functions. *A&A*, 614:A47, June 2018. doi: 10.1051/0004-6361/201731635.

E. F. Ocran, A. R. Taylor, M. Vaccari, and D. A. Green. The nature of the faint low-frequency radio source population. *MNRAS*, 468(1):1156–1168, June 2017. doi: 10.1093/mnras/stx435.

E. F. Ocran, A. R. Taylor, M. Vaccari, C. H. Ishwara-Chand ra, I. Prandoni, M. Prescott, and C. Mancuso. Cosmic evolution of star-forming galaxies to z 1.8 in the faint low-frequency radio source population. *MNRAS*, 491(4):5911–5924, February 2020. doi: 10.1093/mnras/stz3401.

S. S. R. Offner, P. C. Clark, P. Hennebelle, N. Bastian, M. R. Bate, P. F. Hopkins, E. Moraux, and A. P. Whitworth. The Origin and Universality of the Stellar Initial Mass Function. In Henrik Beuther, Ralf S. Klessen, Cornelis P. Dullemond, and Thomas Henning, editors, *Protostars and Planets VI*, page 53, January 2014. doi: 10.2458/azu_uapress_9780816531240-ch003.

J. B. Oke and J. E. Gunn. Secondary standard stars for absolute spectrophotometry. *ApJ*, 266: 713–717, March 1983. doi: 10.1086/160817.

J. B. Oke and Allan Sandage. Energy Distributions, K Corrections, and the Stebbins-Whitford Effect for Giant Elliptical Galaxies. *ApJ*, 154:21, October 1968. doi: 10.1086/149737.

S. J. Oliver, J. Bock, B. Altieri, A. Amblard, V. Arumugam, H. Aussel, T. Babbedge, A. Beelen, M. Béthermin, A. Blain, A. Boselli, C. Bridge, D. Brisbin, V. Buat, D. Burgarella, N. Castro-Rodríguez, A. Cava, P. Chanial, M. Cirasuolo, D. L. Clements, A. Conley, L. Conversi, A. Cooray, C. D. Dowell, E. N. Dubois, E. Dwek, S. Dye, S. Eales, D. Elbaz, D. Farrah, A. Feltre, P. Ferrero, N. Fiolet, M. Fox, A. Franceschini, W. Gear, E. Giovannoli, J. Glenn, Y. Gong, E. A.

González Solares, M. Griffin, M. Halpern, M. Harwit, E. Hatziminaoglou, S. Heinis, P. Hurley, H. S. Hwang, A. Hyde, E. Ibar, O. Ilbert, K. Isaak, R. J. Ivison, G. Lagache, E. Le Floc'h, L. Levenson, B. Lo Faro, N. Lu, S. Madden, B. Maffei, G. Magdis, G. Mainetti, L. Marchetti, G. Marsden, J. Marshall, A. M. J. Mortier, H. T. Nguyen, B. O'Halloran, A. Omont, M. J. Page, P. Panuzzo, A. Papageorgiou, H. Patel, C. P. Pearson, I. Pérez-Fournon, M. Pohlen, J. I. Rawlings, G. Raymond, D. Rigopoulou, L. Riguccini, D. Rizzo, G. Rodighiero, I. G. Roseboom, M. Rowan-Robinson, M. Sánchez Portal, B. Schulz, Douglas Scott, N. Seymour, D. L. Shupe, A. J. Smith, J. A. Stevens, M. Symeonidis, M. Trichas, K. E. Tugwell, M. Vaccari, I. Valtchanov, J. D. Vieira, M. Viero, L. Vigroux, L. Wang, R. Ward, J. Wardlow, G. Wright, C. K. Xu, and M. Zemcov. The Herschel Multi-tiered Extragalactic Survey: HerMES. *MNRAS*, 424(3):1614–1635, August 2012. doi: 10.1111/j.1365-2966.2012.20912.x.

Benjamin D. Oppenheimer, Romeel Davé, Dušan Kereš, Mark Fardal, Neal Katz, Juna A. Kollmeier, and David H. Weinberg. Feedback and recycled wind accretion: assembling the z = 0 galaxy mass function. *MNRAS*, 406(4):2325–2338, August 2010. doi: 10.1111/j.1365-2966.2010.16872.x.

M. Orienti, F. D'Ammando, M. Giroletti, G. Giovannini, and F. Panessa. The physics of the radio emission in the quiet side of the AGN population with the SKA. In *Advancing Astrophysics with the Square Kilometre Array (AASKA14)*, page 87, April 2015.

Ludwig Oster. Free-Free Emission in the Radio-Frequency Range. *AJ*, 70:50, March 1961. doi: 10.1086/108534.

Masami Ouchi, Kazuhiro Shimasaku, Hisanori Furusawa, Tomoki Saito, Makiko Yoshida, Masayuki Akiyama, Yoshiaki Ono, Toru Yamada, Kazuaki Ota, Nobunari Kashikawa, Masanori Iye, Tadayuki Kodama, Sadanori Okamura, Chris Simpson, and Michitoshi Yoshida. Statistics of 207 Lyα Emitters at a Redshift Near 7: Constraints on Reionization and Galaxy Formation Models. *ApJ*, 723(1):869–894, November 2010. doi: 10.1088/0004-637X/723/1/869.

Frazer N. Owen. Deep JVLA Imaging of GOODS-N at 20 cm. *ApJS*, 235(2):34, April 2018. doi: 10.3847/1538-4365/aab4a1.

P. Padovani, P. Giommi, and F. Fiore. Are the X-ray spectra of flat-spectrum radio quasars and BL Lacertae objects different? *MNRAS*, 284:569–575, January 1997. doi: 10.1093/mnras/284.3.569.

P. Padovani, V. Mainieri, P. Tozzi, K. I. Kellermann, E. B. Fomalont, N. Miller, P. Rosati, and P. Shaver. The Very Large Array Survey of the Chandra Deep Field South. IV. Source Population. *ApJ*, 694:235–246, March 2009. doi: 10.1088/0004-637X/694/1/235.

P. Padovani, N. Miller, K. I. Kellermann, V. Mainieri, P. Rosati, and P. Tozzi. The VLA Survey of Chandra Deep Field South. V. Evolution and Luminosity Functions of Sub-millijansky Radio Sources and the Issue of Radio Emission in Radio-quiet Active Galactic Nuclei. *ApJ*, 740:20, October 2011. doi: 10.1088/0004-637X/740/1/20.

P. Padovani, M. Bonzini, N. Miller, K. I. Kellermann, V. Mainieri, P. Rosati, P. Tozzi, and S. Vattakunnel. The AGN content of deep radio surveys and radio emission in radio-quiet AGN. Why every astronomer should care about deep radio fields. In Areg M. Mickaelian and David B. Sanders, editors, *Multiwavelength AGN Surveys and Studies*, volume 304 of *IAU Symposium*, pages 79–85, July 2014. doi: 10.1017/S1743921314003391.

P. Padovani, M. Bonzini, K. I. Kellermann, N. Miller, V. Mainieri, and P. Tozzi. Radio-faint AGN: a tale of two populations. *MNRAS*, 452:1263–1279, September 2015. doi: 10.1093/mnras/stv1375.

Paolo Padovani. The faint radio sky: radio astronomy becomes mainstream. *A&ARv*, 24(1):13, September 2016. doi: 10.1007/s00159-016-0098-6.

Hengxing Pan, Matt J. Jarvis, James R. Allison, Ian Heywood, Mario G. Santos, Natasha Maddox, Bradley S. Frank, and Xi Kang. Measuring the H I mass function below the detection threshold. *MNRAS*, 491(1):1227–1242, January 2020. doi: 10.1093/mnras/stz3030.

F. Panessa, R. D. Baldi, A. Laor, P. Padovani, E. Behar, and I. McHardy. The origin of radio emission from radio-quiet active galactic nuclei. *Nature Astronomy*, 3:387–396, April 2019. doi: 10.1038/s41550-019-0765-4.

I. Pâris, P. Petitjean, E. Aubourg, S. Bailey, N. P. Ross, A. D. Myers, M. A. Strauss, S. F. Anderson, E. Arnau, J. Bautista, D. Bizyaev, A. S. Bolton, J. Bovy, W. N. Brandt, H. Brewington, J. R. Brownstein, N. Busca, D. Capellupo, W. Carithers, R. A. C. Croft, K. Dawson, T. Delubac, G. Ebelke, D. J. Eisenstein, P. Engelke, X. Fan, A. N. Filiz, H. Finley, A. Font-Ribera, J. Ge, R. R. Gibson, P. B. Hall, F. Hamann, J. F. Hennawi, S. Ho, D. W. Hogg, Z. Ivezic, L. Jiang, A. E. Kimball, D. Kirky, J. A. Kirkpatrick, K.-G. Lee, J.-M. Le Goff, B. Lundgren, C. L. MacLeod, E. Malanushenko, V. Malanushenko, C. Maraston, I. D. McGreer, R. G. McMahon, J. Miralda-Escude, D. Muna, P. Noterdaeme, D. Oravetz, N. Palanque-Delabrouille, K. Pan, I. Perez-Fournon, M. M. Pieri, G. T. Richards, E. Rollinde, E. S. Sheldon, D. J. Schlegel, D. P. Schneider, A. Slosar, A. Shelden, Y. Shen, A. Simmons, S. Snedden, N. Suzuki, J. Tinker, M. Viel, B. A. Weaver, D. W. Weinberg, M. White, W. M. Wood-Vasey, and C. Yeche. VizieR Online Data Catalog: SDSS Quasar Catalog, DR9Q (Paris+, 2012). *VizieR Online Data Catalog*, 7269:0, October 2012.

I. Pâris, P. Petitjean, N. P. Ross, A. D. Myers, É. Aubourg, A. Streblyanska, S. Bailey, É. Armengaud, N. Palanque-Delabrouille, C. Yèche, F. Hamann, M. A. Strauss, F. D. Albareti, J. Bovy, D. Bizyaev, W. Niel Brandt, M. Brusa, J. Buchner, J. Comparat, R. A. C. Croft, T. Dwelly, X. Fan, A. Font-Ribera, J. Ge, A. Georgakakis, P. B. Hall, L. Jiang, K. Kinemuchi, E. Malanushenko, V. Malanushenko, R. G. McMahon, M.-L. Menzel, A. Merloni, K. Nandra, P. Noterdaeme, D. Oravetz, K. Pan, M. M. Pieri, F. Prada, M. Salvato, D. J. Schlegel, D. P. Schneider, A. Simmons, M. Viel, D. H. Weinberg, and L. Zhu. The Sloan Digital Sky Survey Quasar Catalog: Twelfth data release. *A&A*, 597:A79, January 2017. doi: 10.1051/0004-6361/201527999.

Guillaume Patanchon, Peter A. R. Ade, James J. Bock, Edward L. Chapin, Mark J. Devlin, Simon R. Dicker, Matthew Griffin, Joshua O. Gundersen, Mark Halpern, Peter C. Hargrave, David H. Hughes, Jeff Klein, Gaelen Marsden, Philip Mauskopf, Lorenzo Moncelsi, Calvin B. Netterfield, Luca Olmi, Enzo Pascale, Marie Rex, Douglas Scott, Christopher Semisch, Nicholas Thomas, Matthew D. P. Truch, Carole Tucker, Gregory S. Tucker, Marco P. Viero, and Donald V. Wiebe. Submillimeter Number Counts from Statistical Analysis of BLAST Maps. *ApJ*, 707(2):1750–1765, December 2009. doi: 10.1088/0004-637X/707/2/1750.

P. J. E. Peebles. Large-scale background temperature and mass fluctuations due to scale-invariant primeval perturbations. *ApJ*, 263:L1–L5, December 1982. doi: 10.1086/183911.

A. A. Penzias and R. W. Wilson. A Measurement of Excess Antenna Temperature at 4080 Mc/s. *ApJ*, 142:419–421, July 1965. doi: 10.1086/148307.

Krisztina Perger, Sándor Frey, Krisztina É. Gabányi, and L. Viktor Tóth. Unveiling the weak radio quasar population at z≥4. *MNRAS*, 490(2):2542–2549, December 2019. doi: 10.1093/mnras/stz2723.

R. A. Perley, C. J. Chandler, B. J. Butler, and J. M. Wrobel. The Expanded Very Large Array: A New Telescope for New Science. *ApJ*, 739(1):L1, September 2011. doi: 10.1088/2041-8205/739/1/L1.

D. Pierini, C. C. Popescu, R. J. Tuffs, and H. J. Völk. The far-infrared/radio correlation in the ISO era. The warm and cold far-infrared/radio correlations. *A&A*, 409:907–916, October 2003. doi: 10.1051/0004-6361:20031220.

G. L. Pilbratt, J. R. Riedinger, T. Passvogel, G. Crone, D. Doyle, U. Gageur, A. M. Heras, C. Jewell, L. Metcalfe, S. Ott, and M. Schmidt. Herschel Space Observatory. An ESA facility for far-infrared and submillimetre astronomy. *A&A*, 518:L1, July 2010. doi: 10.1051/0004-6361/201014759.

M. Polletta, M. Tajer, L. Maraschi, G. Trinchieri, C. J. Lonsdale, L. Chiappetti, S. Andreon, M. Pierre, O. Le Fèvre, G. Zamorani, D. Maccagni, O. Garcet, J. Surdej, A. Franceschini, D. Alloin, D. L. Shupe, J. A. Surace, F. Fang, M. Rowan-Robinson, H. E. Smith, and L. Tresse. Spectral Energy Distributions of Hard X-Ray Selected Active Galactic Nuclei in the XMM-Newton Medium Deep Survey. *ApJ*, 663(1):81–102, Jul 2007. doi: 10.1086/518113.

M. Polletta, L. Maraschi, L. Chiappetti, G. Trinchieri, M. Giorgetti, and M. Molina. Dissecting AGN Spectral Energy Distributions: Obscuration and Host Contribution. In L. Maraschi, G. Ghisellini, R. Della Ceca, and F. Tavecchio, editors, *Accretion and Ejection in AGN: a Global View*, volume 427 of *Astronomical Society of the Pacific Conference Series*, page 116, October 2010.

Andrew Pontzen, Michael Tremmel, Nina Roth, Hiranya V. Peiris, Amélie Saintonge, Marta Volonteri, Tom Quinn, and Fabio Governato. How to quench a galaxy. *MNRAS*, 465(1):547–558, February 2017. doi: 10.1093/mnras/stw2627.

I. Prandoni and N. Seymour. Revealing the Physics and Evolution of Galaxies and Galaxy Clusters with SKA Continuum Surveys. *Advancing Astrophysics with the Square Kilometre Array (AASKA14)*, art. 67, April 2015.

I. Prandoni, L. Gregorini, P. Parma, H. R. de Ruiter, G. Vettolani, A. Zanichelli, M. H. Wieringa, and R. D. Ekers. The ATESP radio survey. IV. Optical identifications and spectroscopy in the EIS-A region. *A&A*, 369:787–796, April 2001. doi: 10.1051/0004-6361:20010170.

Matthew Prescott, T. Mauch, M. J. Jarvis, K. McAlpine, D. J. B. Smith, S. Fine, R. Johnston, M. J. Hardcastle, I. K. Baldry, S. Brough, M. J. I. Brown, M. N. Bremer, S. P. Driver, A. M. Hopkins, L. S. Kelvin, J. Loveday, P. Norberg, D. Obreschkow, and E. M. Sadler. Galaxy And Mass Assembly (GAMA): the 325 MHz radio luminosity function of AGN and star-forming galaxies. *MNRAS*, 457(1):730–744, March 2016. doi: 10.1093/mnras/stv3020.

William H. Press and Paul Schechter. Formation of Galaxies and Clusters of Galaxies by Self-Similar Gravitational Condensation. *ApJ*, 187:425–438, February 1974. doi: 10.1086/152650.

J. F. Radcliffe, M. A. Garrett, T. W. B. Muxlow, R. J. Beswick, P. D. Barthel, A. T. Deller, A. Keimpema, R. M. Campbell, and N. Wrigley. Nowhere to Hide: Radio-faint AGN in GOODS-N field. I. Initial catalogue and radio properties. *A&A*, 619:A48, Nov 2018. doi: 10.1051/0004-6361/201833399.

Steve Rawlings and Matt J. Jarvis. Evidence that powerful radio jets have a profound influence on the evolution of galaxies. *MNRAS*, 355(3):L9–L12, Dec 2004. doi: 10.1111/j.1365-2966.2004.08234.x.

S. C. Read, D. J. B. Smith, G. Gürkan, M. J. Hardcastle, W. L. Williams, P. N. Best, E. Brinks, G. Calistro-Rivera, K. T. ChyŻy, K. Duncan, L. Dunne, M. J. Jarvis, L. K. Morabito, I. Prandoni, H. J. A. Röttgering, J. Sabater, and S. Viaene. The Far-Infrared Radio Correlation at low radio frequency with LOFAR/H-ATLAS. *MNRAS*, 480(4):5625–5644, November 2018. doi: 10.1093/mnras/sty2198.

Grote Reber. Cosmic Static. *ApJ*, 100:279, November 1944. doi: 10.1086/144668.

M. J. Rees. Black Hole Models for Active Galactic Nuclei. *ARA&A*, 22:471–506, 1984. doi: 10.1146/annurev.aa.22.090184.002351.

M. J. Rees and J. P. Ostriker. Cooling, dynamics and fragmentation of massive gas clouds: clues to the masses and radii of galaxies and clusters. *MNRAS*, 179:541–559, June 1977. doi: 10.1093/mnras/179.4.541.

E. A. Richards, E. B. Fomalont, K. I. Kellermann, R. A. Windhorst, R. B. Partridge, L. L. Cowie, and A. J. Barger. Optically Faint Microjansky Radio Sources. *ApJ*, 526(2):L73–L76, December 1999. doi: 10.1086/312373.

G. T. Richards. AGN Outflows in Emission and Absorption: The SDSS Perspective. *ArXiv Astrophysics e-prints*, March 2006.

G. T. Richards, X. Fan, D. P. Schneider, D. E. Vanden Berk, M. A. Strauss, D. G. York, J. E. Anderson, Jr., S. F. Anderson, J. Annis, N. A. Bahcall, M. Bernardi, J. W. Briggs, J. Brinkmann, R. Brunner, S. Burles, L. Carey, F. J. Castander, A. J. Connolly, J. H. Crocker, I. Csabai, M. Doi, D. Finkbeiner, S. D. Friedman, J. A. Frieman, M. Fukugita, J. E. Gunn, R. B. Hindsley, Ž. Ivezić, S. Kent, G. R. Knapp, D. Q. Lamb, R. F. Leger, D. C. Long, J. Loveday, R. H. Lupton, T. A. McKay, A. Meiksin, A. Merrelli, J. A. Munn, H. J. Newberg, M. Newcomb, R. C. Nichol, R. Owen, J. R. Pier, A. Pope, M. W. Richmond, C. M. Rockosi, D. J. Schlegel, W. A. Siegmund, S. Smee, Y. Snir, C. Stoughton, C. Stubbs, M. SubbaRao, A. S. Szalay, G. P. Szokoly, C. Tremonti, A. Uomoto, P. Waddell, B. Yanny, and W. Zheng. Colors of 2625 Quasars at 0Z5 Measured in the Sloan Digital Sky Survey Photometric System. *AJ*, 121:2308–2330, May 2001. doi: 10.1086/320392.

G. T. Richards, X. Fan, H. J. Newberg, M. A. Strauss, D. E. Vanden Berk, D. P. Schneider, B. Yanny, A. Boucher, S. Burles, J. A. Frieman, J. E. Gunn, P. B. Hall, Ž. Ivezić, S. Kent, J. Loveday, R. H. Lupton, C. M. Rockosi, D. J. Schlegel, C. Stoughton, M. SubbaRao, and D. G. York. Spectroscopic Target Selection in the Sloan Digital Sky Survey: The Quasar Sample. *AJ*, 123:2945–2975, June 2002. doi: 10.1086/340187.

G. H. Rieke, E. T. Young, C. W. Engelbracht, D. M. Kelly, F. J. Low, E. E. Haller, J. W. Beeman, K. D. Gordon, J. A. Stansberry, K. A. Misselt, J. Cadien, J. E. Morrison, G. Rivlis, W. B. Latter, A. Noriega-Crespo, D. L. Padgett, K. R. Stapelfeldt, D. C. Hines, E. Egami, J. Muzerolle, A. Alonso-Herrero, M. Blaylock, H. Dole, J. L. Hinz, E. Le Floc'h, C. Papovich, P. G. Pérez-González, P. S. Smith, K. Y. L. Su, L. Bennett, D. T. Frayer, D. Henderson, N. Lu, F. Masci, M. Pesenson, L. Rebull, J. Rho, J. Keene, S. Stolovy, S. Wachter, W. Wheaton, M. W. Werner, and P. L. Richards. The Multiband Imaging Photometer for Spitzer (MIPS). *ApJS*, 154(1):25–29, September 2004. doi: 10.1086/422717.

A. S. G. Robotham, L. J. M. Davies, S. P. Driver, S. Koushan, D. S. Taranu, S. Casura, and J. Liske. ProFound: Source Extraction and Application to Modern Survey Data. *MNRAS*, 476 (3):3137–3159, May 2018. doi: 10.1093/mnras/sty440.

I. G. Roseboom and P. N. Best. Cosmic star formation probed via parametric stack-fitting of known sources to radio imaging. *MNRAS*, 439:1286–1293, April 2014. doi: 10.1093/mnras/stt2452.

Namrata Roy, Kevin Bundy, Edmond Cheung, Wiphu Rujopakarn, Michele Cappellari, Francesco Belfiore, Renbin Yan, Tim Heckman, Matthew Bershady, Jenny Greene, Kyle Westfall, Niv Drory, Kate Rubin, David Law, Kai Zhang, Joseph Gelfand, Dmitry Bizyaev, David Wake, Karen Masters, Daniel Thomas, Cheng Li, and Rogemar A. Riffel. Detecting Radio AGN Signatures in Red Geysers. *ApJ*, 869(2):117, December 2018. doi: 10.3847/1538-4357/aaee72.

B. Rush, M. A. Malkan, and R. A. Edelson. The Radio Properties of Seyfert Galaxies in the 12 Micron and CfA Samples. *ApJ*, 473:130, December 1996. doi: 10.1086/178132.

George B. Rybicki and Alan P. Lightman. *Radiative processes in astrophysics*. 1979.

M. Ryle. Radio stars and their cosmological significance. *The Observatory*, 75:137–147, August 1955.

M. Ryle and P. A. G. Scheuer. The Spatial Distribution and the Nature of Radio Stars. *Proceedings of the Royal Society of London Series A*, 230:448–462, July 1955. doi: 10.1098/rspa.1955.0146.

Elena Sabbi, Linda J. Smith, Lynn R. Carlson, Antonella Nota, Monca Tosi, Michele Cignoni, Jay S. Gallagher, Marco Sirianni, and Margaret Meixner. Young Star Clusters in the Small Magellanic Cloud: Impact of Local and Global Conditions on Star Formation. In Leslie K. Hunt, Suzanne C. Madden, and Raffaella Schneider, editors, *Low-Metallicity Star Formation: From the First Stars to Dwarf Galaxies*, volume 255 of *IAU Symposium*, pages 157–161, December 2008. doi: 10.1017/S1743921308024745.

E. E. Salpeter. The Luminosity Function and Stellar Evolution. *ApJ*, 121:161, January 1955. doi: 10.1086/145971.

A. Sandage. The Existence of a Major New Constituent of the Universe: the Quasistellar Galaxies. *ApJ*, 141:1560, May 1965. doi: 10.1086/148245.

D. B. Sanders and I. F. Mirabel. Luminous Infrared Galaxies. *ARA&A*, 34:749, January 1996. doi: 10.1146/annurev.astro.34.1.749.

E. Scannapieco and S. P. Oh. Quasar Feedback: The Missing Link in Structure Formation. *ApJ*, 608:62–79, June 2004. doi: 10.1086/386542.

Joop Schaye, Robert A. Crain, Richard G. Bower, Michelle Furlong, Matthieu Schaller, Tom Theuns, Claudio Dalla Vecchia, Carlos S. Frenk, I. G. McCarthy, John C. Helly, Adrian Jenkins, Y. M. Rosas-Guevara, Simon D. M. White, Maarten Baes, C. M. Booth, Peter Camps, Julio F. Navarro, Yan Qu, Alireza Rahmati, Till Sawala, Peter A. Thomas, and James Trayford. The EAGLE project: simulating the evolution and assembly of galaxies and their environments. *MNRAS*, 446(1):521–554, January 2015. doi: 10.1093/mnras/stu2058.

P. A. G. Scheuer. A statistical method for analysing observations of faint radio stars. *Proceedings of the Cambridge Philosophical Society*, 53:764–773, January 1957. doi: 10.1017/S0305004100032825.

P. A. G. Scheuer. The absorption coefficient of a plasma at radio frequencies. *MNRAS*, 120:231, January 1960. doi: 10.1093/mnras/120.3.231.

M. Schmidt. 3C 273 : A Star-Like Object with Large Red-Shift. *Nature*, 197:1040, March 1963. doi: 10.1038/1971040a0.

M. Schmidt. Space Distribution and Luminosity Functions of Quasi-Stellar Radio Sources. *ApJ*, 151:393, February 1968. doi: 10.1086/149446.

M. Schmidt. Space Distribution and Luminosity Functions of Quasars. *ApJ*, 162:371, November 1970. doi: 10.1086/150668.

D. P. Schneider, G. T. Richards, P. B. Hall, M. A. Strauss, S. F. Anderson, T. A. Boroson, N. P. Ross, Y. Shen, W. N. Brandt, X. Fan, N. Inada, S. Jester, G. R. Knapp, C. M. Krawczyk, A. R. Thakar, D. E. Vanden Berk, W. Voges, B. Yanny, D. G. York, N. A. Bahcall, D. Bizyaev, M. R. Blanton, H. Brewington, J. Brinkmann, D. Eisenstein, J. A. Frieman, M. Fukugita, J. Gray, J. E. Gunn, P. Hibon, Ž. Ivezić, S. M. Kent, R. G. Kron, M. G. Lee, R. H. Lupton, E. Malanushenko, V. Malanushenko, D. Oravetz, K. Pan, J. R. Pier, T. N. Price, III, D. H. Saxe, D. J. Schlegel, A. Simmons, S. A. Snedden, M. U. SubbaRao, A. S. Szalay, and D. H. Weinberg. The Sloan Digital Sky Survey Quasar Catalog. V. Seventh Data Release. *AJ*, 139:2360, June 2010. doi: 10.1088/0004-6256/139/6/2360.

J. Schober, D. R. G. Schleicher, and R. S. Klessen. X-ray emission from star-forming galaxies - signatures of cosmic rays and magnetic fields. *MNRAS*, 446(1):2–17, January 2015. doi: 10.1093/mnras/stu1999.

A. Schulze, C. Done, Y. Lu, F. Zhang, and Y. Inoue. Evidence for Higher Black Hole Spin in Radio-loud Quasars. *ApJ*, 849:4, November 2017. doi: 10.3847/1538-4357/aa9181.

S. Serjeant, S. Rawlings, M. Lacy, S. J. Maddox, J. C. Baker, D. Clements, and P. B. Lilje. The radio-optical correlation in steep-spectrum quasars. *MNRAS*, 294:494, March 1998. doi: 10.1046/j.1365-8711.1998.01303.x.

Carl K. Seyfert. No. 671. Nuclear emission in spiral nebulae. *Contributions from the Mount Wilson Observatory / Carnegie Institution of Washington*, 671:1–13, January 1943.

Y. Shen, G. T. Richards, M. A. Strauss, P. B. Hall, D. P. Schneider, S. Snedden, D. Bizyaev, H. Brewington, V. Malanushenko, E. Malanushenko, D. Oravetz, K. Pan, and A. Simmons. A Catalog of Quasar Properties from Sloan Digital Sky Survey Data Release 7. *ApJS*, 194:45, June 2011. doi: 10.1088/0067-0049/194/2/45.

J. Silk. On the fragmentation of cosmic gas clouds. I. The formation of galaxies and the first generation of stars. *ApJ*, 211:638–648, February 1977. doi: 10.1086/154972.

J. Silk. Unleashing Positive Feedback: Linking the Rates of Star Formation, Supermassive Black Hole Accretion, and Outflows in Distant Galaxies. *ApJ*, 772:112, August 2013. doi: 10.1088/0004-637X/772/2/112.

C. Simpson, A. Martínez-Sansigre, S. Rawlings, R. Ivison, M. Akiyama, K. Sekiguchi, T. Takata, Y. Ueda, and M. Watson. Radio imaging of the Subaru/XMM-Newton Deep Field - I. The 100-μJy catalogue, optical identifications, and the nature of the faint radio source population. *MNRAS*, 372:741–757, October 2006. doi: 10.1111/j.1365-2966.2006.10907.x.

J. M. Simpson, A. M. Swinbank, Ian Smail, D. M. Alexander, W. N. Brandt, F. Bertoldi, C. de Breuck, S. C. Chapman, K. E. K. Coppin, E. da Cunha, A. L. R. Danielson, H. Dannerbauer, T. R. Greve, J. A. Hodge, R. J. Ivison, A. Karim, K. K. Knudsen, B. M. Poggianti, E. Schinnerer, A. P. Thomson, F. Walter, J. L. Wardlow, A. Weiß, and P. P. van der Werf. An ALMA Survey of Submillimeter Galaxies in the Extended Chandra Deep Field South: The Redshift Distribution and Evolution of Submillimeter Galaxies. *ApJ*, 788(2):125, June 2014. doi: 10.1088/0004-637X/788/2/125.

J. M. Simpson, Ian Smail, U. Dudzevičiūtė, Y. Matsuda, B. C. Hsieh, W. H. Wang, A. M. Swinbank, S. M. Stach, Fang Xia An, J. E. Birkin, Y. Ao, A. J. Bunker, S. C. Chapman, Chian-Chou Chen, K. E. K. Coppin, S. Ikarashi, R. J. Ivison, I. Mitsuhashi, T. Saito, H. Umehata, R. Wang, and Y. Zhao. An ALMA survey of the brightest sub-millimetre sources in the SCUBA-2-COSMOS field. *MNRAS*, 495(3):3409–3430, July 2020. doi: 10.1093/mnras/staa1345.

J. Singal, V. Petrosian, A. Lawrence, and Ł. Stawarz. On the Radio and Optical Luminosity Evolution of Quasars. *ApJ*, 743:104, December 2011. doi: 10.1088/0004-637X/743/2/104.

J. Skilling. Nested Sampling. In R. Fischer, R. Preuss, and U. V. Toussaint, editors, *American Institute of Physics Conference Series*, volume 735 of *American Institute of Physics Conference Series*, pages 395–405, November 2004. doi: 10.1063/1.1835238.

D. J. B. Smith, M. J. Jarvis, M. J. Hardcastle, M. Vaccari, N. Bourne, L. Dunne, E. Ibar, N. Maddox, M. Prescott, C. Vlahakis, S. Eales, S. J. Maddox, M. W. L. Smith, E. Valiante, and G. de Zotti. The temperature dependence of the far-infrared-radio correlation in the Herschel-ATLAS. *MNRAS*, 445(3):2232–2243, December 2014. doi: 10.1093/mnras/stu1830.

Daniel J. B. Smith and Christopher C. Hayward. Panchromatic SED modelling of spatially resolved galaxies. *MNRAS*, 476(2):1705–1725, May 2018. doi: 10.1093/mnras/sty311.

V. Smolčić, G. Zamorani, E. Schinnerer, S. Bardelli, M. Bondi, L. Bîrzan, C. L. Carilli, P. Ciliegi, M. Elvis, C. D. Impey, A. M. Koekemoer, A. Merloni, T. Paglione, M. Salvato, M. Scodeggio, N. Scoville, and J. R. Trump. Cosmic Evolution of Radio Selected Active Galactic Nuclei in the Cosmos Field. *ApJ*, 696:24–39, May 2009. doi: 10.1088/0004-637X/696/1/24.

V. Smolčić, M. Novak, I. Delvecchio, L. Ceraj, M. Bondi, J. Delhaize, S. Marchesi, E. Murphy, E. Schinnerer, E. Vardoulaki, and G. Zamorani. The VLA-COSMOS 3 GHz Large Project: Cosmic evolution of radio AGN and implications for radio-mode feedback since z 5. *A&A*, 602: A6, June 2017. doi: 10.1051/0004-6361/201730685.

V. Smolčić, I. Delvecchio, G. Zamorani, N. Baran, M. Novak, J. Delhaize, E. Schinnerer, S. Berta, M. Bondi, P. Ciliegi, P. Capak, F. Civano, A. Karim, O. Le Fevre, O. Ilbert, C. Laigle, S. Marchesi, H. J. McCracken, L. Tasca, M. Salvato, and E. Vardoulaki. The VLA-COSMOS 3 GHz Large Project: Multiwavelength counterparts and the composition of the faint radio population. *A&A*, 602:A2, June 2017a. doi: 10.1051/0004-6361/201630223.

V. Smolčić, M. Novak, I. Delvecchio, L. Ceraj, M. Bondi, J. Delhaize, S. Marchesi, E. Murphy, E. Schinnerer, E. Vardoulaki, and G. Zamorani. The VLA-COSMOS 3 GHz Large Project: Cosmic evolution of radio AGN and implications for radio-mode feedback since z 5. *A&A*, 602: A6, June 2017b. doi: 10.1051/0004-6361/201730685.

V. Springel, S. D. M. White, A. Jenkins, C. S. Frenk, N. Yoshida, L. Gao, J. Navarro, R. Thacker, D. Croton, J. Helly, J. A. Peacock, S. Cole, P. Thomas, H. Couchman, A. Evrard, J. Colberg, and F. Pearce. Simulations of the formation, evolution and clustering of galaxies and quasars. *Nature*, 435:629–636, June 2005. doi: 10.1038/nature03597.

H. R. Stacey, J. P. McKean, N. C. Robertson, R. J. Ivison, K. G. Isaak, D. R. G. Schleicher, P. P. van der Werf, W. A. Baan, A. Berciano Alba, M. A. Garrett, and A. F. Loenen. Gravitational lensing reveals extreme dust-obscured star formation in quasar host galaxies. *MNRAS*, 476(4): 5075–5114, Jun 2018. doi: 10.1093/mnras/sty458.

T. P. Stecher and B. Donn. On Graphite and Interstellar Extinction. *ApJ*, 142:1681, November 1965. doi: 10.1086/148461.

J. M. Stil. Stacking of Radio Continuum Surveys. In A. R. Taylor and E. Rosolowsky, editors, *Astronomical Data Analysis Software an Systems XXIV (ADASS XXIV)*, volume 495 of *Astronomical Society of the Pacific Conference Series*, page 241, September 2015.

J. M. Stil, B. W. Keller, S. J. George, and A. R. Taylor. Degree of Polarization and Source Counts of Faint Radio Sources from Stacking Polarized Intensity. *ApJ*, 787(2):99, June 2014. doi: 10.1088/0004-637X/787/2/99.

Naoshi Sugiyama. Cosmic Background Anisotropies in Cold Dark Matter Cosmology. *ApJS*, 100: 281, October 1995. doi: 10.1086/192220.

G. A. Tammann, A. Yahil, and A. Sandage. The velocity field of bright nearby galaxies. II - Luminosity functions for various Hubble types and luminosity classes - The peculiar motion of the local group relative to the Virgo cluster. *ApJ*, 234:775–784, December 1979. doi: 10.1086/157556.

R. Terlevich, J. Melnick, and M. Moles. Starburst Models for AGNS. In E. E. Khachikian, K. J. Fricke, and J. Melnick, editors, *Observational Evidence of Activity in Galaxies*, volume 121 of *IAU Symposium*, page 499, 1987.

R. Terlevich, G. Tenorio-Tagle, J. Franco, and J. Melnick. The starburst model for active galactic nuclei - The broad-line region as supernova remnants evolving in a high-density medium. *MNRAS*, 255:713–728, April 1992. doi: 10.1093/mnras/255.4.713.

Ingo Thies and Pavel Kroupa. A Discontinuity in the Low-Mass Initial Mass Function. *ApJ*, 671 (1):767–780, December 2007. doi: 10.1086/522512.

Nicole Thomas, Romeel Davé, Daniel Anglés-Alcázar, and Matt Jarvis. Black hole - Galaxy correlations in SIMBA. *MNRAS*, 487(4):5764–5780, August 2019. doi: 10.1093/mnras/stz1703.

L. Toffolatti and X. Barcons. Clustering Properties of X-Ray Sources from the Analysis of the GINGA P D Distribution. In Wolfgang Brinkmann and Joachim Truemper, editors, *X-ray Emission from Active Galactic Nuclei and the Cosmic X-ray Background*, page 358, March 1992.

L. Toffolatti, F. Argueso Gomez, G. de Zotti, P. Mazzei, A. Franceschini, L. Danese, and C. Burigana. Extragalactic source counts and contributions to the anisotropies of the cosmic microwave background: predictions for the Planck Surveyor mission. *MNRAS*, 297(1):117–127, June 1998. doi: 10.1046/j.1365-8711.1998.01458.x.

J. E. Tohline. Hydrodynamic Collapse. *Fundamentals Cosmic Phys.*, 8:1–82, January 1982.

S. Tremaine, K. Gebhardt, R. Bender, G. Bower, A. Dressler, S. M. Faber, A. V. Filippenko, R. Green, C. Grillmair, L. C. Ho, J. Kormendy, T. R. Lauer, J. Magorrian, J. Pinkney, and D. Richstone. The Slope of the Black Hole Mass versus Velocity Dispersion Correlation. *ApJ*, 574:740–753, August 2002. doi: 10.1086/341002.

C. M. Urry and P. Padovani. Unified Schemes for Radio-Loud Active Galactic Nuclei. *PASP*, 107: 803, September 1995. doi: 10.1086/133630.

Petri Väisänen, Eric V. Tollestrup, and Giovanni G. Fazio. Confusion limit resulting from galaxies: using the Infrared Array Camera on board SIRTF. *MNRAS*, 325(3):1241–1252, August 2001. doi: 10.1046/j.1365-8711.2001.04566.x.

P. C. van der Kruit. Observations of core sources in Seyfert and normal galaxies with the Westerbork synthesis radio telescope at 1415 MHz. *A&A*, 15:110–122, November 1971.

M. P. van Haarlem, M. W. Wise, A. W. Gunst, G. Heald, J. P. McKean, J. W. T. Hessels, A. G. de Bruyn, R. Nijboer, J. Swinbank, R. Fallows, M. Brentjens, A. Nelles, R. Beck, H. Falcke, R. Fender, J. Hörandel, L. V. E. Koopmans, G. Mann, G. Miley, H. Röttgering, B. W. Stappers, R. A. M. J. Wijers, S. Zaroubi, M. van den Akker, A. Alexov, J. Anderson, K. Anderson, A. van Ardenne, M. Arts, A. Asgekar, I. M. Avruch, F. Batejat, L. Bähren, M. E. Bell, M. R. Bell, I. van Bemmel, P. Bennema, M. J. Bentum, G. Bernardi, P. Best, L. Bîrzan, A. Bonafede, A.-J. Boonstra, R. Braun, J. Bregman, F. Breitling, R. H. van de Brink, J. Broderick, P. C. Broekema, W. N. Brouw, M. Brüggen, H. R. Butcher, W. van Cappellen, B. Ciardi, T. Coenen, J. Conway, A. Coolen, A. Corstanje, S. Damstra, O. Davies, A. T. Deller, R.-J. Dettmar, G. van Diepen, K. Dijkstra, P. Donker, A. Doorduin, J. Dromer, M. Drost, A. van Duin, J. Eislöffel, J. van Enst, C. Ferrari, W. Frieswijk, H. Gankema, M. A. Garrett, F. de Gasperin, M. Gerbers, E. de Geus, J.-M. Grießmeier, T. Grit, P. Gruppen, J. P. Hamaker, T. Hassall, M. Hoeft, H. A. Holties, A. Horneffer, A. van der Horst, A. van Houwelingen, A. Huijgen, M. Iacobelli, H. Intema, N. Jackson, V. Jelic, A. de Jong, E. Juette, D. Kant, A. Karastergiou, A. Koers, H. Kollen, V. I. Kondratiev, E. Kooistra, Y. Koopman, A. Koster, M. Kuniyoshi, M. Kramer, G. Kuper, P. Lambropoulos, C. Law, J. van Leeuwen, J. Lemaitre, M. Loose, P. Maat, G. Macario, S. Markoff, J. Masters, R. A. McFadden, D. McKay-Bukowski, H. Meijering, H. Meulman, M. Mevius, E. Middelberg, R. Millenaar, J. C. A. Miller-Jones, R. N. Mohan, J. D. Mol, J. Morawietz, R. Morganti, D. D. Mulcahy, E. Mulder, H. Munk, L. Nieuwenhuis, R. van Nieuwpoort, J. E. Noordam, M. Norden, A. Noutsos, A. R. Offringa, H. Olofsson, A. Omar, E. Orrú, R. Overeem, H. Paas, M. Pandey-Pommier, V. N. Pandey, R. Pizzo, A. Polatidis, D. Rafferty, S. Rawlings, W. Reich, J.-P. de Reijer, J. Reitsma, G. A. Renting, P. Riemers, E. Rol, J. W. Romein, J. Roosjen, M. Ruiter, A. Scaife, K. van der Schaaf, B. Scheers, P. Schellart, A. Schoenmakers, G. Schoonderbeek, M. Serylak, A. Shulevski, J. Sluman, O. Smirnov, C. Sobey, H. Spreeuw, M. Steinmetz, C. G. M. Sterks, H.-J. Stiepel, K. Stuurwold, M. Tagger, Y. Tang, C. Tasse, I. Thomas, S. Thoudam, M. C. Toribio, B. van der Tol, O. Usov, M. van Veelen, A.-J. van der Veen, S. ter Veen, J. P. W. Verbiest, R. Vermeulen, N. Vermaas, C. Vocks, C. Vogt, M. de Vos, E. van der Wal, R. van Weeren, H. Weggemans, P. Weltevrede, S. White, S. J. Wijnholds, T. Wilhelmsson, O. Wucknitz, S. Yatawatta, P. Zarka, A. Zensus, and J. van Zwieten. LOFAR: The LOw-Frequency ARray. *A&A*, 556:A2, August 2013. doi: 10.1051/0004-6361/201220873.

T. Vernstrom, D. Scott, J. V. Wall, J. J. Condon, W. D. Cotton, E. B. Fomalont, K. I. Kellermann, N. Miller, and R. A. Perley. Deep 3 GHz number counts from a P(D) fluctuation analysis. *MNRAS*, 440:2791–2809, May 2014. doi: 10.1093/mnras/stu470.

T. Vernstrom, Douglas Scott, J. V. Wall, J. J. Condon, W. D. Cotton, K. I. Kellermann, and R. A. Perley. Deep 3-GHz observations of the Lockman Hole North with the Very Large Array - II. Catalogue and μJy source properties. *MNRAS*, 462(3):2934–2949, November 2016. doi: 10.1093/mnras/stw1836.

W. H. Wang, L. L. Cowie, and A. J. Barger. A Near-Infrared Analysis of the Submillimeter Background and the Cosmic Star-Formation History. *ApJ*, 647(1):74–85, August 2006. doi: 10.1086/505292.

T. M. A. Webb, M. Brodwin, S. Eales, and S. J. Lilly. The Submillimeter Properties of Extremely Red Objects in the Canada-UK Deep Submillimeter Survey Fields. *ApJ*, 605(2):645–655, April 2004. doi: 10.1086/381796.

Joseph C. Weingartner and B. T. Draine. Dust Grain-Size Distributions and Extinction in the Milky Way, Large Magellanic Cloud, and Small Magellanic Cloud. *ApJ*, 548(1):296–309, February 2001. doi: 10.1086/318651.

M. W. Werner, T. L. Roellig, F. J. Low, G. H. Rieke, M. Rieke, W. F. Hoffmann, E. Young, J. R. Houck, B. Brandl, G. G. Fazio, J. L. Hora, R. D. Gehrz, G. Helou, B. T. Soifer, J. Stauffer, J. Keene, P. Eisenhardt, D. Gallagher, T. N. Gautier, W. Irace, C. R. Lawrence, L. Simmons, J. E. Van Cleve, M. Jura, E. L. Wright, and D. P. Cruikshank. The Spitzer Space Telescope Mission. *ApJS*, 154(1):1–9, September 2004. doi: 10.1086/422992.

Katherine E. Whitaker, Marijn Franx, Joel Leja, Pieter G. van Dokkum, Alaina Henry, Rosalind E. Skelton, Mattia Fumagalli, Ivelina G. Momcheva, Gabriel B. Brammer, Ivo Labbé, Erica J. Nelson, and Jane R. Rigby. Constraining the Low-mass Slope of the Star Formation Sequence at 0.5 < z < 2.5. *ApJ*, 795(2):104, November 2014. doi: 10.1088/0004-637X/795/2/104.

R. L. White, D. J. Helfand, R. H. Becker, E. Glikman, and W. de Vries. Signals from the Noise: Image Stacking for Quasars in the FIRST Survey. *ApJ*, 654:99–114, January 2007. doi: 10.1086/507700.

S. D. M. White and M. J. Rees. Core condensation in heavy halos: a two-stage theory for galaxy formation and clustering. *MNRAS*, 183:341–358, May 1978. doi: 10.1093/mnras/183.3.341.

S. V. White, M. J. Jarvis, B. Häußler, and N. Maddox. Radio-quiet quasars in the VIDEO survey: evidence for AGN-powered radio emission at S_{1.4 GHz 1} mJy. *MNRAS*, 448:2665–2686, April 2015. doi: 10.1093/mnras/stv134.

S. V. White, M. J. Jarvis, E. Kalfountzou, M. J. Hardcastle, A. Verma, J. M. Cao Orjales, and J. Stevens. Evidence that the AGN dominates the radio emission in z
1 radio-quiet quasars. *MNRAS*, 468:217–238, June 2017. doi: 10.1093/mnras/stx284.

Simon D. M. White and Carlos S. Frenk. Galaxy Formation through Hierarchical Clustering. *ApJ*, 379:52, September 1991. doi: 10.1086/170483.

Rik J. Williams, Ryan F. Quadri, Marijn Franx, Pieter van Dokkum, and Ivo Labbé. Detection of Quiescent Galaxies in a Bicolor Sequence from Z = 0-2. *ApJ*, 691(2):1879–1895, February 2009. doi: 10.1088/0004-637X/691/2/1879.

C. J. Willott, S. Rawlings, K. M. Blundell, M. Lacy, and S. A. Eales. The radio luminosity function from the low-frequency 3CRR, 6CE and 7CRS complete samples. *MNRAS*, 322:536–552, April 2001. doi: 10.1046/j.1365-8711.2001.04101.x.

Chris J. Willott, Steve Rawlings, Katherine M. Blundell, and Mark Lacy. The radio luminosity function of radio-loud quasars from the 7C Redshift Survey. *MNRAS*, 300(3):625–648, Nov 1998. doi: 10.1046/j.1365-8711.1998.01946.x.

R. J. Wilman, L. Miller, M. J. Jarvis, T. Mauch, F. Levrier, F. B. Abdalla, S. Rawlings, H.-R. Klöckner, D. Obreschkow, D. Olteanu, and S. Young. A semi-empirical simulation of the extragalactic radio continuum sky for next generation radio telescopes. *MNRAS*, 388:1335–1348, August 2008. doi: 10.1111/j.1365-2966.2008.13486.x.

R. J. Wilman, M. J. Jarvis, T. Mauch, S. Rawlings, and S. Hickey. An infrared-radio simulation of the extragalactic sky: from the Square Kilometre Array to Herschel. *MNRAS*, 405:447–461, June 2010. doi: 10.1111/j.1365-2966.2010.16453.x.

A. S. Wilson and E. J. M. Colbert. The difference between radio-loud and radio-quiet active galaxies. *ApJ*, 438:62–71, January 1995. doi: 10.1086/175054.

R. A. Windhorst, G. M. van Heerde, and P. Katgert. A deep Westerbork survey of areas with multicolor Mayall 4 M plates. I. The 1412 MHz catalogue, source counts and angular size statistics. *A&AS*, 58:1–37, October 1984.

R. A. Windhorst, G. K. Miley, F. N. Owen, R. G. Kron, and D. C. Koo. Sub-millijansky 1.4 GHz source counts and multicolor studies of weak radio galaxy populations. *ApJ*, 289:494–513, February 1985. doi: 10.1086/162911.

Rogier A. Windhorst. The microjansky and nanojansky population. *New Astronomy Reviews*, 47 (4):357 – 365, 2003. ISSN 1387-6473. doi: https://doi.org/10.1016/S1387-6473(03)00045-9. URL http://www.sciencedirect.com/science/article/pii/S1387647303000459. High-redshift radio galaxies - past, present and future.

A. H. Wright, A. S. G. Robotham, N. Bourne, S. P. Driver, L. Dunne, S. J. Maddox, M. Alpaslan, S. K. Andrews, A. E. Bauer, J. Bland-Hawthorn, S. Brough, M. J. I. Brown, C. Clarke, M. Cluver, L. J. M. Davies, M. W. Grootes, B. W. Holwerda, A. M. Hopkins, T. H. Jarrett, P. R. Kafle, R. Lange, J. Liske, J. Loveday, A. J. Moffett, P. Norberg, C. C. Popescu, M. Smith, E. N. Taylor, R. J. Tuffs, L. Wang, and S. M. Wilkins. Galaxy And Mass Assembly: accurate panchromatic photometry from optical priors using LAMBDAR. *MNRAS*, 460(1):765–801, July 2016. doi: 10.1093/mnras/stw832.

Stijn Wuyts, Ivo Labbé, Marijn Franx, Gregory Rudnick, Pieter G. van Dokkum, Giovanni G. Fazio, Natascha M. Förster Schreiber, Jiasheng Huang, Alan F. M. Moorwood, Hans-Walter Rix, Huub Röttgering, and Paul van der Werf. What Do We Learn from IRAC Observations of Galaxies at 2 < z < 3.5? *ApJ*, 655(1):51–65, January 2007. doi: 10.1086/509708.

Ted K. Wyder, D. Christopher Martin, David Schiminovich, Mark Seibert, Tamás Budavári, Marie A. Treyer, Tom A. Barlow, Karl Forster, Peter G. Friedman, Patrick Morrissey, Susan G. Neff, Todd Small, Luciana Bianchi, José Donas, Timothy M. Heckman, Young-Wook Lee, Barry F. Madore, Bruno Milliard, R. Michael Rich, Alex S. Szalay, Barry Y. Welsh, and Sukyoung K. Yi. The UV-Optical Galaxy Color-Magnitude Diagram. I. Basic Properties. *ApJS*, 173(2):293–314, December 2007. doi: 10.1086/521402.

Y. Yamaguchi, K. Kohno, B. Hatsukade, T. Wang, Y. Yoshimura, Y. Ao, J. S. Dunlop, E. Egami, D. Espada, S. Fujimoto, N. H. Hayatsu, R. J. Ivison, T. Kodama, H. Kusakabe, T. Nagao, M. Ouchi, W. Rujopakarn, K. Tadaki, Y. Tamura, Y. Ueda, H. Umehata, and W. H. Wang. ALMA 26 arcmin^2 survey of GOODS-S at one-millimeter (ASAGAO): millimeter properties of stellar mass selected galaxies. *arXiv e-prints*, art. arXiv:2005.13346, May 2020.

D. G. York, J. Adelman, J. E. Anderson, Jr., S. F. Anderson, J. Annis, N. A. Bahcall, J. A. Bakken, R. Barkhouser, S. Bastian, E. Berman, W. N. Boroski, S. Bracker, C. Briegel, J. W. Briggs, J. Brinkmann, R. Brunner, S. Burles, L. Carey, M. A. Carr, F. J. Castander, B. Chen, P. L. Colestock, A. J. Connolly, J. H. Crocker, I. Csabai, P. C. Czarapata, J. E. Davis, M. Doi,

T. Dombeck, D. Eisenstein, N. Ellman, B. R. Elms, M. L. Evans, X. Fan, G. R. Federwitz, L. Fiscelli, S. Friedman, J. A. Frieman, M. Fukugita, B. Gillespie, J. E. Gunn, V. K. Gurbani, E. de Haas, M. Haldeman, F. H. Harris, J. Hayes, T. M. Heckman, G. S. Hennessy, R. B. Hindsley, S. Holm, D. J. Holmgren, C.-h. Huang, C. Hull, D. Husby, S.-I. Ichikawa, T. Ichikawa, Ž. Ivezić, S. Kent, R. S. J. Kim, E. Kinney, M. Klaene, A. N. Kleinman, S. Kleinman, G. R. Knapp, J. Korienek, R. G. Kron, P. Z. Kunszt, D. Q. Lamb, B. Lee, R. F. Leger, S. Limmongkol, C. Lindenmeyer, D. C. Long, C. Loomis, J. Loveday, R. Lucinio, R. H. Lupton, B. MacKinnon, E. J. Mannery, P. M. Mantsch, B. Margon, P. McGehee, T. A. McKay, A. Meiksin, A. Merelli, D. G. Monet, J. A. Munn, V. K. Narayanan, T. Nash, E. Neilsen, R. Neswold, H. J. Newberg, R. C. Nichol, T. Nicinski, M. Nonino, N. Okada, S. Okamura, J. P. Ostriker, R. Owen, A. G. Pauls, J. Peoples, R. L. Peterson, D. Petravick, J. R. Pier, A. Pope, R. Pordes, A. Prosapio, R. Rechenmacher, T. R. Quinn, G. T. Richards, M. W. Richmond, C. H. Rivetta, C. M. Rockosi, K. Ruthmansdorfer, D. Sandford, D. J. Schlegel, D. P. Schneider, M. Sekiguchi, G. Sergey, K. Shimasaku, W. A. Siegmund, S. Smee, J. A. Smith, S. Snedden, R. Stone, C. Stoughton, M. A. Strauss, C. Stubbs, M. SubbaRao, A. S. Szalay, I. Szapudi, G. P. Szokoly, A. R. Thakar, C. Tremonti, D. L. Tucker, A. Uomoto, D. Vanden Berk, M. S. Vogeley, P. Waddell, S.-i. Wang, M. Watanabe, D. H. Weinberg, B. Yanny, N. Yasuda, and SDSS Collaboration. The Sloan Digital Sky Survey: Technical Summary. *AJ*, 120:1579–1587, September 2000. doi: 10.1086/301513.

Naoki Yoshida, Kazuyuki Omukai, Lars Hernquist, and Tom Abel. Formation of Primordial Stars in a ΛCDM Universe. *ApJ*, 652(1):6–25, November 2006. doi: 10.1086/507978.

Zunli Yuan, Jiancheng Wang, Ming Zhou, and Jirong Mao. A Mixture Evolution Scenario of the AGN Radio Luminosity Function. *ApJ*, 820(1):65, March 2016. doi: 10.3847/0004-637X/820/1/65.

N. L. Zakamska, K. Lampayan, A. Petric, D. Dicken, J. E. Greene, T. M. Heckman, R. C. Hickox, L. C. Ho, J. H. Krolik, N. P. H. Nesvadba, M. A. Strauss, J. E. Geach, M. Oguri, and I. V. Strateva. Star formation in quasar hosts and the origin of radio emission in radio-quiet quasars. *MNRAS*, 455:4191–4211, February 2016. doi: 10.1093/mnras/stv2571.

Nadia L. Zakamska and Jenny E. Greene. Quasar feedback and the origin of radio emission in radio-quiet quasars. *MNRAS*, 442(1):784–804, Jul 2014. doi: 10.1093/mnras/stu842.

J. A. Zavala, C. M. Casey, N. Scoville, J. B. Champagne, Y. Chiang, H. Dannerbauer, P. Drew, H. Fu, J. Spilker, L. Spitler, K. V. Tran, E. Treister, and S. Toft. On the Gas Content, Star Formation Efficiency, and Environmental Quenching of Massive Galaxies in Protoclusters at z ≈ 2.02.5. *ApJ*, 887(2):183, December 2019. doi: 10.3847/1538-4357/ab5302.

Stefano Zibetti and Annette M. N. Ferguson. A faint red stellar halo around an edge-on disc galaxy in the Hubble Ultra Deep Field. *MNRAS*, 352(4):L6–L10, August 2004. doi: 10.1111/j.1365-2966.2004.08106.x.

Stefano Zibetti, Brice Ménard, Daniel Nestor, and David Turnshek. Constraining the Photometric Properties of Mg II-absorbing Galaxies with the Sloan Digital Sky Survey. *ApJ*, 631(2):L105–L108, October 2005. doi: 10.1086/497424.

P. C. Zinn, E. Middelberg, R. P. Norris, C. A. Hales, M. Y. Mao, and K. E. Randall. The Australia Telescope Large Area Survey: 2.3 GHz observations of ELAIS-S1 and CDF-S. Spectral index properties of the faint radio sky. *A&A*, 544:A38, August 2012. doi: 10.1051/0004-6361/201219349.

J. Zwart, J. Wall, A. Karim, C. Jackson, R. Norris, J. Condon, J. Afonso, I. Heywood, M. Jarvis, F. Navarrete, I. Prandoni, E. Rigby, H. J. A. Rottgering, M. Santos, M. Sargent, N. Seymour, R. Taylor, and T. Vernstrom. Astronomy Below the Survey Threshold in the SKA Era. *Advancing Astrophysics with the Square Kilometre Array (AASKA14)*, art. 172, 2015a.

J. T. L. Zwart, M. J. Jarvis, R. P. Deane, D. G. Bonfield, K. Knowles, N. Madhanpall, H. Rahmani, and D. J. B. Smith. The star formation history of mass-selected galaxies from the VIDEO survey. *MNRAS*, 439:1459–1471, April 2014. doi: 10.1093/mnras/stu053.

J. T. L. Zwart, M. Santos, and M. J. Jarvis. Far beyond stacking: fully Bayesian constraints on sub-μJy radio source populations over the XMM-LSS-VIDEO field. *MNRAS*, 453:1740–1753, October 2015b. doi: 10.1093/mnras/stv1716.